

# Modification of a High Pressure Test Rig for Thermoacoustic Measurements

vorgelegt von

M. Sc. Sebastian Niether

geboren in Rüdersdorf

von der Fakultät V – Verkehrs- und Maschinensysteme  
der Technischen Universität Berlin  
zur Erlangung des akademischen Grades

Doktor der Ingenieurwissenschaften  
– Dr.-Ing. –

genehmigte Dissertation

Promotionsausschuss:

Vorsitzender: Prof. Dr. rer. nat. Valentin Popov

Gutachter: Prof. Dr.-Ing. Christian Oliver Paschereit  
Dr.-Ing. Mirko Ruben Bothien

Tag der wissenschaftlichen Aussprache: 05.07.2018

Berlin 2018



---

## Vorwort

Diese Dissertation entstand während meiner Arbeit als wissenschaftlicher Mitarbeiter am Fachgebiet für Experimentelle Strömungsmechanik des Instituts für Strömungsmechanik und Technische Akustik an der TU Berlin. In dieser Zeit haben mich viele Menschen unterstützt und diese Arbeit zu dem gemacht, was sie ist.

Zunächst bedanke ich mich bei Prof. Dr.-Ing. Christian Oliver Paschereit, der mir als mein Doktorvater viele Freiheiten sowie das nötige Vertrauen geschenkt hat. Die uneingeschränkte Unterstützung und eine dauerhaft positive Einstellung haben eine sehr angenehme Arbeitatmosphäre geschaffen. Dr.-Ing. Mirko Bothien danke ich zunächst dafür, dass er sich als Gutachter bereit erklärt hat. Weiterhin möchte ich auch seine hervorragende Arbeit am Fachgebiet erwähnen, welche die Grundlage meines Projekts und damit dieser Dissertation darstellt.

Prof. Dr. rer. nat. Valentin Popov, der mich als Prüfungsbobmann über das Studium hinweg begleitet hat, danke ich für den Prüfungsvorsitz.

Dr.-Ing. Lukasz Panek hat mir mit seinem freundschaftlichen Umgang, seinem fachlichen Input und der lösungsorientierten Zusammenarbeit die Projektarbeit sehr erleichtert. Für sein Vertrauen und die Betreuung von SIEMENS-Seite möchte ich mich herzlich bedanken.

Jun.-Prof. Dr. Jonas P. Moeck danke ich für seinen fachlichen Beitrag.

Herzlicher Dank gebührt vor allem auch Anja Lohr, die mich während einem Großteil der Projektlaufzeit als studentische Mitarbeiterin begleitet hat. Nur mit ihrer Hilfe konnten die zahlreichen Messreihen rechtzeitig fertiggestellt werden. Anjas eigenverantwortliches Arbeiten, die gute Kommunikation, ihr Engagement und ihre Gründlichkeit haben viele Inhalte der Arbeit bereichert.

Weiterhin möchte ich Erik Schneehagen und Gerald Schmidt für ihre sehr guten Masterarbeiten danken, deren Ergebnisse wichtige Beiträge zum Projekt geliefert haben.

Natürlich danke ich auch meinen Kollegen (und mittlerweile Freunden) für die außergewöhnlich angenehme Arbeitsatmosphäre und die fruchtbaren fachlichen Gespräche. Besonderer Dank gilt Thoralf Reichel, der sich seit meinem ersten Tag ein Büro mit mir geteilt hat und der auch neben der Arbeit viele Interessen mit mir teilt.

Bei Niclas Hanraths bedanke ich mich für seine sehr gute Abschlussarbeit und die daraus entstandene gemeinsame Veröffentlichung, die einen wichtigen Aspekt der Arbeit beleuchtet. Dank Johann Vinkeloe und Martin Jurisch und deren teilweise außerplanmäßiger Zusammenarbeit, wurden interessante Einblicke in das Verhalten des entwickelten Aktuators möglich. Außerdem bedanke ich mich bei Aditya Saurabh, Olaf Bölke und Moritz Sieber, die mir bei vielen praktischen Fragestellungen helfen konnten und stets ein offenes Ohr hatten. Weiterhin möchte ich Bernhard Bobusch für seine *Schule* danken, durch die ich einiges an Vorwissen für die Stelle mitbringen und anwenden konnte. Auch meinen Bürokollegen Lothar Rukes, Phoebe Kuhn, Tim Rähse und Marvin Jentzsch danke ich für die vielen wichtigen Gespräche, die die Zeit am Institut so angenehm gemacht haben.

Praktische Probleme, die auf dem Weg zu erfolgreichen Messungen aufgetaucht sind wurden stets durch Andy Göhrs, Robert Bahnweg oder Heiko Stolpe gelöst. Alle Arbeiten wurden in kürzester Zeit erledigt und waren durchweg von höchster Qualität. Auch den übrigen Werkstattmitarbeitern, sowie Torsten Dessin danke ich an dieser Stelle für ihren Einsatz

und ihre Hilfsbereitschaft. Bei Computerproblemen sind Angela Pätzold und insbesondere Martin Franke jederzeit schnell und unkompliziert eingesprungen. Maria und Sandy aus dem Sekretariat danke ich für ihren Einsatz und die zugleich freundliche und professionelle Zusammenarbeit.

Ich bedanke mich weiterhin meinen Eltern für ihre Unterstützung und das Vertrauen in meine Fähigkeiten. Ohne euren uneingeschränkten Rückhalt wäre ich nicht da, wo ich jetzt bin.

Zu guter Letzt danke ich der wichtigsten Person in meinem Leben, Maren Wendland. Deine Unterstützung und unsere kritischen sowie aufmunternden Gespräche waren stark beteiligt am Entstehen dieser Arbeit. Unsere beiden Kinder sind der wichtigste Bestandteil meines Lebens geworden und haben letztlich mit ihrem positiven Einfluss auf mich auch einen Anteil an der Arbeit.

---

## Zusammenfassung

Aktuelle stationäre Gasturbinen zur Stromerzeugung setzen auf eine mager vorgemischte Verbrennung, um niedrige Emissionen von schädlichen Abgasen wie  $\text{NO}_x$  zu erreichen. Der Einsatz dieses Verbrennungsprozesses kann jedoch zu thermoakustischen Instabilitäten führen. Dieses Phänomen, das durch starke Druckschwankungen in der Brennkammer gekennzeichnet ist, wirkt sich negativ auf die Abgasemissionen, den Wirkungsgrad, das Geräuschverhalten und die Lebensdauer der Gasturbine aus. Die Vermeidung dieser unerwünschten Druckschwankungen ist von großem Interesse für die Hersteller.

Die Stabilität eines Verbrennungssystems im gesamten Betriebsbereich lässt sich in der Regel nur in Tests an der kompletten Maschine abschließend nachweisen. Allerdings sind diese sehr teuer und daher ineffizient. So werden Tests in Hochdruck-Verbrennungsprüfständen durchgeführt. In diesen Studien sind Parameter wie das Strömungsfeld, das Temperaturprofil und das mittlere Druckniveau gleich derer in der Maschine. Die akustischen Randbedingungen, die einen starken Einfluss auf die Stabilität eines Verbrennungssystems haben, sind jedoch möglicherweise nicht gleich. Dies gilt auch für moderne Can-Brennkammern. Wechselwirkungen mit der Turbine und benachbarten Brennkammern können die akustischen Randbedingungen am Brennkammerauslass beeinflussen. Ein System, das im Hochdruckversuch keine instabilen Betriebspunkte aufweist, kann in der Maschine dennoch anfällig für Druckschwankungen sein. Um dies zu vermeiden, kann eine aktive Veränderung der akustischen Randbedingung im Prüfstand durchgeführt werden. Ein entsprechendes Konzept erlaubt z. B. die Anpassung der Impedanz am Brennkammerauslass des Prüfstands an die der Maschine.

Im Rahmen dieser Arbeit werden Modifikationen zur Ermöglichung akustischer Untersuchungen an einem bestehenden Hochdruck-Verbrennungsprüfstand vorgeschlagen. Unter Beibehaltung der ursprünglichen Geometrie soll der Prüfstand mit geeigneten Vorkehrungen zur Erreichung von zwei Hauptzielen ausgestattet werden. Ein Ziel ist die aktive Veränderung der akustischen Randbedingung (Impedance Tuning), die eine direkte Beurteilung der Stabilitätseigenschaften eines Brennersystems ermöglicht. Das zweite Ziel ist die Messung des Flammenübertragungsverhaltens, das zur Stabilitätsanalyse in einem niederdimensionalen Netzwerkmodell verwendet wird. Da die Ergebnisse aus Hochdruckversuchen stammen, sind sie nicht von vereinfachenden Annahmen abhängig, mit denen üblicherweise Daten von atmosphärischen Prüfständen übernommen werden können.

Zunächst werden die Anforderungen zur Erreichung beider Ziele festgelegt und die notwendigen Hardwaremodifikationen umrissen, die akustische Sensoren und Aktuatoren stromauf und stromab des Brenners umfassen. Eine große Schwierigkeit bei der Umsetzung der Modifikationen liegt in der Anpassung an die bestehende Geometrie, die für akustische Messungen generell eher ungeeignet ist.

Für die akustische Anregung stromauf des Brenners wird eine Sirene vorgeschlagen, dessen Positionierung an zwei Stellen im Prüfstand numerisch untersucht wird. Weiterhin werden zwei Sensorkonzepte für den Bereich stromauf des Brenners vorgeschlagen. Bei beiden werden durch dynamische Drucksensoren die akustischen Größen am Brennereintritt erfasst, die zur Bestimmung des Flammenübertragungsverhaltens benötigt werden.

Die Umsetzung der aktiven Impedanzanpassung erfordert ein Sensorarray in der Brennkammer. Die vorhandene Geometrie erschwert jedoch die Implementierung einer standardisierten Methode zur ebenen Wellenzerlegung. Daher werden Methoden zur Bestimmung der sich stromauf und stromab ausbreitenden Schallwellen für Frequenz- und Zeitbereichsmessungen in einem Kanal mit veränderlichem Querschnitt entwickelt.

Für die akustische Anregung stromab der Brennkammer wird ein neuartiges Anregungskonzept vorgeschlagen. Dabei werden zur Schallerzeugung mit Hilfe eines Proportionalventils hohe Massenströme modulierter Luft in die Verengung am Brennkammerauslass eingedüst. Zudem unterstützt die Anregungsposition die erfolgreiche Umsetzung der aktiven Impedanzanpassung durch vorteilhafte Zeitverzögerungen. Andererseits bewirkt die Eindüsung eines modulierten Luftmassenstroms in den kleinsten Querschnitt eine oszillierende Blockage des Hauptluftmassenstroms. Dadurch wird die erreichbare Anregungsamplitude, gegenüber der Anbringung des gleichen Aktuators an jeder anderen Stelle im Prüfstand, stark erhöht.

Mit den Ergebnissen dieser Arbeit wird ein umfassendes Konzept vorgestellt, das Anpassungen eines Hochdruckprüfstands für thermoakustische Messungen ermöglicht.

---

## Abstract

Current stationary gas turbines for power generation rely on lean premixed combustion, in order to achieve low emissions of detrimental exhaust gases, such as  $\text{NO}_x$ . However, employment of this combustion process can lead to the occurrence of thermoacoustic instabilities. Characterized by strong pressure fluctuations inside the combustion chamber, this phenomenon has negative effects on exhaust gas emissions, efficiency, noise characteristics, and durability of the gas turbine. Thus, inhibition of these unwanted pressure fluctuations is a major concern for manufacturers.

Usually, stability of a combustion system in the entire operating envelope can only be conclusively verified in full-scale engine tests. Yet, they are highly expensive and therefore inefficient. Thus, tests in high pressure combustion test rigs are conducted. In these studies, parameters like the flow field, temperature profiles, and mean the pressure level are similar to the engine. Yet, the acoustic boundary conditions, which have a strong influence on the stability of a combustion system, might not be equal. This is true, even for modern can-annular combustors. Interactions with the turbine and neighboring combustor cans potentially influence the acoustic boundary condition at the combustion chamber outlet. A system that has proven stable operation in high pressure tests might therefore be susceptible to unexpected self-excited pressure oscillations in the engine. To avoid this shortcoming, an active modification of the acoustic boundary condition in high pressure tests is perceived as a viable method. The scheme, e. g., allows for adaptation of the test rig's combustor outlet impedance to that present in the engine.

Within this thesis, modifications for enabling acoustic investigations on an existing high pressure test facility are proposed. Under the premise of retaining the original geometry, the test rig shall be equipped with suitable instruments to realize two main objectives. One goal is the active modification of the acoustic boundary condition (impedance tuning), allowing for a direct assessment of a burner system's stability characteristics. The second goal is the measurement of the flame transfer behavior, which may be used for stability analysis in a low-order network model. As the results are obtained within a high pressure scenario, they are not dependent on any simplifying assumptions usually associated with data from atmospheric test rigs.

Initially, the requirements for achieving both objectives are stated and the necessary hardware modifications, incorporating acoustic sensors and actuators both upstream and downstream of the burner, are outlined. A major difficulty of implementation of the equipment lies in the adaptation to the existing geometry, which is hardly suited for acoustic measurements.

For upstream acoustic forcing, a siren actuator is proposed. Its positioning is numerically investigated at two locations inside the test rig. Furthermore, two sensor concepts for the region upstream of the burner are proposed. Both concepts incorporate dynamic pressure sensors for determination of the acoustic variables at the burner inlet, which is required for measurements of the flame transfer behavior.

Implementation of impedance tuning requires a sensor array inside the combustion chamber. However, the existing geometry impedes the use of a standardized method for plane wave decomposition. Thus, techniques for a frequency-domain and a time-domain determination of

the upstream and downstream propagating waves in a duct of non-uniform cross-section are developed.

For acoustic excitation downstream of the combustion chamber, a novel actuation concept is proposed. It incorporates a proportional valve, which injects high mass flows of modulated air into the restriction at the combustion chamber outlet. On one hand, the location supports a successful implementation of impedance tuning, due to advantageous time delays. On the other hand, injection of a modulated air flow into the smallest cross-section adds the effect of an oscillatory blockage of the main air flow. Thereby, the achievable actuation amplitude is strongly increased versus mounting of the same actuator at any other location in the test rig.

With the results presented in this thesis, a comprehensive concept for the implementation of modifications for thermoacoustic measurements on a high pressure test rig is introduced.

---

## Contents

---

1. Introduction and Objectives	1
1.1. Gas Turbines for Power Generation . . . . .	1
1.2. Practical Relevance of Thermoacoustic Instabilities . . . . .	3
1.3. Driving Mechanisms of Thermoacoustic Instabilities . . . . .	4
1.4. Passive and Active Control . . . . .	6
1.5. Experimental Identification of Thermoacoustic Instabilities . . . . .	7
1.6. Active Control of Acoustic Boundary Conditions . . . . .	8
1.7. Flame Response Measurements for the Thermoacoustic Characterization of Combustor Configurations . . . . .	11
1.8. Objectives and Structure of the Thesis . . . . .	14
2. Theoretical Background on Acoustics and Utilized Methods	17
2.1. Wave Equation . . . . .	17
2.1.1. Mass Source Term and Lighthill's Aeroacoustic Analogy . . . . .	19
2.1.2. One-Dimensional Solution to the Convective Wave Equation . . . . .	20
2.1.3. Boundary Conditions . . . . .	22
2.2. Plane Wave Decomposition with the Multi-Microphone Method . . . . .	23
2.3. Low-Order Network Models . . . . .	24
2.4. Active Modification of the Acoustic Boundary Condition (Impedance Tuning)	27
2.5. Plane Wave Decomposition in Time Domain . . . . .	30
3. Current Test Rig and Requirements	33
3.1. Current High Pressure Combustion Test Rig . . . . .	34
3.2. Requirements for Measurements of Flame Transfer Matrices . . . . .	35
3.3. Requirements for Measurements of Flame Transfer Functions . . . . .	36
3.4. Requirements for Impedance Tuning . . . . .	37
4. Two Sensor Concepts for the Region Upstream of the Flame	41
4.1. Discussion of the Utilized Methods . . . . .	41
4.2. Transfer Matrix Representation of the Plenum Geometry . . . . .	42
4.2.1. FEM Computations for Validation of the Transfer Matrix Representation	44
4.2.2. Computational Parameter Optimization for the Underlying Geometry of the Transfer Matrix Method . . . . .	46
4.2.3. Transfer Matrix Representation with Mean Air Flow . . . . .	49

4.3.	Determination of the Acoustic Variables Using the Unsteady Pressure Loss Over the Burner . . . . .	51
4.4.	Conclusion of the Sensor Design Upstream of the Flame . . . . .	52
5.	Wave Decomposition in the Combustor with Non-Uniform Cross-Section . . . . .	55
5.1.	Multi-Microphone Method in Ducts with Non-Uniform Cross-Sections . . . . .	55
5.1.1.	Particular Solutions to Webster's Horn Equation . . . . .	57
5.2.	Online Wave Decomposition in Ducts with Non-Uniform Cross-Sections . . . . .	58
5.3.	Numerical Validation of the Frequency-Domain Multi-Microphone Method in Non-Uniform Ducts . . . . .	61
5.4.	Experimental Validation of the Multi-Microphone Method in Non-Uniform Ducts . . . . .	67
5.5.	Conclusion and Outlook for the Developed Methods . . . . .	72
6.	Simulations for Positioning of an Actuator Upstream of the Burner . . . . .	75
6.1.	Actuator Types and Their Eligibility . . . . .	75
6.1.1.	Siren Actuator . . . . .	76
6.2.	Acoustic Simulations with Base-Plate-Mounted Actuator . . . . .	77
6.3.	Acoustic Simulations with Flow Box . . . . .	83
6.4.	Comparison of Base-Plate- and Flow-Box-Mounted Actuators . . . . .	87
6.5.	Conclusions Drawn from the Upstream Actuator Positioning . . . . .	89
7.	Development and Verification of the Actuator Concept Downstream of the Burner . . . . .	91
7.1.	Discussion of Various Actuator Concepts . . . . .	91
7.2.	Fluid Injection into Nozzles in the Literature . . . . .	96
7.3.	Numerical Simulations of the Actuator Concept . . . . .	98
7.3.1.	Numerical Setup of the Simulations for the Actuator Concept . . . . .	98
7.3.2.	Results of the CFD Simulations on the Actuator Concept . . . . .	100
7.3.3.	Combined RANS and LEE Simulations for Development of a Time-Domain Network Model . . . . .	101
7.4.	Experimental Setup for Atmospheric Experiments . . . . .	105
7.4.1.	Microphone Measurements . . . . .	109
7.4.2.	Absolute Pressure Sensors . . . . .	110
7.4.3.	Proportional Valves for Air Flow Modulation . . . . .	111
7.5.	Experimental Results for Characterization of the Actuation Concept . . . . .	113
7.5.1.	Characterization of the Proportional Valves . . . . .	113
7.5.2.	Characterization of the Nozzle . . . . .	116
7.5.3.	Modulated Air Injection into a Subsonic Nozzle at Isothermal Conditions . . . . .	118
7.5.4.	Modulated Air Injection into a Subsonic Nozzle at Reacting Conditions . . . . .	125
7.6.	Time-Domain Network Model: Impedance Tuning on the High Pressure Test Rig . . . . .	126
7.6.1.	Verification of the Time-Domain Network Model . . . . .	127
7.6.2.	Results of the Simulations with the Time-Domain Network Model . . . . .	130
7.7.	Discussion of the Downstream Actuator Concept . . . . .	136
8.	Conclusion . . . . .	139
8.1.	Additional Efforts for the Final Implementation . . . . .	141

---

Bibliography	145
A. Validation Case For The Analytical Transfer Matrix Method with Mean Flow	163



---

## List of Figures

---

1.1.	Projected fuel sources for net electricity generation worldwide, according to the International Energy Outlook 2017 by the U.S. Energy Information Administration. Formatted image from reference [179]. Left: total in $10^{18}$ kWh. Right: share in %.	2
1.2.	Left: systems with varying acoustic boundary conditions $Z_n$ , due to terminations with different geometries. Right: system with an actively modifiable boundary condition. Depiction adapted from Bothien [18].	10
2.1.	Acoustic two-ports relating Riemann invariants at both boundaries. Left: scattering matrix $\mathbf{S}(\omega)$ in frequency domain, right: state-space model in time domain.	25
2.2.	Schematic of the impedance tuning concept adapted from reference [112]. The dashed frame symbolizes the end element, the impedance of which is effectively altered by the closed-loop control scheme.	27
2.3.	Schematic of the controller implementation on the <i>dSPACE</i> controller board.	27
2.4.	Schematic of the microphone array and the end element for visualization of the control law derivation.	28
2.5.	Schematic of two pressure sensors for wave identification on a duct with constant cross-sectional area. Image adapted from [21].	30
2.6.	Feedback loop of the online wave identification scheme as developed by Moeck et al. [112] and adapted from the figure in reference [21].	31
3.1.	Render image of a SIEMENS SGT5-9000HL heavy duty gas turbine adapted from reference [166]. One can combustion chamber is highlighted by a colored frame.	33
3.2.	Schematic of the single burner high pressure combustion test rig. The parts are labeled according to the terminology used in the work.	34
3.3.	Schematic of the required instruments for measurements of flame transfer matrices. Blue and orange components denote options, i. e., only one of each is required.	35
3.4.	Schematic of the required instruments for measurements of flame transfer functions. Blue and orange components denote options, i. e., only one of each is required. The optical sensor is an alternative to the sensors denoted in black.	36

3.5.	Schematic of the required instruments for the active modification of the downstream acoustic boundary condition. Blue and orange components denote options, i. e., only one of them is required. . . . .	37
4.1.	Simplified geometry for the development of the transfer matrix method for the region upstream of the burner. Combustion air enters at the righthand face of the flow sleeve, is redirected at the plenum, then enters the two burner passages.	43
4.2.	Left: schematic geometry comprising the flow sleeve, plenum, and burner main passage with highlighted aid lines. Right: schematic of the transfer matrix representation. . . . .	43
4.3.	Sectional view of the computational domain with probe locations in the upstream located flow sleeve and the downstream located burner main passage. The reference planes are highlighted in red and the boundary conditions (a, b, c) are indicated in different colors. The downstream and upstream propagating waves $f$ and $g$ are defined with excitation at the flow sleeve. . . . .	45
4.4.	Stationary transfer matrix from FEM computations (COMSOL, dashed) and from the transfer matrix method (TMM, solid) . . . . .	46
4.5.	Normalized deviation of the analytically found transfer matrix elements from those obtained via numerical computations for the eight investigated settings (cf. TAB. 4.1). . . . .	47
4.6.	Representation of the plenum with 36 straight ducts as extracted from the original geometry (black) and optimized with the <i>fmincon</i> function at setting 6 (cf. TAB. 4.1, blue) . . . . .	48
4.7.	Stationary transfer matrix found with numerical computations (COMSOL, dashed) and the transfer matrix method applied to an optimized geometry incorporating multiple ducts (TMM, solid). . . . .	48
4.8.	Transfer matrices of the plenum representation consisting of a concatenation of straight ducts with mean flow. Absolute values colored in blue, phase in orange. Reference results computed with a stationary FEM simulation (solid). Analytical transfer matrices for various mean flow conditions obtained from the expressions derived by Munjal [121] and Miles [109] (top) and Greitzer et al. [55] (bottom). . . . .	50
5.1.	Schematic of the microphone array for wave identification on a duct with non-constant cross-sectional area. . . . .	57
5.2.	Online wave decomposition scheme for two microphones on a duct with non-constant cross-sectional area. Left: feedback loop, right: model for duct segment incorporating the scattering matrix $\mathbf{S}^{1,2}$ . . . . .	59
5.3.	Feedback loop of the online wave decomposition scheme. Extension for $N$ microphones located along a duct with non-constant cross-sectional area. . . . .	60
5.4.	Left: schematic of the combustion chamber (black) in the test rig (gray). Right: combustion chamber geometry for validation of the Multi-Microphone Method in non-constant cross-sectional area ducts. The dashed blue and orange curves, denote possible sensor locations along the center chord and along the geometry's upper boundary, respectively. . . . .	61

5.5. Mesh for the FEM-validation of the Multi-Microphone Method in ducts with variable cross-sectional area. . . . .	62
5.6. Isosurfaces of the real part of the acoustic pressure obtained with the Helmholtz solver. Left: results for an excitation frequency of $f = 600$ Hz and a sound hard boundary at the domain outlet. Right: results for an excitation frequency of $f = 700$ Hz and a non-reflecting boundary at the domain outlet. . . . .	62
5.7. Residual $\delta^*$ for the frequency-domain Multi-Microphone Method in a non-uniform duct for a non-reflective outlet boundary condition calculated with three different approaches (colors). Left: sensor locations aligned along curve 1 (center chord), right: sensors aligned along curve 2 (close to upper boundary). . . . .	64
5.8. Reflection coefficient for the frequency-domain Multi-Microphone Method in a non-uniform duct for a non-reflective outlet boundary condition calculated with three different approaches (colors). Reference solution from FEM given in black. Left: sensor locations aligned along curve 1 (center chord), right: sensors aligned along curve 2 (close to upper boundary). Top: magnitude, bottom: phase at the inlet plane. . . . .	64
5.9. Residual $\delta^*$ for the frequency-domain Multi-Microphone Method in a non-uniform duct calculated with three different approaches (colors). Microphones are aligned along curve 2. Left: sound hard outlet impedance, right: sound soft outlet impedance. . . . .	66
5.10. Reflection coefficient for the frequency-domain Multi-Microphone Method in a non-uniform duct calculated with three different approaches (colors). Microphones are aligned along curve 2. Reference solution from FEM given in black. Left: sound hard outlet impedance, right: sound soft outlet impedance. Top: magnitude, bottom: phase at the inlet plane. . . . .	66
5.11. Inverse values of the curvature radius $R_c$ (solid, colors) and the typical length scale of the cross-sectional area variation $L_A$ (dashed, black) over the corresponding curves. . . . .	67
5.12. Schematic of the cold acoustic test rig for validation of the Multi-Microphone Method in ducts with variable cross-sectional area. . . . .	68
5.13. Calibration coefficients for five microphones in flush mounted holders. Top: magnitude, bottom: phase. . . . .	68
5.14. Residual of the frequency-domain wave decomposition obtained from microphone readings in the duct segments with constant (black, reference) and variable cross-sectional area (blue). For comparison, the residual $\delta$ is calculated for the same setup with the FEM simulation from SEC. 5.3. . . . .	69
5.15. $\hat{f}$ -wave reconstructed with the frequency-domain Multi-Microphone Method in the constant (black) and variable (yellow) cross-sectional area duct segments, each evaluated at location 13. Top: magnitude, bottom: phase. . . . .	70
5.16. Downstream propagating wave at location 13. Reconstructed with the frequency-domain (black) and time-domain (yellow) Multi-Microphone Method in the constant and variable cross-sectional area duct, respectively. Top: magnitude, bottom: phase. . . . .	71

5.17. Reflection coefficient evaluated at location 13. Reconstructed with the frequency-domain Multi-Microphone Method in the constant (black) and variable (orange) cross-sectional area duct segments, and for the time-domain wave decomposition inside the non-uniform duct (yellow). Top: magnitude, bottom: phase. . . . .	71
6.1. Schematic of a siren actuator. . . . .	76
6.2. Sectional view of the computational domain for a base plate mounted actuator. The boundary condition at plane 1 is an impressed normal velocity or a pressure node and at plane 2 the impedance is adjusted to anechoic conditions. . . . .	78
6.3. <b>(a)</b> Base plate in plan view with four different connection strategies, which are summarized in TAB. 6.1. <b>(b)</b> Computational domain with the employed mesh and the burner base plate highlighted in blue . . . . .	79
6.4. Sectional view of the temperature distribution inside the axisymmetric computational domain. . . . .	80
6.5. Exemplary offset-corrected phase of the axial velocity component with excitation at the flow sleeve (blue) and at the burner base plate with configuration A (orange) at an excitation frequency of $f_{\text{exc}} = 60$ Hz . . . . .	81
6.6. Maximum phase difference of the axial velocity between the reference excitation at the plenum and the four excitation strategies at the burner base plate . . . . .	81
6.7. Exemplary offset-corrected axial velocity component with excitation at the flow sleeve (blue) and the burner base plate with configuration B (orange) at an excitation frequency of $f_{\text{exc}} = 340$ Hz. <b>(a)</b> phase of the sound velocity <b>(b)</b> sound velocity level . . . . .	82
6.8. <b>(a)</b> Sound velocity level and <b>(b)</b> sound pressure level for excitation at the flow sleeve (black) and at the burner base plate with configurations A (blue), B (orange), C (yellow) and D (purple) . . . . .	82
6.9. Computational domain of flow box, burner passage, combustion chamber and vane simulation section with an unstructured mesh. . . . .	84
6.10. Computational domain with flow box and three exponential horns of different lengths . . . . .	85
6.11. Sound pressure level inside the combustion chamber with three horns of different lengths mounted at the flow box, computed with a stationary acoustic simulation . . . . .	85
6.12. Computational domain with flow box (cropped view) and two alternative connection strategies: tube and cone of 1.0 m length, respectively . . . . .	86
6.13. Sound pressure level inside the combustion chamber with a horn, a cone and a tube, of the same length ( $L = 1.0$ m), mounted at the flow box. Computed with a stationary acoustic simulation. . . . .	87
6.14. Sound pressure level at the evaluation plane inside the combustion chamber with three excitation strategies. Simulation of the natural oscillation of the system is colored in black, excitation with a single inlet at the base plate center in blue and actuation at the mouth of a horn (1.0 m) mounted at the flow box in red. . . . .	88
6.15. Sound pressure level at the evaluation plane inside the combustion chamber with horn excitation at the flow box (black) and base plate excitation with four different connector lengths: 0.0 m (blue), 0.25 m (orange), 0.50 m (yellow), 0.75 m (purple) . . . . .	89

7.1.	Schematic of the high pressure test rig's exhaust section in top view. The combustion chamber is located upstream of the VSS. Downstream, the dump and back pressure valve are connected. Possible actuation locations are highlighted blue (vane simulation section) and orange (back pressure valve). . . . .	94
7.2.	General principle of the downstream actuator. In the vane simulation section, fluid is injected in a modulated way in order to block the smallest cross-sectional area and thus introduce a pressure fluctuation in the combustion chamber upstream of the VSS. . . . .	95
7.3.	Computational domain with employed structured mesh for the numerical investigation of the periodic injection into the vane simulation section. Red dots indicate probe locations. Image courtesy of Hanraths [66] . . . . .	99
7.4.	Amplitudes of the upstream propagating wave $\hat{g}$ normalized by the mean pressure. Results obtained at three different mean pressure levels ( $\times$ - engine pressure, $\circ$ - intermediate pressure, $\square$ - atmospheric pressure) and at five exhaust gas temperatures, respectively. . . . .	100
7.5.	Locations for secondary air injection at the vane simulation section normalized by vane length $L_{\text{vane}}$ . . . . .	101
7.6.	Normalized amplitudes of the upstream propagating wave $\hat{g}$ for three different injection locations along the vane and two different main air velocities, respectively. . . . .	102
7.7.	Velocity streamlines superimposed with static pressure (colormap) around the vane for the three different injection locations as introduced in FIG. 7.5 at a nozzle Mach number of $M \approx 0.59$ . Image courtesy of Hanraths [66]. . . . .	102
7.8.	Mesh for the acoustics simulations conducted with COMSOL. Top: total view, bottom: detailed view of the refinement at the (long) injector. . . . .	103
7.9.	Absolute values and phase of the open-loop reflection coefficient $R_{\text{ol}}$ for a long injector, active main flow and full reflection at the outlet boundary. Determined by a combined CFD and LEE approach. Top: magnitude, bottom: phase between excitation signal and pressure at the reference plane. . . . .	104
7.10.	Experimental setup for preliminary atmospheric tests with mean flows up to sonic conditions inside the nozzle throat and simultaneous acoustic excitation with an upstream loudspeaker and a downstream mounted proportional valve. . . . .	105
7.11.	Generic nozzle and an end piece for air injection at $90^\circ$ and $45^\circ$ towards the main air flow. . . . .	106
7.12.	End piece for mechanical-blockage actuation with various contour disks, which are driven by a DC motor. The two exemplary disks on the right hand side feature twelve and two teeth, respectively. . . . .	107
7.13.	Experimental setup for atmospheric combustion tests . . . . .	107
7.14.	Experimental setup for preliminary tests of the active control of the acoustic boundary condition. Simultaneous acoustic excitation is realized with loudspeakers upstream and downstream of the microphone array, respectively. . . . .	108
7.15.	1/4" condenser microphone with additional coupler, electrically insulated and mounted in a metal inlay inside a cooled holder. . . . .	110
7.16.	Difference in the measured pressure fluctuation between the absolute pressure sensor and a condenser microphone. Top: magnitude deviation, bottom: phase deviation. . . . .	111
7.17.	Proportional valves from <i>Moog GmbH</i> . Left: D050-E042, right: D633-7320. . . . .	112

7.18. Mass flow over pressure difference for two proportional valves: Moog D633-7320 (blue) and Moog D050-E042 (black). Markers denote measured values, lines denote square-root fits. . . . .	114
7.19. Estimated number of D050-E04x valves for varying ratios of mean valve supply and test rig pressure. The gray area denotes higher test rig pressure than valve supply. The blue line marks intermediate test rig pressure (standard operation). . . . .	114
7.20. Transfer function between voltage input and piston stroke for the D633-7320 proportional valve, measured by the output voltage of the LVDT module. Top: magnitude, bottom: phase. . . . .	115
7.21. Amplitude of the control voltage input $ \hat{U}_c $ and the measured LVDT voltage amplitude $ \hat{U}_{LVDT} $ of the D633-7320 valve's piston. . . . .	116
7.22. Calculated mean Mach number in the nozzle throat over main air mass flow for non-reacting (*, blue: linear regression) and reacting (+, orange: linear regression) conditions. . . . .	117
7.23. Discharge coefficient of the main nozzle over momentum flux ratio of the injection at three different main air Mach numbers (calculated without injection). Results for injection angles of $90^\circ$ (solid lines) and $45^\circ$ (dashed lines). . . . .	117
7.24. Error bar plot of the total actuator transfer function $G_{tot}$ for the same operating conditions at six different measurements across several weeks. . . . .	119
7.25. Total actuator transfer function $G_{tot}$ for three Mach numbers and two different injection locations. All measurements conducted at a constant ratio of secondary and main air mass flow: $m_s/m_m = 0.1$ . Solid lines denote air injection into the nozzle throat and dash-dotted lines denote injection upstream of the nozzle. . . . .	120
7.26. Total actuator transfer function $G_{tot}$ for a momentum flux ratio of $J = 0.20$ at injection angles of $90^\circ$ (solid) and $45^\circ$ (dash-dotted). The unactuated nozzle Mach number was varied from $M = 0.15$ to $0.60$ (colors). . . . .	121
7.27. Total actuator transfer function $G_{tot}$ for a constant injection mass flow of $m_s = 6.67$ g/s at injection angles of $90^\circ$ (solid) and $45^\circ$ (dash-dotted). The unactuated nozzle Mach number was varied from $M = 0.0$ to $0.60$ (colors). . . . .	122
7.28. Steady pressure difference ( $\square$ ), low frequency pressure amplitudes obtained with an absolute pressure sensor ( $\times$ ) and a condenser microphone ( $\circ$ ). Transfer functions calculated with the time constant (dash-dotted) and from the Fourier transform of the impulse response (solid). . . . .	123
7.29. Steady pressure difference ( $\square$ ), very low frequency pressure amplitudes obtained with an absolute pressure sensor ( $\times$ ), and low frequency pressure fluctuations from a condenser microphone (denoted with dots) for three different actuation types: $90^\circ$ air injection (orange), $45^\circ$ air injection (yellow), and excitation via a scalloped disk (blue). . . . .	124
7.30. Total actuator transfer function $G_{tot}$ for an unactuated main air Mach number of $M = 0.6$ at reacting ( $\phi = 0.43$ , dash-dotted) and non-reacting (solid) conditions. Momentum flux ratios were varied from $J = 0.015$ to $0.140$ (colors). . . . .	125
7.31. Total actuator transfer function $G_{tot}$ for a momentum flux ratio of $J = 0.062$ at reacting ( $\phi = 0.43$ , dash-dotted) and non-reacting (solid) conditions. The unactuated nozzle Mach number was varied from $M = 0.50$ to $0.70$ (colors). . . . .	126

7.32. Schematic of the 1D time-domain network model for verification of the active modification of the acoustic boundary condition . . . . .	127
7.33. Magnitude of the cross power spectral density between excitation and pressure reading at the reference plane in the cold acoustic test rig. Measured in the experiment (blue) and calculated with the 1D network model (orange). . . . .	128
7.34. Downstream traveling wave $f$ for non-zero mean flow conditions in the 1D network model obtained from time-domain (blue) and frequency-domain (orange) Multi-Microphone Method. Top: magnitude with enlarged depiction of a small frequency range, bottom: phase at the reference plane. . . . .	129
7.35. Open-loop (solid) and closed-loop (dashed) reflection coefficients experimentally determined (blue) and calculated with the 1D network model. The closed-loop reflection coefficient was tuned to $ R_{cl}  = 0.7$ in a frequency band from $f = 150$ Hz to 350 Hz. Top: magnitude, bottom: phase between $g$ and $f$ at the reference plane. . . . .	130
7.36. Geometry as implemented in the 1D time-domain network model. Locations of the microphone array and reference planes (blue and orange) are normalized by the combustor length $L_{cc}$ . . . . .	130
7.37. Phase of the controller transfer function $K$ for various offsets of the sensor array along the $x$ -coordinate of the combustion chamber. Left: $\arg(K)$ for $ R_{cl}  = 0.2$ , right: $\arg(K)$ for $ R_{cl}  = 1.0$ . . . . .	131
7.38. Open-loop and closed-loop reflection coefficients. Top: magnitude of $R_{ol}$ (blue), $ R_{cl}  = 0.0$ (orange), $ R_{cl}  = 0.2$ (yellow), $ R_{cl}  = 0.4$ (purple), and $ R_{cl}  = 1.0$ (green). Frequency ranges for control are indicated by dashed lines and the corresponding colors. Bottom: phase between $g$ and $f$ at the reference plane. . . . .	133
7.39. Top: magnitude of the open-loop (blue) and four closed-loop reflection coefficients (remaining colors). Controlled frequency range: $f = 111$ Hz to 671 Hz (black dashed line). Center: phase between $g$ and $f$ at the reference plane. Bottom: Virtual additional lengths for four different target values calculated from phase difference and controlled frequency range. . . . .	134
7.40. Three transient perturbation signals, represented by the reflected wave $R_{ol}f$ (blue), the corresponding actuator response signal $Ge$ (orange) and the resulting superposition (yellow) at a set closed-loop reflection coefficient of $ R_{cl}  = 0.2$ plotted over time. . . . .	135
A.1. Test case for comparison of the results from the two transfer matrix approaches to an analytical result. Two ducts of different diameters are connected via a cross-sectional jump. Mean flow is denoted by the corresponding Mach numbers.	163
A.2. Downstream to upstream ratios of acoustic pressure and particle velocity for a cross-sectional jump with low-Mach number mean flow. Calculated from an analytical reference case (solid) and using the transfer matrix method of Munjal [121] (dashed) and of Greitzer et al. [55] (dotted) . . . . .	164

---

List of Tables

---

4.1. Settings for the optimization of the geometry that is used with the transfer matrix method. . . . .	47
6.1. Configurations for investigation of different actuation locations at the burner base plate. . . . .	79
6.2. Horn lengths and the corresponding horn constants . . . . .	85
7.1. Actuator concepts and their main weakness in the context of eligibility as a downstream acoustic excitation device . . . . .	92
7.2. Excerpt of the flow and excitation parameters for the numerical investigations.	99
7.3. Parameters used in the combined CFD and LEE simulation for development of the time domain network model (SEC. 7.6). . . . .	104

---

## Nomenclature

---

### Abbreviations

ADC	analog-to-digital converter
BPV	back pressure valve
CFD	computational fluid dynamics
CO <sub>x</sub>	carbon oxides
D	wave decomposer
DAC	digital-to-analog converter
DC	direct current
K	controller
LEE	linearized Euler equations
LVDT	linear variable displacement transducer
NO <sub>x</sub>	nitrogen oxides
RANS	Reynolds-averaged Navier-Stokes equations
SPL	sound pressure level
SVL	sound velocity level
TMM	transfer matrix method
VSS	vane simulation section

### Greek Letters

$\alpha$	loss coefficient
$\beta$	volume fraction
$\delta$	error-estimate (residual)
$\delta_{ij}$	Kronecker delta
$\gamma$	isentropic exponent
$\lambda$	wave length
$\Theta$	placeholder function

$\zeta_B$	burner loss coefficient
$\rho$	density
$\Phi$	velocity potential
$\phi$	equivalence ratio
$\varphi$	phase angle
$\tau$	time constant
$\tau_{ij}$	stress tensor
$\omega$	circular frequency ( $\omega = 2\pi f$ )
$\Psi$	placeholder function

### Latin Letters

$a, b, z$	placeholder variables
$A$	(cross-sectional) area
$A_{\text{eff}}$	effective area
<b>A, B, C, D</b>	state-space matrices
$C_d$	nozzle discharge coefficient
$C_1, C_2$	placeholder functions
$C_p$	heat capacity at constant pressure and constant volume, respectively
$c$	speed of sound
$c_n$	constant calibration factor
$d$	diameter
$e$	excitation signal
$F(\omega)$	flame transfer function
$f$	frequency, downstream propagating wave
$f_{\text{lim}}$	lower limit frequency
$G$	actuator transfer function
$G_{\text{sr}}$	transfer function from step response
$g$	upstream propagating wave
$H(\omega)$	transfer function
$H_{\text{LVDT}}$	piston transfer function
<b>H</b>	matrix with time delays for the Multi-Microphone Method
$h$	horn constant
<b>I</b>	identity matrix

**xx**

$i$	imaginary unit, $\sqrt{-1} = i$
$J$	momentum flux coefficient
$J_0, Y_0$	zeroth-order Bessel functions of the first kind and second kind, respectively
$K$	controller transfer function
$k$	wave number
$L$	length
$L_{\text{red}}$	reduced length (of the burner)
$M$	Mach number
$m$	mass flow
$\mathbf{n}$	normal vector (Cartesian coordinates)
$P_1, P_2$	placeholder functions
$p$	pressure
$\hat{\mathbf{p}}$	vector of complex pressure amplitudes
$\dot{Q}$	heat release rate
$\hat{Q}_{\text{mono}}$	monopole source term
$\hat{\mathbf{Q}}_{\text{di}}$	dipole source term
$R$	reflection coefficient
$R_g$	specific gas constant
$S$	swirl number
$\mathbf{S}$	scattering matrix
$s$	entropy
$Str$	Strouhal number
$T$	temperature
$T(\omega)$	transfer function
$\mathbf{T}$	transfer matrix
$t$	time
$U_c$	control voltage
$u$	velocity
$v$	volume flow velocity $v = uA$
$\mathbf{u}$	velocity vector
$x, y, z$	Cartesian coordinates
$\mathbf{x}$	state vector
$Z$	acoustic impedance

$Z_0$	characteristic acoustic impedance
$\mathcal{Z}$	specific acoustic impedance ( $\mathcal{Z} = Z/Z_0$ )

### Superscripts

$\hat{(\cdot)}$	mean component
$(\cdot)'$	fluctuating component
$\dot{(\cdot)}$	partial derivative with respect to time
$\overline{(\cdot)}$	mean component
$(\cdot)^+$	downstream propagating wave
$(\cdot)^-$	upstream propagating wave
$(\cdot)^\dagger$	Moore-Penrose inverse
$(\cdot)^<$	increasing cross-sectional jump
$(\cdot)^>$	decreasing cross-sectional jump
$(\cdot)^A$	case A
$(\cdot)^B$	case B

### Subscripts

$(\cdot)_{\text{base}}$	burner base plate
$(\cdot)_B$	burner
$(\cdot)_{\text{cc}}$	combustion chamber
$(\cdot)_{\text{cl}}$	closed loop
$(\cdot)_{\text{csj}}$	cross-sectional jump
$(\cdot)_d$	downstream
$(\cdot)_{\text{exc}}$	excitation
$(\cdot)_e$	energy
$(\cdot)_F$	flame
$(\cdot)_G$	derived by Greitzer et al. [55]
$(\cdot)_h$	horn
$(\cdot)_{\text{inj}}$	injector
$(\cdot)_{\text{max}}$	maximum
$(\cdot)_{\text{mo}}$	(horn) mouth
$(\cdot)_M$	derived by Munjal [121]
$(\cdot)_m$	main (primary air)

$(\cdot)_{\text{norm}}$	normalized
$(\cdot)_N$	last valid index
$(\cdot)_{\text{ol}}$	open loop
$(\cdot)_{\text{or}}$	original
$(\cdot)_{\text{out}}$	outlet
$(\cdot)_s$	source (secondary air)
$(\cdot)_{\text{tot}}$	total
$(\cdot)_t$	(horn) throat
$(\cdot)_u$	upstream
$(\cdot)_m$	consecutive integer index
$(\cdot)_n$	consecutive integer index



# CHAPTER 1

---

## Introduction and Objectives

---

In the first part of this chapter, the role of stationary gas turbines in the generation of electricity is explained. Since the introduction of lean premixed combustion, which allows for a reduction of poisonous  $\text{NO}_x$  emissions, manufacturers have to deal with the occurrence of thermoacoustic instabilities. The practical relevance and driving mechanisms behind these unsteady combustion phenomena are described. A short overview of passive and active schemes to inhibit self-excited oscillations is given. In SEC. 1.6, the history of active impedance control is summarized, which is of high interest in the context of this work. Subsequently, the investigation of combustion instabilities via flame response measurements in the development process of gas turbines is discussed. In the final section, the motivation for this thesis is extracted and the main objectives are formulated: an existing high pressure test is to be modified in a way that active impedance control and flame response measurements are possible. Lastly, the structure of this work is outlined.

### 1.1. Gas Turbines for Power Generation

The demand for generation of electricity is highly increasing and according to the International Energy Agency [81] it will account for 40 % of the total energy consumption by 2040. On one hand, this is due to a large increase of access to electricity and growing economies with increasing incomes that are able to afford electrical devices. On the other hand, *decarbonization* in transport and also in heat generation promotes the demand for electrical power. The U.S. Energy Information Administration's reference case [179] projects renewable energy sources (including hydropower) to be the fastest growing source of electricity generation within the next 20 years (cf. FIG. 1.1). Among those, solar and wind powered generation will increase the most, accounting for a projected 4.1 % and 7.3 % of the total electricity supply in 2040, respectively. By then, the percentage of renewables will be equal to that of coal, which decreases by approximately 9 %. Natural gas will grow by an average of 2.1 % each year, reaching over 26 %.

The general development of replacing coal with natural gas and renewable energy carriers is a step in the right direction of containing the effects of the global climate change. However, according to the Paris Agreement [178], this can only be achieved, if the greenhouse gas emissions are halved every ten years beginning in 2020. Yet, the reference scenario shown in FIG. 1.1 assumes a worldwide average annual emissions increase of 0.6 %. This implies that

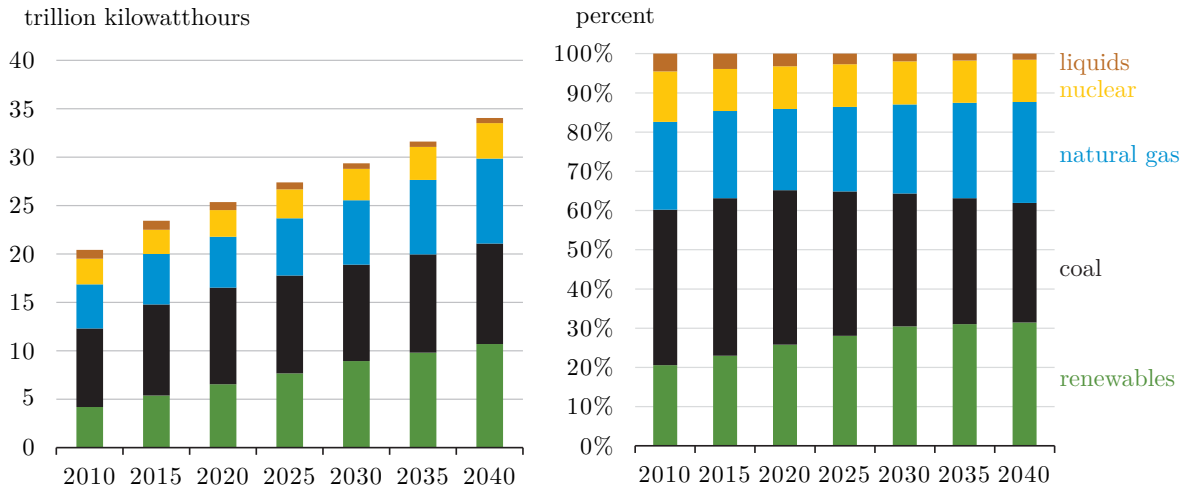


**Figure 1.1.:** Projected fuel sources for net electricity generation worldwide, according to the International Energy Outlook 2017 by the U.S. Energy Information Administration. Formatted image from reference [179]. Left: total in  $10^{18}$  kWh. Right: share in %.

if the agreement is to be fulfilled, the *energy transition* from fossil fuels towards renewables still needs to be accelerated.

Yet, with the increased share of renewable energy sources, volatility of the electricity supply becomes more of an issue. For instance, temporal fluctuations of solar and wind powered electricity generation need to be compensated. This can be realized by energy storage technologies, as for example: power-to-gas, batteries, hydrogen electrolysis, pumped-storage hydroelectricity, and compressed air energy storage. Although these systems are already in use [29], none of them is viable for large-scale coverage, yet. Main reasons are technological constraints in terms of efficiency and cost (power-to-gas, battery, electrolysis) on one hand and geographic restrictions (pumped hydro, compressed air) on the other. In the near future, technological advances will show, whether one of these solutions is suited for large-scale energy storage. Another, already widely available means to cover short term demand for electric energy are gas turbines. They feature the highest ramping rates of any industrial power generation technology and the second highest operational flexibility after hydro-electric plants, which is assessed in terms of minimum load. Thus, gas turbines are well suited for compensation of the variable electric energy supply by renewables. In addition, they are well suited to counterbalance unexpected outages.

Among fossil fuels, natural gas is considered a relatively clean source of electric energy. Compared to hard coal and especially lignite, the emissions of  $\text{CO}_2$ ,  $\text{SO}_2$ ,  $\text{NO}_x$ , and particulates are much lower. Main reasons are the almost two times higher energy output per emitted tons of  $\text{CO}_2$  [180] and natural gas inherently containing less contaminants. Due to the controlled lean combustion process in gas turbines, emissions of nitrogen oxides are much lower than for coal firing plants. Fuel efficiencies of coal plants and gas turbine plants in single cycle are comparable. Under full load, state-of-the-art hard coal and lignite plants reach maxima of  $\approx 47\%$  [70] and  $\approx 44\%$  [181], respectively. Large gas turbines achieve a fuel efficiency of  $\approx 41\%$  [6, 167].

However, the fuel efficiency of gas turbines can be strongly increased by incorporating a steam turbine, which is powered by the excess heat of one or more gas turbines. In *combined cycles*, fuel efficiencies of over 61 % [6, 167] are possible. In 2010, the average efficiencies of German power plants [151] firing natural gas were at 49 %, while hard coal and lignite only reached values of 38 % and 35 %, respectively. Yet, it has to be mentioned that the operation of combined cycle gas turbine power plants is not always financially viable. Thus, many European plants are shut down or converted in order to compensate peak load requirements [30]. Further note that combined cycle plants require higher minimum loads and feature less than 50 % of the ramping rate of gas turbines in single cycle.

Nevertheless, considering the short-term demand for highly flexible and clean generation of electricity induced by the energy transition, gas turbines remain a viable solution.

## 1.2. Practical Relevance of Thermoacoustic Instabilities

Alongside inherent advantages, governmental restrictions on nitrogen oxides ( $\text{NO}_x$ ) emissions are part of the reason for the eco-friendliness of gas turbines. The main contributor, nitrogen monoxide (NO), is a poisonous gas that is also responsible for ozone reduction in the atmosphere and acid rain. The German limit value for gas fired  $\text{NO}_x$  emissions is at  $100 \text{ mg/m}^3$  [28], which is well below that of solid or liquid combustibles. Achieving the limit values, however, required significant engineering effort, as the diffusion-flame combustion process in older gas turbines needed to be revised. In order to reduce the amount of thermal NO production in stationary gas turbines, *lean premixed* combustion was introduced. Lean combustion is characterized by equivalence ratios below unity. It results in an overall lower flame temperature [187], which inhibits formation of  $\text{NO}_x$ . In a premixed combustion, the fuel is injected upstream of the combustion chamber, which reduces local peak temperatures. Thereby, thermal NO production may be further minimized. Note that the fuel to air ratio has a lower boundary, which mainly results from the increased production of carbon monoxide (CO) at low fuel fractions. Thus, a trade-off between CO- and  $\text{NO}_x$  emissions, as well as efficiency, defines the optimal equivalence ratio.

However, a lean combustion process is more likely to suffer from *thermoacoustic instabilities* or *combustion dynamics*. The phenomenon manifests in self-excited pressure fluctuations, which are the result of a positive feedback cycle between the combustion chamber acoustics and unsteady heat release of the flame. Aside from lean combustion itself, accompanying factors encourage these unwanted oscillations. Due to lower flame temperatures in lean premixed combustion, less cooling air is required. Thus, convectively cooled combustor walls are employed, which decreases acoustic damping. Furthermore, the increasing power density of modern can or annular combustor designs magnifies the effects of thermoacoustic oscillations.

As a result, part of the early gas turbines, employing lean premixed combustion, suffered from severe thermoacoustic instabilities [96, 140]. Notable effects are, for instance:

- increased emission of polluting gases like  $\text{NO}_x$  and CO,
- disturbances in flame location, leading to flashback or flame blow-off,
- increased noise levels,
- decreased power output, and

- mechanical wear.

The latter is due to strong pulsations leading to fatigue of components, which is amplified by an increased thermal conductivity, due to the oscillations. Among the first gas turbine generations with a lean premixed combustion concept, fatigue of components even led to total engine failures [96]. When instabilities are encountered in a gas turbine, either the operating envelope has to be adapted or the engine needs to be shut down completely, both being financially problematic for the manufacturer.

However, the issue is not confined to stationary gas turbines. Thermoacoustic instabilities occur in a multitude of combustor applications. Prominent past examples were the solid-propellant boosters of the Space Shuttle, as well as the liquid-fueled F-1 engines of the Saturn rockets [198], which exhibited fluctuations in the range of the mean pressure. Further examples for occurrence of such instabilities are combustion furnaces, heating systems, boilers, and aeronautical applications like ramjets and afterburners. Furthermore, combustion dynamics are one of the main constraints, considering the emissions reduction of aircraft engines. *Lean premixed/prevaporized* combustion, which was for instance described by Lefebvre in 1977 [92], is not applicable, due to inherent reliability issues and corresponding safety concerns. Just recently, lean combustion concepts like the *Twin Annular Premixing Swirler* from GE [51] or the *Advanced Low Emissions Combustion System* from Rolls-Royce [145] have moved from development to application in the field, or are in the process.

Conversely, in *pressure gain combustion* or *quasi-constant volume combustion*, the coupling of heat release to the acoustic field is a necessary requirement. Examples of such concepts are wave rotors [3], pulsed detonation [146], shockless explosion [15], or rotating detonation combustors [99]. These concepts have in common, that the combustion-generated pressure waves are utilized to initiate the consecutive insertion of fresh fuel-air mixture. Due to incorporation of a more efficient thermodynamic cycle, such principles promise a higher fuel efficiency, once implemented in an engine.

### 1.3. Driving Mechanisms of Thermoacoustic Instabilities

The first scientific observation of thermoacoustic instabilities was in 1777, when Higgins [74] observed a phenomenon, he called *singing flame*. He placed a hydrogen flame inside an open tube and documented "*several sweet tones, according to the width, length, and thickness of the [...] sealed tube*". The phenomenon was observed by multiple researchers throughout the following years, but until 1878 the correct reason was not understood. In that year, Lord Rayleigh [170] formulated a criterion for the generation of sound via heat release. He stated that an acoustic vibration is encouraged, only if periodic heat release and pressure fluctuation are in phase. Mathematically, this condition is expressed as

$$\oint p' \dot{Q}' dt > 0, \quad (1.1)$$

where  $p'$  and  $\dot{Q}'$  are pressure and heat release rate fluctuations, respectively. EQ. 1.1 is fulfilled, when the phase between both oscillations accounts to  $|\varphi| < \pi/2$ . In this case, acoustic energy is fed into the system and a self-excited oscillation might develop. However, this condition is not a sufficient criterion for a thermoacoustic instability to occur. For instance,

losses of acoustic energy are not accounted for, which may in practice be large enough to prevent self-excited oscillations.

Due to its practical relevance, the *Rayleigh criterion* was since refined and extended. Bothien [18] derived an alternative formulation for an onset of thermoacoustic instabilities. It states that a system might become unstable, when heat release and pressure fluctuations are in phase and their product exceeds the losses across the system boundaries. Nicoud & Poinot [123] further included influences like entropy, heat conduction, and viscous effects. However, the authors did not include mean flow in their derivation, which is reasonable for very low Mach number flows. Giauque et al. [53] derived a more general criterion, further including mean flow and heat release effects.

In order to understand, which triggers are responsible for the actual formation of an instability, the most influential underlying mechanisms are explained in the following paragraphs. Good overviews of this topic are, for instance, found in references [18, 117, 128, 147, 198].

The initial perturbations generally stem from a turbulent flow exiting the combustor, which results in broadband noise. Depending on the type of combustion chamber and the flame shape, different mechanisms are responsible for perturbations in the flame's heat release. In dump combustors, the main influences are velocity fluctuations that excite shear layers and trigger vortices in the fuel-air mixture. This leads to perturbations of the flame front, and thus, heat release fluctuations, as for example discussed by Schadow & Gutmark [150]. For swirl-stabilized combustors, flow instabilities such as coherent vortical structures are main reasons for heat release oscillations [78, 131, 174]. Furthermore, the mixing of fuel and air in most technical applications is not perfect. Deviations in the impedances of fuel and air supply increase the sensitivity of the mixture to acoustic perturbations [95]. In consequence, locally variable equivalence ratios may also lead to periodic heat release variations. This effect is amplified under lean conditions, where the burning velocity is highly susceptible to varying equivalence ratios.

Lieuwen [94] stated that pressure fluctuations may have a direct, yet marginal, influence on heat release oscillations via the pressure-dependent chemical reaction rate of the fuel-air mixture. On the contrary, liquid fuels are strongly affected by pressure variations due to the pressure sensitivity of fuel vaporization and atomization.

The heat release fluctuations cause variations in density and therefore in acoustic pressure. Acoustic waves then propagate throughout the combustion chamber and are reflected at the system boundaries. Depending on the frequency, and thus mode shape, various types of interactions may occur. In this work, we shall focus on *intermediate frequency dynamics*. The term was, for instance, used by Farisco [46] and describes oscillations with longitudinal wave propagation in an approximate frequency range from 50 Hz to 500 Hz. Thus, the relevant boundary for reflection of the acoustic waves is the combustor outlet, terminated by the highly reflective turbine inlet vanes.

When the *reflected* wave reaches the burner, a velocity (and pressure) fluctuation is induced, which closes the feedback cycle. Given a constructive interference between heat release rate and pressure fluctuations, and an energy input exceeding the acoustic losses, initially small disturbances may grow. The amplitude increases until non-linear effects cause a saturation and an equilibrium is reached. This state is called *limit cycle oscillation* and it is characterized by a high-amplitude fluctuation at a distinct frequency – usually close to the resonance frequency of the combustion chamber.

Although the actual relevance in stationary gas turbines is a matter of frequent discussion, *entropy waves* shall be mentioned, as well. The term might be misleading, as the phenomenon is based on hot or cold pockets of exhaust gas, which are convected downstream from the flame. Their formation can have a multitude of influential factors, as was pointed out by Polifke et al. [136]. If the temperature non-uniformities are not smoothed out until they reach the turbine inlet, they are strongly accelerated. This causes oscillating volume contractions, resulting in pressure fluctuations [104, 188], which may contribute to a closed-loop cycle.

#### 1.4. Passive and Active Control

Mitigation of thermoacoustic instabilities in stationary gas turbine engines can be realized by passive or active means. Overviews of the topics may be found in references [96] and [195] for stationary and airborne gas turbines, respectively. Possible methods either introduce attenuation of unstable modes, shift acoustic energy away from them, or inhibit the feedback cycle between fluctuating heat release and acoustics.

Passive control is possible with various means, some of which are described by Richards et al. [141]. A standard approach lies in the use of Helmholtz dampers, as for instance described within references [41, 44, 107, 125, 176]. These devices transform kinetic energy from the acoustic oscillation into thermal energy by vortex shedding at the damper's neck. Thereby, absorption of acoustic energy in a small frequency band is realized. Helmholtz dampers are employed in stationary gas turbines in order to extend the operating envelope and flexibility, as pointed out by Bellucci et al. [11]. Bothien et al. [25] extended the concept to resonators with multiple cavities, which allows for attenuation in a frequency range from 50 Hz to 150 Hz. Alongside other upgrades, implementation of these devices led to reduced pulsations, and thus, lower emissions and an improved operational range [27]. Alternative approaches are, for instance, based on altering the time lag of key mechanisms like fuel injection [129] or modifying the shape of the swirler in order to reduce the influence of coherent structures [130].

Active control is usually highly expensive and due to the added complexity, regarded as a last resort against thermoacoustic instabilities. A prominent example is found in the publications of Seume et al. [163] and Hermann & Orthmann [71]. The authors outfitted SIEMENS gas turbines with proportional valves for gas flow modulation in order to actuate the fuel supply of each individual burner. Pulsations could be effectively reduced for two differently sized types of annular gas turbines. The step was necessary, as the instabilities were only encountered in a late development phase. According to Bothien [18], *active instability control* provisions were installed in more than 50 engines.

Richards et al. [142] successfully implemented an open-loop active control scheme for a stationary gas turbine. Their approach is based on readily available solenoid valves from reciprocating engines, which also modulate the fuel supply.

In lab scale research experiments, active control is more common. For instance, both Guyot et al. [63] and Hong et al. [77] realized closed-loop control with fuel-modulating valves in atmospheric combustion experiments. While the former was aimed at a burner for stationary gas turbines, the latter focused on a burner found in aviation. Both research groups found the approach to be effective in terms of reducing low-frequency thermoacoustic oscillations.

Ćosić et al. [40] developed an active open-loop control scheme, which incorporates forcing at a non-resonant frequency of the combustor system to mitigate self-excited oscillations. They found the method to be both simple to implement and effective in stabilizing the system.

Lately, the field of plasma assisted combustion has gained popularity. The purpose of the high-voltage spark discharges includes, for instance, control of ignition delay times, suppression of soot formation, extending extinction limits, and also active control of thermoacoustic instabilities [114, 134]. The latter was, for example, investigated by Moeck et al. [115], who used nanosecond repetitively pulsed plasma to actively stabilize an atmospheric combustion system with a swirl-stabilized lean-premixed flame in a closed-loop configuration.

### 1.5. Experimental Identification of Thermoacoustic Instabilities

Control of thermoacoustic instabilities in a gas turbine engine should only be regarded as a last measure. Optimally, the occurrence of thermoacoustic instabilities is prevented within the development phase. This helps to avoid unexpected and possibly significant costs for the manufacturer. The difficulty lies in the complexity of the underlying mechanisms and their prediction in new combustor systems. An early identification of potentially problematic combinations of influential factors is desired. Stability has to be ensured over the entire operational range, which includes engine start up, base load, part load, and turn down.

The earlier a system's susceptibility towards thermoacoustic instabilities is discovered, the more cost efficient the entire development becomes. Therefore, manufacturers and academia have developed several tools to assess stability of burner systems throughout the development process. An extensive overview of the experimental methods applied by various manufacturers is given in the PhD thesis of Bothien [18]. The key component, i. e., the one with the most influence on the occurrence of combustion instabilities, is the burner. Aside from diverse numerical investigations, experimental determination of the relevant characteristics is highly important.

Initial water channel tests are followed by atmospheric investigations with single-burner configurations, which aim at selecting potentially stable combustor designs. Several characteristics, such as the flame shape and its position, can already be assessed here [193]. For annular combustion chambers, atmospheric multi-burner tests are a possible next step, in order to investigate flame interactions. Subsequently, tests under elevated pressure conditions are conducted with the remaining burner designs. Development of a new combustor system for annular combustion chambers would optimally include single- and multi-burner high pressure tests. Investigation of several burners in close proximity might have significant effects on production of polluting gases, for example. Furthermore, radial or transverse mode shapes may be excited, which is not assessable in single-burner configurations.

Especially for liquid fuels, high pressure tests are of great importance, as atomization and vaporization behave very differently under varying mean pressure conditions. Thus, properties like flame shape and fluctuating heat release are hardly assessable under atmospheric conditions.

If can-annular systems are regarded, usually only single-burner configurations are tested. The reason is that interactions between burners are inherently low, as each burner fires into its own combustion chamber. Thereby, testing effort can be reduced to only single-burner configurations without significantly reducing the correspondence of engine and test rig. Properties like exhaust gas composition, fuel flexibility, and thermal loading can be assessed

in highly comparable environments, when geometry and operational parameters are matched with those in the engine. Thereby, close resemblances of flow fields and temperature profiles are possible, which improves comparability and reliability of the results. Most of the acoustic properties may also be well resembled. For instance, damping due to cooling air injection and, to a certain extent, the acoustic boundary conditions may be matched. Furthermore, can-annular combustors inhibit the formation of acoustic modes in radial or transverse direction, as was pointed out by Kaufmann et al. [84]. The above-mentioned SIEMENS gas turbines that were outfitted with active instability control devices [163] featured annular combustion chambers and are therefore a cautionary example.

However, the can-annular design does not preclude any acoustic interactions between adjacent cans in the engine, as was pointed out by Kaufmann et al. [84] and Farisco et al. [47]. So-called *can-to-can interactions* or *can-can modes* between neighboring or pairwise neighboring cans may occur. The phenomenon is characterized by acoustic modes that span over multiple cans, interacting through the gaps at the turbine inlet (or the upstream plenum). These mode shapes cannot be simulated in single-burner test rigs. Combustor systems that have proven resistance to thermoacoustic instabilities in such tests might exhibit unexpected oscillations in the engine, although, otherwise the conditions are the same. Measures to reduce the cross-talk between the combustion chambers were, for instance, discussed by Farisco [46], who conducted numerical simulations of different hardware concepts for the first vane stage. Variants with and without deflection, as well as various gap sizes were investigated. Interactions between neighboring combustion chambers are of high relevance in the context of pulsed detonation combustors, as well. Notable references discussing this issue are, for instance, [7, 31, 138, 139].

The specific test rig regarded in this work features a can-type combustion chamber. As it is further detailed in CHAP. 3, only immediately relevant characteristics shall be mentioned here. For correspondence to the engine, the combustion chamber in the test rig is terminated by a section that imitates the first vane stage. It is comprised of several water cooled profiles that accelerate the main air flow in order to simulate the turbine inlet. This segment is currently adapted to the requirements of each test run on a hardware level. By employing different numbers of vanes, the acoustic reflection at that location can be altered. Thus, different operating conditions are resembled [46, 66]. However, between testing of each hardware configuration, the rig needs to be cooled down, disassembled, reassembled, and heated up again. As a result, significant delays and thus costs are to be expected.

An actively modifiable acoustic boundary condition in the test rig could remedy issues like the resemblance of can-can modes in the test rig or the need for implementation of various hardware configurations. The great practical relevance of such a method was, for instance, stated by the authors in references [35, 84, 87, 105]. The following section gives an overview of the history and currently relevant publications on the topic of active impedance control.

## 1.6. Active Control of Acoustic Boundary Conditions

In general, the active modification of an acoustic boundary condition is quite similar to active noise control, which was initially driven by the desire to cancel or absorb acoustic waves. According to the investigations by Guicking [57], Paul Lueg can be viewed as the inventor of active noise control. In 1933, he handed in his original patent, in which he describes the principle of actively canceling incident sound waves by measuring them and producing

appropriate counteracting fluctuations with a loudspeaker. Remarkably, he already came up with a number of technical applications and different use cases for one-dimensional as well as three-dimensional sound absorption. However, his ideas were far ahead of the capabilities of the available instruments. German officials saw the military potential of sound absorbing devices, but eventually rejected his application. In consequence, Lueg applied for an American patent, which was granted in 1936 [100]. Unfortunately, he did not succeed in proving practical applicability of his concept, although there are indications of him trying [57].

Twenty years after Lueg's initial patent application, Olson & May [127] published their famous work on the laboratory demonstration of sound absorption with an active feedback control scheme. They were able to significantly reduce the acoustic amplitude at a reference microphone over three octaves at low frequencies. A notable advance in this field was marked by the publication of Guicking & Karcher [58]. The authors used two microphones for *wave separation*, a loudspeaker, and an open-loop controller to actively alter the reflection coefficient of a Kundt tube to values between zero and 1.5 in frequency ranges below 800 Hz.

In the 1990s, active noise canceling for mobile applications became feasible, which was of special importance in the field of aviation. A significant reason is that the required precise sensors and micro controllers became widely available. While sealed headphones already passively attenuate acoustics above approximately 500 Hz, low frequency noise needs to be actively reduced. This is due to the occurrent higher wave lengths and therefore low damping. There is an abundance of references on the topic, however, one prominent example is a publication by Bartels from 1992 [8]. He successfully employed a feedback control with a single microphone as input and the headphone's loudspeaker to efficiently reduce noise over a wide frequency range. A review paper on active noise control in mobile applications was written by Kuo & Morgan [88]. Within this publication, several feedback and feedforward control approaches are detailed.

A thorough literature research on the topic of active impedance tuning in the context of combustion experiments is found in the PhD thesis of Bothien [18]. Within his work, he describes the development of a scheme for an active modification of the acoustic boundary condition in combustion test rigs. The basic idea of the concept is depicted in FIG. 1.2. In principle, the boundary condition downstream of an acoustic system can be regarded as a black box, which is denoted by dashed frames in the depiction. On the left-hand side, different geometric terminations are shown, which have varying acoustic properties. For example, a longer duct alters the resonance frequencies of a system. The corresponding reflection properties may be expressed by an acoustic *impedance*  $Z_1$ , which relates the acoustic pressure to the particle velocity (cf. EQ. 2.31). It determines the reflection of acoustic waves at the system boundary. Analogously, a decrease ( $Z_2$ ) or an increase in cross-sectional area ( $Z_3$ ) influence the magnitude and phase of the reflected waves. These geometric variations may be viewed as black boxes featuring different acoustic impedances.

In contrast, the right-hand image depicts a generic hardware boundary, which is characterized by the open-loop impedance  $Z_{ol}$ . Employing an active control scheme, an artificial closed-loop impedance  $Z_{cl}$  may be imposed.

The scheme consists of sensors determining the downstream propagating wave in real-time. It is the input signal for the controller, which then determines a suitable output signal driving an acoustic actuator downstream. This actuator superimposes an acoustic perturbation on the waves that are naturally reflected by the outlet. Thereby, the upstream propagating wave is altered in a way that the acoustic system effectively sees a different boundary condition,

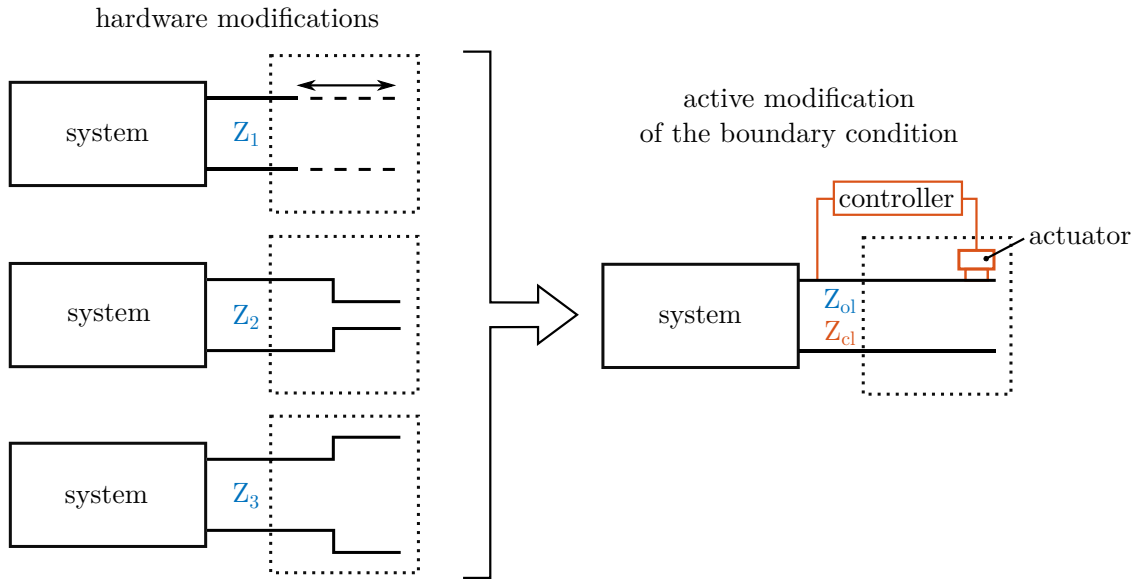


**Figure 1.2.:** Left: systems with varying acoustic boundary conditions  $Z_n$ , due to terminations with different geometries. Right: system with an actively modifiable boundary condition. Depiction adapted from Bothien [18].

i. e., the closed-loop impedance  $Z_{cl}$ . Thereby, for instance, boundary conditions corresponding to the shown hardware modifications may be mimicked. Bothien's concept is summarized in his thesis [18]. He also published several research articles and conference proceedings on the topic, most of which are mentioned in the following passages.

In 2007, Bothien et al. [20] presented their first publication concerned with impedance tuning. Using a model-based feedback controller, they succeeded in actively tuning the outlet impedance of an atmospheric combustion test rig to fully reflecting and fully absorbing boundary conditions. Additionally, they altered the phase of the controlled reflection coefficient in order to add *virtual additional length*, which yields different combustion chamber resonance frequencies. These milestones were achieved under both non-reacting and reacting conditions. In order to measure the controller input signal, Bothien et al. used an online wave identification scheme based on the *Two-Microphone Method*, which is properly introduced in SEC. 2.2. This was done for two sets of sensors, subsequently averaging the results. A low-frequency loudspeaker driver was used for acoustic excitation at the combustion chamber outlet.

Shortly afterwards, Moeck et al. [112] presented the successful implementation of active impedance control using an advanced version of the online wave identification. The method relies on more than two sensors to measure the downstream propagating acoustic waves in real-time, which is effectively easier to implement and delivers more reliable results. Bothien et al. [17, 23, 24] further showed their concept to be applicable for stability analysis in the context of combustion experiments. They continuously varied the controlled reflection coefficient of a test rig and thereby studied the transient behavior of the system. Bothien et al. [21] also pointed out the applicability of the concept for active instability control of combustion systems.

In 2009, the same researchers [22] published an article about the successful employment of high-bandwidth proportional valves for air flow modulation as acoustic actuators allowing for impedance tuning. The results showed that the devices are capable of actively tuning the acoustic boundary conditions in a frequency-band while being able to withstand the harsh environment of a high pressure test rig. One year later, Bothien et al. [26] presented an article dealing with the extension of the scheme to actuators with a non-linear response. However, with these devices, impedance tuning can be implemented at single frequencies, only. So-called *discrete impedance tuning* relies on look-up tables to determine the correct phase and amplitude relations.

Saurabh et al. [149] later applied broadband impedance tuning to realize anechoic conditions at the termination of a combustion test rig. Thereby, the response of a flame to transverse acoustic actuation was studied.

In the context of high pressure tests, the active modification of the acoustic boundary condition may be used to assess susceptibility of a burner system towards thermoacoustic oscillations. By continuously altering the outlet impedance of the test rig, the onset of combustion instabilities may be studied. Furthermore, the entire operating envelope of the engine, incorporating realistic boundary conditions, may be investigated in a test rig environment.

### 1.7. Flame Response Measurements for the Thermoacoustic Characterization of Combustor Configurations

A less direct, but matured approach for stability analyses is the utilization of low-order network models. The elements of the burner system can be described by individual models, which describe their corresponding acoustic input-output behavior in terms of *transfer matrices*. The transfer behavior of most elements may be determined by analytical or numerical methods. Further explanations on this topic are found in SEC. 2.3. At this point, it is sufficient to recognize that one key element can only be determined experimentally. Namely, the *flame transfer matrix* and its influences are not reliably predictable with today's numerical instruments. Thus, measurement of the flame's transfer behavior (or *thermoacoustic characterization*) remains a highly important tool for employing network models in stability analyses.

Examples for experimental investigations of flame transfer matrices, conducted in atmospheric pressure environments, are found in references [11, 52, 128, 157, 161, 162]. Under certain conditions, shape and position of a natural gas flame are independent of the mean pressure, as stated by Zajadatz et al. [193]. Freitag et al. [49] used a burner, which does, however, exhibit a mean-pressure dependent flame transfer behavior. Yet, they also stated that the pressure dependence saturates. I. e., in order to obtain a flame transfer matrix valid at high pressures, the corresponding tests may be conducted at an intermediate pressure level.

In order to elaborate on the required measurements, the mathematical expression of a flame transfer matrix  $\mathbf{T}_F$  is introduced here. It represents a so-called acoustic two-port (cf.

SEC. 2.3), connecting the complex amplitudes of the Fourier-transformed acoustic pressure  $\hat{p}$  and velocity  $\hat{u}$  upstream (index  $(\cdot)_u$ ) of the flame to those downstream (index  $(\cdot)_d$ ):

$$\begin{bmatrix} \hat{p}_d \\ \hat{u}_d \end{bmatrix} = \underbrace{\begin{bmatrix} T_{11} & T_{12} \\ T_{21} & T_{22} \end{bmatrix}}_{\mathbf{T}_F} \begin{bmatrix} \hat{p}_u \\ \hat{u}_u \end{bmatrix} + \begin{bmatrix} \hat{p}_s \\ \hat{u}_s \end{bmatrix}. \quad (1.2)$$

An additional source term, denoted with the index  $(\cdot)_s$ , represents coherent sound emitted by the flow field or the flame and random noise. As stated by Paschereit et al. [128], the source term arises, e. g., from coherent flow instabilities or turbulent fluctuations of the velocity field and the fuel–air mixture ratio. It is not required for assessing thermoacoustic stability. However, it can be used to compute the pressure spectra of the combustor in stable conditions, as it is responsible for driving the combustor acoustics in the absence of self-excited oscillations.

Determination of the four transfer matrix elements requires two independent excitation states [128]. As detailed by Åbom [1], these states may be realized using, for example, the *two-load method* or the *two source-location method*. Application of the two-load method could be less expensive, as only one actuator is required. Two test states are created by altering one of the boundary conditions, which can cause practical issues, as pointed out by Åbom [1]. Firstly, the load impedances may not be unique over the whole frequency range. Secondly, in mean-flow applications, it may be difficult to change the load impedance without changing the flow field. The two source-location method, as introduced by Munjal et al. [118], requires actuators and sensor arrays both upstream and downstream of the investigated acoustic element. Subsequent actuation at the upstream and downstream locations creates the two independent test cases. As the velocity fluctuations cannot be directly measured in most technical applications, usually pressure measurements are conducted. A standard approach is the Multi-Microphone Method (cf. SEC. 2.2), which is considered robust and reliable enough to be applied in gas turbine combustion chambers.

The effect of the source term is removed from the measurements by cross-correlating the pressure signals with the excitation signal [128]. The source terms can then be determined by using data acquired from a third acoustic state, usually one without excitation.

Note that in typical test rig configurations, it is not possible to determine the acoustic state directly upstream of the flame, but only upstream of the burner. Initially, the measured transfer matrix  $\mathbf{T}_{BF}$  will thus include the acoustic properties of burner and flame. The influence of the burner is removed by the following procedure. In addition to the measurement of  $\mathbf{T}_{BF}$  in reacting conditions, a second set of measurements is obtained in non-reacting conditions, but at an identical preheat temperature. The latter allows for determination of the burner transfer matrix  $\mathbf{T}_B$ . Subsequently, the flame transfer matrix  $\mathbf{T}_F$  is calculated according to:

$$\mathbf{T}_F = \mathbf{T}_{BF} \mathbf{T}_B^{-1}. \quad (1.3)$$

Here, it is assumed that the burner transfer matrix is not affected by the presence of the flame. This assumption is typically met when the flow field inside the burner does not change from non-reacting to reacting conditions.

A closely related alternative to the flame transfer matrix is the scalar *flame transfer function*  $F(\omega)$ . It is defined as the ratio of normalized global heat release rate fluctuations to the normalized velocity fluctuations at the burner outlet:

$$F(\omega) = \frac{\hat{Q}/\bar{Q}}{\hat{u}/\bar{u}}. \quad (1.4)$$

The complex amplitudes are normalized by the corresponding mean values (denoted by overbars). The flame transfer function is dependent on the circular frequency  $\omega$ , which results from transformation into frequency domain via the Fourier transform. Note that the theoretic background is properly introduced in CHAP. 2. Under the following conditions:

- acoustic compactness (acoustic wavelength  $\ll$  axial extent of the flame),
- low Mach number of the flow, and
- pressure insensitive fuel injection,

the flame transfer function can be used to formulate a transfer matrix. Thereby, it may be incorporated in a low order network model for stability analysis. With the aforementioned assumptions, the Rankine-Hugoniot relations and the mean energy balance may be invoked, which yields the flame transfer matrix [161]:

$$\mathbf{T}_F(\omega) = \begin{bmatrix} 1 & 0 \\ 0 & H(\omega) \end{bmatrix} \quad \text{with } H(\omega) = 1 + \left( \frac{T_d}{T_u} - 1 \right) F(\omega), \quad (1.5)$$

where  $T_u$  and  $T_d$  denote the temperatures upstream and downstream of the flame, respectively. For completeness, it shall be mentioned that the  $T_{11}$  element changes to the ratio of characteristic impedances  $(\bar{\rho}\bar{c})_u/(\bar{\rho}\bar{c})_d$ , when specific pressure fluctuations are regarded.

Consequently, the determination of the flame transfer function necessitates measurement of the velocity fluctuations upstream of the flame and the global heat release rate fluctuations. For non-perfectly premixed (or *technically premixed*) flames, the latter is a difficult task. In principle, there are methods based on acoustic and optical measurements. The former is discussed in SEC. 3.3, while the latter shall be described here.

Optical methods rely on the radiation of excited intermediate reaction species. Under perfectly premixed conditions, *chemiluminescence* of excited radicals such as  $\text{CH}^*$  or  $\text{OH}^*$  was shown to be reasonably proportional to the heat release rate [67, 73, 126]. However, the chemiluminescence intensity strongly depends on the equivalence ratio. Therefore, it is not a quantitative marker of the heat release rate in technically premixed conditions, as stressed by Schuermans et al. [157] and Lauer & Sattelmayer [91]. Despite this shortcoming, single-species chemiluminescence signals have been used in elevated pressure test rigs to qualitatively characterize the response of technically premixed flames to acoustic perturbations [36, 75].

In recent years, a multi-species method was developed. Simultaneous measurements of the chemiluminescence emissions from multiple species account for fluctuations in the equivalence ratio, as pointed out by Guyot et al. [64] and Schuermans et al. [159]. This approach was successfully applied to measure flame transfer functions in atmospheric conditions [14, 64] and also at full engine pressure [160]. However, the results showed that the method does not give reliable results under all test conditions. Quantitative studies require extensive

calibration of the chemiluminescence intensity as a function of equivalence ratio and mass flow. Further, a correction for the  $\text{CO}_2^*$  background emissions needs to be implemented. At elevated pressure, higher quenching rates of the excited species and self-absorption diminish the chemiluminescence intensity [160] and, thus, make the method more error-prone. Another difficulty encountered in high pressure rigs is limited optical access, which may impede acquisition of the global heat release rate. Due to the mentioned reasons, the optical multi-species method cannot be considered as a reliable standard technique to determine the flame transfer function. Therefore, purely acoustic approaches are discussed throughout this work.

### 1.8. Objectives and Structure of the Thesis

In the preceding sections, the state-of-the-art in analysis of combustion instabilities in stationary gas turbines was outlined. Various methods of determining the susceptibility of new combustion systems towards thermoacoustic instabilities were presented.

This thesis focuses on the modification of an existing high pressure test rig from SIEMENS PG. The rig is designed for testing of combustion systems that are found in the largest gas turbines in the portfolio of the company, and its characteristics will be detailed in CHAP. 3. The modifications aim at achieving two major objectives:

1. thermoacoustic characterization of burner systems by measurement of the flame transfer behavior and
2. active modification of the downstream acoustic boundary condition (impedance tuning) for a direct assessment of the stability characteristics.

Measurement of the flame transfer behavior is proposed in terms of purely acoustic methods, as optical methods are not considered reliable. The choice, whether equipment for measurement of flame transfer functions or flame transfer matrices shall be employed, is discussed in CHAP. 3. In essence, acoustic excitation and measurement of the acoustic fields upstream and downstream of the flame are required to enable a determination of the flame transfer behavior. The resulting data can be used as input for low-order thermoacoustic network models. Thereby, the stability properties of new combustor systems may be assessed based on simulations that are fed by highly reliable data of the acoustic flame transfer behavior.

Furthermore, a *direct* assessment of the susceptibility of combustor systems towards combustion instabilities can be realized. Since the flow fields, pressure levels, and temperature profiles in the geometrically similar test rig correlate well with the engine, the only major difference lies in the acoustic outlet boundary condition. Using impedance tuning, the acoustic properties of the engine can be realized at the test rig, which allows for direct investigations of the stability characteristics of new combustor systems.

Implementation of impedance tuning requires a sensor array capable of real-time determination of the downstream propagating acoustic waves in the combustor, as well as suitable acoustic excitation upstream and downstream of the combustion chamber.

The thesis is structured as follows. In CHAP. 2, the theoretical background on the utilized methods is detailed. Basic acoustic theories are presented, which are required to understand, e. g., data evaluation techniques and network models. Further, the active modification of the acoustic boundary condition is described.

In the first part of CHAP. 3, the regarded high pressure test rig is introduced. Subsequently, the requirements for achieving the two major objectives of the thesis are explained. Mutual requirements are pointed out, which leads to the proposed modifications. Within the next four chapters, the approaches to acoustic sensor and actuator design are described.

The fourth chapter deals with the options of sensor design for the region upstream of the burner, which is required for the thermoacoustic characterization. Two viable methods are presented, both featuring advantages and disadvantages. No commitment to a final decision is made, leaving scope of action for the implementation.

In CHAP. 5, the plane wave decomposition, which is regarded as a standard technique in the determination of the acoustic variables, is extended to ducts with non-uniform cross-sections. This is necessary, as the combustion chamber of the test rig shall keep its current realistic three-dimensional shape. The utilized theory for implementing a frequency-domain and a time-domain variant is detailed. Subsequently, validating numerical and experimental investigations are discussed alongside with possible implications for a practical employment of the method.

Consecutively, acoustic actuation upstream of the burner is discussed, which includes a short discussion on possible devices and investigations on the position inside the test rig. Two main options and variants of these are studied in terms of numerical simulations, and the corresponding advantages and disadvantages are discussed.

CHAP. 7 comprises elaborations on the development of the actuator for the region downstream of the flame. The device has to fulfill several requirements, which are difficult to combine in an industrial high pressure test rig. A discussion on possible actuator types is conducted, leading to a novel concept for acoustic excitation. Time-resolved compressible CFD simulations are presented, which show a promising performance of the concept. They are used as basis for the experimental determination of several characteristics of the actuation mechanism. Finally, eligibility of the concept for the implementation of impedance tuning is verified using a time-domain network model.

In the last chapter, the results are summarized and discussed in terms of their practical implications and contributions to current and future research. Furthermore, an overview of the remaining steps before the final implementation is given.



# CHAPTER 2

---

## Theoretical Background on Acoustics and Utilized Methods

---

After the motivation and the goals of the thesis were presented in the preceding chapter, the theoretical foundation needed for this work shall be summarized. Main references used throughout this chapter are a standard book on acoustics from Rienstra & Hirschberg [143], as well as the PhD theses from Schuermans [156] and Bothien [18]. The latter are comprehensive works on the topics of thermoacoustics in gas turbines and impedance tuning, respectively.

In a first step, the acoustic wave equation is derived for stationary conditions and for cases with mean flow. Lighthill's aeroacoustic analogy delivers a source term, which is of relevance for conclusions made within the actuator development in CHAP. 7. Subsequently, generic solutions to the convective wave equation as well as the connection of Riemann invariants and primitive acoustic variables are presented. Boundary conditions are introduced in terms of acoustic impedance and the reflection coefficient. After a summary of the frequency-domain plane wave decomposition in ducts with constant cross-section, the basics of frequency-domain and time-domain low-order network models are detailed. Finally, the scheme for an active modification of the acoustic boundary condition is reviewed and the required wave identification in time domain is summarized.

### 2.1. Wave Equation

The governing equations for fluid motion are mass, momentum, and energy conservation, which may be found for instance in the works of Pierce [133] or Truckenbrodt [177], and Rienstra & Hirschberg [143]. In linear acoustics, only small perturbations around mean values are regarded. The flow variables pressure, velocity, density, temperature, heat release, and entropy are split into their mean and fluctuating values, which is expressed in terms of a placeholder function  $\Psi$ :

$$\Psi = \bar{\Psi} + \Psi'. \tag{2.1}$$

In linear acoustic theory, the fluctuating part of each quantity is assumed to be much smaller than the mean value. Thus, in a source free and inviscid medium (e. g., references [133, 143]), the linearized conservation equations of mass and momentum read

$$\frac{\partial \rho'}{\partial t} + \bar{\rho} \nabla \cdot \mathbf{u}' = 0 \quad (2.2)$$

$$\bar{\rho} \frac{\partial \mathbf{u}'}{\partial t} + \nabla p' = 0, \quad (2.3)$$

where  $\bar{\rho}$  is the mean density and  $\mathbf{u}'$  and  $p'$  are the fluctuating components of the velocity vector and the pressure, respectively. The linearized conservation of energy reads:

$$\frac{\partial s'}{\partial t} = 0, \quad (2.4)$$

where  $s'$  is the fluctuating entropy component. These equations can be closed by invoking the equation of state

$$p = p(\rho, s) \quad (2.5)$$

and the ideal gas law

$$p = \rho R_g T, \quad (2.6)$$

with  $R_g$  and  $T$  being the specific gas constant and the fluid temperature, respectively.

Forming the total differential of the pressure (EQ. 2.5), subsequent incorporation of EQ. 2.4, and linearization yield the following expression for the fluctuating pressure [143]

$$p' = \underbrace{\left( \frac{\partial p}{\partial \rho} \right)_s}_{:=c^2} \rho'. \quad (2.7)$$

Note that the (italic) index  $(\cdot)_s$  denotes a partial derivation at constant entropy. The introduced factor  $c$  is the speed of sound. In an ideal gas it is calculated with

$$c = \sqrt{\gamma R_g T}, \quad (2.8)$$

where  $\gamma$ , the ratio of specific heats, is considered constant in most technical applications. These primal equations are now used to derive the *wave equation for quiescent fluids*. Subtraction of the time derivative of EQ. 2.2 from the divergence of EQ. 2.3 yields

$$\frac{\partial^2 \rho'}{\partial t^2} - \nabla^2 p' = 0. \quad (2.9)$$

With EQ. 2.7, the wave equation in terms of the pressure fluctuation is obtained:

$$\frac{\partial^2 p'}{\partial t^2} - c^2 \nabla^2 p' = 0. \quad (2.10)$$

Application of a Fourier transform yields the Helmholtz equation:

$$\nabla^2 \hat{p} + k^2 \hat{p} = 0, \quad (2.11)$$

with  $k$  being the wave number. It is defined as the ratio of angular frequency  $\omega = 2\pi f$  and  $\bar{c}$ :

$$k = \frac{\omega}{\bar{c}}. \quad (2.12)$$

With these equations, source-free acoustic fields can be described in ducts with homogeneous and stagnant media. This quiescent formulation is extended to cases with mean flow by replacing the local time derivative  $\frac{\partial}{\partial t}$  in EQ. 2.10 with the total derivative  $\frac{D}{Dt} = \frac{\partial}{\partial t} + \bar{\mathbf{u}} \cdot \nabla$ :

$$\left( \frac{\partial}{\partial t} + \bar{\mathbf{u}} \cdot \nabla \right)^2 p' - \bar{c}^2 \nabla^2 p' = 0. \quad (2.13)$$

Solutions to the *convective wave equation* are presented in SUBSEC. 2.1.2. Equivalently, the replacement of the local with the total derivative in EQ. 2.3 yields the convective acoustic momentum equation, which reads:

$$\bar{\rho} \left( \frac{\partial \mathbf{u}'}{\partial t} + (\bar{\mathbf{u}} \cdot \nabla) \mathbf{u}' \right) + \nabla p' = 0. \quad (2.14)$$

It is also called the *Euler equation* and relates the acoustic pressure to the particle velocity.

### 2.1.1. Mass Source Term and Lighthill's Aeroacoustic Analogy

So far, only source-free formulations of the equations of motion were presented. However, due to its application in this work, a source term for mass injection in a stagnant medium is introduced here. According to Rienstra & Hirschberg [143], the linearized equation of mass conservation can be written as

$$\frac{\partial \rho'}{\partial t} + \bar{\rho} \nabla \cdot \mathbf{u}' = m'_s, \quad (2.15)$$

where  $m_s$  is the source term corresponding to mass injection. Note that throughout the work, mass flow is denoted with  $m$ , missing the otherwise used  $(\dot{\cdot})$  for time derivatives. The fluctuating component of the mass flow is defined here as

$$m'_s = \frac{\partial(\rho_s \beta)}{\partial t}, \quad (2.16)$$

where  $\beta$  is the volume fraction of the injected fluid and  $\rho_s$  the density of the injected fluid. The total mass in the control volume  $\rho$  consists of the injected mass  $\rho_s$  and the original mass  $\rho_{\text{or}}$ , which is displaced in the source region:

$$\rho = \beta \rho_s + (1 - \beta) \rho_{\text{or}} \quad (2.17)$$

Following the steps in SEC. 2.1, the inhomogeneous wave equation outside the source region can be found:

$$\frac{\partial^2 p'}{\partial t^2} - \bar{c}^2 \nabla^2 p' = \bar{c}^2 \frac{\partial^2 (\beta \rho_{\text{or}})}{\partial t^2}. \quad (2.18)$$

Thus, it becomes apparent that the generation of sound through fluid injection depends on a non-vanishing second time derivative of the *displaced* mass.

As mentioned before, EQ. 2.18 only applies to quiescent media. In presence of a mean flow, the effects of flow phenomena have to be incorporated, as well. In the work of Lighthill [97], these effects were first described and his theory has since been referred to as *Lighthill's aeroacoustic analogy*. He introduced an exact wave equation in terms of the density with an aeroacoustic source term written in Einstein's notation, which reads:

$$\frac{\partial^2 \rho}{\partial t^2} - \bar{c}^2 \nabla^2 \rho = \frac{\partial^2 (\rho u_i u_j + \tau_{ij} - \bar{c}^2 \rho \delta_{ij})}{\partial x_i \partial x_j}. \quad (2.19)$$

$\tau_{ij}$  is the stress tensor and  $\delta_{ij}$  the Kronecker delta. The term  $\rho u_i u_j$  describes the unsteady convection of flow, e. g., due to vortices or hydrodynamic instabilities. The remaining terms include sound generation caused by shear and by non-linear effects, as for instance entropy waves.

### 2.1.2. One-Dimensional Solution to the Convective Wave Equation

It is sufficient to account for a purely one-dimensional wave propagation in applications that consider, for instance, intermediate frequency thermoacoustic phenomena in atmospheric acoustic test rigs. For these investigations, constant cross-sectional area ducts are employed, as the corresponding solutions to the convective wave equation are known a priori. Accordingly, possible solutions shall be briefly summarized in this section.

In ducted applications, the sound field can be described by acoustic modes, which are patterns of oscillation that depend on the boundary conditions. These modes are either able to propagate, which is indicated by a purely real wave number or they are evanescent, which is the case, if the wave number is imaginary. In the latter case, the acoustic waves associated to that mode are unable to propagate outside of their near environment, as they are exponentially damped. The distinction between evanescent and propagative modes is the so-called *cut-on frequency*, which was, e. g., derived by Bothien [18] as follows:

$$f_{\text{cut}} = \frac{1.84 \bar{c}}{\pi d} \sqrt{1 - M^2}, \quad (2.20)$$

where  $d$  is the duct diameter and the Mach number is defined as

$$M = \frac{\bar{u}}{\bar{c}}. \quad (2.21)$$

Note that the exponential attenuation of an evanescent mode is frequency-dependent. Thus, in measurements or simulations, the distance between any near-field influences and sensors that rely on plane wave propagation needs to be accounted for.

For acoustic phenomena below the cut-on frequency, solutions to the convective wave equation shall be presented. One option to solve EQ. 2.13, a second order partial differential equation, is the general d'Alembert solution. It consists of a superposition of downstream and upstream propagating waves as functions of shifting arguments:

$$p'(x,t) = f\left(t - \frac{x}{\bar{c} + \bar{u}}\right) + g\left(t + \frac{x}{\bar{c} - \bar{u}}\right). \quad (2.22)$$

$f$  and  $g$  are the *Riemann invariants* that travel with the speed of sound, which is superimposed by the mean flow velocity  $\bar{u}$ .

If one considers time-harmonic oscillations, a separation ansatz can be made with an exponential function. A detailed derivation, which is suitable for the purpose of this work, is for example found in the works of Schuermans [156] or Bothien [18]. Incorporating the wave number for downstream (+) and upstream (-) propagating waves:

$$k^\pm = \frac{k}{1 \pm M}, \quad (2.23)$$

the pressure field in frequency domain can be described by

$$\hat{p} = \bar{\rho}\bar{c}(\hat{f}e^{-ik^+x} + \hat{g}e^{ik^-x}). \quad (2.24)$$

The constant factor  $\bar{\rho}\bar{c}$  is referred to as the characteristic impedance ( $Z_0$ ) of the fluid. Substitution of EQ. 2.24 into EQ. 2.14 yields the frequency-domain particle velocity field:

$$\hat{u} = \hat{f}e^{-ik^+x} - \hat{g}e^{ik^-x}. \quad (2.25)$$

Due to linearity, EQ. 2.24 and EQ. 2.25 can be expressed in time domain as follows:

$$p' = \bar{\rho}\bar{c}(f + g) \quad (2.26)$$

$$u' = f - g. \quad (2.27)$$

Accordingly, the Riemann invariants can be calculated from the primitive acoustic variables using the following equations:

$$\hat{f} = \frac{1}{2} \left( \frac{\hat{p}}{\bar{\rho}\bar{c}} + \hat{u} \right) \quad (2.28)$$

$$\hat{g} = \frac{1}{2} \left( \frac{\hat{p}}{\bar{\rho}\bar{c}} - \hat{u} \right) \quad (2.29)$$

Thus, the foundation for analyses of low-frequency acoustics in ducts with constant cross-sectional area is laid. As mentioned before, ducted acoustic fields are highly dependent on boundary conditions, which are therefore covered in the following subsection.

### 2.1.3. Boundary Conditions

A descriptive way to define a boundary condition is the *reflection coefficient*, which is defined as the ratio of the reflected and the incident sound waves at the boundary of a duct:

$$R(x,\omega) = \frac{\hat{g}(x,\omega)}{\hat{f}(x,\omega)}. \quad (2.30)$$

This relation is valid for a downstream boundary, while the upstream equivalent is defined as the reciprocal value. The reflection coefficient is a complex-valued frequency-dependent function. Its phase is further dependent on the axial coordinate, at which it is evaluated. An analogous way to describe the reflectivity of a boundary is the acoustic impedance, which correlates sound pressure to particle velocity:

$$Z(x,\omega) = \frac{\hat{p}(x,\omega)}{\hat{u}(x,\omega) \cdot \mathbf{n}(x)}. \quad (2.31)$$

This expression includes the normal vector  $\mathbf{n}(x)$ , which is defined to point out of the control volume. Thus, its relation to the axial coordinate has to be taken into consideration. The reflection coefficient can be calculated from the impedance by considering EQ. 2.26 and EQ. 2.27:

$$R = \frac{Z - \bar{\rho}c}{Z + \bar{\rho}c}. \quad (2.32)$$

Often, the specific impedance  $\mathcal{Z} = Z/\bar{\rho}c$  is considered. The conversion between reflection coefficient and specific impedance is possible with:

$$R = \frac{\mathcal{Z} - 1}{\mathcal{Z} + 1}, \quad \mathcal{Z} = \frac{1 + R}{1 - R}. \quad (2.33)$$

The reflection coefficient is a measure for the amount of acoustic energy that is conserved or radiated from a boundary. Three specific cases are presented, which are frequently referred to in this work:

- $R = 1$  (closed end)  
At rigid boundaries, the impedance approaches infinity, which manifests in a velocity node ( $\hat{u} = 0$ ). The acoustic particles do not oscillate, which results in a total reflection of the incident acoustic waves. The phase is not shifted in this case and it is referred to as a *sound hard* boundary.
- $R = 0$  (anechoic end)  
The impedance of the fluid is  $Z = \bar{\rho}c$ , i. e., it is equal to the characteristic impedance. Thus, the relation between acoustic pressure and particle velocity is  $\hat{p} = \bar{\rho}c\hat{u}$ . Acoustic waves leave the boundary without any reflection.
- $R = -1$  (open end)  
At an impedance of  $Z = 0$ , a pressure node ( $\hat{p} = 0$ ) is present. The acoustic energy is conserved and the incident waves are fully reflected with a phase shift of  $180^\circ$ . It is referred to as a *sound soft* boundary.

However, in practice, an open end will not be a fully reflecting boundary for most frequencies. An exact solution incorporating an end correction for circular unflanged pipes was derived by Levine & Schwinger [93] for stationary conditions.

Further note that with mean flow, the reflection coefficient may even assume values of  $|R| > 1$ . An elaboration on this is found, for instance, in the works of Munt [122] and Cargill [34].

## 2.2. Plane Wave Decomposition with the Multi-Microphone Method

Experimental determination of the Riemann invariants in a duct with constant temperature profile and constant cross-section is theoretically possible by measuring the acoustic pressure and particle velocity at one axial location. Subsequent employment of EQ. 2.28 and EQ. 2.29 yields the sought downstream and upstream propagating waves. However, due to practical issues in reliably determining acoustic velocities, e.g., using hot-wires or laser Doppler velocimetry, this approach is inapplicable in most technical scenarios. A solution to this issue is found by employing multiple pressure sensors at an axial distance and fitting the measurements to analytical solutions of the wave equation. The first application of this concept was the Two-Microphone Method, which was introduced by Seybert [164] and refined by Chung & Blaser [37]. In both works, the method was used to calculate reflection and absorption characteristics of test materials in impedance tubes. However, the method entails the significant disadvantage of producing infinite errors when the microphone spacing takes values that are multiples of half a wavelength. Moreover, erroneous results are to be expected in the vicinity of those frequencies. This was elaborated by Bodén & Åbom [16] for stationary conditions and additionally for cases with mean flow [2]. Poinsot et al. [135] extended the Two-Microphone Method to multiple sensors and applied it to impedance measurements of a premixed turbulent flame. In that way, the mentioned disadvantages of the Two-Microphone Method may be circumvented. Additionally, the accuracy of the technique is improved, as the calculation is based on a least-squares solution of an over-determined equation system. Paschereit et al. [128] later applied the *Multi-Microphone Method* upstream and downstream of a swirl-stabilized premixed flame to obtain a transfer matrix, which is the key element for thermoacoustic stability investigations with low-order network models.

For the scheme introduced here, a straight duct of uniform cross-sectional area, speed of sound, and mean velocity is assumed. With  $N$  pressure sensors aligned along the duct, the following equation can be established:

$$\bar{\rho}\bar{c} \begin{bmatrix} \hat{f}(\omega) \\ \hat{g}(\omega) \end{bmatrix} = \mathbf{H}^\dagger \underbrace{\begin{bmatrix} \hat{p}(x_1, \omega) \\ \hat{p}(x_2, \omega) \\ \vdots \\ \hat{p}(x_N, \omega) \end{bmatrix}}_{\hat{\mathbf{p}}}, \quad (2.34)$$

where  $\mathbf{H}^\dagger$  is the Moore-Penrose inverse of

$$\mathbf{H} = \begin{bmatrix} e^{-ik^+x_1} & e^{ik^-x_1} \\ e^{-ik^+x_2} & e^{ik^-x_2} \\ \vdots & \vdots \\ e^{-ik^+x_N} & e^{ik^-x_N} \end{bmatrix}. \quad (2.35)$$

The matrix  $\mathbf{H}$  includes the time delays of the acoustic waves between the reference location and each pressure probe. The wave numbers are defined as per EQ. 2.23. An error-estimate can be calculated with:

$$\delta = \frac{\|(\mathbf{I} - \mathbf{H}\mathbf{H}^\dagger)\hat{\mathbf{p}}\|_2}{\|\hat{\mathbf{p}}\|_2}, \quad (2.36)$$

where  $\hat{\mathbf{p}}$  is the vector containing the measured complex pressure amplitudes (cf. EQ. 2.34). Low residuals indicate a good accordance of measured and calculated  $f$  and  $g$  waves. Typical values for good fits do not exceed low single digit percentages.

### 2.3. Low-Order Network Models

Linear stability of complex (thermo-) acoustic systems can be assessed using several methods. One option are detailed CFD simulations, as for instance, conducted by the following research groups. Hernández et al. [72] investigated academic single burner configurations, Schmitt et al. [154] computed heat transfer, emissions and thermoacoustic phenomena of a single high pressure combustor, and Wolf et al. [191] investigated thermoacoustic characteristics for entire annular aeronautical gas turbine combustors. However, such simulations are highly time-consuming and involve significant expenditure. Furthermore, implementation of exact acoustic boundary conditions is a challenge in time-domain CFD, which was for example elaborated by Lamarque et al. [90] and Widenhorn et al. [190]. As a means to resolve this issue, CFD simulations have been coupled to low-order acoustic models of boundary conditions, as e. g. realized by Moeck et al. [113]. Another means to determine linear stability of thermoacoustic systems are finite element methods (FEM), which were for example conducted by Campa et al. [32, 33] and Laera et al. [89]. With FEM simulations, computational times can be reduced, while still incorporating for example three-dimensional geometries and the corresponding physical effects.

In both academic and industrial research, it is common practice to describe the behavior of thermoacoustic systems with low-order network models, which only incorporate the relevant physical system properties. Thus, computation times are further shortened, for example allowing for large numbers of parameters to be altered, which poses a strong advantage over CFD or FEM simulations.

The system is divided into multiple elements that are either described by transfer matrices or scattering matrices in frequency domain or by state-space models in time domain. Both can be set up in a modular way, which is especially useful in early design stages. In that way, single elements can be swapped in order to investigate particular aspects of the system. A standard application is, e. g. the implementation of experimentally determined flame transfer matrices, whose impact on system stability can thus be assessed. Besides experimental means

(e. g., references [128, 160]), subsystems can be determined with analytical methods [10, 161], FEM [5, 32, 132] or CFD simulations [80, 82, 86, 197]. In frequency domain, stability can be assessed on one hand by solving the system's dispersion relation, which is elaborated in references [79, 116, 156, 162]. On the other hand, linear stability can be predicted by inspecting Nyquist plots, as for instance described in references [85, 137, 148]. In time domain, thermoacoustic stability is assessed by solving a matrix eigenvalue problem of the state-space realization of the system, which was detailed by Schuermans et al. [158] and Bellucci et al. [11].

The elements of a network model can be described with various means. Transfer matrices, for example, connect the Fourier-transformed acoustic pressure and particle velocity on both sides of the linear time-invariant subsystems. This relation is expressed as

$$\begin{bmatrix} \hat{p}_d \\ \hat{u}_d \end{bmatrix} = \underbrace{\begin{bmatrix} T_{11} & T_{12} \\ T_{21} & T_{22} \end{bmatrix}}_{\mathbf{T}} \begin{bmatrix} \hat{p}_u \\ \hat{u}_u \end{bmatrix}. \quad (2.37)$$

where the index  $(\cdot)_d$  denotes properties at the subsystem's downstream boundary and  $(\cdot)_u$  those upstream. The entries of  $\mathbf{T}$  are complex valued functions of the angular frequency  $\omega$ . Assuming plane wave propagation, the conversion introduced in SEC. 2.1.2 can be used to describe pressure and velocity at the boundaries with the Riemann invariants. Thus, the same subsystem can be characterized by a scattering matrix  $\mathbf{S}$ :

$$\begin{bmatrix} \hat{f}_d \\ \hat{g}_u \end{bmatrix} = \underbrace{\begin{bmatrix} S_{11} & S_{12} \\ S_{21} & S_{22} \end{bmatrix}}_{\mathbf{S}} \begin{bmatrix} \hat{f}_u \\ \hat{g}_d \end{bmatrix}, \quad (2.38)$$

which is schematically depicted in FIG. 2.1. Scattering matrices (and transfer matrices)

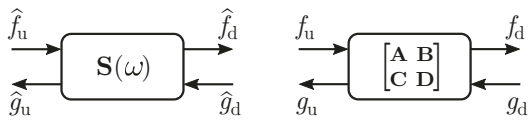


**Figure 2.1.:** Acoustic two-ports relating Riemann invariants at both boundaries. Left: scattering matrix  $\mathbf{S}(\omega)$  in frequency domain, right: state-space model in time domain.

consist of two sets of equations with a total of four unknowns, i. e., the entries of  $\mathbf{S}$  (or  $\mathbf{T}$ ). Hence, in order to solve for the unknowns, two linearly independent acoustic states have to be investigated, which is realized by obtaining the input and output properties in two different excitation scenarios. The subsystem in question is once perturbed from the upstream direction and once from downstream, allowing for calculation of the transfer behavior.

As it is an essential part of a time-domain network model, the procedure of obtaining a state-space realization of a duct's transfer behavior by analytical means is detailed here. Assuming inviscid acoustic transfer behavior and sound-hard walls, a constant cross-sectional area duct only imposes a time-delay on the passing acoustic waves. Thus, the scattering matrix reads

$$\mathbf{S}_{\text{duct}} = \begin{bmatrix} e^{\frac{-ikL}{1+M}} & 0 \\ 0 & e^{\frac{-ikL}{1-M}} \end{bmatrix}, \quad (2.39)$$

where the delay  $\Delta\tau$  of the incoming acoustic waves is described only by the length of the duct  $L$ , the speed of sound  $c$ , and the Mach number  $M$  of the mean flow. However, due to the complex exponential in the elements of  $\mathbf{S}_{\text{duct}}$ , its transfer function has an infinite number of poles. Thus, the state vector of its exact state-space realization would need to have an infinite number of entries [117]. Of course, this is not possible and therefore, the time delay needs to be translated into a rational transfer function, which is realized using a finite-dimensional Padé-approximation [18]. The order of the Padé-approximation depends on the frequency range of the respective investigation and the time-delay. In choosing the numerator degree higher than that of the denominator, the low-pass characteristic of the associated transfer function is taken advantage of. This is especially useful in the conducted simulations, where attenuation at higher frequencies is critical to ensure system stability. Subsequently, the obtained transfer function is converted to a discrete state-space realization, which is conveniently done with integrated MATLAB commands.

The input-output behavior of a subsystem in time domain is expressed in state-space form (cf. FIG. 2.1), reading:

$$\dot{\mathbf{x}} = \mathbf{A}\mathbf{x} + \mathbf{B} \begin{bmatrix} f_u \\ g_d \end{bmatrix} \quad (2.40)$$

$$\begin{bmatrix} f_d \\ g_u \end{bmatrix} = \mathbf{C}\mathbf{x} + \mathbf{D} \begin{bmatrix} f_u \\ g_d \end{bmatrix}. \quad (2.41)$$

$\mathbf{x}$  is the  $N$ -dimensional state vector and  $\mathbf{A}$ ,  $\mathbf{B}$ ,  $\mathbf{C}$ , and  $\mathbf{D}$  are real constant matrices of the appropriate dimensions [196]. The state dimension is dependent on the requirements and has to be high enough in order to represent the acoustic transfer behavior of the element with sufficient accuracy. Performing a Laplace transform on a state-space model yields the transfer function

$$T(\omega) = \mathbf{C}(i\omega\mathbf{I} - \mathbf{A})^{-1}\mathbf{B} + \mathbf{D}, \quad (2.42)$$

where  $\mathbf{I}$  is the identity matrix. Note that a state-space model is not unique and several different realizations can be found for one transfer matrix.

For simple elements like ducts, transfer matrices or state-space realizations are determined analytically, an example of which was described above. More complex transfer behavior requires system identification tools, a comprehensive overview of which is found in the work of Ljung [98]. In this thesis the public-domain MATLAB routine *Vector Fitting* written by Gustavsen & Semlyen [60, 61] is used, which provides a robust and efficient tool for finding rational models to frequency-domain data. As pointed out by Bothien [18], the code enforces stable poles, which is a necessary requirement for the controller transfer function that is introduced in SEC. 2.4. Input to the *Vector Fitting* algorithm are discrete frequency responses obtained from experimental or numerical investigations. A rational approximation of desired order, i. e., number of poles of the state-space realization, is found by means of a partial fraction expansion. An increasing number of poles helps to accurately fit the model to the input data in the regarded frequency range. The obtained models, however, are valid in the whole frequency spectrum. Increasing numbers of poles usually increase the amplitude response of the identified models at frequencies below and above the regarded range. This may lead to an unwanted excitation and render the active control scheme unstable. Therefore,

the complete spectra of the models have to be examined prior to implementing them in the control loop.

#### 2.4. Active Modification of the Acoustic Boundary Condition (Impedance Tuning)

As one of the main objectives of this work is implementation of an active modification of the acoustic outlet impedance of a test rig, the corresponding scheme shall be introduced here. It was originally developed by Bothien [18], thus, his comprehensive PhD thesis on the topic is taken as main reference for this section. FIG. 2.2 depicts the general setup for the active

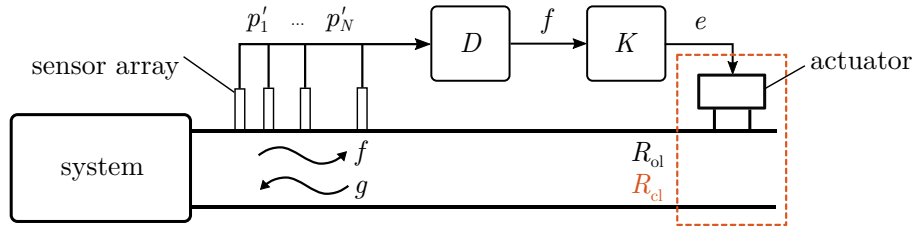


**Figure 2.2.:** Schematic of the impedance tuning concept adapted from reference [112]. The dashed frame symbolizes the end element, the impedance of which is effectively altered by the closed-loop control scheme.

control scheme. On the left-hand side, the combustion system is located, which emits acoustic waves. Physically it is connected to the outlet boundary on the right-hand side via a duct. The duct is considered to feature a constant cross-sectional area in the work of Bothien [18], which is sufficient for introducing the scheme at this point. Furthermore, only plane wave propagation is regarded, which is a valid assumption in any of the cases reviewed in this work. The outlet boundary is supposed to be altered, which is indicated by the dashed orange frame in FIG. 2.2. The entire end element is regarded as a black box with an uncontrolled reflection coefficient  $R_{ol}$ , where the index  $(\cdot)_{ol}$  stands for open loop. Given that the active control scheme is correctly implemented and enabled, the outlet reflection coefficient is altered to the value  $R_{cl}$  (closed loop). This is based on the superposition of the natural reflection at the outlet boundary and the actuator's influence on the acoustic field, the validity of which was shown by Bothien et al. [19]. The actuator's driving signal  $e$  is calculated in the controller, which is segmented into the wave decomposer  $D$  and the control law  $K$ . The control law's input is the downstream propagating wave  $f$ , which is obtained from the pressure signals  $p'_1 \dots p'_N$  in the wave decomposer block. The scheme for the online wave identification used in this work was first detailed by Moeck et al. [112] and it is summarized in SEC. 2.5.

Hardware implementation of the presented scheme is realized on a DS1103 PPC controller board from *dSPACE*. A schematic of the implementation is given in FIG. 2.3. The fluctuating pressure signals  $p'_n$  from the sensor array are amplified externally and digitalized in an analog-digital converter (ADC). The predetermined complex calibration coefficients (cf.

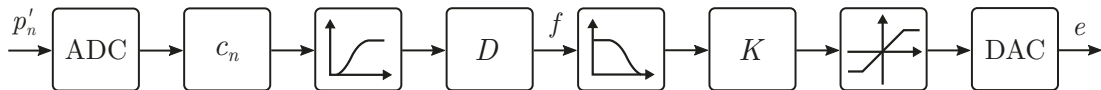


**Figure 2.3.:** Schematic of the controller implementation on the *dSPACE* controller board.

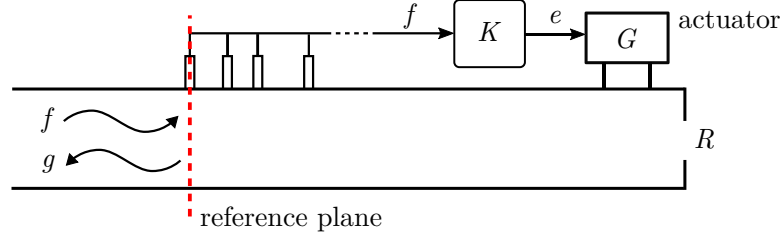


**Figure 2.4.:** Schematic of the microphone array and the end element for visualization of the control law derivation.

SUBSEC. 7.4.1) of the sensors could be implemented on the controller board, as well. However, with the utilized condenser microphones, this is not necessary and therefore omitted in order to save processing capacity. Instead, the absolute value of the calibration coefficient for each microphone is implemented as a constant factor  $c_n$ . In order to yield correct results with this simplification, sensors with a similar phase run need to be chosen among those available. Furthermore, the DC component of the sensor signals has to be filtered out, in order to avoid incorrect processing. This is realized with a high-pass filter using a cut-off frequency of  $\approx 20$  Hz. Attention has to be paid to the filter, which introduces a delay dependent on the filter family and its order. The influence of all filters needs to be taken into account in the calculation of the control law. Subsequently, the pressure signals enter the wave identification block  $D$ , which is detailed in SEC. 2.5 and SEC. 5.2, for constant and non-constant cross-sectional area ducts, respectively. The obtained downstream propagating wave  $f$  is then high-pass filtered, to avoid unwanted high-frequency oscillations. Subsequently, the actual control law  $K$ , which is detailed in the following passages, is applied. Finally, the controller signal is limited by a saturation element, protecting the actuator from damage. The output is handled by a digital-analog converter (ADC) and then emitted as the control command  $e$ .

The derivation of the control law is explained in detail in reference [18] and the essentials are repeated here for completeness. Initially, the approach to obtain the necessary transfer functions is summarized using the schematic in FIG. 2.4.

As explained before, the upstream propagating wave  $\hat{g}$  in the duct can be regarded as a superposition of the natural reflection of the downstream propagating wave  $\hat{f}$  at the duct termination and the actuator output signal, which consists of an input signal  $\hat{e}$  and the actuator transfer function  $G$ :

$$\hat{g} = R_{\text{ol}}\hat{f} + G\hat{e}. \quad (2.43)$$

Note that all quantities are given in frequency domain. Both the *open-loop reflection coefficient*  $R_{\text{ol}}$  (without active control) and the actuator transfer function can be determined experimentally or numerically, depending on the type of investigation. In a first step,  $R_{\text{ol}}$  is obtained by excitation upstream of the reference plane, which is referred to as excitation case A. The Multi-Microphone Method is used to calculate the Riemann invariants  $\hat{f}$  and  $\hat{g}$ . As no downstream forcing is present ( $\hat{e} = 0$ ), EQ. 2.43 simplifies to:

$$\hat{g}^{\text{A}} = R_{\text{ol}}\hat{f}^{\text{A}}. \quad (2.44)$$

Subsequently, in excitation case B, the downstream actuator is used for acoustic forcing. Transposing EQ. 2.43, the actuator transfer function  $G$  can be calculated with

$$G = \frac{\hat{g}^B - R_{\text{ol}}\hat{f}^B}{\hat{e}}. \quad (2.45)$$

In order to calculate  $K$ , the control command  $\hat{e}$  is written in terms of the controller transfer function and its input signal:  $\hat{e} = K\hat{f}$  (cf. FIG. 2.4). It is then inserted into EQ. 2.43:

$$\hat{g} = (R_{\text{ol}} + GK)\hat{f}. \quad (2.46)$$

Division by the downstream propagating wave yields the closed-loop reflection coefficient:

$$R_{\text{cl}} = \frac{\hat{g}}{\hat{f}} = R_{\text{ol}} + GK. \quad (2.47)$$

The control law can thus be calculated with

$$K = \frac{R_{\text{cl}} - R_{\text{ol}}}{G}. \quad (2.48)$$

In summary, the open-loop reflection coefficient  $R_{\text{ol}}$  and the actuator transfer function  $G$  need to be determined and translated into state-space models according to the procedure detailed in SEC. 2.3, in order to calculate a control law  $K$ . Thereby, the closed-loop reflection coefficient  $R_{\text{cl}}$  is defined to a complex-valued and frequency-dependent function. The result is an altered upstream propagating wave  $\hat{g}$  that satisfies EQ. 2.46. Provided, the control scheme is implemented correctly, the impedance of the outlet can thus be altered to prescribed values. The scheme's application is described in SEC. 7.6.

In practice, it is possible that the time delay of the actuator transfer function is larger than that of  $R_{\text{cl}} - R_{\text{ol}}$ , which violates causality of the controller. In other words, the actuator command signal would need to be sent before its input signal reaches the controller. In general a large time lag between emission of the actuator output and arrival of the acoustic wave at the sensor array results in an unfavorable ratio of time lags. This aspect is further detailed in SEC. 7.6. Another important issue with broadband impedance tuning is the identification of the control law and the behavior of the identified model at frequencies below and above the regarded frequency band. As mentioned in SEC. 2.3, the response at frequencies towards zero and infinity have to be carefully examined in order to avoid an unstable control loop.

These issues can be prevented by actively modifying the acoustic boundary condition only at discrete frequencies, as was elaborated by Bothien [18]. In this case, the control law is only valid at a single frequency and it only consists of a gain, a delay, and a band-pass filter, which removes the demand for system identification. A significant advantage is that the phase of the controller transfer function can be shifted by a constant value. Thus, the time delay ratio of the actuator's output signal and the controller's input signal is not a limitative factor any more. As was discussed by Bothien et al. [22], it is important to note that tuning at discrete frequencies for the investigation of limit-cycle oscillations in a combustion test rig may lead to instabilities at several frequencies, while in a real application only the mode with the highest growth rate may prevail. Depending on the aim of the investigation, this may be a disadvantage in assessing the thermoacoustic properties of a burner setup. Thus,

discrete impedance tuning can be viewed as a backup solution. However, in this work, only a broadband modification of the boundary condition is regarded.

## 2.5. Plane Wave Decomposition in Time Domain

Determination of the downstream propagating wave in real-time is a key component of the impedance tuning scheme. The theoretic basis of the method shall be summarized here, as it is used in SEC. 7.6 and required for the extension to ducts with variable cross-sections in SEC. 5.2.

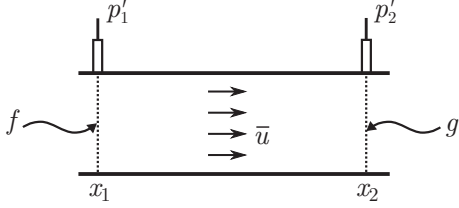


**Figure 2.5.:** Schematic of two pressure sensors for wave identification on a duct with constant cross-sectional area. Image adapted from [21].

As depicted in FIG. 2.5, a duct of constant cross-sectional area with uniform mean flow ( $\bar{u}$ ) is considered. Initially, two pressure sensors are mounted along the duct in order to calculate the Riemann invariant  $f(t)$ , which allows for calculation of  $g(t)$ , directly. Analog to EQ. 2.22, the pressure readings at the sensors can be written in terms of the downstream and upstream propagating waves, which are delayed in time:

$$\frac{p'_1}{\bar{\rho}\bar{c}} = f_1(t) + g_2(t - \tau_{1,2}^-) \quad (2.49)$$

$$\frac{p'_2}{\bar{\rho}\bar{c}} = f_1(t - \tau_{1,2}^+) + g_2(t). \quad (2.50)$$

Here,  $\tau_{1,n}^\pm = (x_n - x_1)/(\bar{c} \pm \bar{u})$  are the time delays of the acoustic waves between locations  $x_1$  and  $x_n$ , traveling downstream and upstream, respectively. With evaluation of EQ. 2.50 at  $t - \tau_{1,2}^-$  and insertion into EQ. 2.49,  $g_2(t)$  can be eliminated, which yields:

$$f_1(t) = \frac{p'_1(t)}{\bar{\rho}\bar{c}} - \frac{p'_2(t - \tau_{1,2}^-)}{\bar{\rho}\bar{c}} + f_1(t - \tau_{1,2}^+ - \tau_{1,2}^-). \quad (2.51)$$

This expression can be solved in real-time by employing a feedback loop, which is depicted in reference [18] or can be deduced from FIG. 2.6. As mentioned in SEC. 2.2, the Two-Microphone Method features the disadvantage of singular frequencies, which occur at

$$\omega_m = \frac{2\pi m}{\tau_{1,2}^+ + \tau_{1,2}^-}, \quad m \in \mathbb{Z}. \quad (2.52)$$

In order to circumvent this issue and to increase the accuracy, the scheme is extended to more than two pressure probes. Thus, instead of evaluation of EQ. 2.50 at  $t - \tau_{1,2}^-$ , the arithmetic

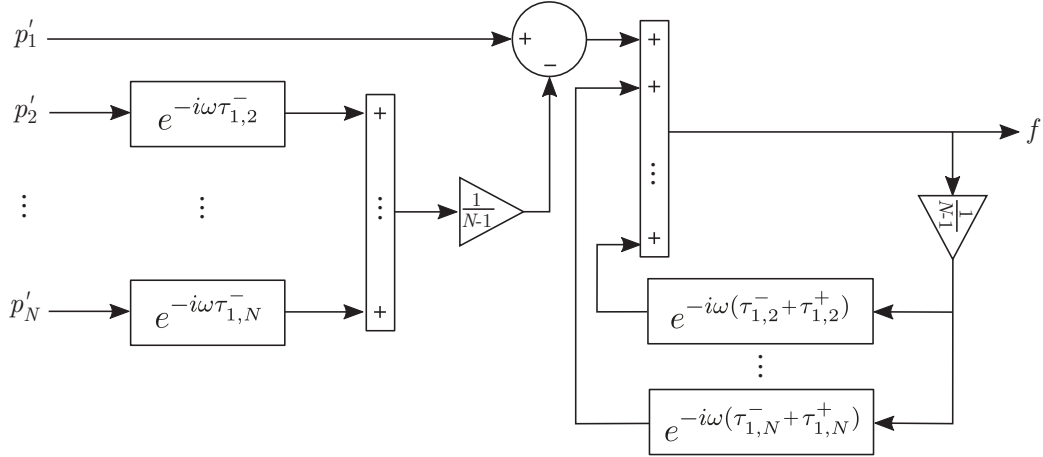


**Figure 2.6.:** Feedback loop of the online wave identification scheme as developed by Moeck et al. [112] and adapted from the figure in reference [21].

mean of the remaining  $N - 1$  pressure sensors at their respective time delays is inserted, which then yields:

$$f_1(t) = \frac{p'_1(t)}{\bar{\rho}c} - \frac{1}{N-1} \sum_{n=2}^N \frac{p'_n(t - \tau_{1,n}^-)}{\bar{\rho}c} + f_1(t - \tau_{1,n}^+ - \tau_{1,n}^-). \quad (2.53)$$

In order to be applicable in conjunction with the controller, described in SEC. 2.4, this expression needs to be implemented in a programming environment. To that end, a block diagram was derived, which is shown in FIG. 2.6. Note that the time delays are expressed in exponential form, which is the frequency-domain equivalent. The block diagram basically represents EQ. 2.53 in a graphical way. Initially, the mean values of the delayed pressure readings from all but microphone 1 are subtracted from  $p'_1$ . Then, a feedback loop is entered, in which the arithmetic mean values of the delayed  $f$ -waves (last term on the right-hand side of EQ. 2.53) are added.

Thus, the required steps for applying an active modification of the acoustic boundary condition in a suitable actuated measurement duct were presented. The scheme is used in CHAP. 7, where additional information on the implementation at the high pressure test rig is given.



# CHAPTER 3

---

## Current Test Rig and Requirements

---

In this chapter, the regarded single-burner high pressure test rig is described. Initially, the test site housing the rig is shortly introduced. Subsequently, the test rig itself and its relevant characteristics are detailed. The final three sections aim at explaining the various instruments, which are required for achieving the main objectives of a thermoacoustic characterization and the active impedance control.

The test site, referred to as *Clean Energy Center*, is operated by SIEMENS Energy and located in Ludwigsfelde, Germany. It is used for material and component testing of combustion chamber parts under realistic operating conditions [101]. I. a., the site features two test cells dimensioned for combustor systems of large power plant turbines. This includes, for instance, SGTx-4000F, SGTx-8000H, and SGTx-9000HL engines. The latter is depicted in FIG. 3.1, where the colored frame highlights one of the can-annular combustors. Depending on the power frequency, twelve or sixteen of these cans are employed in the engine. One of the combustor can segments is represented by the combustion test rig described in the following section.

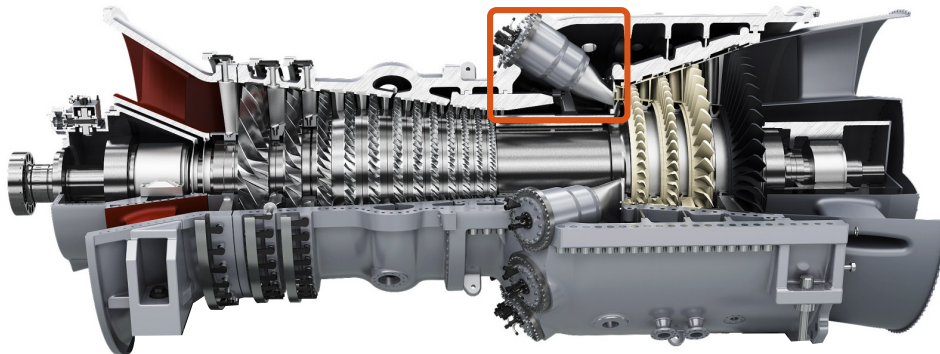


**Figure 3.1.:** Render image of a SIEMENS SGT5-9000HL heavy duty gas turbine adapted from reference [166]. One can combustion chamber is highlighted by a colored frame.

### 3.1. Current High Pressure Combustion Test Rig

With the current test rig, measurements of various parameters like power output, efficiency, and emissions are possible. Furthermore, thermoacoustic oscillations can be detected using *CP235 piezoelectric pressure transducers* from *Meggit SA*, which are specifically designed for gas turbine applications [184]. They measure pressure fluctuations in characteristic locations, in order to maintain comparability between different test rigs. However, currently they cannot be used to identify upstream and downstream propagating waves, as they are not mounted in an array allowing for wave decomposition.

The test rig consists of an outer pressure housing. Inside, interchangeable *flow boxes* can be mounted in order to simulate different burner systems. The engine's combustor annulus is reduced to single burner configurations, which corresponds to 1/12th or 1/16th of the engine's combustion segment, which is represented by the flow box. Thus, for can-annular systems, incorporation of one can yields very close resemblance of the flow and combustion parameters. FIG. 3.2 depicts a schematic of the components of the test rig located inside the pressure housing.

The flow box guides compressed air from the compressor outlet on the lower left-hand side to the combustor in the upper-left part. As in the engine, the air flow around the combustion chamber is used to cool the combustor walls. Subsequently, the air enters the annulus-shaped *flow sleeve*, which directs it to the plenum upstream of the burner. The entire burner and parts of the combustion chamber are connected to the *burner base plate*, which is accessible from the outside. The schematic burner depiction is divided into an inner pilot and an outer main stage. Downstream, the combustion chamber is located, which can be further separated into the upstream *basket* and the downstream *transition*. As the name implies, the latter is responsible for transition of the circular shape at the *basket* to the annulus-segment, present at the turbine inlet. The first vane stage is resembled by the *vane simulation section* (VSS), which consists of airfoil-shaped profiles accelerating the exhaust air flow. Downstream, the *dump* segment realizes the transition back to a circular cross-section. The *back pressure valve*, featuring a movable cone-shaped piston, regulates the mean pressure inside the test rig.

In order to allow for a thermoacoustic characterization and impedance tuning (cf. SEC. 1.8), the test rig has to meet various requirements that have thus far never been incorporated in an industrial high pressure test facility. Main challenge is the implementation of impedance

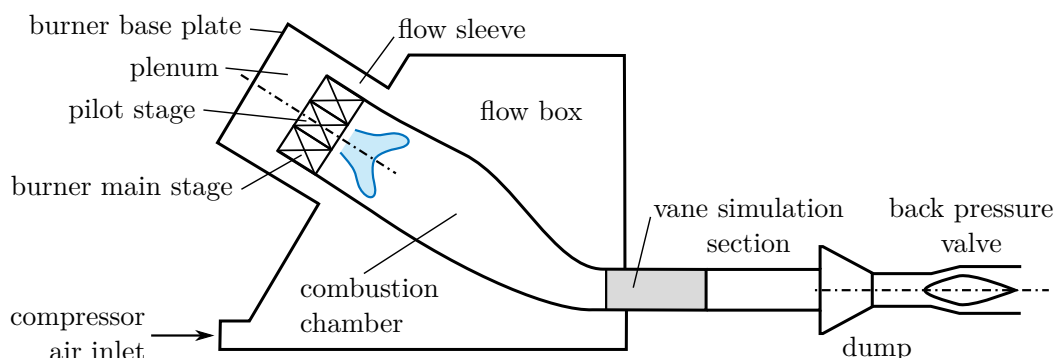


**Figure 3.2.:** Schematic of the single burner high pressure combustion test rig. The parts are labeled according to the terminology used in the work.

tuning while retaining the original test rig geometry. The following sections give an overview of the requirements for achieving the objectives of this work. Mutual requirements are highlighted and first implications on the realization are given.

### 3.2. Requirements for Measurements of Flame Transfer Matrices

An overview of the basics regarding measurements of flame transfer matrices was given in SEC. 1.7. In summary, determination of the flame transfer matrix requires acoustic forcing and measurement of the acoustic variables both upstream and downstream of the flame. Possible provisions in the test rig are schematically depicted in FIG. 3.3.

The upstream sensors are needed for determination of the primitive acoustic variables at the burner outlet. Yet, these cannot be measured directly under reacting conditions, as previously described in SEC. 1.7. However, with knowledge of the *burner transfer matrix*, they can be deduced from the sound field at the burner inlet. The burner transfer matrix is obtained either experimentally or using the partially empirical *L- $\zeta$ -model*, which was developed by Schuermans et al. [161].

Acoustic pressure and particle velocity upstream of the burner are, for instance, determined using the Multi-Microphone Method. For application of this technique, the sensors need to be calibrated. Their relative amplitude and phase runs have to be incorporated in the corresponding evaluation scripts in terms of complex calibration coefficients.

Due to the geometry of the burner plenum (cf. FIG. 3.2), a geometric modification, allowing for a wave identification directly upstream of the burner, would be the prime option. However, as the test rig's concept relies on a close resemblance of the engine, another solution has to be found. Two options are discussed in CHAP. 4. The first incorporates an experimental wave decomposition in the flow sleeve, which is denoted by blue crosses in FIG. 3.3. In conjunction with the numerically obtained transfer behavior from the slow sleeve outlet to the burner inlet, the required variables can be calculated. The second approach employs the unsteady pressure drop over the burner [160], which is discussed in SEC. 4.3. In the schematic, this option is denoted with orange crosses.

Similarly, the complex test rig geometry impedes a straightforward determination of the acoustic variables downstream of the flame with the standard Multi-Microphone Method. As

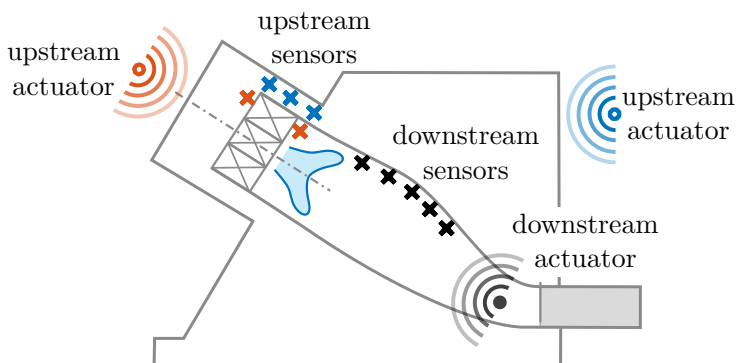


**Figure 3.3.:** Schematic of the required instruments for measurements of flame transfer matrices. Blue and orange components denote options, i. e., only one of each is required.

no duct of constant cross-sectional area is present, the technique needs to be extended to ducts with non-uniform cross-sections. This topic is discussed in CHAP. 5.

High amplitude acoustic excitation needs to be realized upstream of the implemented (upstream) sensor array. The reason for that is explained in CHAP. 4. For measurements of the flame transfer behavior, forcing may be realized via mono-frequency or sweep excitation.

As shown in FIG. 3.3, incorporation of the sensors in the flow sleeve requires an actuator mounted upstream of that location, which is denoted by a blue loudspeaker. Note that loudspeakers only act as a schematic tool in this case and are generally unsuited for application in industrial test rigs. In case of the sensors being mounted upstream and downstream of the burner, positioning of the actuator at the burner base plate (orange loudspeaker) would be viable, as well. The suggested type of actuator and its positioning are investigated and discussed in CHAP. 6.

Furthermore, high amplitude acoustic forcing downstream of the flame is required, which is indicated by a black loudspeaker in FIG. 3.3. Requirements on the actuator in terms of measurement of the flame transfer matrix are essentially similar to those in the upstream region. However, as will be seen in SUBSEC. 3.4, a highly capable actuator needs to be employed for impedance tuning, anyways. Development of a suitable device is described in CHAP. 7.

### 3.3. Requirements for Measurements of Flame Transfer Functions

In comparison to measurement of a flame transfer matrix, determination of a flame transfer function generally requires less modifications to the high pressure test rig. Different options for the necessary equipment are depicted in FIG. 3.4.

The required input variables for this type of thermoacoustic characterization are the particle velocity upstream of the flame, as well as the global heat release of the flame. As described in the preceding section, the velocity at the burner outlet cannot be directly measured under reacting conditions. Analogously, knowledge of the burner transfer matrix, allows to deduce the velocity fluctuations at the burner outlet from those at the inlet. Again, two actuator locations and two sensor concepts are possible.

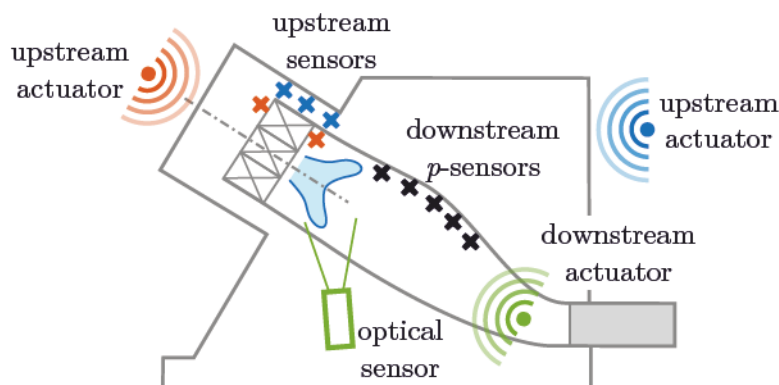


**Figure 3.4.:** Schematic of the required instruments for measurements of flame transfer functions. Blue and orange components denote options, i. e., only one of each is required. The optical sensor is an alternative to the sensors denoted in black.

The flame response is measured in the combustion chamber. This may be realized using various methods, which are generally divided into acoustic and optical techniques. The optical approach (green sensor in FIG. 3.4) focuses on the determination of the global heat release rate fluctuations, the advantages and disadvantages of which are mentioned in SEC. 1.7. In summary, multi-species chemiluminescence measurements deliver the most accurate results. That said, they are still not regarded reliable under all operating conditions and require extensive sensor calibration, as well as an ample optical access to the flame.

For the acoustic approach, the  $T_{22}$ -element in EQ. 1.5 simplifies to  $H(\omega) = \hat{u}_d/\hat{u}_u$ . In consequence, the velocity fluctuation inside the combustion chamber is sought. It may, for instance, be measured using the Multi-Microphone Method, which is indicated by black crosses in FIG. 3.4. Under the premise of the fixed non-constant cross-sectional combustor, the wave decomposition needs to be adapted, which is elaborated in CHAP. 5.

In general, determination of the flame transfer function can be realized by acoustic forcing from upstream or downstream of burner and flame. As the equation system (EQ. 1.5) contains two equations and two unknown variables, only one acoustically excited state is necessary to solve it. Thus, if optical sensors were incorporated, acoustic excitation could theoretically be implemented downstream of the flame, which is denoted by a green loudspeaker in FIG. 3.4, or upstream of the burner. Conversely, *acoustic* sensors inside the combustor require excitation in the upstream region. Options are highlighted analogously to the elaborations in SEC. 3.2.

### 3.4. Requirements for Impedance Tuning

The concept of an active modification of the acoustic boundary condition was detailed in SEC. 2.4. Initially, the open-loop reflection coefficient of the combustion chamber outlet needs to be determined. In theory, acoustic forcing would not be imperative for this task. However, the signal-to-noise ratio can be drastically increased by acoustic forcing and cross-correlating the measured pressure fluctuations with the actuator signal. Thus, implementation of an upstream acoustic excitation is preferable, which coincides with the requirement for the thermoacoustic characterization, discussed in the preceding sections. Possible locations are highlighted in blue and orange in FIG. 3.5 and their performance is investigated in CHAP. 6.

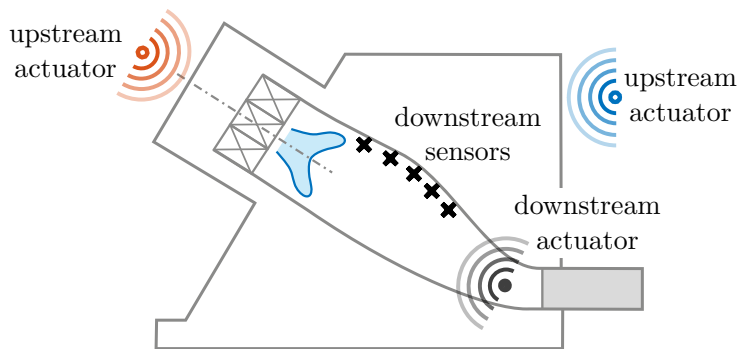


**Figure 3.5.:** Schematic of the required instruments for the active modification of the downstream acoustic boundary condition. Blue and orange components denote options, i. e., only one of them is required.

In order to measure the Riemann invariants for calculation of the combustor's open-loop reflection coefficient, a sensor array facilitating the Multi-Microphone Method is required. A schematic depiction of such an array is denoted with black crosses in FIG. 3.5. The same sensor array is further needed for the *online* wave identification, mandatory for implementation of the impedance tuning concept. Extension of the frequency-domain and the time-domain Multi-Microphone Method to ducts with variable cross-sectional area is detailed in CHAP. 5. Attention has to be paid to the phase runs of the utilized pressure transducers. In order to apply the scheme shown in FIG. 2.3, the phase relations need to be similar for each of the sensors. Furthermore, the amplitude deviations between the microphones are ideally close to constant in the regarded frequency range. Otherwise, corresponding complex calibration coefficients need to be implemented in the controller software.

The key component in the realization of the active modification of the combustor outlet impedance is a suitable acoustic actuator downstream of the sensor array. I. a., the device has to be capable of a high-bandwidth and high-amplitude excitation. The required amplitude is difficult to quantify, as it depends on several parameters, such as the operating point and the aimed closed-loop reflection coefficient. A good indication are, for instance, the incident sound waves. In order to achieve non-reflecting conditions, they need to be canceled. Thereby, the required amplitude can be estimated.

Note that pressure fluctuations due to combustion noise or thermoacoustic phenomena increase with mean pressure, which was for example shown by Freitag [50]. This is related to an increased reaction rate at elevated pressures due to a higher concentration of reactants. Thus, an increased heat release rate is promoted, which in turn, constitutes an acoustic source term [108]. High peak amplitudes of approximately 210 mbar, caused by self-excited thermoacoustic instabilities, were measured while testing a prototype SGT6-4000F gas turbine by Seume et al. [163]. These considerations yielded a target amplitude requirement, which is not disclosed in this thesis, however.

In order to enable broadband impedance tuning, the actuator should additionally feature a linear response between its input and the generated perturbation at the sensor array. Furthermore, a high-bandwidth excitation in the determined frequency range should be possible. In sum, these three requirements are currently not met by any actuating device known to the author. Development of an appropriate actuator concept via numerical and experimental methods is presented in CHAP. 7.

Another crucial prerequisite for a functioning active broadband modification of the acoustic boundary condition is a proper phase run of the actuator transfer function, which was explained in SEC. 2.4. It is determined by the time lags associated to the numerator and the denominator in EQ. 2.48 and corresponding investigations are discussed in SEC. 7.6.

In conclusion, impedance tuning requires actuators upstream and downstream of the flame, as well as sensors inside the combustion chamber. A thermoacoustic characterization, i. e., measurement of the flame transfer behavior generally leaves more options. Yet, acoustic sensors are needed in the combustor for impedance tuning, in any case. Thus, the complexity can be strongly reduced by using the same sensor array for measurement of the flame transfer behavior. In consequence, the optical determination of the flame transfer function becomes obsolete.

Furthermore, both methods for thermoacoustic characterizations require sensors upstream of the flame. Thus, the minimum requirements consist of acoustic sensors and actuators both upstream and downstream of the flame (as depicted in FIG. 3.3). Therefore, the determination

of the flame transfer function does not yield any reduction in the amount of necessary test rig modifications. However, the main focus lies in the implementation of flame transfer matrix measurements and the active modification of the acoustic boundary condition at the combustor outlet.



# CHAPTER 4

---

## Two Sensor Concepts for the Region Upstream of the Flame

---

Within this chapter, sensor concepts for the region upstream of the burner are discussed. They are required for the determination of acoustic variables to obtain the flame transfer behavior. Initially, suitable concepts are discussed, which account for the existing geometry of the regarded test rig. In the following section, the first option is discussed in more detail. A hybrid approach is presented, which uses analytical transfer matrix elements and FEM or CFD simulations for conditioning of the analytical method. In SEC. 4.3, another method is presented, which is based on determination of the unsteady pressure drop over the burner. Finally, both methods are discussed in terms of additionally required investigations and practical considerations.

### 4.1. Discussion of the Utilized Methods

Part of the thermoacoustic characterization of a burner system is the determination of the acoustic flame transfer behavior in terms of a flame transfer matrix or a flame transfer function. As detailed in CHAP. 3, measurement of the flame transfer function requires sensors capable of measuring at least the velocity fluctuations at the burner inlet. Experimental determination of the flame transfer matrix, additionally requires measurement of the acoustic pressure. However, as direct velocity measurements are not viable in most test rigs, and especially in high pressure facilities, pressure measurements are required in any case.

One option to obtain the velocity fluctuation at the burner inlet is measuring the unsteady pressure drop over the burner. Both variables are related via the burner transfer matrix. The theoretical background was detailed by Schuermans [156] and the specific procedure is explained in reference [160]. The required hardware consists of two pressure sensors, one at the burner inlet and one in the combustion chamber. The method is explained in more detail in SEC. 4.3.

A standard approach to measure the primitive acoustic variables in combustion test rigs is the Multi-Microphone Method (e. g., references [11, 49, 69, 128, 135, 157]), which necessitates a duct with constant cross-section and a constant temperature profile. However, as the regarded test rig closely resembles the real engine's combustion segment, it does not feature a duct of uniform cross-section directly upstream of the burner. An option to deal with this issue is locating the upstream sensor array in the flow sleeve (cf. FIG. 3.2). This section features a constant cross-sectional passage, where the Multi-Microphone Method can be applied.

Thereby, the acoustic variables at the flow sleeve outlet can be determined. The transition to the burner inlet is formed by a plenum with an unknown acoustic transfer behavior. It is characterized by a transfer matrix, which can be obtained using several approaches. If an experimental approach was chosen, a test rig resembling the flow sleeve, plenum, and burner section would be required. Accordingly designed, it could even allow for the same operational parameters, such as temperature and flow field. Acoustic excitation and sensor arrays needed to be employed both at the flow sleeve and in the burner passage. However, this approach is highly expensive and once the measurements are conducted, extrapolation to other operational parameters might be difficult.

Another option is to conduct numerical analyses, i. e., CFD or FEM simulations. The major issue with CFD are expenses, strongly increasing with geometrical complexity and mean flow conditions. Furthermore, flexibility in terms of operational parameters is quite low. FEM simulations can be conducted using, for instance, Helmholtz solvers (no mean flow) or LEE solvers. Such methods were applied in a similar context, for example, by Laera et al. [89]. Compared to CFD, expenditures can be decreased, as computations execute much faster. However, setting up a reliable and accurate simulation still requires considerable validation effort.

Transfer matrices may also be derived in an analytic way. Comprehensive collections of transfer matrices representing numerous geometries are found in the publications of Munjal [119, 121]. Such analytically derived expressions bear the advantage of a straightforward implementation and high flexibility in terms of operational parameters. However, accuracy in the regarded parameter space has to be verified beforehand.

Hence, in SEC. 4.2, a procedure for developing and validating an analytical transfer matrix of the plenum is presented. In the first step, the geometry in question is introduced. A suited transfer matrix representation for the stationary case is detailed and later validated with an FEM simulation. A means for optimizing the analytical method by fitting the underlying geometry is presented in SUBSEC. 4.2.2. Subsequently, analytically determined transfer matrices with mean flow are presented. In a final step, the resulting transfer matrices need to be validated and optimized for the operational parameter space using experimental or numerical methods. However, this step was not in the scope of this work.

The result is a conditioned analytical method of obtaining the plenum's transfer matrix, which can be quickly evaluated for a large range of operational parameters, as computational demands are extremely low.

## 4.2. Transfer Matrix Representation of the Plenum Geometry

The method used in this section is comparable to the procedure of setting up a low-order network model, as introduced in SEC. 2.3. Several transfer matrices  $\mathbf{T}$ , representing the acoustic input-output behavior of the system's elements, are multiplied to characterize the acoustic system:

$$\mathbf{T} = \prod_{i=1}^N \mathbf{T}_i, \quad (4.1)$$

where  $N$  is the total number of elements. Note that transfer matrices in this chapter are denoted differently than in SEC. 2.3, as the particle velocity  $\hat{u}$  is replaced by the volume flow velocity  $\hat{v} = \hat{u}A$ :

$$\begin{bmatrix} \hat{p}_d \\ \hat{v}_d \end{bmatrix} = \underbrace{\begin{bmatrix} T_{11} & T_{12} \\ T_{21} & T_{22} \end{bmatrix}}_{\mathbf{T}} \begin{bmatrix} \hat{p}_u \\ \hat{v}_u \end{bmatrix}. \quad (4.2)$$

This notation stems from Munjal [121] and it simplifies calculations, especially at jumps in the cross-sectional area of duct elements. As explained above, the acoustic transfer behavior of the plenum upstream of the burner shall be investigated. The employed geometry is a simplified model of the actual parts in the high pressure test rig and is shown in FIG. 4.1. The geometry is an excerpt from that depicted in FIG. 6.2. Lengths, cross-sectional areas,

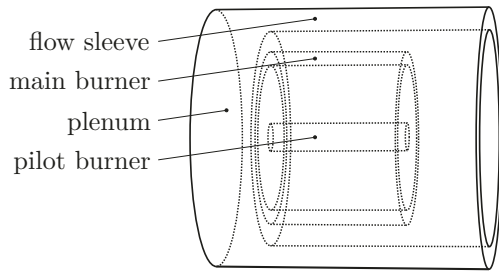


**Figure 4.1.:** Simplified geometry for the development of the transfer matrix method for the region upstream of the burner. Combustion air enters at the righthand face of the flow sleeve, is redirected at the plenum, then enters the two burner passages.

and volumes are similar to those found in the test rig. However, constructional details were excluded for this study.

Eventually, measurement of the acoustic pressure field is realized at the flow sleeve via the Multi-Microphone Method. In the plenum, the acoustic waves and the combustion air are deflected and enter the burner passages. As approximately 90 % of the air passes through the burner main stage, the pilot's influence is omitted. The regions downstream of the burner passage and upstream of the flow sleeve are represented by according boundary conditions.

In the books of Munjal [121] and Mechel et al. [120], numerous geometric shapes and their transfer matrix representations are described. However, by default, no representation from the literature fits the plenum geometry. A total of six presumably suitable expressions were investigated throughout the conducted work. They were initially validated using analytic test cases and then evaluated in terms of their accuracy when compared to FEM results. Yet, only the expression delivering the most accurate results is introduced here. It consists of a

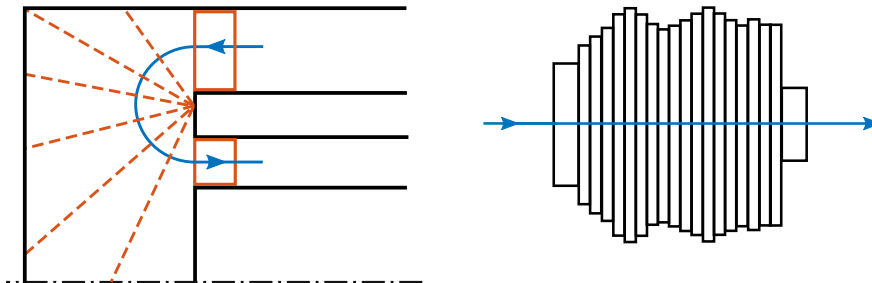


**Figure 4.2.:** Left: schematic geometry comprising the flow sleeve, plenum, and burner main passage with highlighted aid lines. Right: schematic of the transfer matrix representation.

concatenation of basic duct elements, the geometry of which was extracted as described in FIG. 4.2. The left-hand image shows the axisymmetric plenum geometry with its neighboring elements. Flow sleeve and burner passage are represented by short pieces of 4 mm length to incorporate reflection at the cross-sectional jumps into and out of the plenum. The blue line denotes a possible acoustic path, along which the straight ducts are aligned. Their individual length is defined by the center distance from one dashed orange line to the next. The cross-sectional area for each duct is calculated from the dashed lines, rotated around the symmetry line, forming a conical surface. The number of ducts, the plenum is approximated with, was part of the investigation, with 36 elements emerging as the optimum. Less ducts produced inferior results and more elements did not improve accuracy. The right-hand image displays a schematic of the corresponding representation in the form of an unrolled depiction of these ducts. Lengths and cross-sectional areas are calculated using an automated script, capable of treating the number of elements as a variable input parameter. Further note that the annulus-shaped flow sleeve and burner passage are represented by circular duct elements, as well.

Under the assumption of inviscid plane wave propagation at stationary conditions, each element is described by a transfer matrix [109, 121]:

$$\mathbf{T} = \begin{bmatrix} \cos(kL) & -iZ_0 \sin(kL) \\ \frac{1}{iZ_0} \sin(kL) & \cos(kL) \end{bmatrix}, \quad (4.3)$$

with the wave number  $k$ , duct length  $L$ , and the characteristic acoustic impedance  $Z_0 = \frac{\bar{\rho}c}{A}$  incorporating the duct's circular cross-section. Due to incorporation of the volume flow velocity, cross-sectional jumps are simply described by the identity matrix.

#### 4.2.1. FEM Computations for Validation of the Transfer Matrix Representation

In order to evaluate the performance of the found representation, numerical simulations were conducted with the commercial finite-elements software COMSOL Multiphysics 5.2a. The stationary simulations were conducted using the *Pressure Acoustics, Frequency Domain Interface*. Operational parameters, sans mean flow, were set to typical values found in the high pressure test rig. A frequency range from  $f = 20$  Hz to 600 Hz was investigated, which allows for plane wave propagation, only.

In order to compare the results, transfer matrices need to be calculated from the simulation. As mentioned in SEC. 2.3, two linearly independent states of excitation (cases A and B) need to be realized to determine the four unknown elements of the transfer matrix. FIG. 4.3 depicts a sectional view of the utilized computational domain with the highlighted planes a, b, and c, where different boundary conditions were set. In excitation case A, forcing is applied at face a and faces b and c are set to non-reflective conditions. In case B, face b is excited, whereas a and c are set to anechoic conditions.

Acoustic excitation was realized via the *Plane Wave Radiation* boundary condition in conjunction with the *Incident Pressure Field* node. The forcing amplitude was set to

$$\hat{p} = (\bar{\rho}c) 2.4 \times 10^{-4} \text{ m/s}, \quad (4.4)$$

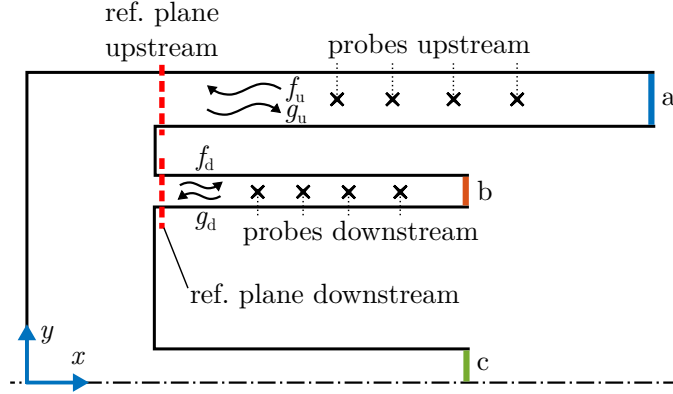


**Figure 4.3.:** Sectional view of the computational domain with probe locations in the upstream located flow sleeve and the downstream located burner main passage. The reference planes are highlighted in red and the boundary conditions (a, b, c) are indicated in different colors. The downstream and upstream propagating waves  $f$  and  $g$  are defined with excitation at the flow sleeve.

which corresponds to the value employed in SEC. 6.2, ensuring linear acoustics. Non-reflecting boundary conditions were implemented by setting the corresponding faces to the characteristic acoustic impedance with the *Impedance* node. All other boundaries were set to *Sound Hard Boundary Walls*. Measurement of acoustic pressure and particle velocity directly upstream and downstream of the plenum is prone to errors due to near-field effects. Therefore, the Multi-Microphone Method was employed to obtain the required variables at the reference locations, which coincide with those used in the transfer matrix representation.

FIG. 4.3 further shows the mentioned reference planes, as well as the utilized sensor arrays. From the simulated excitation cases, the following pressure fluctuations are obtained:

$$\hat{\mathbf{p}}^{A,B} = \begin{bmatrix} \hat{p}_1^A & \hat{p}_1^B \\ \vdots & \vdots \\ \hat{p}_N^A & \hat{p}_N^B \end{bmatrix}. \quad (4.5)$$

Subsequently, the Riemann invariants are determined using EQ. 2.35 and  $\hat{p}$  and  $\hat{u}$  are calculated at the respective reference planes with EQ. 2.28 and EQ. 2.29. Note that the particle velocity needs to be replaced by the volume flow velocity  $\hat{v} = \hat{u}A$ , in order to arrive at directly comparable results. The transfer matrix is then calculated with the acoustic pressures and volume flow velocities evaluated at the reference planes via:

$$\begin{bmatrix} T_{11} & T_{12} \\ T_{21} & T_{22} \end{bmatrix} = \begin{bmatrix} \hat{p}_d^A & \hat{p}_d^B \\ \hat{v}_d^A & \hat{v}_d^B \end{bmatrix} \begin{bmatrix} \hat{p}_u^A & \hat{p}_u^B \\ \hat{v}_u^A & \hat{v}_u^B \end{bmatrix}^{-1}. \quad (4.6)$$

The resulting transfer matrix is depicted in FIG. 4.4, where solid lines correspond to results obtained from the transfer matrix method and dashed lines denote results from FEM simulations. The phase, colored in orange, is well approximated by the analytical expression. Phase jumps are computed as smooth transitions by the Helmholtz solver. Absolute values, colored in blue, obtained with both methods match relatively well up to 400 Hz. The frequency

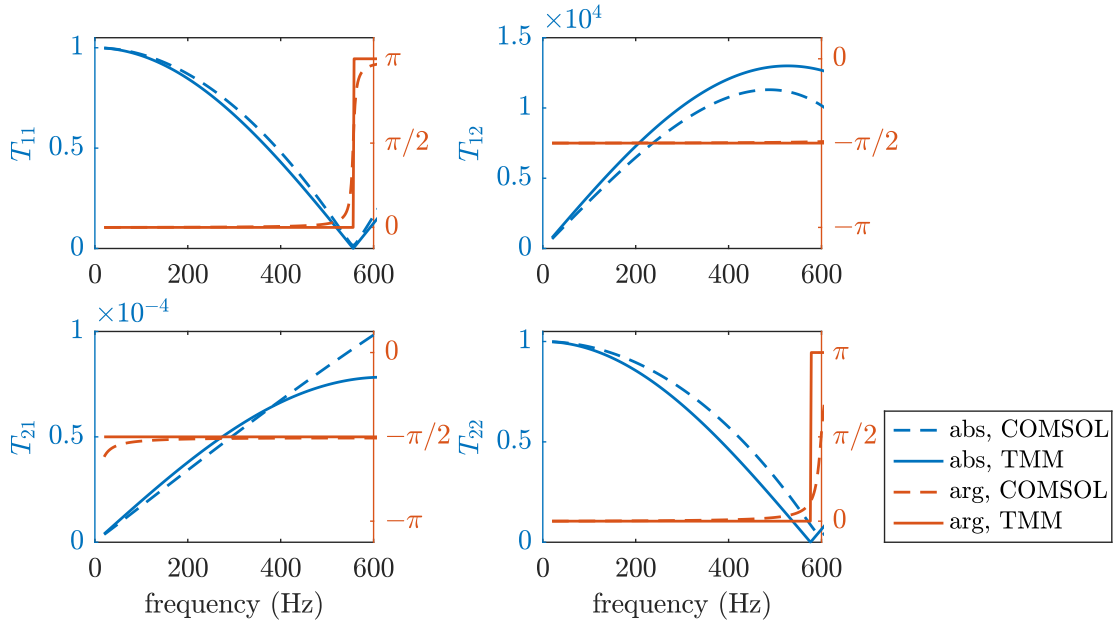


**Figure 4.4.:** Stationary transfer matrix from FEM computations (COMSOL, dashed) and from the transfer matrix method (TMM, solid)

of the minimum in  $T_{11}$  is met exactly and the one in  $T_{22}$  is off by  $\approx 26$  Hz. Maximum deviations of the magnitudes are about 20% for  $T_{22}$  and approximately 10% for the remaining transfer matrix elements. Given the apparent errors, especially of the physically relevant  $T_{22}$ -element, a correction needs to be implemented.

The transfer matrix obtained with a concatenation of multiple ducts yielded by far the best results among the investigated representations. However, it remains a simplified model of the three dimensional plenum. Further note, the exact approach to extracting the duct geometries, as indicated in FIG. 4.2 is by no means straightforward, which is compensated in the following subsection.

#### 4.2.2. Computational Parameter Optimization for the Underlying Geometry of the Transfer Matrix Method

In this subsection, the procedure of optimizing the underlying geometry for the transfer matrix method is explained. This step is necessary, as the determination of the acoustic path and the corresponding geometries of the straight ducts (cf. FIG. 4.2) are error-prone. Optimization of the transfer matrix elements was realized using the *fmincon* function in MATLAB, which minimizes the deviations between analytical results and those from the FEM simulations. Considered parameters for the optimization encompassed:

- a maximum deviation from the geometric baseline dimensions of each duct element (10% or 15%),
- a regarded frequency range for optimization (50 Hz to 400 Hz or 50 Hz to 600 Hz), and

setting	allowed deviation	frequency range	weighting
1	10 %	50 Hz to 400 Hz	$\min(\delta T_{22})$
2	10 %	50 Hz to 400 Hz	$\min(\delta T_{22} + 0.25 \cdot \delta T_{11})$
3	10 %	50 Hz to 600 Hz	$\min(\delta T_{22})$
4	10 %	50 Hz to 600 Hz	$\min(\delta T_{22} + 0.25 \cdot \delta T_{11})$
5	15 %	50 Hz to 400 Hz	$\min(\delta T_{22})$
6	15 %	50 Hz to 400 Hz	$\min(\delta T_{22} + 0.25 \cdot \delta T_{11})$
7	15 %	50 Hz to 600 Hz	$\min(\delta T_{22})$
8	15 %	50 Hz to 600 Hz	$\min(\delta T_{22} + 0.25 \cdot \delta T_{11})$

**Table 4.1.:** Settings for the optimization of the geometry that is used with the transfer matrix method.

- weighting of the most influential transfer matrix elements ( $T_{22}$  with 100 % or  $T_{22}$  with 80 % and  $T_{11}$  with 20 %).

TAB. 4.1 shows the simulated configurations.  $\delta T$  stands for the deviation between the magnitudes of the transfer matrix elements obtained from both methods.

For the optimization, the deviations are summed up over the frequency range indicated in TAB. 4.1. However, in the final evaluation of the optimization settings, only the frequency range from 50 Hz to 400 Hz is considered. Due to the varying orders of magnitude, the results are normalized by the minimum value, among the respective transfer matrix elements of all settings. Accordingly, the optimal value is unity, while higher values indicate stronger divergence.

The results are graphically summarized in FIG. 4.5. With setting 6, the ensemble of deviations is the lowest and the deviation of the  $T_{22}$ -element is among the lowest of all settings. Comparing settings 8 and 6, optimization in the smaller frequency range proves to be advantageous, as the lower deviations are found across all elements of  $\mathbf{T}$ . Moreover, weighting the  $T_{11}$ -element with 20 % benefits the results for all three other transfer matrix elements, as seen in settings 4, 6, and 8. Setting 2 is an exception here, as the  $T_{12}$ -element is poorly approximated. Settings 6 and 8 performing best, indicates that the maximum allowed

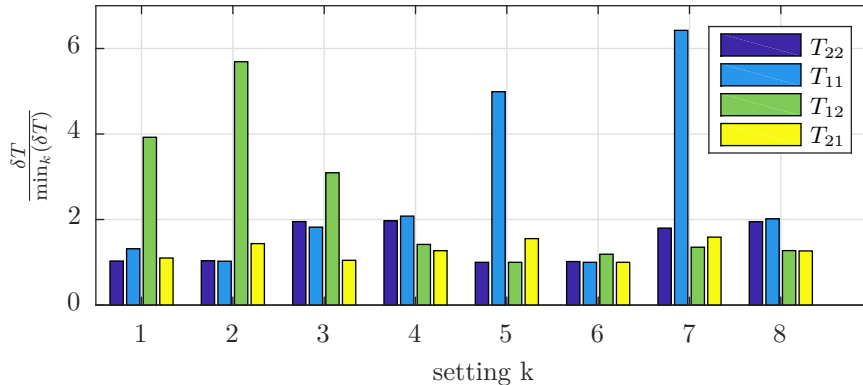


**Figure 4.5.:** Normalized deviation of the analytically found transfer matrix elements from those obtained via numerical computations for the eight investigated settings (cf. TAB. 4.1).

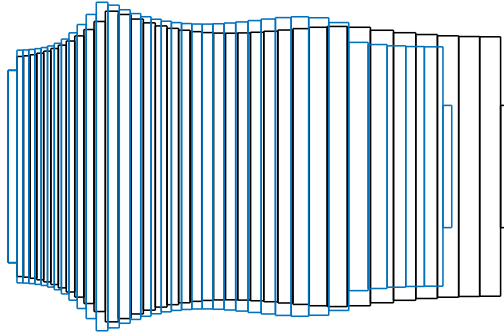


**Figure 4.6.:** Representation of the plenum with 36 straight ducts as extracted from the original geometry (black) and optimized with the *fmincon* function at setting 6 (cf. TAB. 4.1, blue)

deviation from the original duct area and length of 15% benefits the approximation. However, increasing this value to 20% yielded worse results, as the solver did not converge any more. The resulting geometrical modifications,

as computed by the optimization routine, are depicted in FIG. 4.6. With the optimized geometry as basis, the transfer matrix was calculated.

It is shown in FIG. 4.7. Both magnitudes and phases of the analytically obtained transfer matrix elements concur with those from the numerical simulations with the Helmholtz solver in the frequency range from 50 Hz to 400 Hz.

Up to now, the transfer matrix method was implemented for stationary conditions. The results were validated and optimized using FEM simulations. The scheme is easily applied and can be adapted to any plenum geometry with minor modifications. The next step in the development of the sensor concept for the region upstream of the burner is incorporation

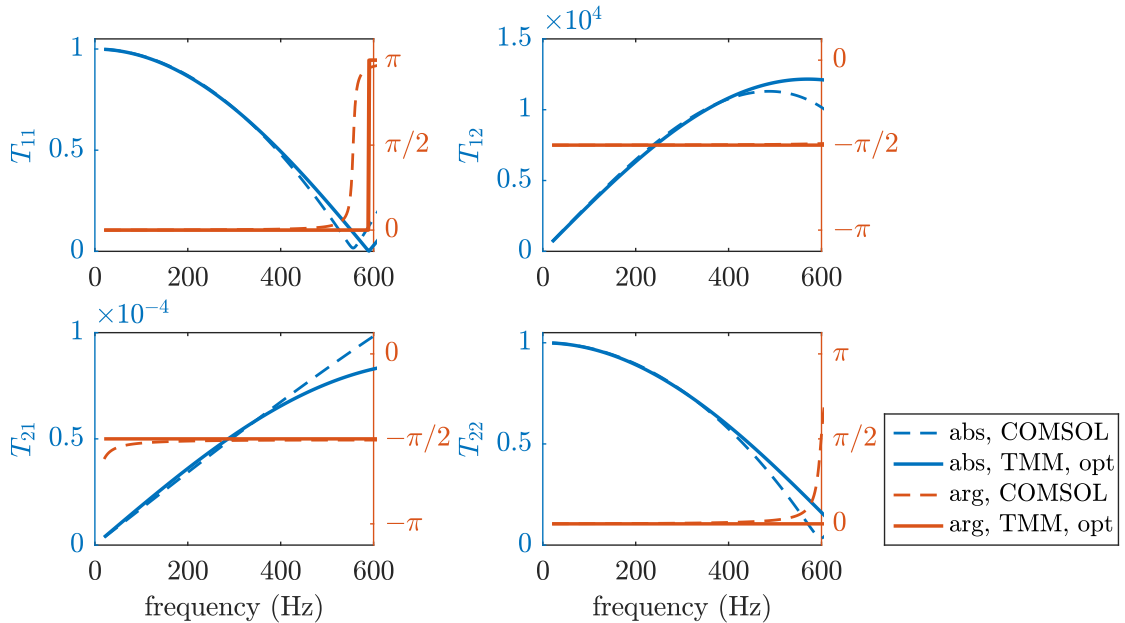


**Figure 4.7.:** Stationary transfer matrix found with numerical computations (COMSOL, dashed) and the transfer matrix method applied to an optimized geometry incorporating multiple ducts (TMM, solid).

of the mean flow present in the high pressure test rig, which is discussed in the following subsection.

#### 4.2.3. Transfer Matrix Representation with Mean Air Flow

Analog to the analytically found transfer matrix under stationary conditions, expressions for ducts with steady mean flow can be derived. As different variants are mentioned in the literature, two of them are introduced here. According to Munjal [121] and Miles [109], the transfer matrix of a straight duct of length  $L$  with mean flow reads

$$\mathbf{T}_{\text{duct},M} = e^{-iMk_c L} \begin{bmatrix} \cos(k_c L) & -iZ_0 \sin(k_c L) \\ \frac{1}{iZ_0} \sin(k_c L) & \cos(k_c L) \end{bmatrix}, \quad (4.7)$$

where the characteristic acoustic impedance  $Z_0$  is defined as in EQ. 4.3,  $k_c = \frac{k}{1-M^2}$  is a convective wave number, and  $M$  the mean duct Mach number. With steady flow, the transfer matrix for a cross-sectional area jump reads:

$$\mathbf{T}_{\text{csj},M} = \begin{bmatrix} 1 & M_u Z_u - (1 + K_{\text{csj}}) M_d Z_d \\ 0 & 1 \end{bmatrix}, \quad (4.8)$$

with  $K_{\text{csj}}$  describing cross-sectional jumps. It is defined for increasing (superscript  $(\cdot)^<$ ) and decreasing jumps (superscript  $(\cdot)^>$ ):

$$K_{\text{csj}}^< = \left( \frac{A_d}{A_u} - 1 \right)^2, \quad K_{\text{csj}}^> = \frac{1}{2} \left( 1 - \frac{A_d}{A_u} \right) \quad (4.9)$$

Based on a slightly different derivation, Greitzer et al. [55] arrived at the following definition for duct transfer matrices with mean flow:

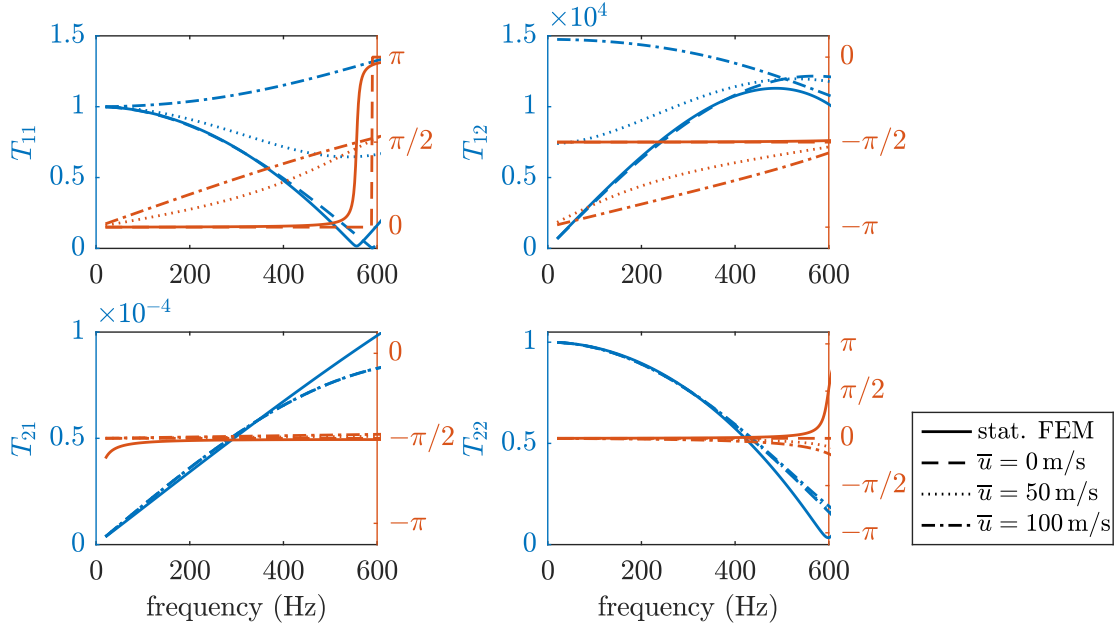
$$\mathbf{T}_{\text{duct},G} = \frac{1}{2} \begin{bmatrix} \frac{A_u}{A_d} \left( e^{ik^+L} + e^{-ik^-L} \right) & -\frac{Z_0}{A_d} \left( e^{ik^+L} - e^{-ik^-L} \right) \\ -\frac{A_u}{Z_0} \left( e^{ik^+L} - e^{-ik^-L} \right) & \left( e^{ik^+L} + e^{-ik^-L} \right) \end{bmatrix}, \quad (4.10)$$

where the wave numbers  $k^\pm$ , traveling in downstream and upstream direction, are defined as per EQ. 2.23, respectively. Greitzer et al. [55] describe increasing and decreasing jumps in the cross-sectional area with the following two expressions:

$$\mathbf{T}_{\text{csj},G}^< = \begin{bmatrix} 1 & -\frac{2M_u Z_0}{A_d} \left( 1 - \frac{A_d}{A_u} \right) \\ 0 & 1 \end{bmatrix}, \quad \mathbf{T}_{\text{csj},G}^> = \begin{bmatrix} 1 & -\frac{M_u Z_0 A_u}{A_d^2} \left( 1 - \left( \frac{A_d}{A_u} \right)^2 \right) \\ 0 & 1 \end{bmatrix}. \quad (4.11)$$

Validity of both derived transfer matrices was successfully shown within the work, with both methods exhibiting only minor errors. One of the validation cases is presented in APP. A. However, at this point, only the final transfer matrix of the plenum for several main air velocities shall be presented. Firstly, the expressions derived by Munjal [121] and Miles [109] (EQ. 4.7 and EQ. 4.8) were applied to the optimized geometry, as depicted in FIG. 4.6. The resulting transfer matrices for three different levels of mean flow velocities in the flow sleeve is shown in the top image of FIG. 4.8. Considering the frequency range from 50 Hz to 400 Hz, the transfer matrix representation at  $\bar{u} = 0$  m/s delivers absolute and phase values that

### Munjal and Miles



### Greitzer et al.

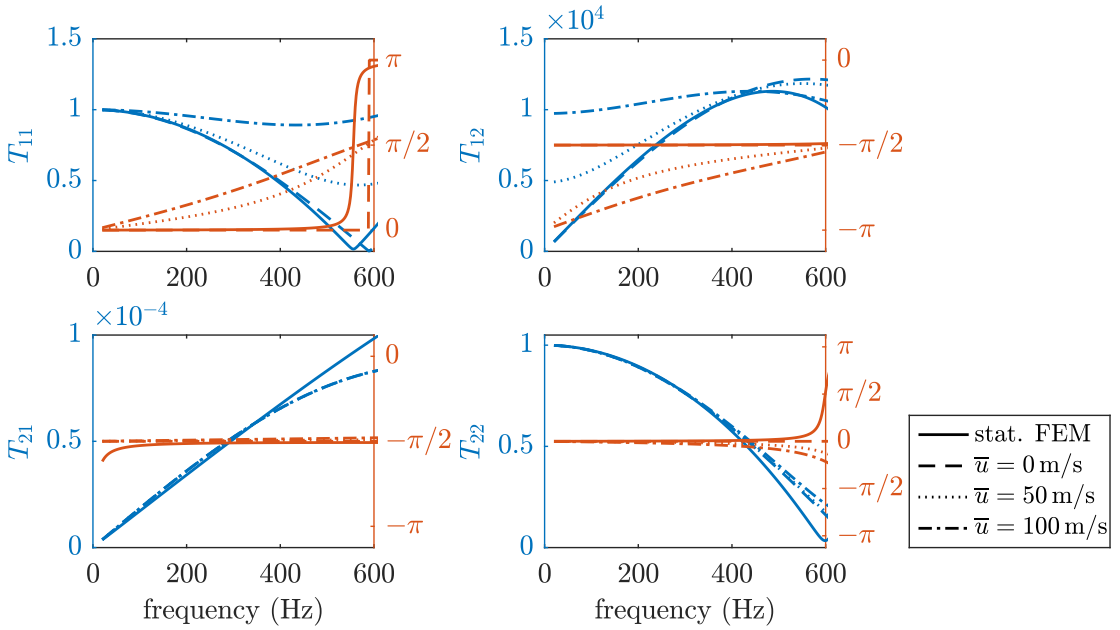


**Figure 4.8.:** Transfer matrices of the plenum representation consisting of a concatenation of straight ducts with mean flow. Absolute values colored in blue, phase in orange. Reference results computed with a stationary FEM simulation (solid). Analytical transfer matrices for various mean flow conditions obtained from the expressions derived by Munjal [121] and Miles [109] (top) and Greitzer et al. [55] (bottom).

match those obtained with the previously used stationary FEM simulations. With increasing mean flow, the matrix elements  $T_{11}$  and  $T_{12}$  show significantly different curves, indicating a dependence of the downstream pressure fluctuations on the mean flow conditions. Considering  $T_{11}$ , the pressure amplitude is indifferent to the flow at very low frequencies. However, towards higher frequencies, an increasing mean velocity increases the ratio of downstream to upstream pressure fluctuations. A reverse trend is observed with  $T_{12}$ , where at higher frequencies, the downstream pressure amplitudes become indifferent to changes in mean flow. At lower frequencies, the highest differences in the ratios of downstream pressure to upstream velocity fluctuations are apparent.

The  $T_{21}$  and  $T_{22}$ -element however, are very weakly affected by a steady mean flow up to 400 Hz. This indicates that the downstream velocity fluctuations are insensitive to mean flow variations. Greitzer et al. [55] explain this observation with the assumed incompressibility at low Mach numbers. In this regime, no mass storage occurs and the volume flow velocities at the inlet and outlet of a duct or cross-sectional jump element are equal. Accordingly, a similar result is found when implementing the transfer matrix method according to Greitzer et al. [55] (EQ. 4.10 and EQ. 4.11), which is depicted in the bottom image of FIG. 4.8. Qualitatively, the differently derived transfer matrices concur. However, deviations between the different levels of flow velocities for the  $T_{11}$  and  $T_{12}$  elements are less pronounced than with the expressions of Munjal and Miles.

The next step in the development of the upstream sensor design would be CFD simulations or experiments with a range of realistic operational parameters and the original geometry of the plenum. By validation and presumably necessary optimization of the underlying geometry, reliability and accuracy of the results would be provided. Thus, the analytical expressions could be used to efficiently calculate the plenum's transfer behavior for variable operational parameters. However, as it is unclear, which approach for the upstream sensors (SEC. 4.2 or SEC. 4.3) will be applied, the highly expensive numerical or experimental investigations were out of scope within the current work.

### 4.3. Determination of the Acoustic Variables Using the Unsteady Pressure Loss Over the Burner

As mentioned in the beginning of this chapter, a second method for determination of the acoustic pressure and particle velocity at the burner inlet exists. It is based on the relation of the unsteady pressure loss over the burner to the velocity fluctuation at the burner inlet. According to Schuermans [156], assuming an unsteady compact velocity potential field without combustion or external forces, the burner transfer matrix  $\mathbf{T}_B(\omega)$  can be expressed as an area discontinuity with mean flow:

$$\begin{bmatrix} \hat{p}_d / \bar{\rho} \bar{c} \\ \hat{u}_d \end{bmatrix} = \underbrace{\begin{bmatrix} 1 & M_B \frac{A_B}{A_u} \left( 1 - \zeta_B \left( \frac{A_u}{A_B} \right)^2 - \left( \frac{A_u}{A_d} \right)^2 \right) - i \frac{\omega}{\bar{c}} L_{\text{red}} \frac{A_B}{A_u} \\ 0 & \frac{A_u}{A_d} \end{bmatrix}}_{\mathbf{T}_B(\omega)} \begin{bmatrix} \hat{p}_u / \bar{\rho} \bar{c} \\ \hat{u}_u \end{bmatrix}. \quad (4.12)$$

The frequency-dependent  $\mathbf{T}_B(\omega)$  is thus characterized by a reduced length  $L_{\text{red}}$ , the cross-sectional areas upstream ( $A_u$ ), inside ( $A_B$ ), and downstream of the burner ( $A_d$ ), the burner Mach number  $M_B$ , and the burner loss coefficient  $\zeta_B$ . The latter factor incorporates viscous losses resulting from large velocity gradients in the vicinity of sharp edges. In practice, both

the reduced length and the loss coefficient are curve fitted while measuring the burner transfer function.

Substituting the  $(\cdot)_{12}$ -element of  $\mathbf{T}_B(\omega)$  with the burner transfer function  $T_{B,12}$ , the first line of EQ. 4.12 reads

$$\hat{p}_d/\bar{\rho}\bar{c} = \hat{p}_u/\bar{\rho}\bar{c} + T_{B,12}\hat{u}_u. \quad (4.13)$$

Thus,  $T_{B,12}$  can be expressed by the unsteady pressure drop  $\hat{p}_d - \hat{p}_u$  over the burner and the velocity fluctuation  $\hat{u}_u$  at its inlet. This procedure was successfully applied by Schuermans et al. [160] at a high pressure test rig. The authors determined burner and flame transfer matrices on the basis of pressure measurements upstream and downstream of the burner, in conjunction with the Two-Microphone Method inside the combustion chamber.

Note that this method requires a curve fit of the reduced length  $L_{\text{red}}$  and the burner loss coefficient  $\zeta_B$  at various operational parameters, as detailed in the work of Schuermans [156]. Therefore, practical applicability at the high pressure test rig might be intricate and thus expensive.

#### 4.4. Conclusion of the Sensor Design Upstream of the Flame

In this chapter, two methods for obtaining the required acoustic variables at the burner inlet are described. The quantities are needed for a thermoacoustic characterization, i. e., determination of the flame transfer behavior of the burner system. As the geometry of the regarded high pressure test rig does not allow for a direct measurement of acoustic pressure and particle velocity, alternative methods are proposed.

The method described in SEC. 4.2 is based on a standardized approach on determining the primitive acoustic variables with the Multi-Microphone Method in a suitable location further upstream of the burner inlet and then incorporating the transfer behavior of the section in between both locations. The plenum, which lies between the flow sleeve and the burner, has an initially unknown acoustic input-output behavior. It is characterized by its transfer matrix, which depends on the test rig's operational parameters. The proposed method incorporates an analytical determination of the transfer matrix with suitable expressions derived by Munjal [121], Miles [109] and Greitzer et al. [55]. The results need to be validated using either numerical simulations or experiments, delivering reliable results for the acoustic transfer behavior of the plenum. This is especially necessary, as the pilot burner passage was omitted in the present study and the overall geometry was a simplified version of that found in the test rig. Presumably, the underlying geometry for the analytically derived transfer matrices needs to be optimized using, e. g., the algorithm detailed in SUBSEC. 4.2.2. By following this procedure, only a small number of reference CFD simulations or experiments is required in order to condition the transfer matrix method. This method can then be used out-of-the-box with instant results of transfer matrices for various operational parameters. This approach is presumed to be far more practical in application than a lookup table with data from a potentially large amount of expensive CFD simulations or experiments. Another significant advantage of this method is that it can be applied a priori, and therefore, does not extend the required measurement time at the high pressure test rig.

In SEC. 4.3, a second approach for determination of the sought acoustic variables is described, which was successfully implemented by Schuermans et al. [160]. The method

is based on two pressure sensors, upstream and downstream of the burner, respectively. These measure the unsteady pressure drop over the burner, which is related to the velocity fluctuation at its inlet. Note that in order to apply this method, two characteristic quantities, describing the burner geometry, need to be curve fitted. This potentially poses an issue, as testing time at the high pressure test rig is highly expensive.

Further note that the upstream actuator positioning is dependent on which type of sensor design is finally chosen. With the probe array in the flow sleeve, the actuator would need to be located somewhere upstream, i. e., mounting at the burner base plate would not be possible.



# CHAPTER 5

---

## Wave Decomposition in the Combustor with Non-Uniform Cross-Section

---

Both the active modification of the acoustic boundary condition at the combustor outlet and the measurement of the flame transfer matrix require implementation of the Multi-Microphone Method inside the combustion chamber of the regarded test rig. However, the standard method can only be applied in ducts of constant cross-section. Therefore, an extension of the technique to ducts with variable cross-sectional areas is presented within this chapter. Initially, the Multi-Microphone Method in frequency-domain is extended to account for slowly varying cross-sections and curvatures. The corresponding wave equation may be solved analytically in some special cases. However, the geometry of the regarded test rig dictates the use of numerical methods for obtaining the required solutions. Subsequently, a scheme for a time-domain wave decomposition in ducts with variable cross-sections is presented. The methods are validated with numerical and experimental means. Lastly, potential for errors and recommendations on the final implementation are discussed.

### 5.1. Multi-Microphone Method in Ducts with Non-Uniform Cross-Sections

In specifically designed acoustical test rigs, the measurement ducts are of constant cross-sectional area, as for instance in references [11, 49, 128, 152, 162]. In that case, the wave identification introduced in SEC. 2.2 can be employed. However, the high pressure test rig regarded in this work needs to maintain its geometrical design, which features a curved combustion chamber of non-uniform cross-sectional area. Therefore, the methodology for pressure measurements in this segment needs to be revised.

In summary, the original Multi-Microphone Method is based on fitting the solution of the one-dimensional wave equation to the pressure measurements inside the duct (cf. SEC. 2.2). Subsequently, the Riemann invariants can be calculated, which enables reconstruction of sound pressure and particle velocity at an arbitrary reference plane within the same duct. This method was further developed for applicability in time domain by Moeck et al. [112], which is described in SEC. 2.5. Both methods are to be applied on the high pressure test rig, regarded in this work. The frequency-domain approach is necessary for the thermoacoustic characterization and the time-domain Multi-Microphone Method is needed for the active modification of the acoustic boundary condition of the combustion chamber outlet. Hence, an extension of both to non-uniform cross-sectional area ducts is required.

Previous work on this topic is, for instance, found in the publications of Subrahmanyam et al. [171, 172]. The authors developed special solutions to the wave equation for particular families of variations in cross-sectional area at stationary conditions. In this work however, the publications by Webster [189] and Rienstra [144] are used as a basis to find a suitable wave equation and its solutions. Part of the contents of this chapter was conducted within the master thesis of Schmidt [153].

Basis for the development of the Multi-Microphone Method in non-constant cross-sectional area ducts is Webster's horn equation [189]. In essence, he found a one-dimensional second-order ordinary differential equation that approximates the sound pressure field in non-uniform ducts at stationary conditions. An equivalent of this equation is given by Rienstra & Hirschberg [143]:

$$\frac{d^2 \hat{p}}{dx^2} + \frac{d \log A}{dx} \frac{d \hat{p}}{dx} + k^2 \hat{p} = 0 \quad (5.1)$$

$$\Leftrightarrow \frac{d^2 \hat{p}}{dx^2} + \frac{1}{A} \frac{d}{dx} \left( A \frac{d \hat{p}}{dx} \right) + k^2 \hat{p} = 0. \quad (5.2)$$

Derivation of EQ. 5.2 and a detailed discussion of the assumptions are carried out in reference [144]. The following assumptions are considered the most relevant for the development of the wave identification scheme:

- small ratio of duct diameter to typical length scale of the cross-sectional area variation  $d/L_A \ll 1$
- ratio of area-variation length scale to wave length  $L_A/\lambda = \mathcal{O}(1)$
- sound hard boundaries
- duct and coordinate system may be bent as long as the curvature radius  $R_c = \left| \frac{\left[ 1 + \left( \frac{dy}{dx} \right)^2 \right]^{\frac{3}{2}}}{\frac{d^2 y}{dx^2}} \right|$  is not smaller than  $L_A$  or  $\lambda$ .

Rienstra [144] further derived an extension of this equation to ducts with irrotational isentropic mean flow and rigid walls:

$$\frac{1}{\bar{\rho} A} \frac{\partial}{\partial x} \left( \bar{\rho} A \frac{\partial \hat{p}}{\partial x} \right) = \left( i\omega + \bar{u} \frac{\partial}{\partial x} \right) \left[ \frac{1}{\bar{c}^2} \left( i\omega + \bar{u} \frac{\partial}{\partial x} \right) \hat{p} \right]. \quad (5.3)$$

Here,  $A$ ,  $\bar{\rho}$ ,  $\bar{u}$ , and  $\bar{c}$  are slowly varying functions of the axial coordinate  $x$ . In order to numerically calculate a solution of the sound propagation, these parameters need to be determined with sufficient accuracy.

The goal is to find the Riemann invariants analog to EQ. 2.34 in the duct with non-constant cross-sectional area, which is depicted in FIG. 5.1. However, the entries of  $\mathbf{H}$  are no longer given by the solution to the convective 1D wave equation, but either that to Webster's horn equation (EQ. 5.2) or Webster's horn equation in generalized form (EQ. 5.3) for mean flow applications. Both are second-order ordinary homogeneous differential equations with the general solution

$$\hat{p}(x, \omega) = \hat{f}(\omega) P_1(x, \omega) + \hat{g}(\omega) P_2(x, \omega). \quad (5.4)$$

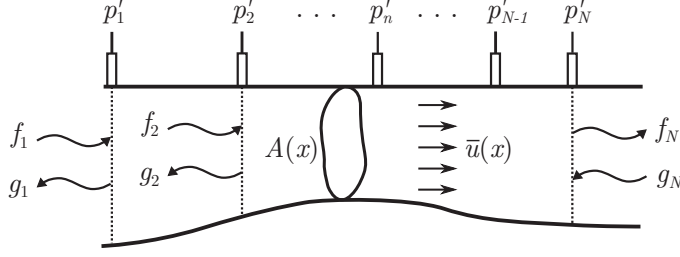


**Figure 5.1.:** Schematic of the microphone array for wave identification on a duct with non-constant cross-sectional area.

As  $P_1$  and  $P_2$  form a fundamental system, an equation analog to EQ. 2.34 can be found:

$$\begin{bmatrix} \hat{p}(x_1, \omega) \\ \hat{p}(x_2, \omega) \\ \vdots \\ \hat{p}(x_N, \omega) \end{bmatrix} = \underbrace{\begin{bmatrix} P_1(x_1, \omega) & P_2(x_1, \omega) \\ P_1(x_2, \omega) & P_2(x_2, \omega) \\ \vdots & \vdots \\ P_1(x_N, \omega) & P_2(x_N, \omega) \end{bmatrix}}_{\mathbf{H}} \begin{bmatrix} \hat{f}(\omega) \\ \hat{g}(\omega) \end{bmatrix}. \quad (5.5)$$

In general, numerical methods are required to determine  $\mathbf{H}(x_n, \omega, A(x), \bar{u}(x), \bar{\rho}(x), \bar{c}(x))$  for a given setup in the regarded frequency range. In the case of stationary investigations, a Helmholtz solver is well suited due to its efficiency. If a non-vanishing mean flow is to be incorporated, linearized Euler solvers or more complex CFD simulations are required.

In special cases, however, the coefficients  $P_1$  and  $P_2$  can be determined analytically or with an approximation, as is shown in the following subsection.

### 5.1.1. Particular Solutions to Webster's Horn Equation

A particular solution to Webster's horn equation may be found by substitution of  $A = \Theta^2$  and  $\Psi = \Theta \hat{p}$  in EQ. 5.2 [143], which yields

$$\Psi'' + \left( k^2 - \frac{\Theta''}{\Theta} \right) \Psi = 0. \quad (5.6)$$

For families of area variations of the form  $A(x) = (ae^{mx} + be^{-mx})^2$ , such as cones or exponential horns,  $\Theta''/\Theta$  becomes constant and a solution to EQ. 5.6 is found with:

$$\Psi = \hat{p}(x)\sqrt{A} = C_1 e^{(-i\sqrt{(k^2-m^2)x})} + C_2 e^{(i\sqrt{(k^2-m^2)x})}. \quad (5.7)$$

For linear area variations of the type  $A(x) = a + bx$ , EQ. 5.2 simplifies to

$$\frac{d^2 \hat{p}}{dx^2} + \frac{b}{a + bx} \frac{d}{dx} + k^2 \hat{p} = 0, \quad (5.8)$$

which is very similar to Bessel's differential equation of order zero:

$$z^2 \frac{d^2 y}{dz^2} + z \frac{dy}{dz} + z^2 y = 0, \quad \text{for } z \neq 0 \quad (5.9)$$

$$\Leftrightarrow \frac{d^2 y}{dz^2} + \frac{1}{z} \frac{dy}{dz} + y = 0. \quad (5.10)$$

Substitution of  $z = k(x + a/b)$  and  $dz = kdx$  yields

$$\frac{1}{k^2} \frac{d^2 y}{dx^2} + \frac{b}{k^2(xb + a)} \frac{dy}{dx} + y = 0 \quad (5.11)$$

$$\Leftrightarrow \frac{d^2 y}{dz^2} + \frac{b}{xb + a} \frac{dy}{dx} + k^2 y = 0, \quad (5.12)$$

which is similar to EQ. 5.8. As  $y(z)$  is a solution to Bessel's differential equation, the pressure field  $\hat{p}$  can be determined by:

$$\hat{p}(x, \omega) = C_1 J_0(x, \omega) \left( kx + \frac{ax}{b} \right) + C_2 Y_0(x, \omega) \left( kx + \frac{ax}{b} \right), \quad (5.13)$$

where  $J_0$  and  $Y_0$  are zeroth-order Bessel functions of the first and second kind, respectively.

## 5.2. Online Wave Decomposition in Ducts with Non-Uniform Cross-Sections

Compared to the time-domain wave decomposition scheme detailed in SEC. 2.5, the downstream (and upstream) propagating waves in ducts with variable cross-section are not functions of shifted arguments, i. e.,

$$f(x, t) \neq f\left(t - \frac{x}{\bar{c} + \bar{u}}\right), \quad g(x, t) \neq g\left(t + \frac{x}{\bar{c} - \bar{u}}\right). \quad (5.14)$$

The reason is that parts of the acoustic waves are continuously reflected due to the variation in cross-sectional area [172]. Thus, the Riemann invariants  $g_1$  and  $f_2$  emitted from a duct segment are expressed as functions of the incident waves  $f_1$  and  $g_2$  (cf. FIG. 5.1):

$$g_1(t) = F_{1,2,g}(f_1, g_2) \quad (5.15)$$

$$f_2(t) = F_{1,2,f}(f_1, g_2) \quad (5.16)$$

Hence, the incident waves can be related to the fluctuating pressures and the emitted waves analog to EQ. 2.49 and EQ. 2.50:

$$f_1(t) = \frac{p'_1}{\rho \bar{c}} - F_{1,2,g}(f_1, g_2) \quad (5.17)$$

$$g_2(t) = \frac{p'_2}{\rho \bar{c}} - F_{1,2,f}(f_1, g_2). \quad (5.18)$$

Once a model for  $F_{1,2}$  is found, both equations can be solved with the feedback loop presented in FIG. 5.2. As detailed in SEC. 2.5, the Two-Microphone Method is only marginally stable, as it features singular frequencies. Furthermore, accuracy can be improved by incorporating

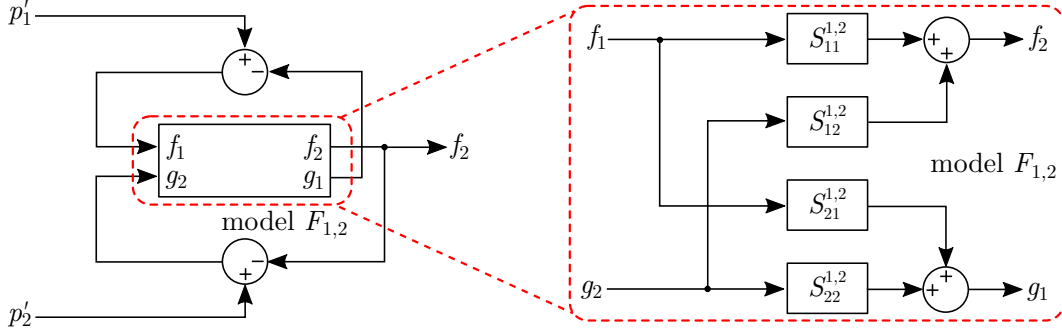


**Figure 5.2.:** Online wave decomposition scheme for two microphones on a duct with non-constant cross-sectional area. Left: feedback loop, right: model for duct segment incorporating the scattering matrix  $\mathbf{S}^{1,2}$ .

multiple sensors, effectively lowering the influence of noise. Thus, the introduced loop is extended to  $N > 2$  sensors by incorporating the arithmetic mean of  $g_1$ , which is depicted in FIG. 5.3. The aim is to find state-space representations for  $F_{1,n}$ , which necessitates determination of the scattering matrices  $\mathbf{S}^{1,n}$ :

$$\begin{bmatrix} \hat{f}_n \\ \hat{g}_1 \end{bmatrix} = \underbrace{\begin{bmatrix} S_{11}^{1,n}(\omega) & S_{12}^{1,n}(\omega) \\ S_{21}^{1,n}(\omega) & S_{22}^{1,n}(\omega) \end{bmatrix}}_{\mathbf{S}^{1,n}} \begin{bmatrix} \hat{f}_1 \\ \hat{g}_n \end{bmatrix}. \quad (5.19)$$

This is done a priori in frequency domain, whereby experimental or numerical means would be an option. A theoretical approximation, incorporating Webster's horn equation is possible, as well. Insertion of EQ. 5.4 into the one-dimensional linearized conservation of momentum (EQ. 2.14)

$$\bar{\rho}i\omega\hat{u} = -\frac{\partial\hat{p}}{\partial x} \quad (5.20)$$

yields

$$\hat{u}(x,\omega) = -\frac{C_1}{\bar{\rho}i\omega} \frac{\partial P_1(x,k)}{\partial x} - \frac{C_2}{\bar{\rho}i\omega} \frac{\partial P_2(x,k)}{\partial x}. \quad (5.21)$$

Assuming small distances between the microphone locations, the Riemann invariants may be expressed in terms of the primitive acoustic variables, as per EQ. 2.28 and EQ. 2.29. Substitution of EQ. 5.4 and EQ. 5.21 into these equations yields

$$\hat{f} = \frac{C_1}{2\bar{\rho}\bar{c}} \left( P_1 + \frac{i}{k} \frac{\partial P_1}{\partial x} \right) + \frac{C_2}{2\bar{\rho}\bar{c}} \left( P_2 + \frac{i}{k} \frac{\partial P_2}{\partial x} \right), \quad (5.22)$$

$$\hat{g} = \frac{C_1}{2\bar{\rho}\bar{c}} \left( P_1 - \frac{i}{k} \frac{\partial P_1}{\partial x} \right) + \frac{C_2}{2\bar{\rho}\bar{c}} \left( P_2 - \frac{i}{k} \frac{\partial P_2}{\partial x} \right) \quad (5.23)$$

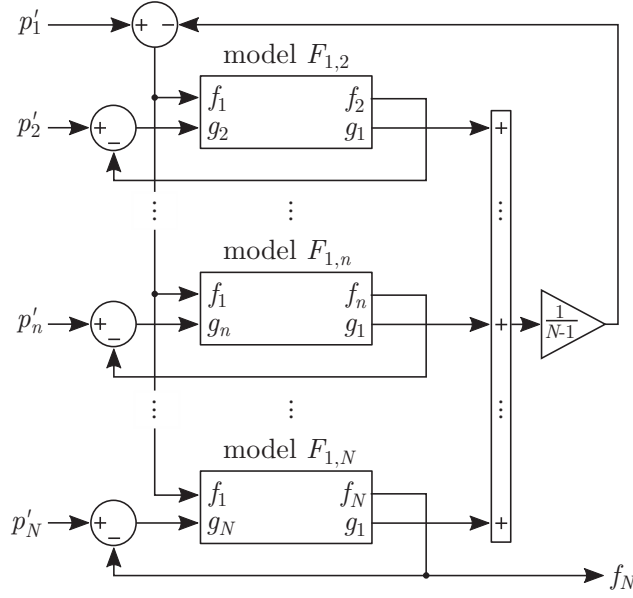


**Figure 5.3.:** Feedback loop of the online wave decomposition scheme. Extension for  $N$  microphones located along a duct with non-constant cross-sectional area.

Subsequently,  $\hat{f}$  and  $\hat{g}$  are evaluated at  $x_1$  and  $x_2$ , respectively. They are sorted by emitted and incident waves and written into an equation systems as follows:

$$\begin{bmatrix} \hat{f}_2 \\ \hat{g}_1 \end{bmatrix} = \underbrace{\begin{bmatrix} P_1(x_2) + \frac{i}{k} \frac{\partial P_1}{\partial x}(x_2) & P_2(x_2) + \frac{i}{k} \frac{\partial P_2}{\partial x}(x_2) \\ P_1(x_1) - \frac{i}{k} \frac{\partial P_1}{\partial x}(x_1) & P_2(x_1) - \frac{i}{k} \frac{\partial P_2}{\partial x}(x_1) \end{bmatrix}}_{:=\mathbf{P}_{x_2, x_1}} \begin{bmatrix} \frac{C_1}{2\rho c} \\ \frac{C_2}{2\rho c} \end{bmatrix}, \quad (5.24)$$

$$\begin{bmatrix} \hat{f}_1 \\ \hat{g}_2 \end{bmatrix} = \underbrace{\begin{bmatrix} P_1(x_1) + \frac{i}{k} \frac{\partial P_1}{\partial x}(x_1) & P_2(x_1) + \frac{i}{k} \frac{\partial P_2}{\partial x}(x_1) \\ P_1(x_2) - \frac{i}{k} \frac{\partial P_1}{\partial x}(x_2) & P_2(x_2) - \frac{i}{k} \frac{\partial P_2}{\partial x}(x_2) \end{bmatrix}}_{:=\mathbf{P}_{x_1, x_2}} \begin{bmatrix} \frac{C_1}{2\rho c} \\ \frac{C_2}{2\rho c} \end{bmatrix}. \quad (5.25)$$

Solving EQ. 5.25 for the unknown constants  $\frac{C_1}{2\rho c}$  and  $\frac{C_2}{2\rho c}$  by inversion of  $\mathbf{P}_{x_1, x_2}$  and inserting the constants into EQ. 5.24, the following expression can be obtained:

$$\begin{bmatrix} \hat{f}_2 \\ \hat{g}_1 \end{bmatrix} = \underbrace{\mathbf{P}_{x_2, x_1} \mathbf{P}_{x_1, x_2}^{-1}}_{\mathbf{S}^{1,2}} \begin{bmatrix} \hat{f}_1 \\ \hat{g}_2 \end{bmatrix}. \quad (5.26)$$

Hence,  $\mathbf{S}^{1,2}$  and thus  $\mathbf{S}^{1,n}$  can be calculated from  $P_n$  and their spacial derivatives. Again, these quantities have to be determined using numerical or analytical means. Once the scattering matrices for all duct segments are known, they can be translated into state-space realizations using the tools introduced in SEC. 2.3.

### 5.3. Numerical Validation of the Frequency-Domain Multi-Microphone Method in Non-Uniform Ducts

In this section the frequency-domain Multi-Microphone Method for non-constant cross-sectional area ducts, developed in SEC. 5.1, shall be validated using numerical methods. The geometry, employed for validation, is a model of the high pressure test rig’s combustion chamber, which is shown in FIG. 5.4. As the results shall be compared to experimental results

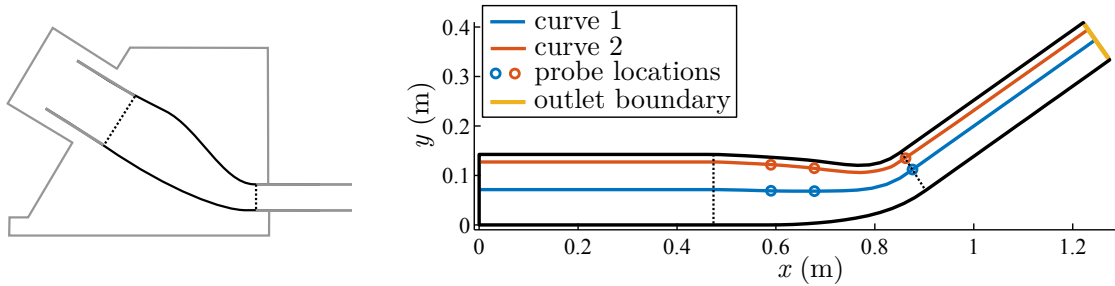


**Figure 5.4.:** Left: schematic of the combustion chamber (black) in the test rig (gray). Right: combustion chamber geometry for validation of the Multi-Microphone Method in non-constant cross-sectional area ducts. The dashed blue and orange curves, denote possible sensor locations along the center chord and along the geometry’s upper boundary, respectively.

in SEC. 5.4, the geometry’s dimensions were scaled according to the expected temperatures in the test rigs and the corresponding wave lengths. A conversion factor of  $\lambda_{hp}/\lambda_a \approx 2.48$  was calculated for a typical temperature ratio between high pressure and atmospheric test rig. According to the capabilities of the cold acoustic test rig, no mean flow is incorporated. The exact geometry of the test rig features a complex three-dimensional shape, which was simplified by effectively turning it into a 2D geometry. The  $z$ -dimension, pointing out of the drawing layer in FIG. 5.4, is kept constant. Due to the low-frequency acoustics and thus only longitudinal wave propagation, this does not pose a significant limitation in accuracy. The cross-sectional area and the curvature of the model between the black dotted lines, corrected by the aforementioned conversion factor, match the values of the high pressure test rig. Upstream and downstream of the dotted lines, ducts of constant cross-sectional area are attached, in order to calculate the Riemann invariants at the boundaries of the curved shape with the original Multi-Microphone Method. Two curves are depicted for the sensor locations, which is due to practical considerations in the high pressure test rig. As the sensors cannot be located close to the center chord (curve 1, blue line), they are placed close to the upper wall (orange line), which was initially regarded as well suited in terms of practicability. Assuming low curvatures [144], the  $x$ -coordinate in EQ. 5.2 can be substituted with the resulting curves 1 and 2 without loss of accuracy.

The geometry was built using the *Pressure Acoustics, Frequency Domain Interface* of COMSOL Multiphysics 5.2a, which was chosen due to stationary conditions. FIG. 5.5 depicts the employed mesh for the FEM solver, which was automatically generated and features 21 491 elements. The solution was obtained in a frequency range from 50 Hz to 1200 Hz. The upper boundary corresponds to the lowest cut-on frequency of the test rig. However, results are only shown up to  $f = 800$  Hz for clarity. Boundary conditions were implemented as follows:

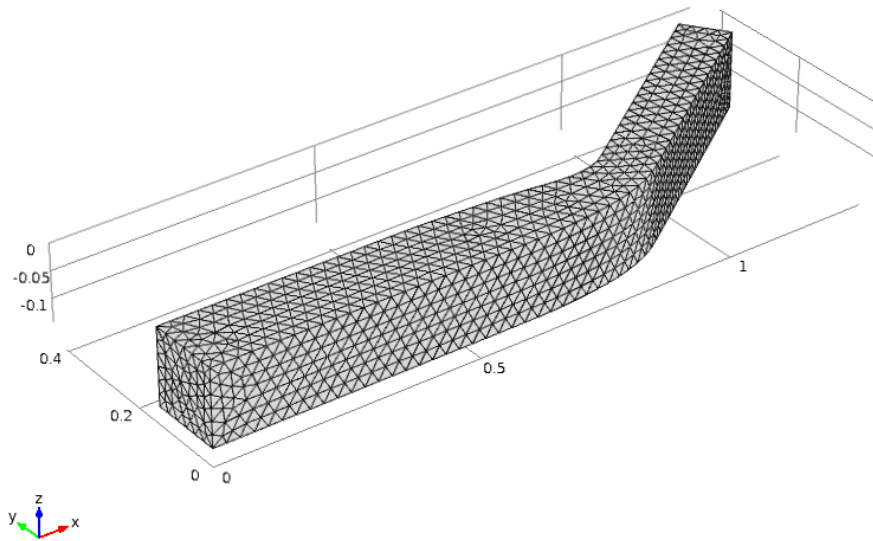


**Figure 5.5.:** Mesh for the FEM-validation of the Multi-Microphone Method in ducts with variable cross-sectional area.

- Upstream: *Plane Wave Radiation*, non-reflective boundary condition for plane waves, allowing for simultaneous excitation.
- Downstream: depending on the type of investigation either non-reflecting ( $R = 0$ ) with *Impedance* node, fully reflecting ( $R = 1$ ) with *Sound Hard Boundary Wall*, or fully reflecting ( $R = -1$ ) with *Sound Soft Boundary Wall*.
- All other walls are *Sound Hard Boundary Walls*.

A qualitative examination of the pressure field obtained from the FEM simulation can be conducted using FIG. 5.6. The real part of the calculated pressure fluctuations is depicted

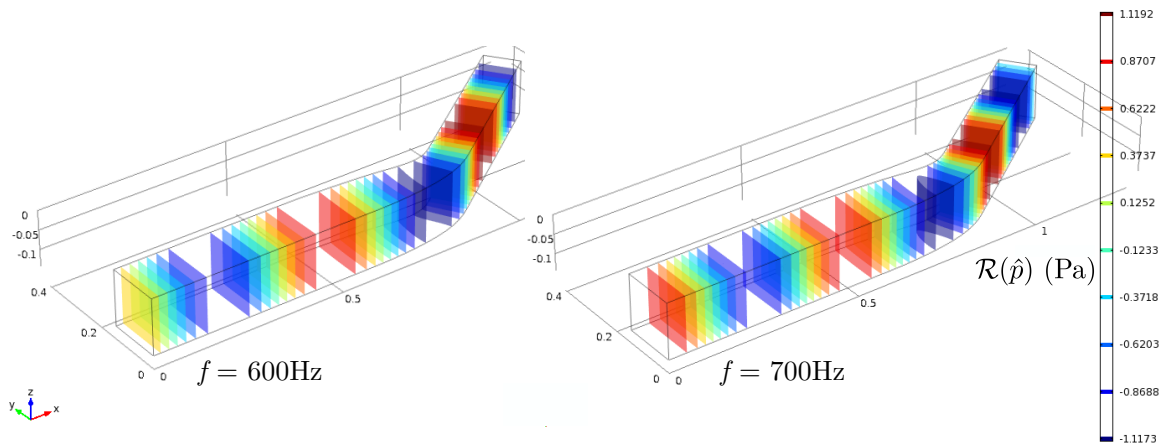


**Figure 5.6.:** Isosurfaces of the real part of the acoustic pressure obtained with the Helmholtz solver. Left: results for an excitation frequency of  $f = 600\text{Hz}$  and a sound hard boundary at the domain outlet. Right: results for an excitation frequency of  $f = 700\text{Hz}$  and a non-reflecting boundary at the domain outlet.

using isosurfaces for two cases. The left-hand image shows the result for a sound hard boundary at the outlet plane of the domain and a plane-wave excitation at the inlet with an excitation frequency of  $f = 600$  Hz. In the right-hand image, the outlet boundary is non-reflecting and the image was captured at  $f = 700$  Hz, while the legend is enforced to the same scaling for both. Most isosurfaces show that plane wave propagation is present. In regions of strong variations of the cross-sectional area, however they are deformed. At the bend in the left-hand image, the isosurfaces are curved, suggesting that a pressure reading at the top of the duct may lead to a different result than at the center chord. In the right-hand image, this is even more pronounced, as one of the isosurfaces forms a U-bend. Note that the images were chosen in order to specifically display this inaccuracy, which is not as severe in all cases, especially for lower frequencies. However, in practice, the issue's impact is not negligible and it is discussed in several passages throughout the remainder of the chapter.

In order to quantitatively assess the accuracy of the developed wave identification scheme, a residual is defined:

$$\delta^* = \frac{\|\hat{\mathbf{P}}_{\text{FEM}} - \hat{\mathbf{P}}_{\text{MMM}}\|_2}{\|\hat{\mathbf{P}}_{\text{MMM}}\|_2}, \quad (5.27)$$

which gives an estimate of the error made by reconstruction of the pressure field in comparison to the underlying FEM results. The pressure field is reconstructed using three complex-valued pressure readings from the FEM simulation, which are denoted by circles along curves 1 and 2 in FIG. 5.4. In order to put the accuracy of the scheme into perspective, three methods for the reconstruction are employed:

1. 1D wave equation: original Multi-Microphone Method, not incorporating the variation of the cross-sectional area (cf. SEC. 2.2),
2. Webster, analytical: solution to Webster's horn equation (EQ. 5.13) assuming a linear decrease of the cross-sectional area between the black dotted lines in FIG. 5.4,
3. Webster, numerical:  $\mathbf{H}$  is determined from two linearly independent solutions of Webster's horn equation (EQ. 5.13) with the exact function of the cross-sectional area  $A(x)$ .

The error-estimate, as calculated per EQ. 5.27, is depicted for an anechoic outlet boundary condition in FIG. 5.7. The residuals of each reconstruction are displayed for the two curves of sensor alignment, as introduced in FIG. 5.4. Sensor alignment along the center chord (curve 1) and reconstruction of the pressure field with the 1D wave equation yields a maximum residual of approximately 10% in the regarded frequency range from 50 Hz to 400 Hz. Approximating the area variation by a linear decrease and solving Webster's equation analytically, lowers the maximum error-estimate in the same range to  $\approx 3.5\%$ . By solving Webster's horn equation numerically, the residual is reduced to less than 1.0%. With sensor locations close to the upper boundary of the geometry, an overall increase of  $\delta^{ast}$  is observed versus center chord locations. Again, the 1D wave equation yields the worst results, as expected. The analytical solution to the simplified case shows a residual of  $\approx 8.0\%$ , while the numerical solution for the exact geometry is the most accurate with a maximum error-estimate of approximately 5.3% in the regarded frequency range.

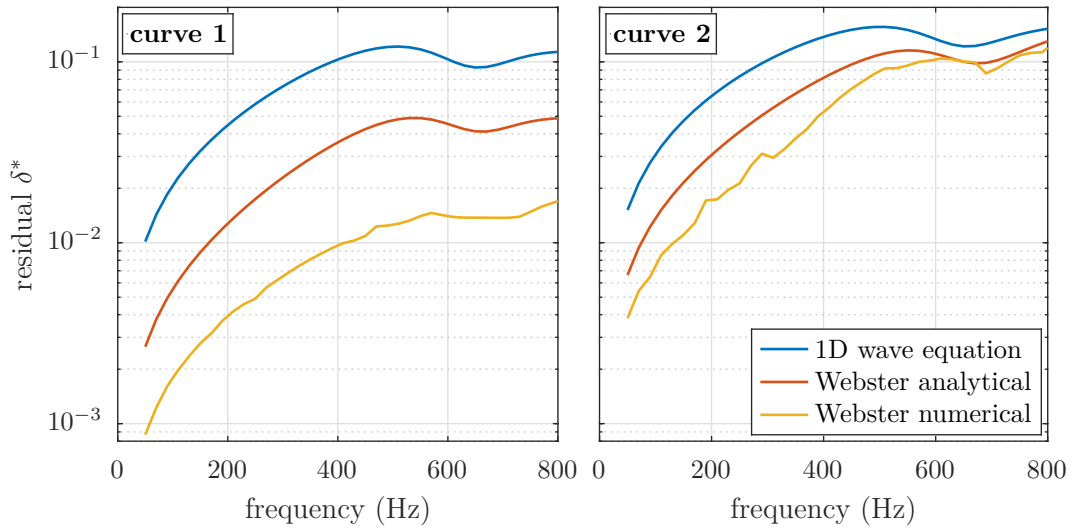


**Figure 5.7.:** Residual  $\delta^*$  for the frequency-domain Multi-Microphone Method in a non-uniform duct for a non-reflective outlet boundary condition calculated with three different approaches (colors). Left: sensor locations aligned along curve 1 (center chord), right: sensors aligned along curve 2 (close to upper boundary).

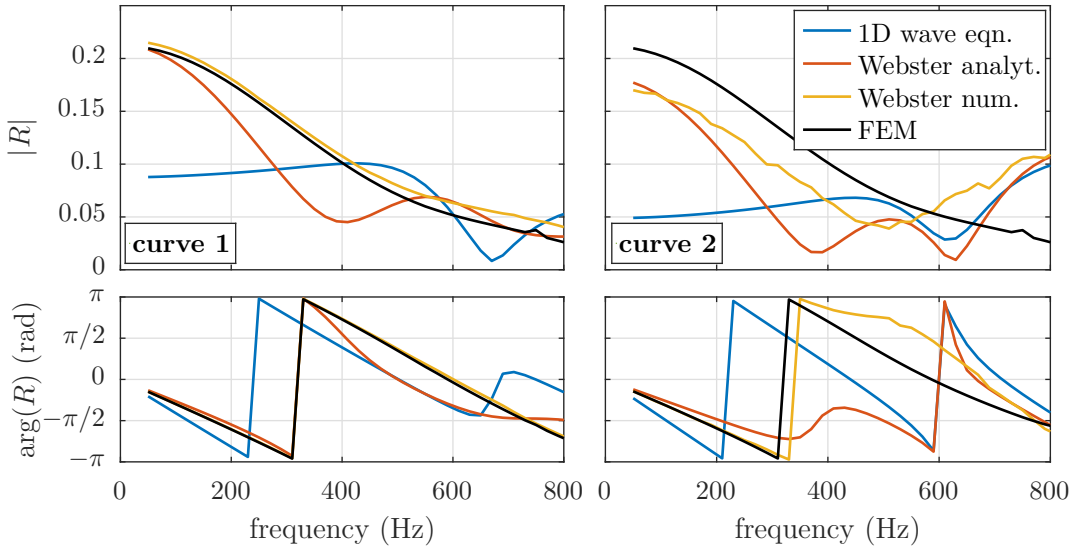


**Figure 5.8.:** Reflection coefficient for the frequency-domain Multi-Microphone Method in a non-uniform duct for a non-reflective outlet boundary condition calculated with three different approaches (colors). Reference solution from FEM given in black. Left: sensor locations aligned along curve 1 (center chord), right: sensors aligned along curve 2 (close to upper boundary). Top: magnitude, bottom: phase at the inlet plane.

An important measure for the verification of the wave decomposition is the reflection coefficient, which is calculated from the ratio of the Riemann invariants at the inlet plane of the geometry. This is done for the two sensor-alignment curves, analog to the previous image.

FIG. 5.8 shows the magnitude and phase of said reflection coefficients for the three reconstructions and the reference solution obtained from the FEM simulation is given in black.

A general verification of the FEM simulations is conducted using an analytical approximation of the reflection coefficient of a compact and smooth contraction for very low frequencies. Analog to Rienstra [143], the linearized mass conservation

$$\bar{\rho}A_1u'_1 = \bar{\rho}A_2u'_2 \quad (5.28)$$

in conjunction with EQ. 2.32 yields a low-frequency approximation of the restriction's reflection factor. Inserting the contraction ratio  $\alpha = A_1/A_2 = 1.54$  of the duct, a reflection coefficient of  $R = 0.21$  is calculated. The result from the FEM simulation indicates a slightly higher reflection for  $f \rightarrow 0$ . This is presumably due to the assumption of a straight duct in the analytical approximation, which is not fulfilled. It is expected that the additional reflection stems from the curvature of the duct, which implies that the result of the FEM simulation is reasonable.

Reconstruction at curve 1 (left-hand image in FIG. 5.8) shows that both magnitude and phase of the reflection coefficient are well approximated with the numerical solution to Webster's horn equation. However, for the analytical solution of the linear approximation of the cross-sectional area variation the results are less accurate, aside from very low frequencies. The results for the 1D wave equation yields the worst results, as is the case for the sensors being located along curve 2 (right-hand image in FIG. 5.8). For this setup, the analytical solution does not yield reliable results, as the reflection coefficient's magnitude diverts by  $\approx 0.04$  to 0.95 in the regarded frequency range from 50 Hz to 400 Hz. The phase shows a significant error of about 2.6 rad at  $f = 400$  Hz. The reconstruction with the numerical solution yields an almost constant magnitude deviation from the reference solution of  $\approx 0.04$  with a maximum phase error of 0.4 rad.

From FIG. 5.7 and FIG. 5.8 it is apparent that locating the sensors along curve 1 is beneficial compared to curve 2. However, due to practical considerations in the high pressure test rig, a sensor positioning at the upper wall was determined to be readily applicable. For that reason, this option was preferred and the acoustic test rig was set up accordingly. In order to maintain comparability, the following elaboration will focus on a sensor positioning at curve 2.

Validity of the developed method is further investigated by plotting the error-estimate  $\delta^*$  for fully reflecting boundary conditions at the outlet plane of the geometry in FIG. 5.9.

Again, the three introduced reconstruction methods are used and the qualitative result is similar to those previously shown. Overall, the solution to the 1D-wave equation yields the highest residuals for both sound hard ( $R_{\text{out}} = 1$ ) and sound soft ( $R_{\text{out}} = -1$ ) outlet impedances. In the regarded frequency range from  $f = 50$  Hz to 400 Hz, the analytical solution to the linear approximation of the cross-sectional area variation yields maximum residuals of approximately 6.6% and 10% for  $R_{\text{out}} = 1$  and  $R_{\text{out}} = -1$ , respectively. The numerical solution to Webster's horn equation lowers the error-estimate to  $\approx 3.5\%$  and  $\approx 6.8\%$  for sound hard and sound soft terminations, respectively. Note that these results were obtained at curve 2, which is close to the upper wall of the geometry and therefore in the region of the strongest curvature.

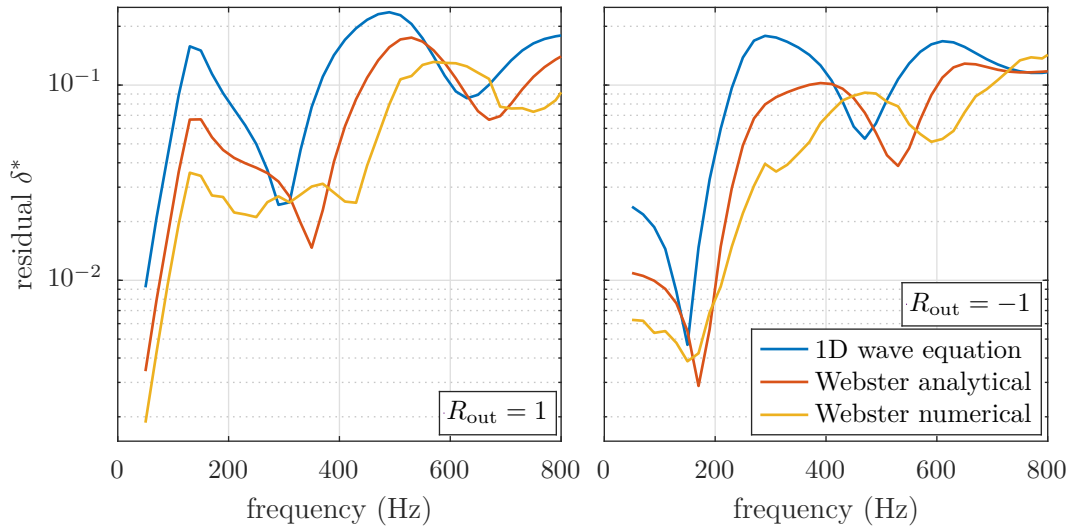


**Figure 5.9.:** Residual  $\delta^*$  for the frequency-domain Multi-Microphone Method in a non-uniform duct calculated with three different approaches (colors). Microphones are aligned along curve 2. Left: sound hard outlet impedance, right: sound soft outlet impedance.

Further verification is conducted for the same test cases using the practically relevant reflection coefficient, evaluated at the inlet plane. FIG. 5.10 depicts the reconstructed reflection factors for each of the utilized methods and the reference value obtained from acoustic pressure and particle velocity in the FEM simulation (black). Both magnitude and

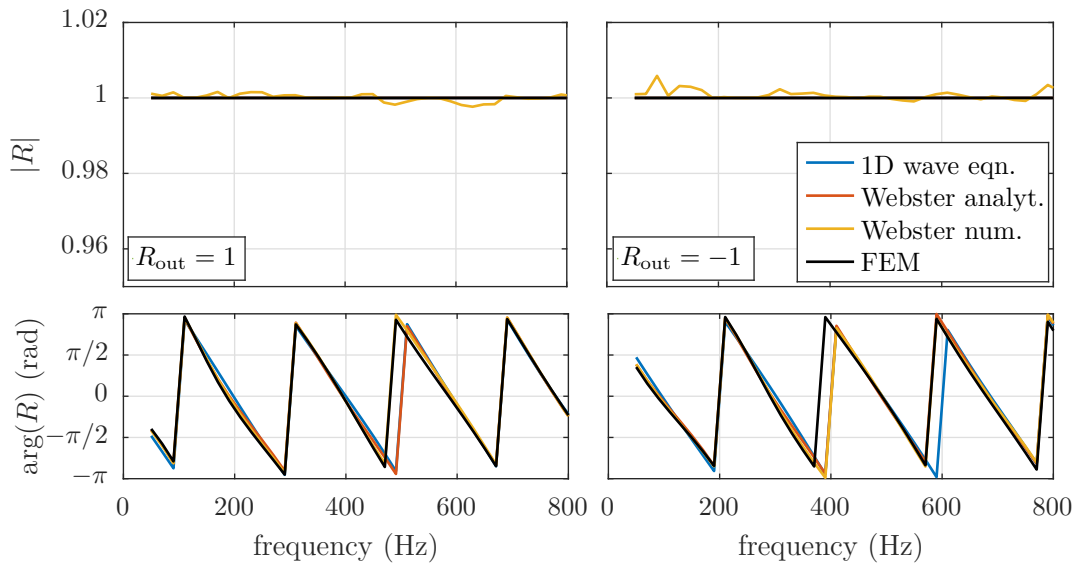


**Figure 5.10.:** Reflection coefficient for the frequency-domain Multi-Microphone Method in a non-uniform duct calculated with three different approaches (colors). Microphones are aligned along curve 2. Reference solution from FEM given in black. Left: sound hard outlet impedance, right: sound soft outlet impedance. Top: magnitude, bottom: phase at the inlet plane.

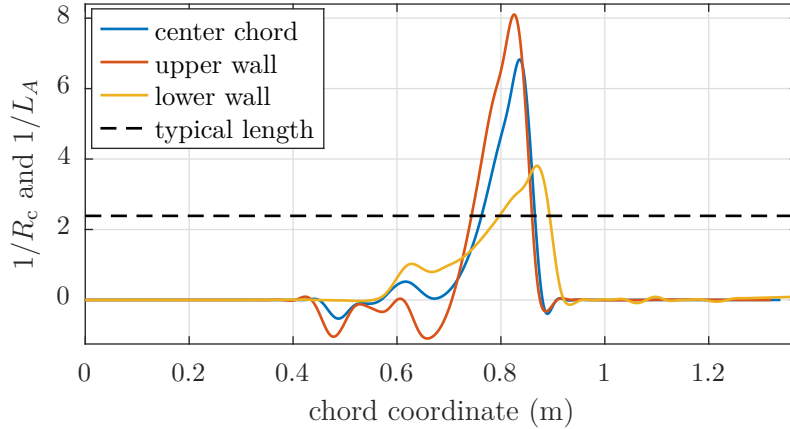


**Figure 5.11.:** Inverse values of the curvature radius  $R_c$  (solid, colors) and the typical length scale of the cross-sectional area variation  $L_A$  (dashed, black) over the corresponding curves.

phase of all reconstruction methods show good accordance to the expected reference values. The magnitude of the numerical solution fluctuates slightly more than those obtained with the remaining reconstruction methods. With deviations of  $\approx 0.3$ , the phase error at low frequencies, is largest for the reconstruction with the 1D wave equation. The numerical solution yields the lowest phase error compared to the FEM results.

The high residuals and lack of accuracy of the reconstruction with the numerical solution to Webster’s horn equation with sensors located along the upper wall (cf. FIG. 5.8, left) imply that the applicability of the theory detailed in SEC. 5.1 is reduced. Critical assumptions involve the maximum duct diameter  $d/L_A \ll 1$  and the curvature:  $R_c \geq L_A$ . With  $L_A$  assumed to be the length of the cross-sectional area variation, the former assumption is adequately satisfied at  $d/L_A \approx 1/3$ . However, attention needs to be paid to the curvature. Especially that of curve 2, which is located close to the upper wall of the geometry, does not satisfy the assumption. In FIG. 5.11, the inverse values of the curvature radii  $R_c$  along curve 1 (center chord, blue), curve 2 (close to upper wall, orange), and additionally along the lower wall (yellow) are plotted over their corresponding chord coordinates. Furthermore, the inverse value of the typical length scale  $L_A$ , set to the length of the cross-sectional area variation at the center chord, is plotted as a black dashed line. The assumption made in the beginning of SEC. 5.1 would be satisfied, if the reciprocals of  $R_c$  were below the threshold of the typical length scale. It is apparent that the curvature is strongest for curve 2, which is unfavorable in the context of applying the Multi-Microphone Method with sensors along that curve. Moving towards the lower wall decreases the curvature and thereby potentially lowers the error made with the developed wave decomposition scheme.

#### 5.4. Experimental Validation of the Multi-Microphone Method in Non-Uniform Ducts

In order to experimentally validate the extended Multi-Microphone Method in frequency domain and in time domain, a cold acoustic test rig was designed and built from acrylic glass with a thickness of 20 mm. FIG. 5.12 shows the setup in a top view. A total of 16 microphones can be mounted along curve 2 close to the upper boundary of the curved duct. The first and last four sensor locations are situated inside constant cross-sectional area parts of the ducts,

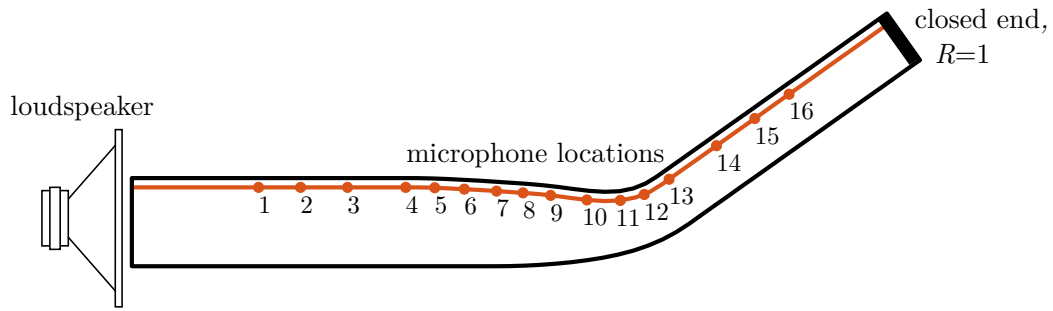


**Figure 5.12.:** Schematic of the cold acoustic test rig for validation of the Multi-Microphone Method in ducts with variable cross-sectional area.

allowing for application of the original, and therefore reference, Multi-Microphone Method. The downstream end of the duct is sealed, realizing a sound hard boundary condition. The upstream end is used for excitation with a swept sine ( $f = 50 \text{ Hz to } 800 \text{ Hz}$ ) as well as a pre-recorded combustion noise signal. As sound transducer, an 18" woofer without enclosure was used.

The microphones are calibrated according to the elaborations in SUBSEC. 7.4.1. However, a key difference in the cold acoustic tests in this section are the microphone holders. They are not cooled and can therefore be flush-mounted to the inside walls. Microphones in cooled holders are comparably more complex in handling. Yet, when the according attention is paid to calibration steps, residuals of both flush-mounted and microphones in cooled holders are in the same range.

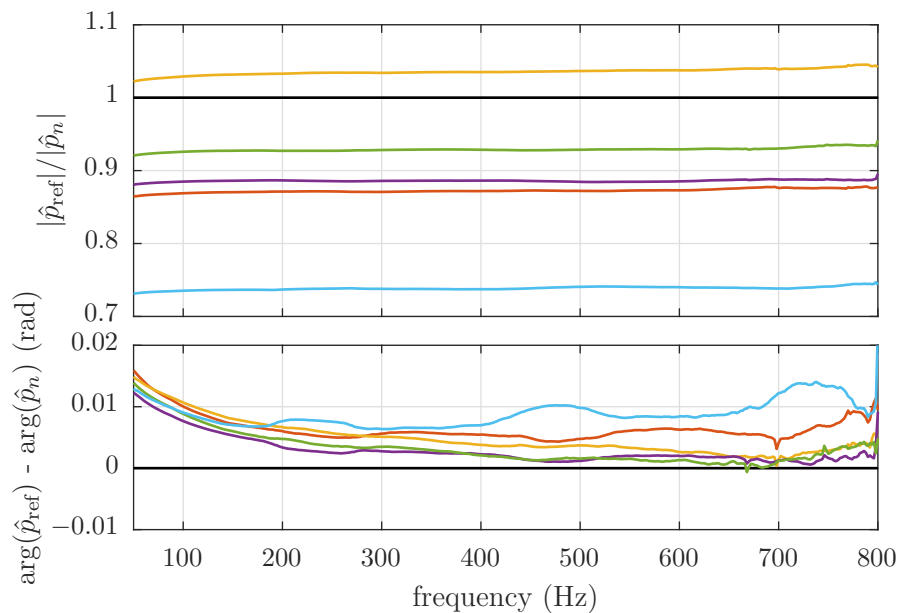


**Figure 5.13.:** Calibration coefficients for five microphones in flush mounted holders. Top: magnitude, bottom: phase.

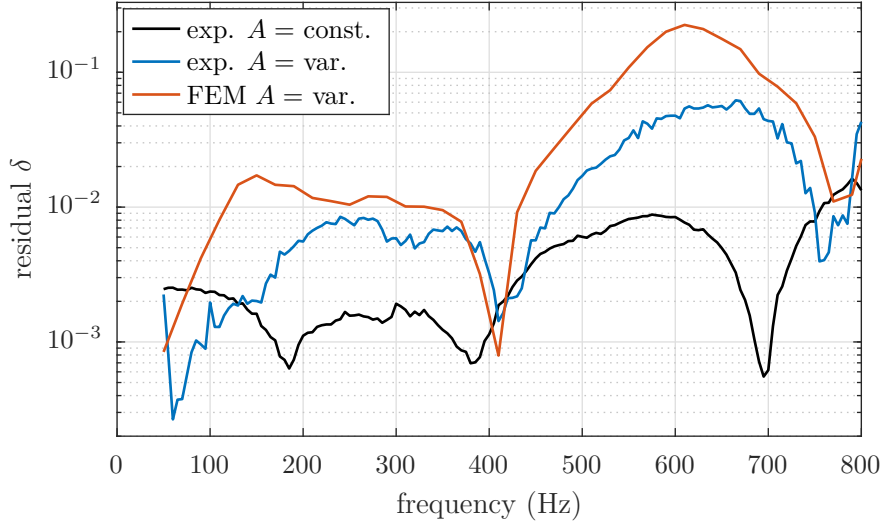


**Figure 5.14.:** Residual of the frequency-domain wave decomposition obtained from microphone readings in the duct segments with constant (black, reference) and variable cross-sectional area (blue). For comparison, the residual  $\delta$  is calculated for the same setup with the FEM simulation from SEC. 5.3.

As mentioned in SEC. 2.4, microphones with a similar phase and a constant amplitude response are chosen among those available. The calibration coefficients are depicted in FIG. 5.13.

Three of the microphones are mounted at locations 13, 15, and 16 (cf. FIG. 5.12) for the reference measurement in the downstream duct segment with constant cross-sectional area. Two additional sensors are located at positions 7 and 9, together with the microphone at location 13, forming the sensor array in the bend. Both arrays are thus capable of measuring the Riemann invariants at location 13, which shall be investigated later on. Initially, the residuals of both methods are calculated with EQ. 2.36 and depicted in FIG. 5.14.

The original Multi-Microphone Method (black), which acts as reference, shows very low residuals of  $\delta < 0.2\%$  at  $f = 50$  Hz to 400 Hz, indicating a good accordance of the measured and calculated Riemann invariants inside the uniform duct. In the same range, the extended Multi-Microphone Method (blue) applied in the duct with variable cross-sectional area reaches a maximum of  $\delta = 0.8\%$ , which indicates a high-accuracy reconstruction of the pressure field. For comparison, the error-estimate  $\delta$  is calculated for the reconstruction based on data obtained from the FEM simulation in SEC. 5.3 (orange). A qualitative similarity is observed, however, the maximum residual is more than two times higher.

In the same experiment, the downstream traveling waves  $\hat{f}$ , generated with consecutive sine-signals, were calculated using the two sensor arrays in the constant and variable cross-sectional area segments, respectively. FIG. 5.15 depicts the reconstructed Riemann invariant at location 13 for both methods. The amplitude of  $\hat{f}$  is in good accordance with both methods up to  $\approx 400$  Hz. However, the phase shows slowly increasing deviations of 0.05 rad to 0.2 rad in a range from 300 Hz to 400 Hz.

In the next step, the time-domain implementation of the Multi-Microphone Method for non-uniform ducts was validated experimentally. Microphone locations were kept the same

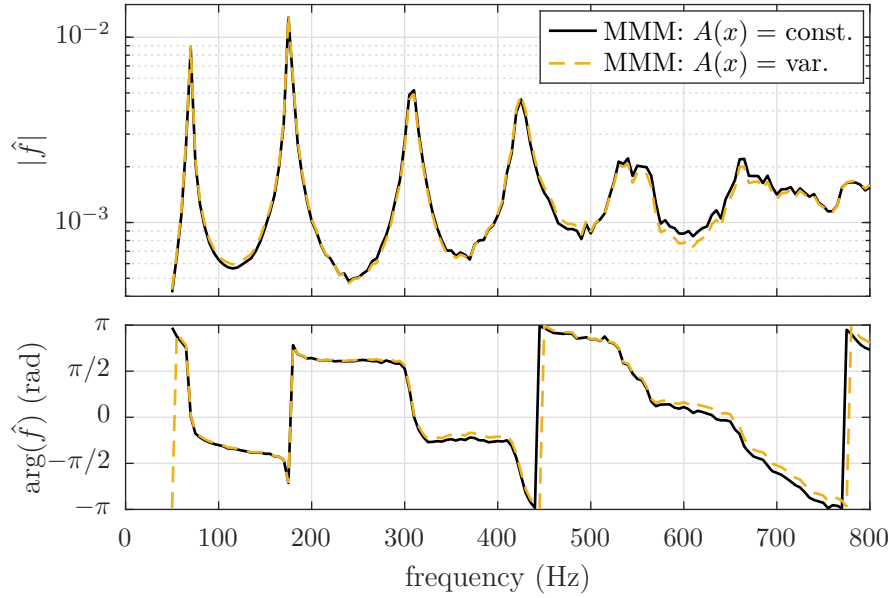


**Figure 5.15.:**  $\hat{f}$ -wave reconstructed with the frequency-domain Multi-Microphone Method in the constant (black) and variable (yellow) cross-sectional area duct segments, each evaluated at location 13. Top: magnitude, bottom: phase.

as in the frequency-domain investigation (7, 9, 13). However, the forcing signal was altered to typical combustion noise, which was extracted from an atmospheric combustion test with a lean premixed swirl stabilized flame. The code for online wave identification was implemented on the *dSPACE* controller board according to the schematic depicted in FIG. 5.3. The scattering matrices  $\mathbf{S}_n(\omega)$  were analytically calculated assuming linear variations of the cross-sectional areas between neighboring microphones (EQ. 5.26). Subsequently, they were translated into state-space realizations, according to the description in SEC. 2.3.

Again, the downstream propagating waves at location 13 were evaluated, this time with previously recorded combustion noise as input signal. Reference values of the obtained  $f$ -wave were calculated using the frequency-domain Multi-Microphone Method for uniform ducts at the probe locations in the segment with constant cross-section. From FIG. 5.16, a good accordance of the  $f$ -wave obtained from the time-domain wave decomposition inside the non-uniform duct with that of the reference approach is apparent. Deviations in both magnitude and phase are observed in the lower frequency range, as well as above 500 Hz. Due to the importance of an online identification of the downstream propagating wave for the active modification of the acoustic boundary condition, errors have to be reduced to a minimum. This topic is further discussed in the outlook in SEC. 5.5.

Another estimate of the accuracy is obtained from investigating the reflection coefficient at the same location, which simplifies identification of weaknesses due to an inherent normalization of the Riemann invariants. FIG. 5.17 depicts the reflection coefficient at probe location 13 for the reference case with the frequency-domain wave decomposition performed in the uniform duct segment in black. The time-domain reconstruction of the Riemann invariants at the same location is colored in yellow. Regarding a frequency range from 50 Hz to 400 Hz, good accordance of the magnitude is obtained at frequencies between 100 and 240 Hz. Stronger

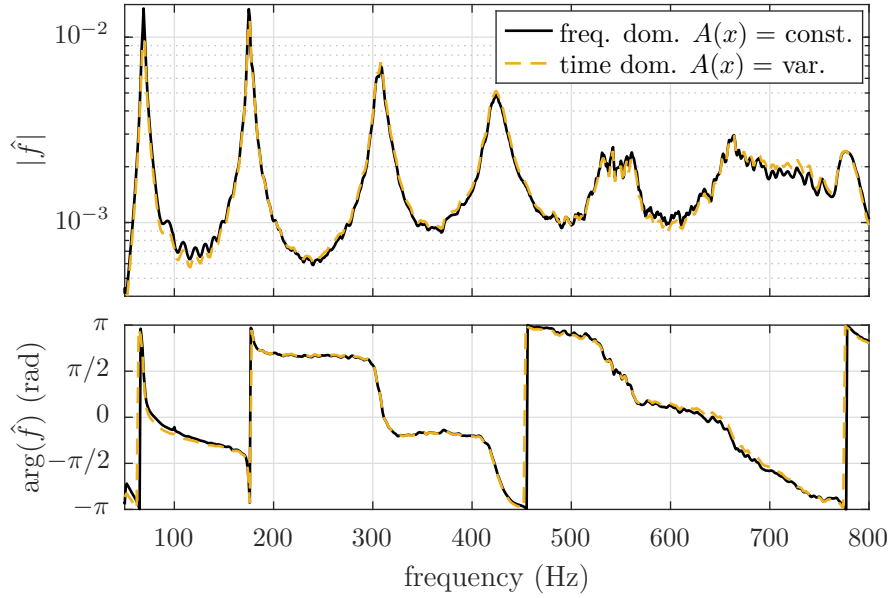


**Figure 5.16.:** Downstream propagating wave at location 13. Reconstructed with the frequency-domain (black) and time-domain (yellow) Multi-Microphone Method in the constant and variable cross-sectional area duct, respectively. Top: magnitude, bottom: phase.

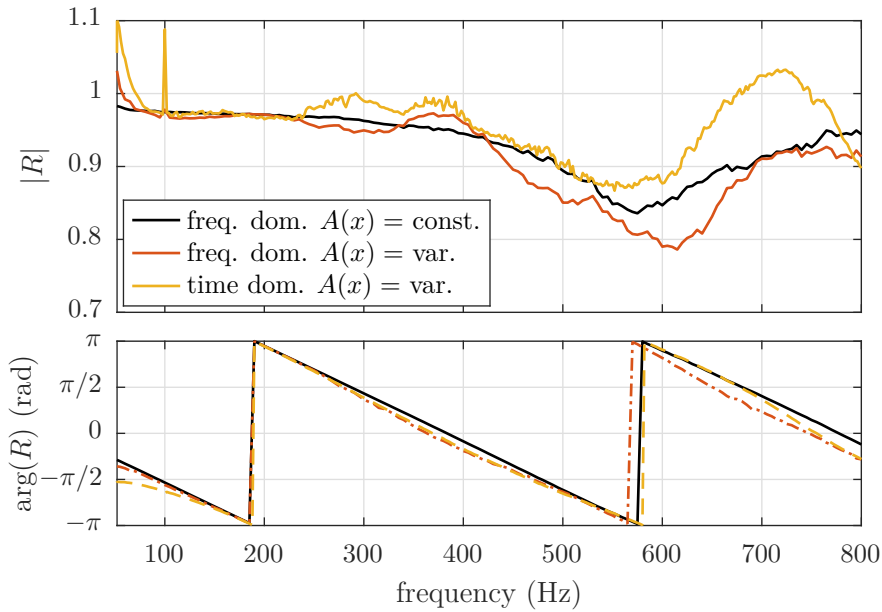


**Figure 5.17.:** Reflection coefficient evaluated at location 13. Reconstructed with the frequency-domain Multi-Microphone Method in the constant (black) and variable (orange) cross-sectional area duct segments, and for the time-domain wave decomposition inside the non-uniform duct (yellow). Top: magnitude, bottom: phase.

deviations occur towards 50 Hz and there is a distinct peak at 100 Hz, which is expected to be due to electric hum. The deviations between 240 and 400 Hz reach maximum values of

5.0%. For further comparison, the result of the frequency-domain wave decomposition in the non-uniform duct is highlighted in orange. The achieved accuracy is higher compared to that of the time-domain implementation. The phase of both methods of wave decomposition in the non-uniform duct shows deviations towards higher frequencies. Towards lower frequencies, the frequency-domain method yields better accuracy than its time-domain counterpart.

## 5.5. Conclusion and Outlook for the Developed Methods

Throughout SEC. 5.3 and SEC. 5.4 it becomes obvious that the accuracy of the developed scheme offers potential for improvement. From FIG. 5.7 a general trend can be derived, stating that a better reconstruction is possible when moving the probe locations to the center chord, instead of the upper wall. The physical reason for that can be found inspecting the shape of the isosurfaces in FIG. 5.6, which are strongly bent towards the upper surface. However, the development of the wave identification scheme inside a non-uniform duct as presented in SEC. 5.1, among others, relies on the assumption of low curvature. This was investigated in FIG. 5.11, where the ratio of curvature to typical length of the variation of the cross-sectional area is presented. In conclusion, these findings indicate that probe locations close to the lower boundary potentially deliver superior results.

However, prior to the final implementation of the developed methods, simulations for acquiring the scattering matrices need to be conducted under realistic flow conditions, in any case. Within this investigation, practically applicable sensor locations need to be incorporated. The transfer behavior in between these locations and to the desired reference planes are to be determined, respectively. This was not done for the development of the scheme, as further simulations with mean flow were required, anyways. The results of the additional investigations can easily be evaluated for arbitrary sensor locations. The additional effort to obtain error-estimates for positioning close to the lower boundary is expected to be minor. Seeing the potential gain in accuracy (cf. FIG. 5.11), this step is highly recommended.

Implementation at the high pressure test rig may invoke further sources of inaccuracy that are to be mentioned for completeness. An insight into the influence of wave attenuation is given by Tijdeman [175] and is an important factor to incorporate in future investigations. However, the complexity in finding the acoustic transfer relations is highly increased and their experimental determination may be necessary.

Furthermore, incorporation of the influence of a significant axial temperature gradient due to cooling might be necessary. For stationary conditions, Subrahmanyam et al. [171, 172] developed solutions to the wave equation for particular families of cross-sectional area variations and temperature profiles. Furthermore, Sujith et al. [173] developed solutions to the wave equation for exponential, quadratic, and square root-shaped temperature profiles. Manoj Kumar & Sujith [103] analogously derived solutions for polynomial temperature profiles, however both of these studies also neglected convection. The results are therefore only valid with mean flow Mach numbers  $M < 0.1$ , which is a value that might be exceeded in the regarded test rig at certain operating points. Thus, an extension of the proposed methods to variations in mean temperature could become necessary for ensuring a reliable wave decomposition technique.

Note that the method is not restricted to use in combustion chambers. Any technical applications that require determination of acoustic variables in segments of slowly-varying cross-sections may profit from this approach. Usually, the system is redesigned and straight

ducts are incorporated under the assumption that the acoustic fields are equal. This step could be omitted by employing the developed wave decomposition scheme. Thereby, costs for redesigning may be reduced and the reliability of the results may be enhanced, as no simplifying assumptions are made.



# CHAPTER 6

---

## Simulations for Positioning of an Actuator Upstream of the Burner

---

Thermoacoustic characterization of a combustor system by means of a flame transfer matrix measurement at the high pressure test rig requires acoustic excitation upstream of the burner section. In this chapter, different actuator types are discussed and eventually a siren actuator is proposed.

Depending on the type of sensor array that is employed, different actuator locations are possible. Therefore, SEC. 6.2 deals with different mounting options at the burner base plate, which are investigated with FEM simulations. Subsequently, various options for mounting further upstream at the flow box are studied on the basis of additional simulations. Finally, both options are compared and practical implications are discussed.

### 6.1. Actuator Types and Their Eligibility

The type of actuator that is chosen is highly relevant in the context of an elevated pressure scenario, as present in the regarded industrial test rig. Only few actuation methods provide a sufficient acoustic pressure amplitude, cover the required frequency range and endure the harsh environment. In atmospheric test rigs, *loudspeaker drivers* are the optimal choice as a means of acoustic excitation. They feature a linear behavior in frequency and amplitude response, are easy to operate, and inexpensive to replace. However, even in atmospheric tests loudspeakers are prone to destruction due to high pressure peaks occurring in reacting tests, need to be cooled and monitored extensively, and require considerable installation space. Oftentimes, several loudspeakers are used to achieve the required control authority. In high pressure tests, the necessary sound pressure amplitude (cf. SEC. 3.2) increases linearly with the mean pressure (and thereby density), making loudspeakers unfeasible due to their lack of control authority. Furthermore, the occurrent pressure peaks make a reliable operation with loudspeakers impossible.

In intermediate or high pressure test rigs, several types of acoustic actuators come into consideration. Bothien [18] investigated various interesting concepts. For instance, an oil combustor was developed, the fuel supply of which could be modulated with a proportional valve. The idea was to generate a sound source by utilizing a fluctuating heat release. However, the generated acoustic amplitude was not sufficient, especially at frequencies higher than 100 Hz and the overall achievable frequency range was too small. Furthermore, flame blow off was a problem at high excitation amplitudes and frequencies. In addition, Bothien investigated

the electro-pneumatic actuator *Ling Electronics model EPT-94B* (cf. references [26, 96]). The electronically controlled device modulates a driving airflow of up to 0.26 kg/s using a pneumatic valve. This type of actuator is capable of generating sinusoidal wave shapes in a frequency range of 20 Hz to 500 Hz, as well as noise or any other wave form. However, the piston stroke amplitude is frequency dependent, making the actuator somewhat intricate to handle. This is especially important considering the active modification of the acoustic boundary condition. In case of upstream acoustic excitation, this is not an issue as long as the required amplitudes are achieved in the combustion chamber. Another type of actuator discussed by Bothien [18] is a proportional valve for air flow modulation. These devices are fed by a constant supply mass flow, which is modulated by linear displacement of a piston. High actuation amplitudes can be achieved and the devices may be operated in the harsh environment of a high pressure test rig. Further information on proportional valves is found in SUBSEC. 7.4.3.

A detailed discussion on additional actuator types, such as electro-dynamic, magneto-restrictive, or piezo-electric zero-net-mass-flux drivers, and their suitability in high pressure environments is carried out in SEC. 7.1.

#### 6.1.1. Siren Actuator

In contrast to those previously mentioned, one actuator type is frequently employed in high pressure test rigs. *Siren* actuators (e. g. employed in references [36, 49, 68, 83, 152, 160]) are wide spread due to their capability of providing high amplitude excitation, ruggedness, and general simplicity of design. Sirens modulate a driving air flow and can be operated in a wide frequency range. However, they are only capable of excitation at one single frequency at a time, due to their working principle. In the case of incorporation as an upstream actuator, this is sufficient. A schematic of a siren is given in FIG. 6.1. Pressurized air enters the vessel on the left hand side and exits from the duct on the top right. The outlet duct is alternately opened and closed by rotation of a disk outfitted with holes, teeth, or a scalloped contour, as realized in the actuator design described in SEC. 7.4. Thereby, the air flow is modulated and high amplitude velocity fluctuations are induced. According to Freitag [50], the waveform of the outgoing signal correlates with the open area, thus a sinusoidal variation of the open area is desirable in the context of a high signal-to-distortion ratio. The shape of the rotating disk may be altered in order to adjust the wave shape or to cover a different frequency range.

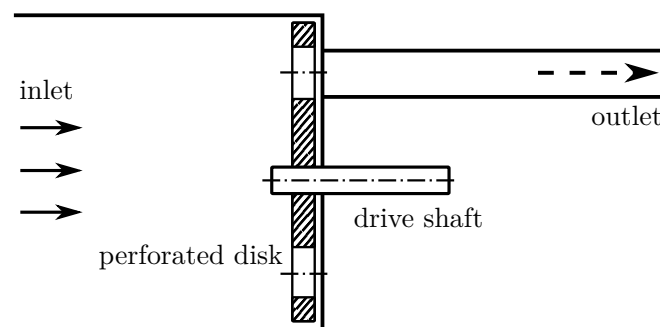


**Figure 6.1.:** Schematic of a siren actuator.

Sirens are manufactured individually, thus cost and manufacturing time depend on the design parameters. Main matters of expense are the desired level of usability as well as pressure and temperature rating. The latter factors are obvious, as the cost increases with more solid housing and robust sealing, especially of the moving parts. Usability can be improved by addressing an issue in the amplitude behavior inherent to siren actuators, which is the dependence of the actuation amplitude on the driving air flow. Increasing the rotational frequency of the perforated disk decreases the amplitude of the velocity fluctuations. Therefore, exciting at constant amplitudes in a given frequency range demands the siren air flow to be adjusted by implementing a variable bypass. However, this would result in varying combustion parameters such as equivalence ratio and bulk velocity. Accordingly, the variation in air mass flow and possibly preheat temperature needs to be compensated for, making the experiments time-consuming and, therefore, costly on high pressure test rigs. This issue can be addressed, e. g., by using two sirens with controllable phases in a specifically designed arrangement. In this setup the phase of each actuator's outgoing velocity fluctuation can be controlled according to the amplitude requirement at each operational point. When high amplitudes are desired, the phase relation of both outgoing signals is set to a constructive interference. When lower amplitudes are required, e. g., due to resonances or low damping inside the test rig, the phase relation is altered and the total amplitude of the outgoing signal is lowered, although the total air mass flow through the siren actuators remains constant. The increased cost of such a setup is mostly due to the manufacturing of a second identical siren and its necessity needs to be evaluated case by case.

The siren's overall effectiveness is strongly dependent on its location in the test rig and the type of mounting that is employed. In the following sections, the influence of those contributing factors is investigated by means of FEM simulations that were mostly conducted within the master thesis of Schneehagen [155].

## 6.2. Acoustic Simulations with Base-Plate-Mounted Actuator

On one hand, the positioning depends on practical considerations, i. e., the connector for the siren may only be implemented in locations with enough space. Further, the pressure housing of the test rig might need to be perforated and adapted, in order to fit the connector. On the other hand, the achievable acoustic amplitude in the combustor may vary, when incorporating different locations. For instance, segments of smaller cross-section will lower the amplitudes due to reflection and damping.

Additionally, the location is dependent on the sensor concept employed for the thermoacoustic characterization. Specifically, the sensors need to be located downstream of the actuator. This is necessary, as the sound field is strongly affected by an acoustic source. Therefore, placing the source in between the sensor array and the evaluation location of the acoustic variables yields false results. This becomes relevant, when considering the sensor concept introduced in SEC. 4.2, which employs a pressure transducer array in the flow sleeve upstream of the burner. Thus, acoustic excitation needs to be implemented upstream of the flow sleeve to ensure proper functionality of the sensor concept. However, if the unsteady pressure loss over the burner (cf. SEC. 4.3) is utilized, the upstream actuator may also be located downstream of the flow sleeve.

Two main options for mounting of the upstream actuator were identified. The first is the burner base plate, which is shown in FIG. 3.2. Actuation at this location is expected to

yield low losses in acoustic amplitude, as it is in close proximity to the burner. The pressure housing would not need to be adapted in this case. However, the burner base plate already features manifold connectors for cables and fuel lines, which impedes mounting of a siren connector. Furthermore, the sensor array in the flow sleeve (cf. SEC. 4.2) does not comply with this option, as it is located upstream of the burner base plate.

The second identified location is further upstream at the flow box (cf. FIG. 3.3). This option requires perforation and adaptation of the pressure housing and the achievable amplitude in the combustor might suffer, as the acoustic waves need to pass the flow sleeve. Yet, the sensor array in the flow sleeve could be employed and mounting space at this location is ample.

Accordingly, the first investigation presented here focuses on mounting locations of a siren actuator at the burner base plate. FIG. 6.2 shows the sectional view of the corresponding computational domain. It is axially symmetric around the  $x$ -axis and features the same proportions in length, area, and volume as present in the high pressure test rig. Compared to the complete CAD geometry, the domain was reduced in complexity. Besides confidentiality and lower requirements on computational resources, the main reason lies in the regarded low frequency acoustics. Hence, geometric details of dimensions well below the acoustic wave lengths have only minor influence.

The axisymmetric domain in FIG. 6.2 consists of several parts. The flow sleeve is confined at plane 1, which is the boundary to the flow box (omitted in the first part of the study). Plane 1 is set to two different boundary conditions. For the reference case, an impressed normal particle velocity is set, simulating the natural oscillation of the entire system. This reference case is then compared to a case with the actuator attached to various locations on the burner base plate. For these cases, boundary 1 is set to a pressure node, which is expected to be a realistic representation of the actual case, because of the sudden area increase at the connection to the flow box. From plane 1, the flow sleeve extends to the plenum on the left-hand side, which is terminated by the burner base plate coinciding with the  $y$ -axis. Inside the plenum, the combustion air is deflected into two channels, the inner one being the pilot stage of the burner. The outer channel is an annulus resembling the burner main stage. The combustion chamber extends from the burner outlet to the restriction on the right-hand side, representing the vane simulation section (VSS, cf. SEC. 3.1). The circular plane marked with a 2 is the domain outlet, featuring anechoic conditions, which is done by setting the

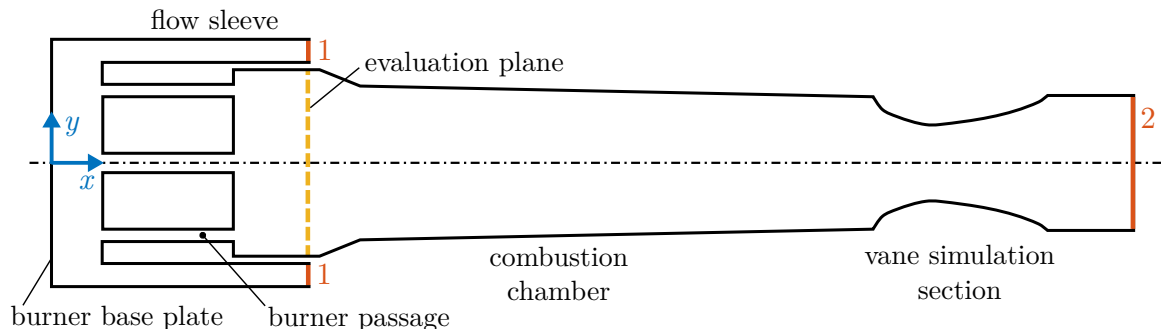


**Figure 6.2.:** Sectional view of the computational domain for a base plate mounted actuator. The boundary condition at plane 1 is an impressed normal velocity or a pressure node and at plane 2 the impedance is adjusted to anechoic conditions.

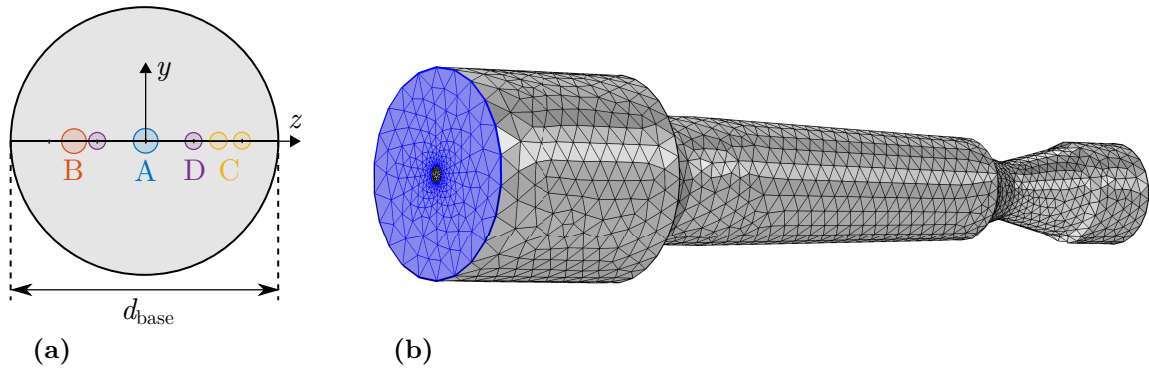


**Figure 6.3.:** (a) Base plate in plan view with four different connection strategies, which are summarized in TAB. 6.1. (b) Computational domain with the employed mesh and the burner base plate highlighted in blue

impedance boundary condition to the characteristic acoustic impedance. All other boundaries are sound hard.

FIG. 6.3b shows the unstructured mesh of tetrahedrons generated by COMSOL, featuring a relatively fine grid for low frequency acoustics. It was made sure that the maximum element size is smaller than 10% of the minimum wave length at the lowest temperature, as advised in the COMSOL User Guide [38]. The burner base plate, which contains the siren connectors is highlighted in blue and shown in top view in FIG. 6.3a, featuring the four connection strategies used in this study. The base configuration is a  $d = 50$  mm circular inlet at the center point of the burner base plate (A). The diameter was chosen, as it is considered the standard connector size for a siren on combustion test rigs. However, there are spacial restrictions to where the connector can be placed on the burner base plate. Several ducts and cable connections run through the base plate, leaving very few mounting possibilities. In order to acquire information on how various installation alternatives perform compared to the baseline, three other representative cases were investigated. Configuration B is a circular inlet of the same diameter as A, but placed at  $z/d_{\text{base}} = -0.26$  out of center. The  $z$ -coordinate is normalized by the total diameter  $d_{\text{base}}$  of the burner base plate. Option C consists of two identical inlets, located at  $z/d_{\text{base}} = 0.26$  and  $0.35$  off center. Configuration D features two identical inlets, as well, which are placed symmetrically around the center point at  $z/d_{\text{base}} = \pm 0.18$ . The test cases are summarized in TAB. 6.1.

configuration	# of connectors	symmetric	$z/d_{\text{base}}$
A	1	yes	0.0
B	1	no	-0.26
C	2	no	0.26 & 0.35
D	2	yes	-0.18 & 0.18

**Table 6.1.:** Configurations for investigation of different actuation locations at the burner base plate.

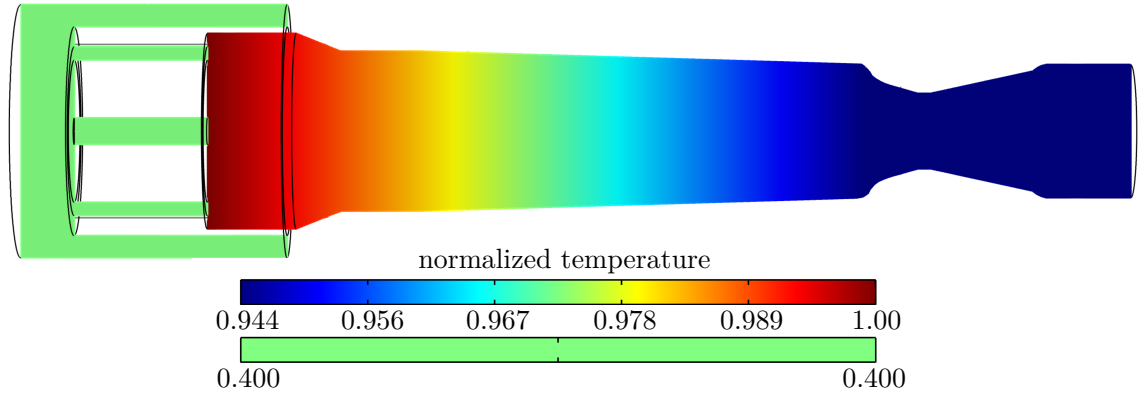


**Figure 6.4.:** Sectional view of the temperature distribution inside the axisymmetric computational domain.

Acoustic excitation with the four configurations was realized using a normal velocity boundary condition with an amplitude of  $\hat{u}_{\text{exc}} = 0.01$  m/s. The value was chosen in order to stay within the linear regime, due to the solver not being able to reproduce non-linear behavior. For the reference case, i. e., excitation at plane 1 in FIG. 6.2, the amplitude was scaled. In order to achieve the same sound energy flux, an excitation amplitude of  $\hat{u}_{\text{exc}} = 2.4 \times 10^{-4}$  m/s was set.

FIG. 6.4 displays the temperature distribution in a sectional view of the computational domain. From the flow sleeve to the burner outlet, the normalized temperature is set to a constant value of 0.400, which matches the compressor outlet temperature at an intermediate pressure level. Inside the combustion chamber, the temperature follows a linear decline from 1.00 to 0.944 from the burner outlet to the throat of the VSS. Downstream of the throat, the temperature remains constant. The working fluid is air, assumed to be an ideal gas, with a temperature-dependent isentropic exponent.

For the calculations carried out in this section, the *Pressure Acoustics, Frequency Domain Interface* was used. Results were passed to an evaluation program in MATLAB, as is the case for the following sections, as well. As the focus lies on comparably low frequency acoustics up to 400 Hz in this study, only plane wave propagation is regarded. The assumption was verified by evaluating EQ. 2.20 for the generic combustion chamber. At the burner outlet, an area jump leads to a spherical sound wave propagation, initially. The non-axial velocity components decline exponentially. A suitable location for data evaluation is found at an axial distance of  $\Delta x = 0.18$  m from the burner plate, which is highlighted in yellow in FIG. 6.2. Here, the non-axial velocity components are reduced to values below  $\approx 10\%$  of the axial component. In order to compare the *native* oscillation with excitation at the flow sleeve inlet to the configurations A to D, the phase difference in the plane normal to the axial direction is evaluated.

FIG. 6.5 depicts the phases of the axial velocity over the  $z$ -coordinate for mono-frequency excitation at the flow sleeve (blue) and at the burner base plate (orange), each corrected by its offset. The largest difference between both phases is found at the combustion chamber wall in this example. The difference varies depending on the frequency as well as the burner base plate configuration that is employed. The maximum value of the phase difference in the reference plane is taken as a performance parameter for the studied configurations.

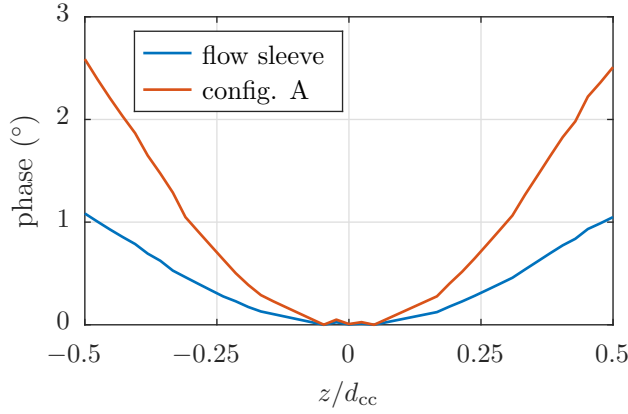


**Figure 6.5.:** Exemplary offset-corrected phase of the axial velocity component with excitation at the flow sleeve (blue) and at the burner base plate with configuration A (orange) at an excitation frequency of  $f_{exc} = 60$  Hz

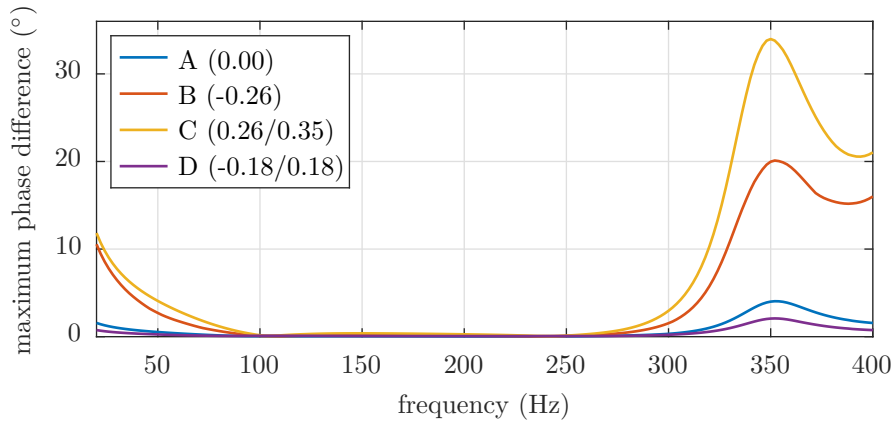


**Figure 6.6.:** Maximum phase difference of the axial velocity between the reference excitation at the plenum and the four excitation strategies at the burner base plate

The resulting maximum phase difference between the reference excitation and each configuration over the frequency is shown in FIG. 6.6. In a range from 100 Hz to 250 Hz the maximum differences are smaller than  $1.0^\circ$ . Above 250 Hz, the strongest deviations of the symmetric configurations (A, D) are smaller than with asymmetric excitation (B, C). The maxima of the latter configurations reach  $34^\circ$  and  $20^\circ$ , respectively, while those of excitation locations A and D stay below  $5^\circ$ . Those two configurations perform quite similarly. However, configuration D with two smaller excitation holes delivers less deviations from the case simulating the natural oscillation. This can be attributed to a more evenly spread excitation with less variance of the phase over the radial coordinate than with the single large excitation plane in configuration A.

Comparing cases A, B and C, it is apparent that the phase difference increases with the level of asymmetry. Furthermore, the influence of asymmetry on the performance of each configuration is larger than the influence of the amount of excitation planes. This becomes obvious comparing A and D, where two excitation planes are beneficial to the actuator performance, to B and C, where this relationship is reversed. Here, two excitation planes perform worse, while the only difference is the radial arrangement. In conclusion, the symmetric configurations result in a velocity distribution far more similar to the naturally

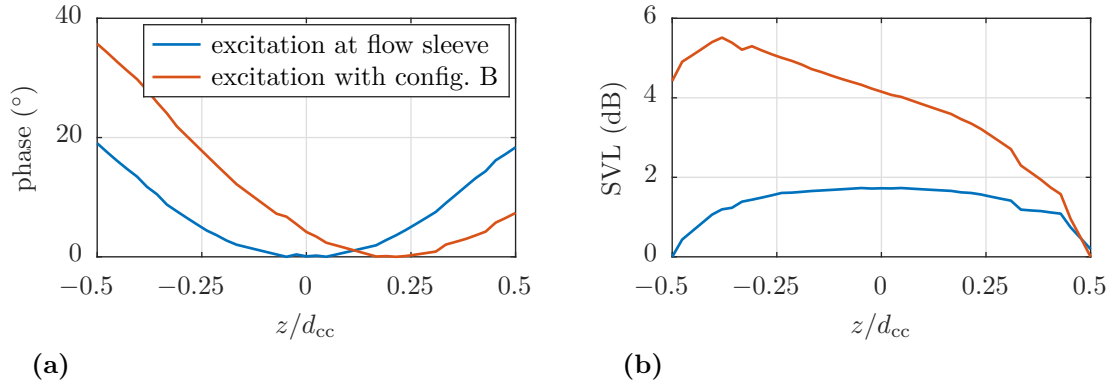


**Figure 6.7.:** Exemplary offset-corrected axial velocity component with excitation at the flow sleeve (blue) and the burner base plate with configuration B (orange) at an excitation frequency of  $f_{\text{exc}} = 340$  Hz. (a) phase of the sound velocity (b) sound velocity level

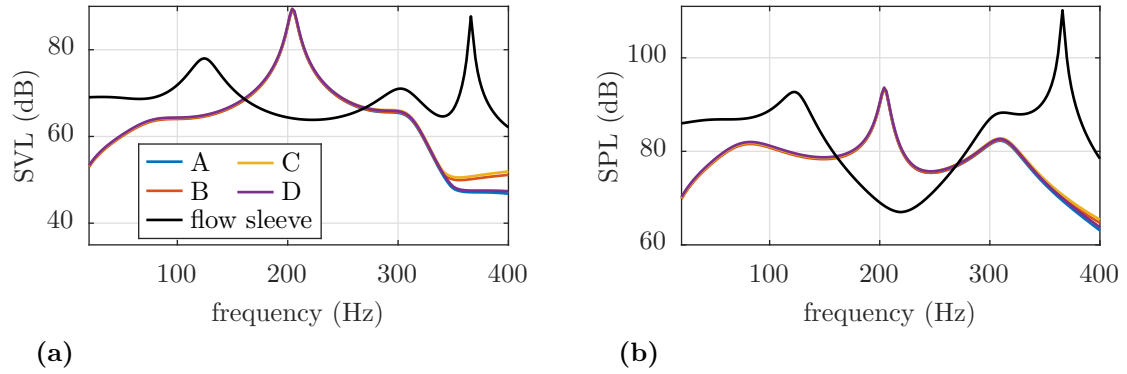


**Figure 6.8.:** (a) Sound velocity level and (b) sound pressure level for excitation at the flow sleeve (black) and at the burner base plate with configurations A (blue), B (orange), C (yellow) and D (purple)

occurring sound velocity field in the combustion chamber. In order to investigate the influence of asymmetry, an exemplary spatial sound velocity distribution is evaluated.

FIG. 6.7 shows the phase and the sound velocity level over the  $z$ -coordinate at  $f_{\text{exc}} = 340$  Hz for simulation of the natural oscillation and an asymmetric base plate excitation (B), each corrected by their individual offsets. For asymmetric excitation, the radial distributions of phase and SVL are asymmetric as well. In the exemplary result shown here, the SVL is  $\approx 5$  dB larger on the side of the excitation location than at the opposite wall. Various data points reveal the same correlation between the phase and SVL of asymmetric velocity distributions. Analogously, symmetric mounting locations result in symmetric distributions and, therefore, low phase deviations from excitation at the flow sleeve.

The maximum SVL and SPL values of the aforementioned configurations were measured in the radial coordinate and plotted over the frequency in FIG. 6.8. The velocity amplitudes of the base plate configurations behave very similarly, up to  $\approx 350$  Hz. The asymmetric excitation locations lead to slightly higher sound velocity levels, with  $\Delta\text{SVL} \approx 3$  dB to 5 dB.

This can be attributed to the asymmetric velocity fields and their locally higher maximum sound velocities. The decline in SVL above 310 Hz, observed in the four configurations, might be a disadvantage in the final execution. However, the issue could be corrected by using, for instance,  $\lambda/4$ -connector tubes. Using suitable resonator tubes, the frequency response can be equalized, as for instance, shown by Bothien [18]. Obvious differences to excitation at the flow sleeve, are the resonance frequencies in the amplitude spectrum. They are due to the boundary condition at the flow sleeve, which is set to a normal velocity in the reference case and a pressure node, otherwise. The overall undulation of the amplitude spectra is in a similar range for the reference case versus the four investigated excitation locations. The right-hand plot in FIG. 6.8 shows the sound pressure level for the same configurations as before. The individual base plate excitation alternatives do not deviate from each other significantly and the SPL decline above 310 Hz is not as pronounced as in the SVL plot. Compared to the simulation of the natural oscillation, the amplitude deviation over the frequency is lower with base plate excitation.

In summary, the first investigation on the optimal siren location shows that with mounting at the burner base plate, symmetric excitation profiles lead to a more even acoustic actuation inside the combustion chamber than an asymmetric setup. Whether a single large tube or two smaller tubes are used, depends on the available space at the burner base plate and on the type of siren that is used. For example, if two sirens are incorporated (cf. SUBSEC. 6.1.1), the setup with two inlets would become easier to implement. Otherwise, a configuration with only one connector would be preferable, as the influence of a Y-piece is unknown. The study, so far, does not include the connector tube(s) of the siren, which is due to a lack of specifications.

### 6.3. Acoustic Simulations with Flow Box

As stated in the introduction of this chapter, locating the upstream actuator at the burner base plate has two main disadvantages. The first being a limited amount of available space at the burner base plate, which houses numerous tubes and cables for cooling, fuel, and sensors. A further disadvantage is that the sensor design proposed in SEC. 4.2 demands an actuator upstream of the flow sleeve, in order to enable the thermoacoustic characterization. Therefore, an alternative upstream actuation location was investigated and is discussed in the following paragraphs.

The domain designed in SEC. 6.2 was supplemented with a generic flow box (cf. FIG. 3.2) that features realistic volume and area proportions. In the test rig, this box forms the plenum upstream of the flow sleeve and downstream of the compressor inlet. It is used to investigate actuator locations upstream of the flow sleeve. A possible position is found at the top right wall of the flow box in FIG. 6.9. Here, a comparably large space allows for the connection of an actuator. In fact the area is large enough to fit a horn-shaped connection, which aids mitigating the impact of the impedance jump at the area discontinuity. Due to more available space and therefore higher flexibility, the optimal connection type shall be investigated. In total, three different exponential horns are compared to a simple tube and a connection with linearly increasing area.

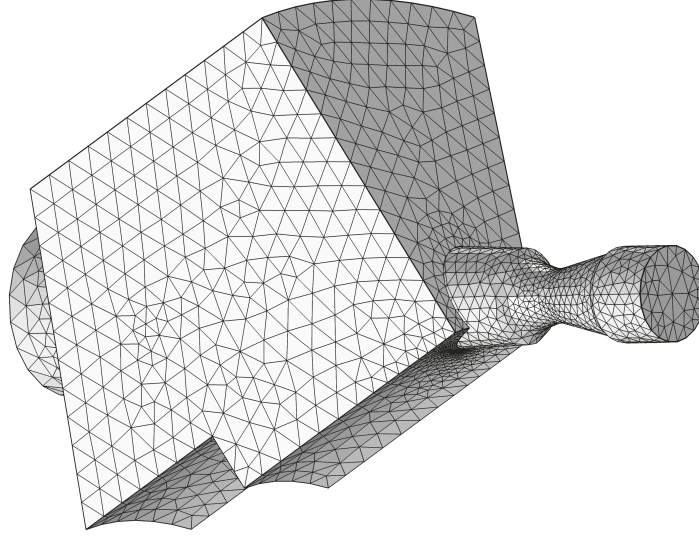


**Figure 6.9.:** Computational domain of flow box, burner passage, combustion chamber and vane simulation section with an unstructured mesh.

In a preliminary step, the exponential horn geometries are designed. According to Hanna & Slepian [65], the cross-sectional area of the horn needs to follow an exponential function of the form

$$A_{\text{mo}} = A_{\text{t}} e^{hL_{\text{h}}} \quad (6.1)$$

$$\Rightarrow h = \frac{\ln\left(\frac{A_{\text{mo}}}{A_{\text{t}}}\right)}{L_{\text{h}}}. \quad (6.2)$$

where  $A_{\text{mo}}$  stands for mouth area, which is the large opening of the horn. The smaller opening, where the acoustic driver is located at, is denoted with  $A_{\text{t}}$  for throat area.  $h$  is the horn constant and  $L_{\text{h}}$  is the horn length. The throat diameter is fixed at  $d_{\text{t}} = 50$  mm, the same as in SEC. 6.2. The lower limit frequency  $f_{\text{lim}}$  of the horn is defined by

$$f_{\text{lim}} = \frac{hc}{4\pi}. \quad (6.3)$$

A defining parameter for the limit frequency is the mouth diameter, which is set to  $d_{\text{mo}} = 500$  mm. This is the maximum value allowed by the flow box geometry. In theory, smaller mouth areas lead to a lower limit frequency, but simulations have shown that the configurations with larger mouth areas actually perform better. Presumably, this is due to a decreased impedance jump at the flow box boundary with a larger mouth.

Furthermore, the limit frequency is highly dependent on the horn length, as becomes obvious when inserting EQ. 6.2 into EQ. 6.3. Consequently,  $L_{\text{h}}$  shall be subject to investigations. The three employed lengths are shown in TAB. 6.2 with their corresponding horn constants as per EQ. 6.2.

horn length $L_h$ (m)	0.5	0.75	1
horn constant $h$ (1/m)	9.2	6.14	4.6

**Table 6.2.:** Horn lengths and the corresponding horn constants

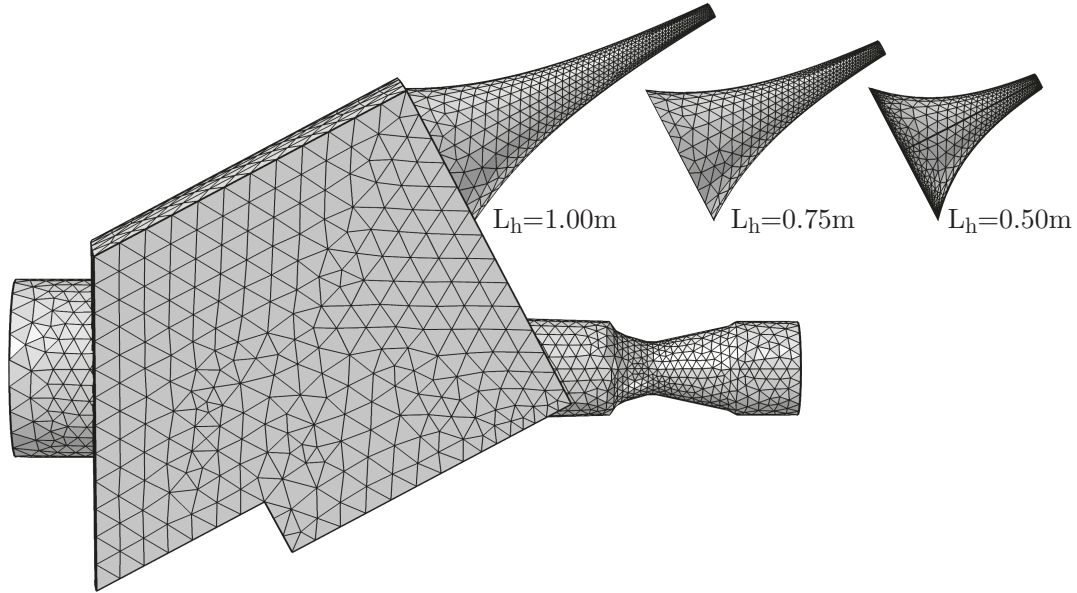


**Figure 6.10.:** Computational domain with flow box and three exponential horns of different lengths

Lower horn constants, i. e., higher horn lengths lead to a lower limit frequency and are therefore preferable in theory. The performance of each configuration shall be investigated by simulating the acoustic behavior when mounted at the flow box wall.

The considered horns are shown in FIG. 6.10, with their connection location indicated by the longest horn, only. The small distance from the upper edge of the horn to the corner of

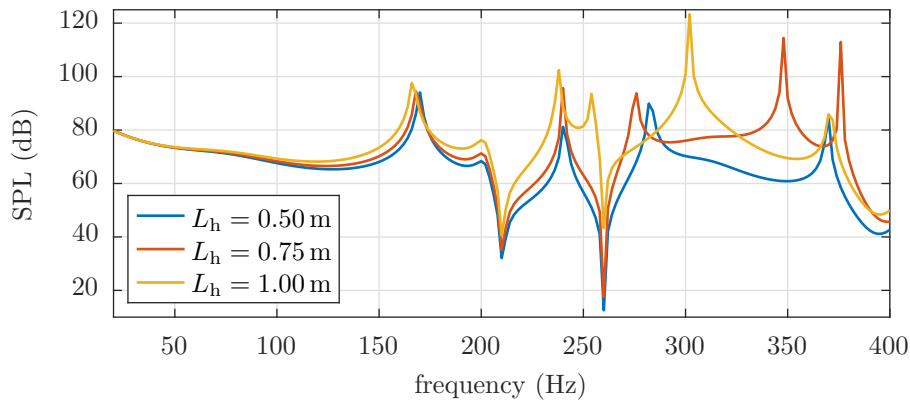


**Figure 6.11.:** Sound pressure level inside the combustion chamber with three horns of different lengths mounted at the flow box, computed with a stationary acoustic simulation

the flow box is deliberately chosen, in order to utilize the upper wall as a horn extension, potentially lowering its limit frequency. The temperature profiles are chosen as in the preceding investigations, with the flow box being set to the constant compressor outlet temperature. Due to the domain's complexity, only stationary acoustic simulations are run with the flow box setup. Consequently, the *Pressure Acoustics* module of COMSOL is used. Boundary conditions are set similarly as in SEC. 6.2. I.e., the domain outlet downstream of the vane simulation section is set to anechoic conditions and at the horn's throat, a normal velocity boundary condition with an amplitude of  $\hat{u} = 0.01$  m/s is employed. The sound pressure level is evaluated at the same location in the combustion chamber as in the preceding sections and it is shown for the aforementioned configurations in FIG. 6.11.

Below 100 Hz the sound pressure level in the combustion chamber is almost independent of the horn length. At higher frequencies, however, there are differences to be observed. While the maxima and minima of the SPL occur at roughly the same frequencies up to 250 Hz, the amplitude increases with horn length in this frequency range. In the whole considered frequency range of 20 Hz to 400 Hz, the mean SPL of the longest horn is  $\approx 8$  dB higher than with the shortest horn and  $\approx 2$  dB above that of the medium-length horn. Further, the minimum at 260 Hz is by far the least distinct with the lengthiest horn.

It can be stated that the longest horn performs best among the configurations considered here. It is able to mitigate the impedance jump and the associated loss in acoustic energy better than the shorter horns, which makes it preferable in this application. A horn-shaped connection requires a comparably high production expenditure. Therefore, two further connection types were simulated in a similar arrangement. Those are a straight tube with  $d = 50$  mm and a length of  $L = 1.0$  m, and a cone of the same length with mouth and throat diameters of  $d_{\text{mo}} = 500$  mm and  $d_t = 50$  mm, respectively.

As depicted in FIG. 6.12, the mounting location has been chosen in a similar way as with the horn configurations, placing the upper edges of the connectors close to the flow box corner. Excitation was realized in a similar manner as before and the results are shown in FIG. 6.13.

The tube connection allows for a higher sound pressure level in the lower and in the higher part of the considered frequency range, when compared to the horn and cone connections. However, from 210 Hz to 260 Hz, the SPL is significantly lower, leading to a strong variance in amplitude depending on the excitation frequency. This issue can usually be addressed by tuning the resonance frequency of the connector tube differently, in order to shift the

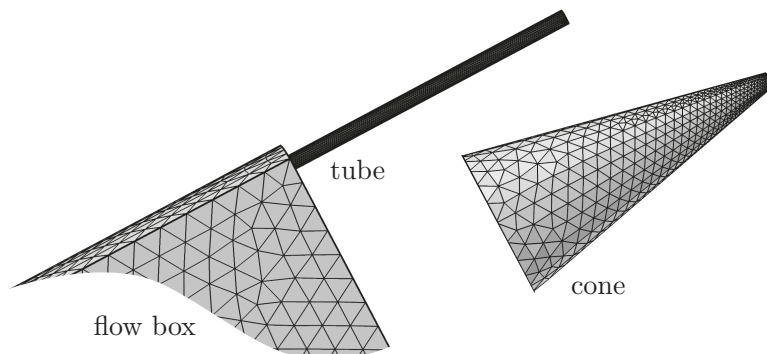


**Figure 6.12.:** Computational domain with flow box (cropped view) and two alternative connection strategies: tube and cone of 1.0 m length, respectively

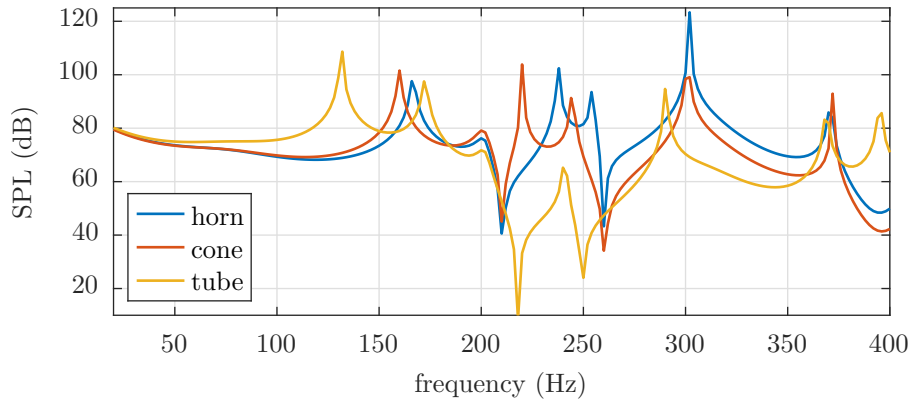


**Figure 6.13.:** Sound pressure level inside the combustion chamber with a horn, a cone and a tube, of the same length ( $L = 1.0$  m), mounted at the flow box. Computed with a stationary acoustic simulation.

extremal values of the SPL spectrum. Shorter tube connections were investigated, yet, did not produce any remarkable advantages in terms of amplitude spectra. Within these studies, the connections were no shorter than the aforementioned 0.5 m. The reason is that the test rig is encased in a large pressure vessel, which prohibits any shorter connectors.

Connecting the actuator with a cone leads to an SPL spectrum quite similar to the horn of the same length. Most of the resonance frequencies are shifted but the amplitudes generally remain in the same range. However, the extremal values at 260 Hz and 302 Hz differ quite strongly, with the cone performing worse than the horn connector. This places the mean SPL of the cone about 2.5 dB below that of the horn. In summary, depending on the available space and the production expenditures, the siren's connection to the flow box should preferably be realized by a horn- or cone-shaped junction. The main reason is the frequency dependent amplitude variance of the tube connector, which performs poorly in the medium frequency range.

#### 6.4. Comparison of Base-Plate- and Flow-Box-Mounted Actuators

In order to compare the two basic mounting locations, the acoustic fields with excitation at the base plate are compared to those with excitation at the flow box. At each location, the best performing configuration is employed. Thus, data acquired with the longest horn configuration ( $L_h = 1.0$  m) represents the flow box mounted actuator. For the base plate excitation, another simulation is conducted using the computational domain shown in FIG. 6.9. In this case, actuation is applied via configuration A (cf. FIG. 6.3a), i.e., one connection in the base plate center. Reasons are its good performance and its direct comparability to excitation at the flow box wall, which is also realized with only one connection. The excitation amplitudes for each of the investigated cases was kept the same in terms of sound energy flux at the boundaries.

In FIG. 6.14 both aforementioned excitation cases are evaluated in terms of the sound pressure level. As reference, data from excitation at the flow sleeve inlet from SEC. 6.2 is displayed in black. It simulates the natural oscillation of the combustor system, however, the flow box was not included in this computation and is approximated with a sound soft

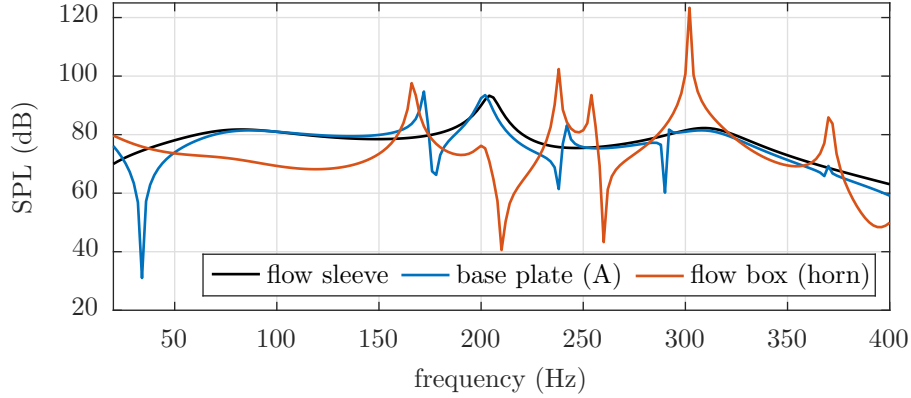


**Figure 6.14.:** Sound pressure level at the evaluation plane inside the combustion chamber with three excitation strategies. Simulation of the natural oscillation of the system is colored in black, excitation with a single inlet at the base plate center in blue and actuation at the mouth of a horn (1.0 m) mounted at the flow box in red.

boundary condition. Comparing the curves for the simulated natural oscillation and the base plate excitation (blue), the results coincide quite well, except for cavity resonances. This indicates that the sound soft boundary condition is a good approximation of the area jump from the flow box to the flow sleeve. Focusing on the relevant frequency range from 50 Hz to 400 Hz, the deviation of the base plate excitation from the natural oscillation is rather small. For excitation at the flow box (orange), this difference is more pronounced, with strong destructive and constructive interferences at e. g., 210 Hz, 260 Hz and 302 Hz. Furthermore, in the lower frequency range from 50 Hz to 150 Hz, flow box excitation yields amplitudes that are approximately 10 dB lower than with base plate excitation.

In order to compare more realistic configurations, the base plate excitation shall be modified by incorporating connector tubes like they would be required in a real application. As the burner base plate is not encased in a pressure vessel like the flow box, the connection lengths can be somewhat shorter than those of the connectors in SEC. 6.3. Computations are carried out with the domain shown in FIG. 6.9, the only difference is the tubes that are attached to face A from FIG. 6.3. The domain boundary condition, where the normal velocity fluctuation is applied, is connected to three tubes with  $d = 50$  mm and lengths of  $L = 0.25$  m, 0.50 m, and 0.75 m. The results of the generated sound pressure level at the evaluation plane in the combustion chamber for the above mentioned connector lengths are shown in FIG. 6.15. For comparison, the SPL for actuation directly at the burner base plate (0.0 m, blue) and for the 1.0 m-horn excitation at the flow box (black) are shown, as well. Below 75 Hz, the spectra generated with the three tube lengths practically match. The  $\lambda/4$ -resonances for the tubes of 0.50 m and 0.75 m lie within the regarded frequency range and generate strong peaks of the sound pressure level. For the shortest tube, the resonance frequency lies at approximately 540 Hz. From 50 Hz to 400 Hz, the differences between minima and maxima for the three configurations is highest for the longest tube and lowest for the shortest tube, which is mainly due to the higher resonance frequency of the shortest configuration. For a smooth amplitude spectrum, the tube length should be  $L < \frac{c}{4f_{\max}}$ . Here,  $f_{\max}$  is the maximum relevant frequency for the investigations. Note that the speed of sound is dependent on the actual temperature

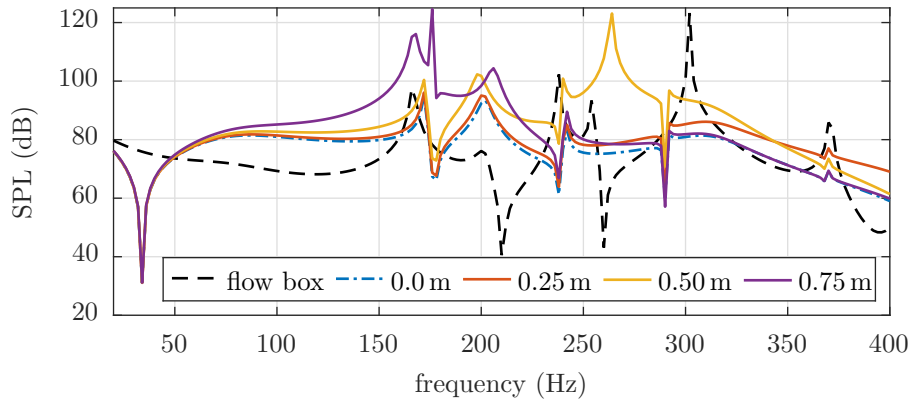


**Figure 6.15.:** Sound pressure level at the evaluation plane inside the combustion chamber with horn excitation at the flow box (black) and base plate excitation with four different connector lengths: 0.0 m (blue), 0.25 m (orange), 0.50 m (yellow), 0.75 m (purple)

inside the connector tube, which depends i. a. on the maximum temperature tolerance of the actuator components.

In summary, it can be stated that excitation at the burner base plate is preferable in terms of deviations between minimal and maximal achievable amplitude. Furthermore, the minima are more pronounced with excitation at the flow sleeve.

## 6.5. Conclusions Drawn from the Upstream Actuator Positioning

In this chapter, possible actuators for the region upstream of the burner in the high pressure test rig were discussed. A siren actuator was found to be the most suitable type of actuator due to its strengths in acoustic amplitude, coverage of the required frequency range, and robustness. Due to its widespread application in academia and industry, and therefore profound experience of the manufacturer, the risk of failures can be minimized. It can be uniquely designed according to the required specifications, making it an optimal choice for the specialized application at hand.

According to the identified locations for the upstream actuator, several connector types were investigated by means of FEM simulations. The two main regions for actuation were the burner base plate, and the flow box wall, as depicted in FIG. 6.3 and FIG. 6.10. Overall, connecting the actuator to the burner base plate delivers the most consistent amplitude response, as the strong reflection at the flow sleeve does not interfere with sound propagation. However, the general mounting location is potentially restricted by the sensor concept, employed upstream of the burner. As stated in SEC. 6.2, the use of a sensor array in the flow sleeve (cf. SEC. 4.2) prohibits mounting of the actuator at the burner base plate. The sensor concept from SEC. 4.3 would allow both mounting locations of the upstream actuator.

Comparing different mounting options at the burner base plate, it was found that an asymmetric arrangement yields skewed velocity fluctuations, which poses a disadvantage. However, the performance difference between one and two symmetric mounting holes of the same total area was rather small. Later it was shown that the connector length has a strong influence on the amplitude spectrum, giving an advantage to short tubes with higher  $\lambda/4$ -resonance frequencies.

Excitation at the flow box was realized using several connector types, of which the longest horn connection performed best. Compared to shorter horns, the minima of the amplitude response were least pronounced. In comparison to a tube and a cone-shaped connection, the horn led to the least difference between the extrema and the weakest amplitude drop at minimal values. Production expenditure versus performance has to be taken into account prior to realization, especially when comparing the horn with the cone connector.

# CHAPTER 7

---

## Development and Verification of the Actuator Concept Downstream of the Burner

---

Development of a suitable downstream actuator concept for the regarded high pressure test rig is a crucial element of this work. The fulfillment of the two main objectives (cf. SEC. 1.8) relies on a viable excitation mechanism downstream of the flame. Especially, the implementation of impedance tuning at the combustion chamber outlet poses diverse demands on the downstream actuator. The same device may be used for the experimental determination of flame transfer matrices. The individual demands for both application cases are outlined in SEC. 3.2 and SEC. 3.4, respectively.

In this chapter, the downstream actuator development is elaborated. Initially, various concepts are discussed. The modulated injection of secondary air into the throat of the vane simulation section emerges as a possible concept. A literature survey on comparable applications is given in SEC. 7.2. Subsequently, numerical investigations are detailed. They aim at gaining information about the achievable amplitude and the mean pressure dependence. The results are used as basis for the experimental investigations presented in the following sections. Several questions are addressed, such as, the estimated amount of required actuators and dependence on operational parameters such as mass flux ratio, momentum flux ratio, and mean temperature. The concept is furthermore extended to an angled injection and compared to a siren-type excitation principle. Finally, the applicability of impedance tuning at the regarded test rig is investigated using a time-domain network model with input data from a CFD simulation.

### 7.1. Discussion of Various Actuator Concepts

Several actuator types have been investigated in order to find a device capable of meeting key requirements such as high amplitudes, coverage of the frequency range of interest, linear behavior in amplitude and phase and robustness in the harsh test rig environment. Loudspeakers are not an option due to a lack of ruggedness and acoustic power density, as was discussed in the beginning of CHAP. 6. In the mentioned chapter, further acoustic actuators, such as a siren, proportional valves, electro-pneumatic, magneto-restrictive, piezo-electric, and electro-dynamic devices were mentioned. However, as no suitable concept emerges from this list, further actuator types were discussed in the course of this work. The evaluated concepts

are shown in TAB. 7.1 with their corresponding main weakness related to applicability as the downstream actuator.

actuator type/concept	main weakness
siren	phase response
proportional valves	amplitude
electro-pneumatic transducer	amplitude linearity
intake/outlet valves (automotive)	frequency range
injector valves (automotive)	amplitude and wave form
fluidic oscillators	phase response
electro-dynamic drivers	robustness and amplitude
magneto-restrictive devices	robustness and amplitude
piezo-electric devices	robustness and amplitude
linear motors	robustness and frequency range
movable parts in the VSS	robustness (temperature)
movable parts in the BPV	safety, reflection at VSS
water injection	time lag for evaporation

**Table 7.1.:** Actuator concepts and their main weakness in the context of eligibility as a downstream acoustic excitation device

The siren’s major disadvantage is its inability to follow the phase of the input signal (cf. CHAP. 6), rendering it unsuitable for impedance tuning. While based on a similar principle of modulating a driving air flow, a proportional valve for gas flow modulation (cf. SUBSEC. 7.4.3) might be considered. Such actuators were successfully employed in high pressure test rigs, e.g. by Hermann & Orthmann [71] and Kapucu et al. [83], showing their robustness in industrial applications. They feature a linear response in terms of amplitude and frequency. Amplitude-linearity describes a linear relation of the actuator output to varying input voltages and air mass flows. Frequency-linearity implies that the generated response is only dependent on the input signal at a certain frequency, i. e., the (sub-) harmonics of the input signal have no influence on the system response [26]. Bothien et al. [18, 22] used proportional valves for application of impedance tuning on an atmospheric combustion test rig, proving their general suitability. However, the maximum achievable actuation amplitude is dependent on the fluctuating mass flow output. In order to achieve the required amplitudes (cf. SEC. 1.8) in an industrial test rig, according to Bothien [18], approximately ten to 20 valves are needed. Note that this estimation is based on the devices being mounted on the combustion chamber wall via (resonance) tubes. This point is discussed further below. Major disadvantages of using large quantities of actuators are scarce availability and cost of acquisition, which is detailed in SUBSEC. 7.4.3. Technical challenges include limitations in the available space, which influences the required length of the connector tubes to the test rig. As impedance tuning is highly dependent on the time lag between input and output signal, connections are required to be as short as possible.

Furthermore, Bothien et al. [26] investigated an electro-pneumatic transducer (or *Ling driver*), which generates a higher mass flow modulation than proportional valves. They found that the lack of amplitude and frequency linearity necessitates the use of an alternative control scheme, which accounts for the non-linearities. A major difference to the previously employed method [21, 22], was the restriction to discrete frequencies. Although a successful employment

of the non-linear actuator was achieved, disadvantages had to be accepted. For instance, tuning to sound hard conditions at any mode can cause a different mode to enter limit-cycle oscillations, therefore impeding a study of the actual mode of interest. For this reason non-linear actuators like electro-pneumatic transducers are not regarded in the development of the downstream actuator for this work.

Similarly to the aforementioned actuator types that generate a modulated air flow, further types of devices with such features were investigated. In the automotive industry, intake and outlet valves are used for gas flow control inside the combustion engine's cylinders. Several high performance devices operating at significant engine speeds, were considered. In modern applications there is no need for mechanical cam shafts, any more, as triggering of the driving rods for opening and closing the valves is done electronically. Thus, wave form and phase of the outgoing signals could be adjusted to the requirements. However, the maximum achievable frequency is highly dependent on the mass of the moving components and the corresponding inertial forces. An initial estimation showed that the relevant frequency range could not be covered with current high performance components.

In the automotive sector further actuator types are used, including injector valves for direct fuel injection into the combustion cylinder. Those components are able to handle high pressures during injection. However, their low maximum mass flow and exclusive square wave output render them unsuitable in the prospect of this work.

So called *fluidic components* were first invented in the late 1950s, in an effort to develop controllable systems without any moving parts. Belsterling [12] gives an early overview about system design with such components. A design that emerged from logic switches was the fluidic oscillator, which was first described by Spyropoulos [169] and subsequently refined by Viets [185]. Basically, a fluidic oscillator incorporates bi-stable flow patterns that are usually governed by the *Coandă* effect, which describes the tendency of a fluid stream to stay attached to an adjacent surface. More recent research expanded possible applications into the field of instability control in gas turbine combustors, as for instance shown by Guyot et al. [62]. Obvious advantages are the omission of any moving parts and a nearly arbitrary oscillation frequency depending on the design. However, the lack of control over the phase makes this actuator type inadequate for the required application. A design with a controllable output, which is basically a fluidic switch, has various other disadvantages. Most prominently, the necessary implementation to achieve a time-harmonic pressure signal in a confined space is intricate. Another critical disadvantage is the direct dependency of the oscillation frequency on the driving mass flow.

Conversely to fluid-injecting actuators, mechanical actuation could be employed. For instance, electro-dynamic drivers such as *shakers* may be used in a similar fashion to loudspeakers, but deliver significantly higher stroke and displacement force. They could be mounted to robust membranes or movable walls to realize acoustic actuation, which is explained further below. However, implementation of such a driver is intricate, as the coil has to be cooled extensively. This is even complicated by the requirement to ventilate the membrane. Ventilation is necessary in order to avoid preloading, which results from the elevated mean pressure inside the test rig. In addition, due to the potentially very low resonance frequency of such an assembly, it becomes challenging to cover the required frequency range.

In analogy to electro-dynamic drivers, magneto-restrictive and piezo-electric devices could be utilized. Their main advantage is a high displacement force, while still covering a large frequency range. One downside is the low deflection amplitude, which to some extent can

be compensated by stacking. Specifically, piezo-ceramics feature slightly higher deflection amplitudes than piezo-crystals, although displacements are still in the sub-millimeter range. In turn, crystals are more tolerant to high temperatures due to their higher Curie-temperature (the temperature at which piezo-electric devices lose their polarization) of up to approximately 1200 K. However, for piezo-ceramics and magneto-restrictive devices, the main disadvantage remains the low temperature tolerance. Another drawback is that the displacement of magneto-restrictive and piezo-electric devices is pressure-dependent.

The three aforementioned actuator types, i. e., electro-dynamic, magneto-restrictive, and piezo-electric drivers, require special mounting concepts for their implementation inside the high pressure test rig. One such concept consists of the driver and membrane being mounted inside a cabinet, much like the loudspeaker housings used in atmospheric test rigs. However, in such an assembly, complex modifications to the test rig are required and various issues concerning available space, cooling and back-ventilation have to be solved. The complexity for the implementation of such a system is high and likewise there is a significant probability of failure. In summary, the advantages over using conventional loudspeakers is not sufficient to justify the additional development expenditure.

Another group of concepts involves oscillating parts being mounted directly into the exhaust section of the test rig. For instance, in the works of Hochgreb et al. [75] and Macquisten et al. [102], a siren-type actuator was used at the throat of the combustion chamber outlet of a high pressure test rig. A scalloped rotor blocks the smallest cross-section of the choked outlet in a harmonic way, thereby generating high amplitude pressure fluctuations inside the test rig. The specific concept may not be used for an active control of the acoustic boundary condition, due to the inability to follow the phase of the input signal. Yet, the mechanical manipulation of the downstream boundary may be adapted to fulfill the requirements at hand. For example, parts in the vane simulation section could be outfitted with suitable mechanical actuators in order to generate an oscillating blockage ratio of the vanes. The idea is depicted in FIG. 7.1, where blue dotted lines indicate the areas that could be actuated. Fluctuation of the smallest cross-sectional area introduces sound pressure variations, both upstream and downstream of the restriction due to modulations imposed on the flow velocity. Located inside a nozzle throat, mechanical actuation has a comparably high influence on sound generation. However, as the VSS is in sub-critical conditions at most operational points, prediction of the resulting amplitude is difficult. Preliminary calculations showed that the deflection amplitudes of both magneto-restrictive and piezo-electric devices are not sufficient, even with extensive stacking

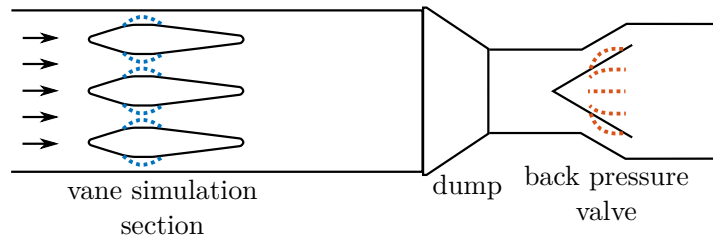


**Figure 7.1.:** Schematic of the high pressure test rig's exhaust section in top view. The combustion chamber is located upstream of the VSS. Downstream, the dump and back pressure valve are connected. Possible actuation locations are highlighted blue (vane simulation section) and orange (back pressure valve).

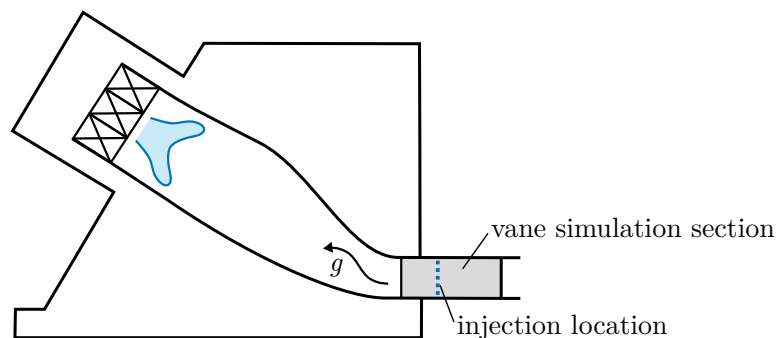
or the use of levers. As previously stated, installation of mechanical actuators into the exhaust section remains problematic due to their lack of robustness against high temperatures.

FIG. 7.1 further depicts the second proposed location with a high contraction, which is found in the back pressure valve of the test rig. It is choked in operation, thus cross-sectional area fluctuations at this location have an even higher and also more predictable influence on sound generation. However, besides the aforementioned temperature concerns even more restrictive disadvantages arise from safety concerns, which complicate modifications of related components. Furthermore, the upstream located vane simulation section is responsible for strong reflections, thus attenuating the possible acoustic amplitude inside the combustion chamber.

Another option to drive movable parts (e. g., in the VSS) is a linear motor. In principle, such devices are capable of any wave form and feature high deflection amplitudes. However, inertial forces are responsible for a trade-off between displacement and covered frequency range, which was the reason that none of the reviewed devices could fulfill the posed requirements.

An exotic way of generating acoustic pressure fluctuations is injecting liquids into the exhaust section of the test rig. Water injection could benefit from a relatively low injector volume flow, which generate a comparatively high pressure fluctuation due to evaporation. However, preliminary calculations showed that the thermal power of the test rig at the relevant operating conditions does not suffice to evaporate an adequate amount of water. Alternatively, injection of a liquid propellant could be considered. In the 1970s, injection of exothermal fluids into the divergent parts of rocket nozzles was studied, as presented in references [192, 194]. This specific application for the generation of acoustic fluctuations was investigated by Bothien [18], who used an oil combustor, driven by a proportional valve. However, due to intricate handling and unreliable operation, this concept was not followed any further.

As previously mentioned, mounting an actuator inside a restriction or nozzle throat increases its efficiency. Thus, a modulated fluid injection into the smallest cross-section of the vane simulation section is regarded a promising approach. Employment of proportional valves for gas flow modulation is proposed, as they feature a linear response in terms of amplitude and frequency, which has been shown in a comprehensive way by Bothien et al. [18, 22]. If the efficiency in terms of amplitude can be sufficiently increased by mounting inside the smallest cross-section of the VSS, a suitable actuator concept might be found.



**Figure 7.2.:** General principle of the downstream actuator. In the vane simulation section, fluid is injected in a modulated way in order to block the smallest cross-sectional area and thus introduce a pressure fluctuation in the combustion chamber upstream of the VSS.

The idea is depicted in FIG. 7.2, where the dotted blue line represents the injector location. The aim is an oscillatory blockage, which in return modulates the throat velocity and generates high amplitude acoustic fluctuations upstream and downstream of the throat.

An additional advantage of the actuation location inside the vane simulation section is its distance from the sensor array, which needs to be located inside the combustion chamber. As discussed in SEC. 2.4, the time lag between determination of the downstream propagating sound waves and incidence of the actuator's response at the sensor array is crucial for impedance tuning to function. Thus, a location as far downstream as possible is desired. However, downstream of the VSS is not expected to be a suitable region, as upstream propagating waves would be reflected by the sudden cross-sectional variation.

## 7.2. Fluid Injection into Nozzles in the Literature

The concept of injecting fluid into a restriction was already applied several decades ago in thrust modulation for the convergent-divergent nozzles of rocket engines. For instance, Gunter and Fahrenholz [59] used steady air injection into the throat of a fixed-geometry supersonic exhaust nozzle in order to control the effective throat area. Thereby, the operating conditions inside the laval nozzle could be altered, thus enabling thrust control of the engine without moving parts. Baruzzini et al. [9] extended the concept to pulsed injection at various incidence angles, axial locations, duty cycles, and injector Strouhal numbers, the latter of which is defined as:

$$Sr_s = \frac{f d_s}{\bar{u}_s}. \quad (7.1)$$

Using numerical methods, they compared the achievable blockage of steady and pulsed injection at the throat. Baruzzini et al. [9] reported that at very low values of  $Sr_s$ , the main flow through the nozzle was subject to severe fluctuations. At high Strouhal numbers, fluctuations vanished, as the time-invariant solution was approached. Lately, numerical simulations have been conducted in order to find optimizations to fluidic injection for area control used in fixed-geometry nozzles for throttling [4, 186]. Note that these studies focus on a choked laval nozzle and supersonic injector velocities. These conditions are not expected in the test rig application of this work and the results might not be comparable.

Another application of injection into nozzles is thrust vectoring. In modern fighter aircraft or rockets, mechanical thrust vectoring is being phased out in favor of various types of bleed air injection into the exhaust nozzles. Mason and Crowther [106] give an overview of subsonic and supersonic thrust vectoring techniques. Considering injecting methods, subsonic control is represented by skewing with the *co-flow technique*, which relies on the *Coandă* effect. In order to attach the exhaust jet to one side of the nozzle, a fluid stream is injected at the corresponding wall in exhaust flow direction. More related to the injection scheme of this thesis, however, are methods for supersonic thrust vectoring, such as *Shock Thrust Vector Control* and *Fluidic Throat Skewing*. Main aim of the methods is to increase control efficiency (deflection angle per injected mass flow) and achieve low thrust loss. The foundation for these

fields of research were laid by research groups investigating jets in crossflow. An extensive amount of literature can be found on this topic. However, usually, the momentum flux ratio

$$J = \frac{\bar{\rho}_s \bar{u}_s^2}{\bar{\rho}_m \bar{u}_m^2}, \quad (7.2)$$

is quite high in these works.  $J$  relates the momentum of the injector jet (index  $(\cdot)_s$  for source) to that of the main air stream (index  $(\cdot)_m$  for main). This is mostly due to low main air Mach numbers. Holdeman & Walker [76] used acoustically excited jets in a confined crossflow to enhance dilution mixing in gas turbine burners. They found that the momentum flux ratio is the most important factor for jet penetration and mixing. Yet, the density ratio of main and injector air did not significantly influence their results. Further, they found that a large number of actuator holes with the same total injector area decreases penetration depth and at the same time increases blockage of the main stream. Vermeulen et al. conducted experimental investigations of acoustically excited air jets in cold [182] and hot [183] confined crossflows. Momentum flux ratios were in the range of  $J \approx 3$  and Strouhal numbers  $Sr_s \approx 0.2$  to  $0.3$ . With pulsating jets they also found that entrainment and mixing was strongly increased versus steady injection. At the investigated high momentum flux ratios they further observed a strong dependence of Strouhal number and the penetration depth, which was at its maximum at  $Sr_s = 0.3$ . Later, Miller et al. [110] from Lockheed Martin invented a concept of *fluidic throat skewing* for exhaust laval nozzles of fighter airplanes. The nozzle throat is either symmetrically actuated in order to achieve area control for throttling or asymmetrically for subsonic thrust skewing. The latter is complemented by an injection at the divergent nozzle's exit flap, which adds the effects of *shock vector control* to subsonic skewing, thereby increasing efficiency. They observed an increased main air jet deflection efficiency at a lower loss in nozzle discharge coefficient

$$C_d = \frac{\bar{m}}{\bar{m}_{\text{ideal}}} = \frac{\bar{m}}{A_t \sqrt{2\rho \Delta p}} \quad (7.3)$$

which is a measure of blockage. The authors worked together with Vermeulen's research group, for instance, conducting numerical simulations [13] of steady and pulsating jets in crossflow in a duct with constant cross-section. High momentum flux ratios of  $J \approx 3.7$  were considered in this work. They further extended the *fluidic throat skewing* concept to incorporate pulsed injection [111]. The nozzle in this study featured a pressure ratio of 2.0 and a low contraction ratio of  $\approx 2.22 : 1$  with a subsequent opening of 1:1.1. The authors found that blockage is a weak function of pulsation frequency, however, the opposite is true for penetration depth. Furthermore, at mean injection Mach numbers  $M_{\text{inj}} > 0.5$ , the pulsed injection delivers higher blockage than steady injection. This result suggests that momentum flux is the driving mechanism for blockage. In addition, an increasing injector Mach number strongly increases the penetration depth, but has little influence on blockage, which they account to vortex entrainment effects. They further confirmed the result of Holdeman and Walker [76], regarding the above-mentioned relation between the number of holes and blockage. With an angled injection of  $45^\circ$  towards the incoming mean air stream the authors observed maximum blockage and jet penetration. They accounted this to a reduction of vortex ring entrainment.

The concept of fluidic thrust vectoring was developed further by NASA researchers. Deere [42] presented the *dual throat nozzle*, which features an additional cavity. The first throat is used for fluidic actuation, while the cavity aids the main air jet deflection by harnessing the feedback due to formation of characteristic vortices. An injector angle of  $45^\circ$  became standard, lowering the required injector mass flow at the same jet deflection. Deere [43] et al. later investigated pulsed injection in order to decrease the required secondary mass flow, which yielded no significant advantage for the dual throat nozzle concept. Several numerical investigations [48, 56, 165] seeking to optimize thrust vectoring were conducted in the following years. Injector mass flows in the range of 10% of the main air mass flow were found to be sufficient. However, due to the high nozzle pressure ratios, a direct comparison to this thesis might not be justified.

In summary, the concept of fluid injection into a nozzle throat has been a prominent research topic. However, the specific operational parameters expected in this work have not yet been examined. Therefore, initial investigations with numerical methods were conducted, which are described in the following section.

### 7.3. Numerical Simulations of the Actuator Concept

One of the first key questions in the actuator design was whether the described concept is able to provide an excitation of sufficient amplitude, when implemented in the high pressure test rig. The reason is that impedance tuning at the combustion chamber outlet requires a minimum amplitude of the upstream propagating wave  $g$ , which was elaborated in SEC. 3.4. An answer to this question was found by Hanraths [66], who conducted a CFD simulation during his master thesis. Additionally, several other characteristics of a modulated air injection into the throat of the VSS were studied. This included the dependence on mean pressure and temperature, as well as a variation of the injector location. The numerical simulation's setup is described in SUBSEC. 7.3.1 and results of the mentioned investigations are summarized in SUBSEC. 7.3.2.

In SUBSEC. 7.3.3, the frame of these simulations was used to efficiently compute input parameters for setup of the 1D time-domain network model for investigation of impedance tuning on the high pressure test rig in SEC. 7.6.

#### 7.3.1. Numerical Setup of the Simulations for the Actuator Concept

The CFD simulation was implemented using the *sonicFoam* solver, which is capable of compressible, transient, and transsonic computations. It is included in the C++-based CFD software suite *OpenFOAM*, which is documented in the user guide authored by Greenshields [54]. The solver employs a finite volume method to solve the Euler equations, i. e., neglecting diffusive and turbulent effects. An implicit Euler algorithm solves for the total pressure, temperature and velocity fields. Under the assumption that only planar waves are able to propagate inside the constant area ducts, the Multi-Microphone Method (cf. SEC. 2.2) was applied to axially distributed probe readings. The implementation of the Multi-Microphone Method needed to be adapted to the available data sets collected from the computation, i. a. by filtering with a Hann-window and zero padding [66].

The employed CFD setup was initially validated using several test cases, which are found in the work of Hanraths [66]. Among others, the atmospheric experiment described in SEC. 7.4

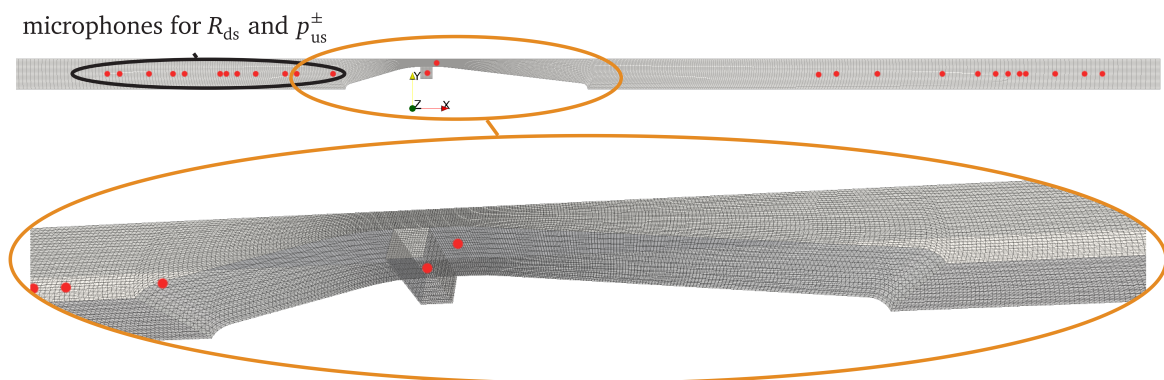


**Figure 7.3.:** Computational domain with employed structured mesh for the numerical investigation of the periodic injection into the vane simulation section. Red dots indicate probe locations. Image courtesy of Hanraths [66]

was used as reference. The results of the simulations showed good accordance with the respective validation cases.

Subsequently, a domain resembling the high pressure test rig geometry was created and realistic operational parameters were implemented. The domain is depicted in FIG. 7.3.

The segments upstream and downstream of the vane simulation section are replaced by constant cross-sectional area ducts in order to apply the Multi-Microphone Method. A lengthy downstream duct was included to simulate numerical dissipation, mitigating the influence of flow phenomena like vortices interacting with the non-reflective boundary condition. Making use of symmetry, the VSS is resembled by only one half of a vane. Secondary air injection is by default realized at the bottom face of the patch added to the restriction's throat using the *oscillatingFixedValue* boundary condition provided by *OpenFOAM*. The main air inlet and outlet are represented by non-reflective boundary conditions, while the VSS itself uses the *fixedValue* boundary condition in order to generate an (adiabatic) no-slip wall. All other boundaries are slip walls due to symmetry.

	$\bar{p}_{\text{out}}$	$\bar{u}_m$ (m/s)	$\bar{T}_{\text{m.norm}}$	$\bar{u}_s$ (m/s)	$\hat{u}_s$ (m/s)	$\bar{T}_s$ (K)	$f_{\text{exc}}$ (Hz)
<b>I</b>	3 levels	110.0	.882..1	5.0	1.0	723	300
<b>II</b>	engine	[34, 110]	1	(location	altered)	723	300

**Table 7.2.:** Excerpt of the flow and excitation parameters for the numerical investigations.

TAB. 7.2 gives an overview of the key parameters of the two investigations (denoted **I** and **II**) that are summarized here. Further studies were conducted throughout the work of Hanraths [66], yet, only the most relevant for this work are adopted here. In FIG. 7.3, the main air mass flow  $\bar{m}_m$  is oriented from left to right and consists of air at temperature  $\bar{T}_{\text{m.norm}}$  (normalized), and a mean velocity of  $\bar{u}_m$ . The mean pressure  $\bar{p}_{\text{out}}$  is fixed at the outlet on the right-hand side domain boundary. Secondary air injection consists of a mean mass flow (represented by  $\bar{u}_s$ ) and a superimposed harmonic component ( $\hat{u}_s$ ). The excitation frequency is fixed to a value of  $f = 300$  Hz.

### 7.3.2. Results of the CFD Simulations on the Actuator Concept

The first investigation discussed here primarily aimed at finding the required actuation intensity at standard operating conditions to achieve the prescribed amplitude of the upstream propagating wave  $\hat{g}$ . Secondary objectives were the dependence on mean pressure and exhaust gas temperature. Accordingly, the operational parameters from row **I** in TAB. 7.2 are employed. Thus, three mean pressure levels were investigated alongside exhaust gas temperature variations within a range of practical relevance. The resulting amplitudes of  $\hat{g}$  are presented in FIG. 7.4. Due to normalization by the mean pressure, all three graphs approximately collapse. Thus, a linear dependence of the  $|\hat{g}|$  to mean pressure or the mean density in the test rig can be deduced. Furthermore, there is no apparent temperature dependence for any of the pressure levels. Standard deviations in the amplitudes of each curve range from 3.3% to 5.5%. These observations can be substantiated with the mass source term of EQ. 2.18. It may be linearized as follows:

$$\frac{\bar{c}^2}{\gamma} \frac{\partial m}{\partial t} = \frac{\bar{c}^2}{\gamma} \left[ A\bar{u} \frac{\partial \rho'}{\partial t} + A\bar{p} \frac{\partial u'}{\partial t} \right]_s = A_s \left[ R_g T \bar{u} \frac{\partial \rho'}{\partial t} + \bar{p} \frac{\partial u'}{\partial t} \right]_s. \quad (7.4)$$

Contributors to the source term are two expressions, which include the fluctuating density and velocity, respectively. The first expression is further dependent on the temperature and mean velocity of the injected fluid, which are both kept constant in the obtained simulations. The second is additionally dependent on the mean pressure, which is the reason for the aforementioned scaling of the pressure amplitude.

Note that the targeted sound pressure amplitude was achieved with the operational values as mentioned above. With the determined value of the injection velocity, the required fluctuating mass flow through the actuator valves can be calculated, which is detailed in SUBSEC. 7.5.2.

The operational parameters of the second investigation are presented in row **II** in TAB. 7.2. With this study, the underlying principle of the sound generation shall be investigated. Therefore, the main air inlet velocity was varied ( $\bar{u} = [34, 110]$ m/s), which resulted in throat Mach numbers of  $M \approx [0.15, 0.59]$ . Furthermore, the injection location along the vane was altered, as indicated in FIG. 7.5. Note that with each configuration, only one of the injector channels was actually implemented in the computational domain. In the default configuration,

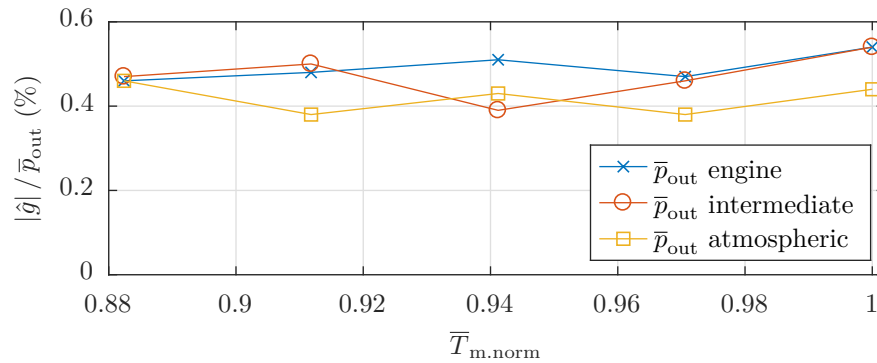


**Figure 7.4.:** Amplitudes of the upstream propagating wave  $\hat{g}$  normalized by the mean pressure. Results obtained at three different mean pressure levels ( $\times$  - engine pressure,  $\circ$  - intermediate pressure,  $\square$  - atmospheric pressure) and at five exhaust gas temperatures, respectively.

air is injected at the smallest cross-section, which is located at  $x/L_{\text{vane}} = 0.33$ . The other two injection locations are distributed upstream along the contraction at  $x/L_{\text{vane}} = 0.05$  and  $x/L_{\text{vane}} = 0.14$ , i. e., close to the leading edge and approximately in the center of the nozzle inlet. The result of investigation **II** is depicted in FIG. 7.6, with  $|\hat{g}|$  being normalized by the maximum amplitude of the data set. At the lower throat Mach number ( $\times$ ), injection of modulated air at the three locations does not yield any significant amplitude differences. The magnitude of  $\hat{g}$  is always in the range of 16% to 19% of the maximum value. This hints at the sound generation at low nozzle Mach numbers being mainly due to a volume source (EQ. 7.3.2). With a higher throat Mach number, however, the blowing location has a strong influence on the sound generation. Injection close to the leading edge results in an amplitude of  $\approx 35\%$  of the maximum value. With injection at the center of the nozzle inlet, the amplitude drops to about 17%, while throat excitation at the higher Mach number yields by far the largest amplitude value of the six configurations. In order to gain insight into the reason for this strong performance, the velocity streamlines with superimposed static pressure for all three cases at the higher throat Mach numbers are shown in FIG. 7.7. The bottom configuration, representing throat injection, displays large regions of vortex shedding along the diverging part of the nozzle. Connected to these vortices are periodic pressure minima traveling downstream. This is in contrast to injection at the upstream locations, where periodic vortex shedding does not seem to play a major role. Further, the upstream pressure is largely increased due to direct injection into the throat, which again is different from the other two configurations. This hints at an increased blockage with injection directly into the smallest cross-section. According to Hanraths [66], the significant increase in sound generation is most likely due to the hydrodynamic fluctuations interacting with the upstream pressure field. This induces high amplitude acoustic pressure (and velocity) fluctuations, which is in accordance with Lighthill's theory introduced in SUBSEC. 2.1.1.

### 7.3.3. Combined RANS and LEE Simulations for Development of a Time-Domain Network Model

On the basis of the CFD setup detailed in the preceding subsections, another numerical investigation of the downstream actuator was conducted. The primary motivation for this study was to obtain data for the development of the 1D time-domain network model for impedance tuning in SEC. 7.6. At this point it is important to note that the simulation does not need to fulfill the requirement of giving an accurate prediction of the actuator's amplitude, which was done in SUBSEC. 7.3.2. Instead, the simulations were used to investigate the time delays present in the high pressure test rig. In order to implement the network model for simulation of the impedance tuning concept, the corresponding phase relations for the two main input parameters, i. e., the open-loop downstream acoustic reflection coefficient  $R_{\text{ol}}$  and

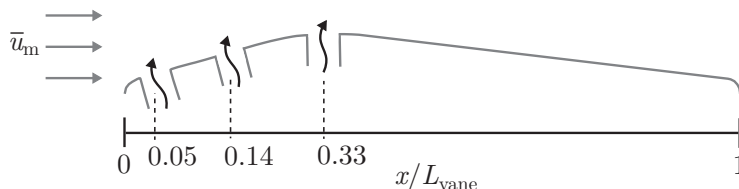


**Figure 7.5.:** Locations for secondary air injection at the vane simulation section normalized by vane length  $L_{\text{vane}}$ .

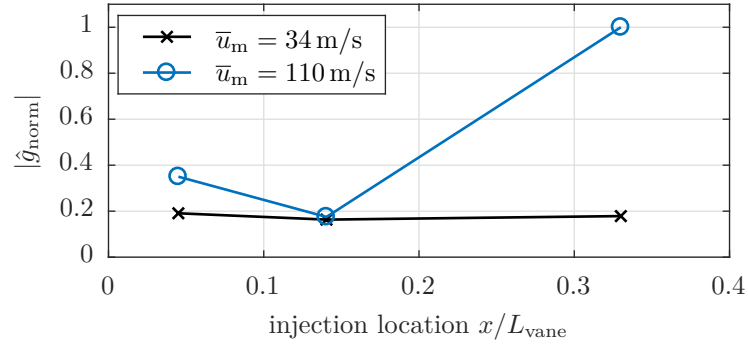


**Figure 7.6.:** Normalized amplitudes of the upstream propagating wave  $\hat{g}$  for three different injection locations along the vane and two different main air velocities, respectively.

the actuator transfer function  $G$ , need to be determined. As detailed in SEC. 2.4,  $R_{ol}$  and  $G$  are used to calculate the control law  $K$ , which is responsible for the actuator’s response to the downstream traveling wave  $f$ . The phase information in  $K$  gives insight into the causality of the controller, i. e., whether the active control loop receives the required input in time before it needs to send the output signal – which is the key question to be answered in SEC. 7.6.

Initially, a multitude of parameters were studied. However, only the results for the final operational parameters are shown here. Note that with the utilized parameter space, the full CFD simulation from SUBSEC. 7.3.1 would be highly cost- and time-consuming. However, as the focus does not lie on the amplitudes, but on the time delays, the simulations were simplified. As a result, the steady-state flow field was calculated using a 2D-RANS simulation set up in *sonicFoam* with the  $k-\omega$  turbulence model. The boundary conditions were similar to those in SUBSEC. 7.3.1, except for the slip-walls (symmetry). In this study they were set to adiabatic no-slip walls with functions for a turbulence model in the shear layer. The

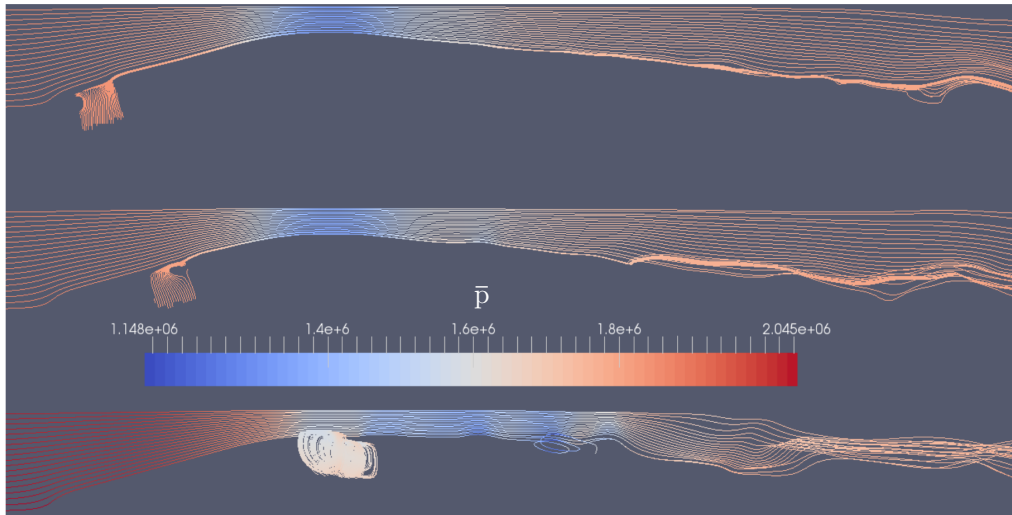


**Figure 7.7.:** Velocity streamlines superimposed with static pressure (colormap) around the vane for the three different injection locations as introduced in FIG. 7.5 at a nozzle Mach number of  $M \approx 0.59$ . Image courtesy of Hanraths [66].

unstructured mesh featured 32 000 hexahedrons, refined at the injector location, as depicted in FIG. 7.8.

Using the steady-state velocity and pressure fields, a 2D linearized Euler equation (LEE) model neglecting entropy fluctuations was set up. The *Weak Form PDE* module [39] in COMSOL Multiphysics was configured to incorporate the steady-state flow field into the acoustics mesh of 40 000 linear triangular elements by interpolation. Spatial discretization is implemented using the FEM Galerkin method, which was stabilized using the *Galerkin Least-Squares* method.

Acoustic boundary conditions, with some exceptions, were set in compliance with the previous simulations. In order to determine the open loop reflection coefficient, sound hard walls, a non-reflecting outlet and an imposed pressure fluctuation at the domain inlet were set. By means of a Multi-Microphone Method, the downstream and upstream propagating waves  $f$  and  $g$  were determined at the domain inlet, the ratio of which is the open-loop reflection coefficient  $R_{ol}$ . For obtaining the actuator transfer function  $G$ , a non-reflecting inlet and acoustic excitation in the VSS channel via an imposed particle velocity were set. Thereby, the transfer function from the excitation signal to the upstream traveling wave at the domain inlet was obtained. As the non-reflecting boundary conditions in the implemented LEE simulation do not usually work infallibly, the upstream traveling wave  $g$  was corrected by the reflected wave  $R_{ol}f$ , as expressed in EQ. 2.45.

In order to test the control-loop scheme under more realistic conditions, further alterations to the boundary conditions were introduced. Firstly, the acoustic boundary condition at the domain outlet was set to full reflection, by implementing a velocity node ( $R = 1$ ). This simulates the sound hard property of the back pressure valve in the actual test rig. In SUBSEC. 7.3.1, the inlet for the secondary air mass flow for actuation was set to a short length to reduce additional complexity, for instance, related to large vortical structures in the injection channel. However, in this simulation, realistic time delays between injection and response in the combustion chamber were sought. Therefore, the short injector used in the

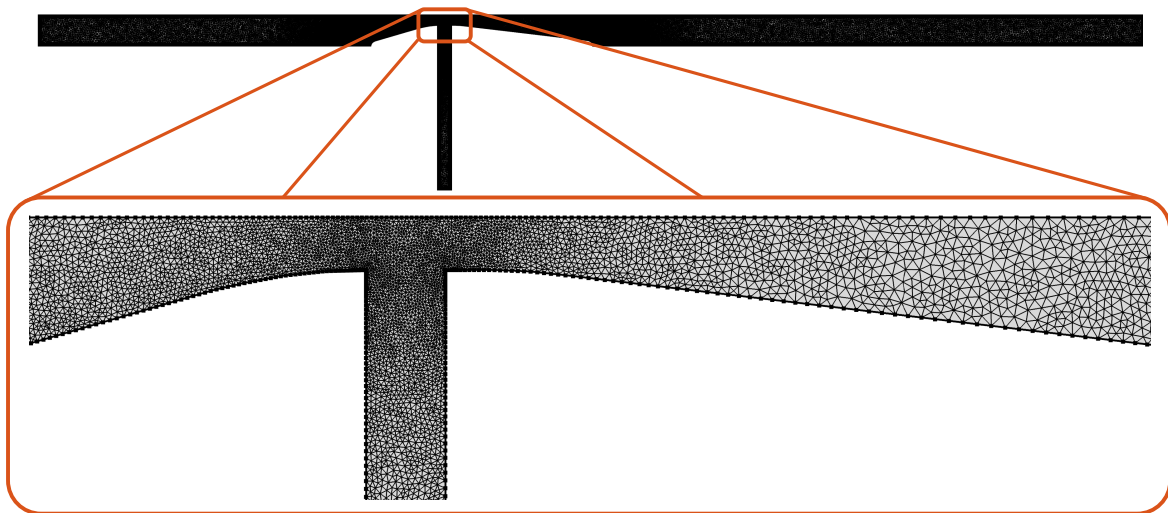


**Figure 7.8.:** Mesh for the acoustics simulations conducted with COMSOL. Top: total view, bottom: detailed view of the refinement at the (long) injector.

preceding simulation ( $L_{inj} = 0.02$  m) was replaced by a longer one. As a realistic estimate of the actual length of the connector channel from the proportional valve to the inlet at the vane simulation section in the high pressure test rig, a length of  $L_{inj} = 0.3$  m was chosen. An

$\bar{p}_{out}, \bar{T}_m, \bar{u}_s, \hat{u}_s, \bar{T}_s$	$\bar{u}_m$	$f_{exc}$	$L_{inj}$	outlet BC
see TAB. 7.2	100 m/s	0 Hz to 800 Hz	0.3 m	$R = 1$

**Table 7.3.:** Parameters used in the combined CFD and LEE simulation for development of the time domain network model (SEC. 7.6).

overview of the parameters that differ from the default case in TAB. 7.2 is given in TAB. 7.3. Results of this simulation are shown in FIG. 7.9.

The obtained  $R_{ol}$  is initially used for calculation of the actuator transfer function  $G$ , which is displayed in the same plot. Subsequently, both are used for the time-domain network model in SEC. 7.6.

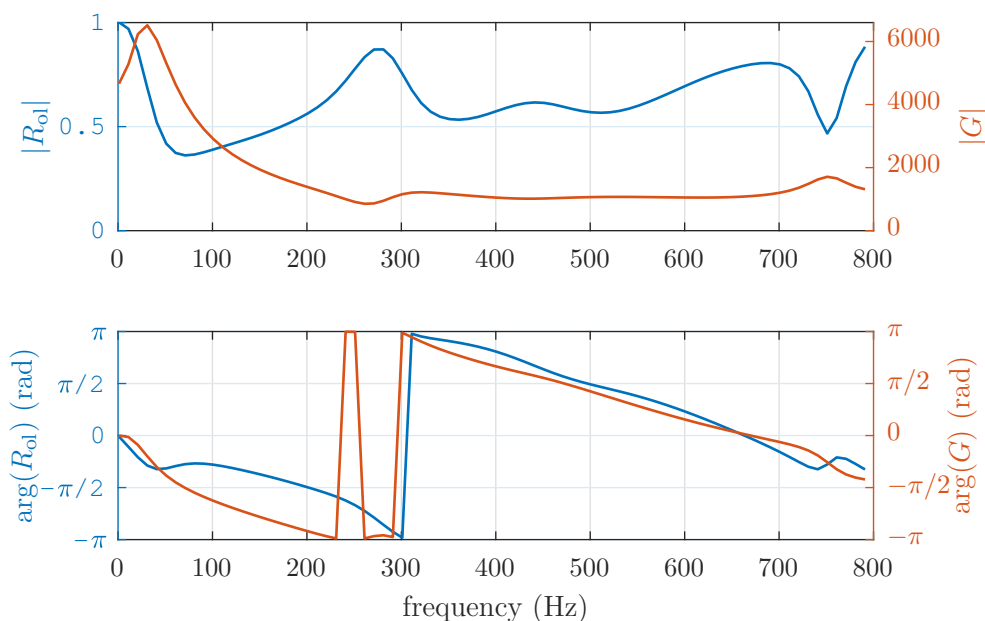


**Figure 7.9.:** Absolute values and phase of the open-loop reflection coefficient  $R_{ol}$  for a long injector, active main flow and full reflection at the outlet boundary. Determined by a combined CFD and LEE approach. Top: magnitude, bottom: phase between excitation signal and pressure at the reference plane.

## 7.4. Experimental Setup for Atmospheric Experiments

After the concept of air injection into a subsonic nozzle for an effective upstream generation of sound was investigated with numerical simulations, some of the concept's aspects were characterized experimentally. To that end, an atmospheric test rig with a generic nozzle for fluid injection was designed, which is detailed later in this section. Proportional valves of two types, specifically designed for air flow modulation (cf. SUBSEC. 7.4.3) were used for excitation of the secondary air flow. Initially, characteristics of the valves were investigated, for instance, yielding an estimated amount of devices necessary for the implementation of the concept on the regarded high pressure test rig. Subsequently, the injector concept itself was examined in terms of multiple parameter variations. Those included dependence on excitation frequency, variable main air mass flows, injector mass flows, and temperature ratios. Furthermore, the injection angle was varied, as proposed in the literature [9, 43, 111], and the concept was compared to mechanical excitation with a siren-type actuator.

Some of the results and explanations in the following sections were already published in reference [124]. Attention has been paid that no co-authors are quoted without explicit labeling as such.

Several hardware configurations were implemented. The basic setup for non-reacting (or cold) acoustic measurements is depicted in FIG. 7.10. For instance, the setup was used to validate CFD simulations, which was mentioned in SUBSEC. 7.3.1. Furthermore, it was used for the measurements that are detailed in SUBSEC. 7.5.2 and SUBSEC. 7.5.3. On the left hand side, air at a maximum pressure of 10 bar is fed into the system. The main air is homogenized by multiple meshes. An 18" low-frequency loudspeaker driver (woofer) from *B&C Speakers*, driven by a *Behringer EP2500* (500 W @ 8 $\Omega$ ) amplifier, is mounted perpendicularly to the main duct. Downstream of the T-piece, the measurement duct is located. Along this duct, provisions for cooled and flush-mounted microphones are found. In the cold tests, flush-mounted holders were used due to easier handling. These sensors are employed for the Multi-Microphone Method. An absolute pressure sensor is mounted at the axial location of the downstream microphone. The termination of the test rig consists of a generic cone-shaped nozzle featuring a contraction

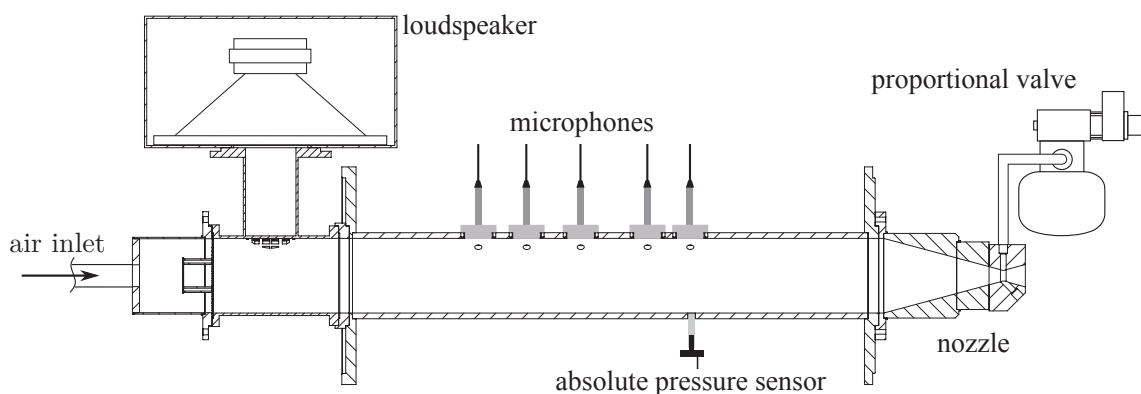


**Figure 7.10.:** Experimental setup for preliminary atmospheric tests with mean flows up to sonic conditions inside the nozzle throat and simultaneous acoustic excitation with an upstream loudspeaker and a downstream mounted proportional valve.

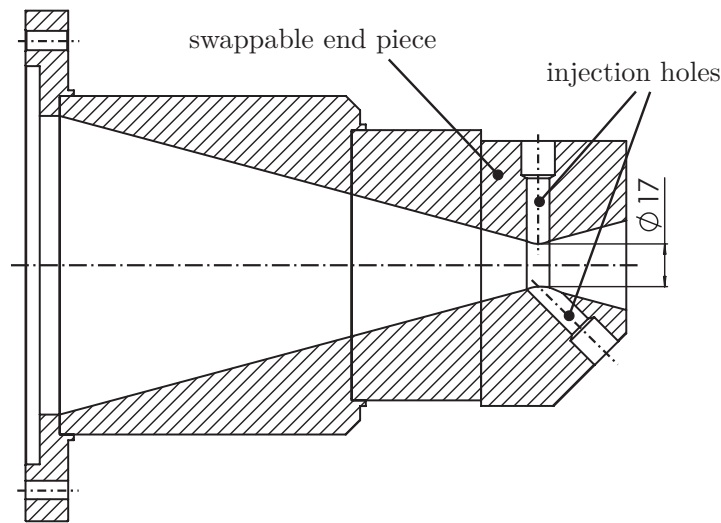


**Figure 7.11.:** Generic nozzle and an end piece for air injection at  $90^\circ$  and  $45^\circ$  towards the main air flow.

ratio of  $\alpha = 38 : 1$ . It enables sonic conditions in the throat, both, under reacting and non-reacting conditions. The nozzle is designed to facilitate several end pieces, allowing for various types of actuation, two of which are presented here. FIG. 7.11 shows the generic nozzle with an installed end piece for air injection, all manufactured from refractory steel.

The depicted termination is used for steady measurements with air injection and for excitation with a proportional valve. The end piece accommodates two drill holes that guide fluid from each connector to the axial center of the nozzle's throat. One is oriented perpendicular to the main air flow, the other is tilted at an angle of  $45^\circ$  towards the incoming flow. A proportional valve can be mounted at either one of the connectors, while the other can be sealed air tight with a plug made of stainless steel. Both plugs are shaped so that minimum flow disturbance is introduced in the throat. The connections feature a constant inner diameter from the valve outlet to the throat entry for low losses. During Mach number measurements (cf. FIG. 7.22), an adapter can be inserted into the  $90^\circ$  hole to facilitate mounting of an absolute pressure sensor.

FIG. 7.12 depicts the second swappable end piece, which has the same minimum diameter as the termination in FIG. 7.11, but does not feature a constant area throat. At the outlet a scalloped rotating disk, driven by a brushless DC motor (*Ott GmbH*, BL4240B), is installed. The motor has a total power output of 47 W and a minimum and maximum shaft speed of 120 rpm and 1500 rpm, respectively. In order to keep the setup as simple as possible, the contour disks are directly mounted onto the shaft, which necessitated the use of a right-angled drive. The gear features a transmission ratio of 3:1. Additionally, FIG. 7.12 shows two exemplary disks, one with two and another with twelve teeth of the same root and head diameter. They feature an area blockage amplitude of 5%, while two other designs with 16.7% and 25% were manufactured, as well. The shape of the teeth was designed in a way that the cross-sectional area of the nozzle outlet is alternately blocked and opened in a sinusoidal way. According to the investigations by Freitag [50], this delivers optimal results, as the sound generation is dependent on a harmonic fluctuation of the opening cross-section.

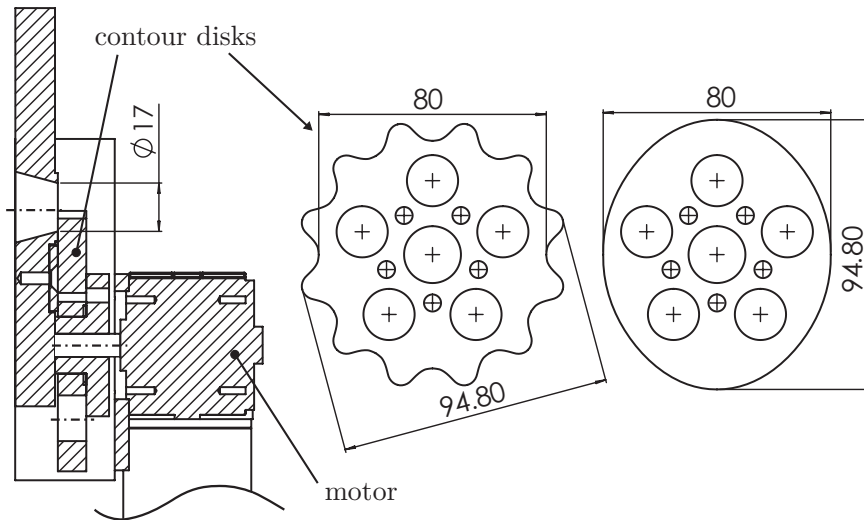


**Figure 7.12.:** End piece for mechanical-blockage actuation with various contour disks, which are driven by a DC motor. The two exemplary disks on the right hand side feature twelve and two teeth, respectively.

Incorporating two contoured disks for each amplitude, respectively, a combined excitation frequency range of 4 Hz to 300 Hz at the same blockage amplitude was achieved.

The test rig setup for combustion experiments is depicted in FIG. 7.13. It was used for the measurements, detailed in SUBSEC. 7.5.4. The downstream section is the same as in the cold acoustic test rig, however, several segments are added upstream in order to allow for reacting test conditions resulting in elevated temperature. The main air inlet is followed by a T-piece,

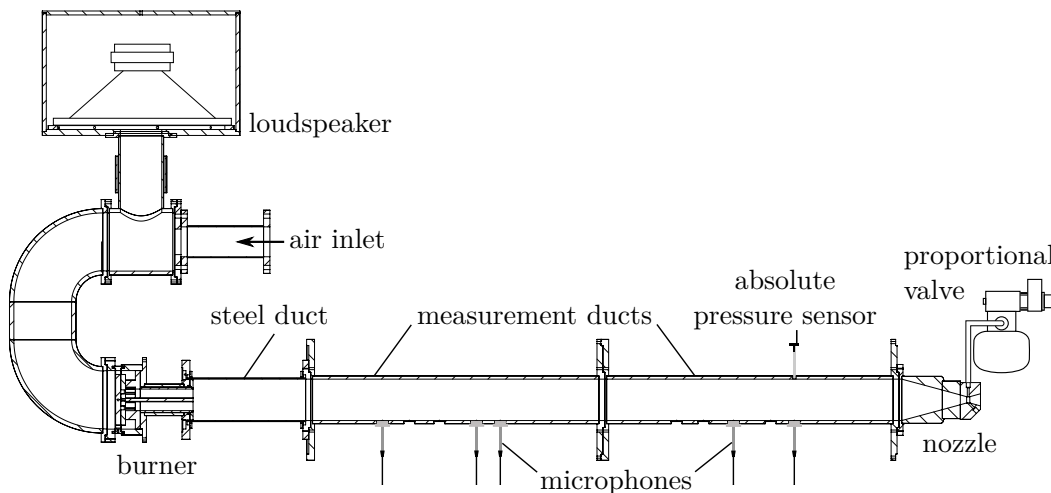


**Figure 7.13.:** Experimental setup for atmospheric combustion tests

connecting a housed 18" woofer to the rig. A U-bend guides the air to a movable-block swirl generator. In an annular mixing tube, natural gas is injected to allow for a technically premixed combustion. The burner also features pilot fuel injection at the downstream end of a

center body that sits flushed with the burner exit plane. The theoretical swirl number was set to  $S = 0.7$  throughout the experiments. The acoustic boundary condition with the nozzle at the combustion chamber outlet was close to total reflection, which caused strong self-excited combustion instabilities. To achieve sufficiently small oscillation levels, a very lean fuel to air ratio was set, resulting in a global equivalence ratio of  $\phi = 0.38$  to  $0.48$ . This required a fuel ratio of pilot to main stage of approximately  $3 : 7$ . As exhaust gas temperatures are a necessary input for the multi microphone method, they were monitored using several type K thermocouples distributed throughout the setup, e. g., directly upstream and downstream of the microphone arrays.

Due to employment of the nozzle, moderately elevated pressures were expected in this experiment. Thus, no quartz glass tube was used downstream of the burner. Instead, a solid steel tube of 300 mm length was used, in which the flame is located. Two measurement tubes were installed that both featured an array of mounting positions for cooled microphone holders. Details are given in SUBSEC. 7.4.1. Only the nozzle end piece depicted in FIG. 7.11 was utilized at reacting conditions. The reason is that the siren actuator from FIG. 7.12 was not designed to withstand hot exhaust gas.

Another test rig configuration is depicted in FIG. 7.14. It was employed for preliminary impedance tuning experiments, which were mainly used for the validation of a time-domain network model, simulating the scheme on the high pressure test rig. In the process, reflection coefficients and the actuator transfer function were determined via system identification tools. The utilized reference planes are denoted with red dashed lines. Furthermore, the power spectral density at the highlighted microphone was calculated, the result of which is depicted in FIG. 7.33. The setup is similar to the cold acoustic test rig, introduced in FIG. 7.10, the only difference being its termination. Instead of a nozzle, a simple duct extension and a second (open) 18" woofer were mounted downstream. The extension was necessary in order to maintain a working phase difference between detection of the downstream propagating wave and response of the downstream actuator.

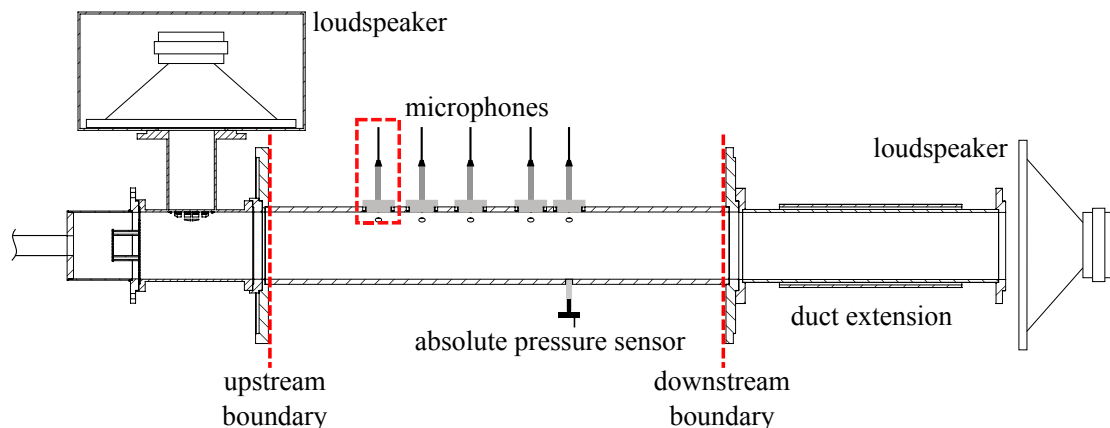


**Figure 7.14.:** Experimental setup for preliminary tests of the active control of the acoustic boundary condition. Simultaneous acoustic excitation is realized with loudspeakers upstream and downstream of the microphone array, respectively.

#### 7.4.1. Microphone Measurements

The theoretical basis for axially aligned pressure sensors utilized for the Multi-Microphone Method was detailed in SEC. 2.2. During all measurements, five 1/4" condenser microphones from *G.R.A.S. Sound & Vibration A/S* were installed at the test rig. An in-house built amplifier provided analog signal conditioning features, i.e., a low-pass filter and a gain. The amplifier output signals were detected via *NI-9215* BNC-modules mounted in a *NI cDAQ-9188* from *National Instruments* and passed to a connected PC. A LabVIEW based manual data acquisition tool was employed, in case the excitation signal was generated externally by a signal conditioner. The subsequent mono-frequency harmonic excitation (e.g., SUBSEC. 7.5.3 and SUBSEC. 7.5.4) was realized by an automated LabVIEW script. Therefore, the corresponding excitation frequencies, amplitudes, and the recording time were specified in an input. Recording times were dynamically defined, such that at least 20 oscillation periods were obtained.

Before installation at the rig, all microphones need to be calibrated to a reference microphone, which is done via a calibrator duct, specifically designed for this purpose. The output signals are complex calibration coefficients, which contain amplitude and phase information. They are used throughout data evaluation or implemented (as a constant factor) on the controller board for impedance tuning. Exemplary values of these calibration coefficients are depicted in FIG. 5.13.

In case of cold acoustic measurements (cf. FIG. 7.10 and FIG. 7.14), small axial distances between the microphones were employed. The distance between first and last microphone was  $L_{\text{array}} = 0.3$  m. For low frequencies down to 50 Hz, this setup causes reasonably low errors. For the combustion experiments, however, the residuals at low frequencies increased to values of the order of 10%. Therefore, the total extent of the array was increased to a maximum distance of 1 m from the microphone located most upstream to that downstream (cf. FIG. 7.13). Thereby, in the range from  $f = 50$  Hz to 80 Hz, the maximum error could be significantly lowered. An issue arising with the longer sensor array is that the constant temperature assumption of the Multi-Microphone Method is violated for combustion experiments. The burned gas temperature noticeably decreases with downstream distance, due to the water-cooled combustor walls. Thus, under reacting conditions, the results were analyzed separately, depending on the acoustic forcing frequency. The larger array was only used for low frequency analyses below 80 Hz, while in case of higher acoustic excitation frequencies, microphones in a shorter array were evaluated for the measurements.

Under reacting conditions in the combustor, the microphones initially did not work properly for more than a couple of minutes. Their response became superimposed by low-frequency oscillations and they showed general unresponsiveness. Those typical signs of overheating were either permanent or could be remedied by purging of the combustion chamber with cold air.

The sensors worked fine under reacting conditions without the nozzle installed, and conversely, they also worked at non-reacting conditions with an installed nozzle. Thus, apparently the combination of hot exhaust gas and elevated pressures posed an issue. Hot gas passage through the microphones, and in particular their pre-amplifiers, was identified as the main reason for the malfunctions. Thus, the microphones were supplemented by an additional coupler that was sealed using a high temperature silicone, as depicted in FIG. 7.15. The threads between capsule, coupler, and pre-amplifier were also sealed to prevent any hot

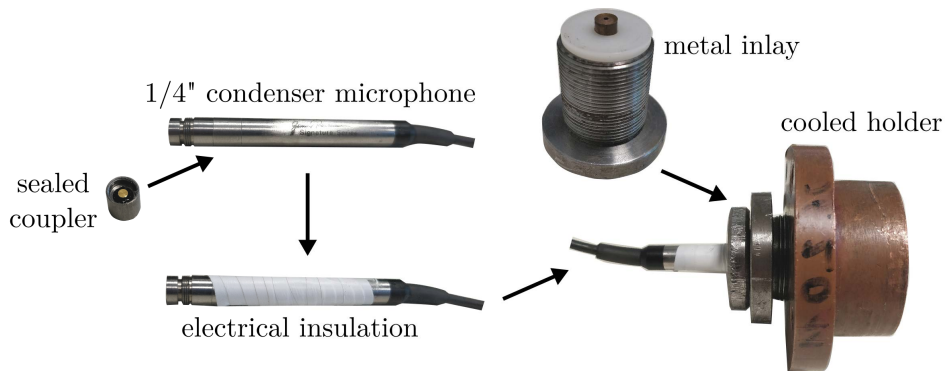


**Figure 7.15.:** 1/4" condenser microphone with additional coupler, electrically insulated and mounted in a metal inlay inside a cooled holder.

gas from entering the pre-amplifier. In consequence, the calibration process became more elaborate. The microphones first needed to be installed at the test rig and checked for air tightness at the highest possible pressure inside the measurement section. Subsequently, they were calibrated with the designated equipment and again installed at the test rig.

In order to decouple the microphones from electric hum, the cooled holders are equipped with several inlays and a fixture made of polyoxymethylene. The holders were used for atmospheric combustion experiments at the institute for several years and never showed any weaknesses in keeping the microphones sufficiently cooled. However, in the case of elevated pressures their thermal conductivity was deficient. Although hot gas passage through the microphones had been eliminated, overheating was still an issue. Therefore the plastic material inside the holders was replaced by metal inlays that needed to be adapted to fit a layer of electrical insulation around the microphones. The required parts are shown in FIG. 7.15. Ultimately, by combining the above-mentioned sealing and measures to increase thermal conductivity, microphone measurements under reacting conditions with elevated pressures could be conducted without any hardware failures.

#### 7.4.2. Absolute Pressure Sensors

Static pressure was measured using calibrated compensated absolute pressure sensors of the type HDOB002AY8P from *First Sensor AG*. For an initial determination of the nozzle Mach number at each hardware configuration, two of such sensors were employed. One probe was installed in the measurement duct at the axial location of the downstream microphone and one at the nozzle throat. Data from both was then used for calculation of the (unactuated) nozzle Mach number by evaluation of EQ. 7.7. Thus, a relation of the nozzle Mach number to the static upstream pressure was found. The acquired lookup tables could then be used to determine the nozzle Mach number based solely on measurements with the upstream pressure sensor. This procedure became necessary, as injection into the throat inhibits reliable measurement results from the downstream sensor, which is situated in the vicinity of the injector connection.

The sensors were further used for dynamic pressure measurements at very low frequencies, where microphones with static pressure equilibration cannot be used (below 5 Hz). Results

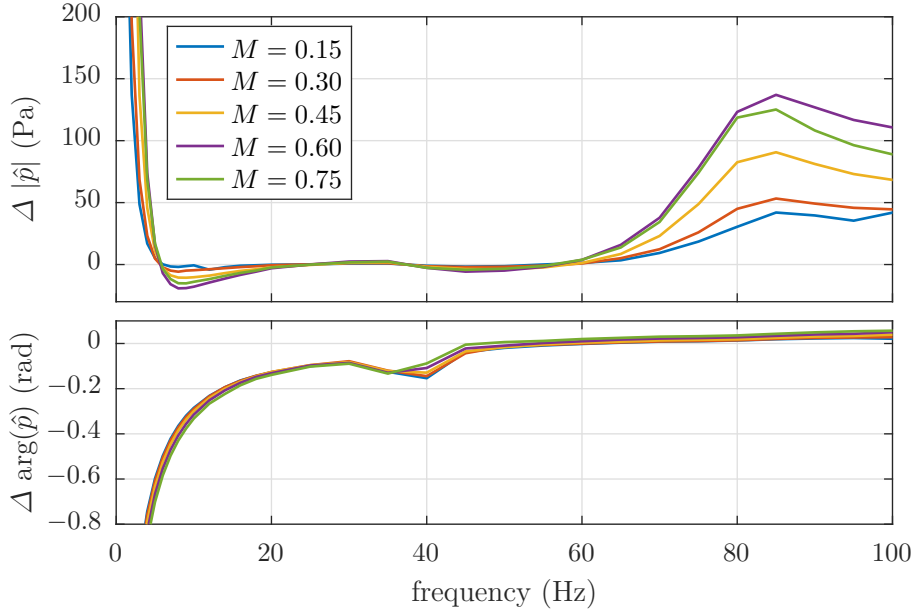


**Figure 7.16.:** Difference in the measured pressure fluctuation between the absolute pressure sensor and a condenser microphone. Top: magnitude deviation, bottom: phase deviation.

incorporating both dynamic measurements with an absolute pressure sensor and a microphone at the same axial position are presented in SUBSEC. 7.5.3.

FIG. 7.16 depicts the difference in absolute values and phases of the pressure signals between the absolute pressure sensor and a condenser microphone at the same axial location. The microphone is connected to the measurement duct via the holder’s internal channel ( $l \approx 8 \text{ mm}$  and  $d = 1.0 \text{ mm}$ ). The absolute pressure sensor is mounted via a rigid tube of  $l \approx 50 \text{ mm}$  and  $d = 3 \text{ mm}$ . Each curve corresponds to a different main air mass flow and, thus, to a different nozzle Mach number. Hence, multiple levels of mean pressure, fluctuation amplitude, and noise are represented. As actuation device, a proportional valve was operated with a source mass flow of  $m_s/m_m = 0.1$ . The difference in amplitude is very large at very low frequencies due to the pressure sensor being able to capture low frequency fluctuations, which the microphone is not able to detect. Up to 20 Hz the difference is not negligible, but can be explained by large values of the total amplitude (cf. FIG. 7.28). There is a small difference from 20 Hz to 60 Hz, until the pressure sensor’s readings start deviating from the microphone’s again. The phase difference exhibits an increasing divergence towards very low frequencies and has a minimum at  $\approx 55 \text{ Hz}$ . The varying excitation amplitudes only have an effect on the amplitude difference, while that of the phase remains largely unaffected. In summary, as the absolute pressure sensor is capable of accurately measuring the amplitude in a frequency range from 20 Hz to 60 Hz, it is assumed that the absolute pressure sensor’s accuracy below 20 Hz is acceptable for the prospected measurements.

#### 7.4.3. Proportional Valves for Air Flow Modulation

Two types of *direct drive valves* or proportional valves from *Moog GmbH* were used throughout the work. They are based on a linear motor that deflects a piston in the flow path of pressurized

supply air. At 0 V control voltage, the piston is in 50 % opening position. An arbitrarily-shaped input signal can be applied, thus moving the piston and modulating the outgoing mass flow. The D050-E042 proportional valve has a maximum pressure rating of  $\bar{p}_{\max} = 35$  bar and a maximum fluid temperature rating of  $T_{\max} = 473$  K (maximum ambient temperature 373 K). Similar valves (type D050-E043) have been produced that can withstand fluid temperatures up to  $T_{\max} = 573$  K. Such valves are sufficiently robust to operate in close vicinity of a running high pressure test rig. The operating frequency ranges from 0 Hz to  $\approx 330$  Hz. FIG. 7.17 (left) shows a photograph of the utilized device, which is similar to the valves used within the studies of Bothien et al. [18, 22]. The right-hand image in FIG. 7.17 depicts the D633-7320 proportional valve. It is smaller than the above-mentioned with about a third of the effective cross-sectional area. In contrast to the D050-E042 valve, this valve's piston has limiting stops. Thus, to prevent damage, the maximum control voltage must not be exceeded. Similar valves were used for active instability control in gas turbine engines via fuel supply modulation by Seume et al. [163] and Hermann & Orthmann [71]. The operating frequency range is 0 Hz to  $\approx 400$  Hz and their maximum pressure rating is  $\bar{p}_{\max} = 140$  bar.

As pointed out by Bothien [18], the valves feature linearity between input signal and actuator output. I. e., the acoustic excitation is linearly dependent on the control command and the inlet mass flow. Both valves are equipped with dampers, connected to the air inlet. Their purpose is to minimize upstream propagating fluctuations, thus supporting a constant amplitude response. The valves can be controlled with a designated control unit from Moog GmbH or any amplifier capable of a 48 V pulse-width modulated output signal. The piston deflection is measured with the LVDT (linear variable displacement transducer) module of the Moog control unit. The excitation signal for general sweep or mono-frequency forcing is either provided by a *Keysight Technologies 33210A* signal generator or an automated LabVIEW-based script. For implementation of impedance tuning, the valve's input signal is calculated within the controller, which is loaded on a *DS1103 PPC Controller Board* from *dSPACE*. The controller script is written in Simulink, while monitoring is done via the *dSPACE* software *ControlDesk*.

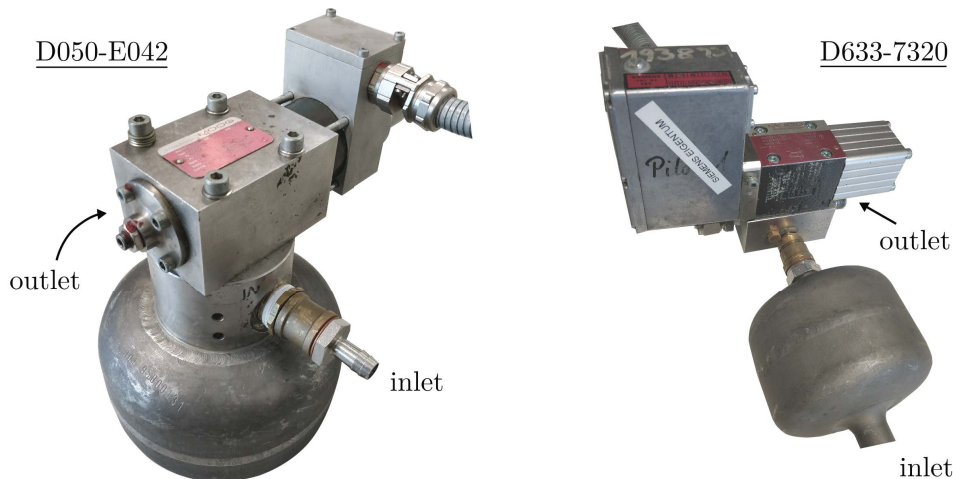


**Figure 7.17.:** Proportional valves from *Moog GmbH*. Left: D050-E042, right: D633-7320.

None of the valves are currently being produced and an inquiry to Moog GmbH for a medium amount of proportional valves was answered negatively. A new production would require approximately 100 valves of minimum purchase quantity per year, and therefore significant expenses. However, a small (but supposedly sufficient) number of D050-E04x valves is available to SIEMENS Energy, justifying further investigation of the actuator concept. Availability of the D633-7320 valves is comparable.

## 7.5. Experimental Results for Characterization of the Actuation Concept

In the preceding sections, a suitable actuator concept was proposed, numerical simulations for an initial assessment were detailed, and the experimental setup was elucidated. The latter elaborations are the foundation to this section, which focuses on the results of the atmospheric experimental investigations conducted throughout the work.

In SUBSEC. 7.5.1, part of the initial tests for characterization of the utilized proportional valves are detailed, as they are the core of the actuation principle. The key question, as to whether the valves will be able to provide the required mass flow modulation in the industrial test rig, is answered. Later, investigations for characterization of the generic nozzle, which simulates the VSS, are presented. In SUBSEC. 7.5.3, various results from tests with modulated air injection into the nozzle are shown. Several properties, such as the dependence on nozzle Mach number, momentum flux ratio, and injection angle are discussed. Subsequently, a comparison to results under reacting conditions is presented.

### 7.5.1. Characterization of the Proportional Valves

The amount of valves required to achieve sufficient pressure amplitudes at the high pressure test rig, was experimentally evaluated. The CFD simulations in SEC. 7.3 provide the target mass flow fluctuation (not disclosed).

In an initial experiment, the dependence of the valves' mass flows on their supply pressure is investigated. The underlying equation for this correlation was derived by Sigloch [168] for subsonic ejection, isentropic compression, and small approach Mach numbers:

$$\bar{m}_{\text{subsonic}} = \alpha A_{\text{eff}} \sqrt{2\bar{p}_1 \bar{\rho}_1} \sqrt{\frac{\gamma}{\gamma-1} \left[ \left( \frac{\bar{p}_2}{\bar{p}_1} \right)^{\frac{2}{\gamma}} - \left( \frac{\bar{p}_2}{\bar{p}_1} \right)^{\frac{\gamma+1}{\gamma}} \right]}, \quad (7.5)$$

where the indices  $(\cdot)_1$  and  $(\cdot)_2$  denote locations upstream and downstream of the restriction, respectively.  $A_{\text{eff}}$  is the effective area of the smallest cross-section and the loss coefficient  $\alpha$  is equivalent to the nozzle discharge coefficient (cf. EQ. 7.3) for low ejection Mach numbers. Personal communication with a lead designer of the D050-E042 valves revealed a value for the loss coefficient of  $\alpha \approx 0.63$  for both valves. Due to a lack of documentation on the used devices, this information was initially used for the subsequent calculations and later verified.

The hardware setup consisted of a mass flow meter for control of the steady mass flow, while pressure sensors measured the absolute mean pressures upstream and downstream of the valves. FIG. 7.18 shows the resulting mass flows over pressure difference ( $\circ$ ) and square-root fits for the D050-E042 (black) and the D633-7320 valve (blue), respectively. Expectedly, the mass flow through the larger valve is significantly higher at the same pressure differential.

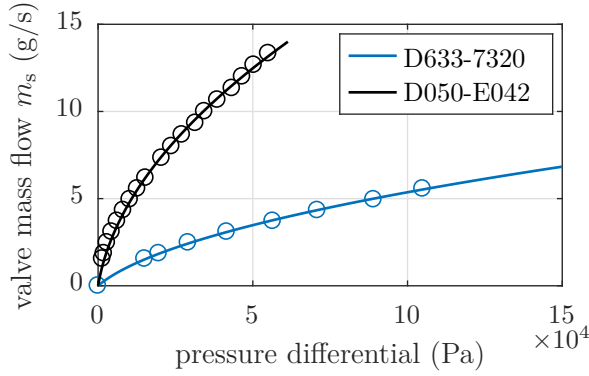


**Figure 7.18.:** Mass flow over pressure difference for two proportional valves: Moog D633-7320 (blue) and Moog D050-E042 (black). Markers denote measured values, lines denote square-root fits.

Subsequently, the effective opening area  $A_{\text{eff}}$  of the piston at 0 V control voltage (50% opening) was calculated according to EQ. 7.5 and averaged. For the D633-7320 valve, an effective opening area of  $A_{\text{eff}} = 15 \text{ mm}^2$  was calculated. The D050-E042's effective cross-section was determined as  $A_{\text{eff}} = 48 \text{ mm}^2$ . It was further found that all D050-E04x valves feature the same geometry. Thus, the effective opening area could be confirmed by an available data sheet for a D050-E041 valve, which in return confirmed the previously stated value for the loss coefficient. The effective opening areas were then used to determine the mean valve mass flows for the expected pressure differentials, supposed to occur in the industrial test rig.

However, as EQ. 7.5 only holds for subsonic conditions in the smallest cross-section, a corresponding equivalent for sonic conditions was required. Sigloch [168] derived the following expression, again for isentropic compression and small approach Mach numbers:

$$\bar{m}_{\text{sonic}} = \alpha A_{\text{eff}} \sqrt{2\bar{p}_1 \bar{\rho}_1} \sqrt{\frac{\gamma}{\gamma+1}} \left[ \frac{2}{\gamma+1} \right]^{\frac{1}{\gamma-1}}. \quad (7.6)$$

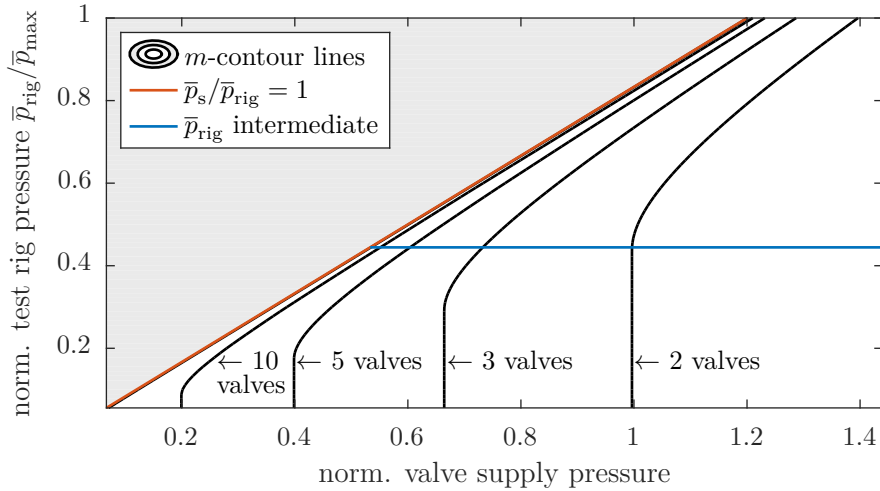


**Figure 7.19.:** Estimated number of D050-E04x valves for varying ratios of mean valve supply and test rig pressure. The gray area denotes higher test rig pressure than valve supply. The blue line marks intermediate test rig pressure (standard operation).

By means of EQ. 7.5 and EQ. 7.6 and the evaluated values for  $A_{\text{eff}}$  and  $\alpha$ , the mass flows through the valves were calculated for various static pressures in the test rig and valve supply pressures. FIG. 7.19 depicts the result in terms of a mass flow contour plot for a D050-E042 valve. A constant target mass flow and a fluid temperature of  $T = 473 \text{ K}$  were assumed.

Both, test rig and valve supply pressure are normalized. A negative pressure differential is denoted in gray, as in this case no fluid would be injected through the valves. Depending on the pressure difference, a certain amount of valves needs to be employed, to obtain the required fluctuating air mass flow through the valve. The black lines denote the lower boundary, down to which each configuration is viable. The blue line corresponds to a typical operating pressure of the rig. With five valves, for instance, a normalized supply pressure of at least 0.4 needs to be set to achieve the mass flow and thus, pressure fluctuation requirement. Note that these calculations include the assumption of an optimal distribution of the inlet holes in the nozzle. In practice, this may be difficult in cases where the amount of valves is no integer fraction of the number of installed vanes.

Note that the fluid temperature has an influence on the results. If it is larger than  $473 \text{ K}$ , as would be possible with D050-E043 valves, the density would decrease. Thus, the supply pressure would need to be increased in order to achieve the same mass flow, which follows directly from EQ. 7.6.

In summary, the prospected amount of D050-E04x valves is considered feasible for application at the high pressure test rig. Yet, for the atmospheric investigations planned within this work, they are hardly suited. Practical issues arose due to the G1" connectors, which had to be reduced to smaller connectors to fit the nozzle injector holes. The associated losses and the reduced frequency range were reasons enough for employing the smaller D633-7320 valves in the atmospheric experiments. An analog calculation according to EQ. 7.5 and EQ. 7.6 reveals an increase of the required number by factors of 2 to 3, compared to D050-E04x valves, at

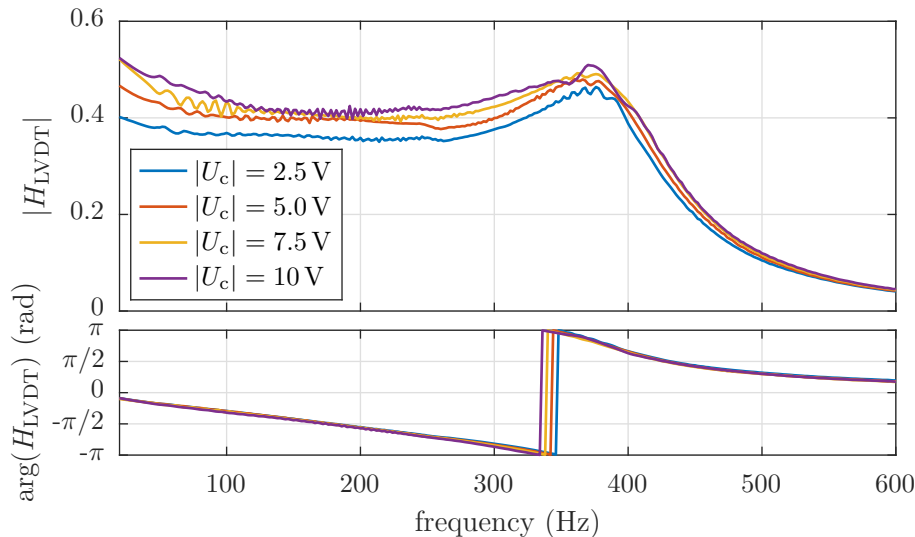


**Figure 7.20.:** Transfer function between voltage input and piston stroke for the D633-7320 proportional valve, measured by the output voltage of the LVDT module. Top: magnitude, bottom: phase.

the same pressure differentials. Thus, assuming sufficient availability or large-enough supply pressures, the smaller valves are also viable for application at the high pressure test rig.

Further preliminary experiments were conducted, to characterize the frequency-dependent piston deflection. At first, the amplitude of the piston movement was measured in dependence of the excitation frequency, which was done for different input voltages. FIG. 7.20 shows the result for a mean valve mass flow of  $\bar{m}_s = 5.0$  g/s. No significant deviation from the mentioned linear behavior is apparent, as the curves for various input voltage amplitudes collapse. The deflection amplitude shows a slight dependence on the actuation frequency. For impedance tuning, this influence needs to be taken into account, so that the actuator transfer function is determined correctly. For experiments regarding the actuation concept of fluid injection into the nozzle, this influence is canceled by normalization of the input voltage. By doing so, the frequency response of the piston stroke amplitude can be flattened, as depicted in FIG. 7.21 (orange line).

The normalized control voltage was used throughout all experiments that are concerned with sound generation due to injection into the nozzle. In that way, the biasing influence of the valve was removed. These results conclude the relevant preparatory investigations of the valves. Within the following section, the generic nozzle shown in FIG. 7.11 is characterized.

### 7.5.2. Characterization of the Nozzle

The atmospheric test rig, shown in FIG. 7.13, was employed to investigate the Mach number in the nozzle throat for various main air mass flows with steady-state injection at reacting and non-reacting conditions. Absolute pressure sensors were installed upstream of the nozzle and inside the nozzle throat, as described in SEC. 7.4. Assuming adiabatic compression [168], the throat Mach number is calculated as follows:

$$M = \sqrt{\frac{2}{\gamma - 1} \left[ \left( \frac{\bar{p}_1}{\bar{p}_2} \right)^{\frac{\gamma-1}{\gamma}} - 1 \right]}, \quad (7.7)$$

where  $\bar{p}_1$  corresponds to the static pressure upstream of the nozzle and  $\bar{p}_2$  to the static pressure inside the nozzle throat. FIG. 7.22 depicts the Mach number over main air mass flow in the throat for the non-reacting case (blue line, \*) and the reacting case at an equivalence ratio of

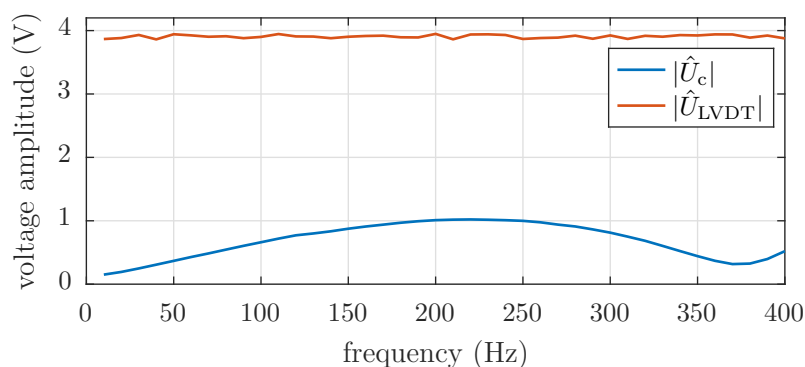


**Figure 7.21.:** Amplitude of the control voltage input  $|\hat{U}_c|$  and the measured LVDT voltage amplitude  $|\hat{U}_{\text{LVDt}}|$  of the D633-7320 valve's piston.

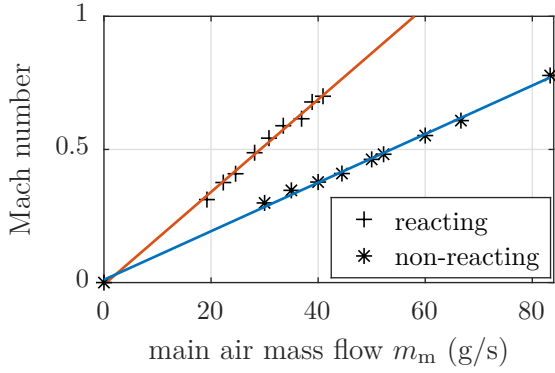


**Figure 7.22.:** Calculated mean Mach number in the nozzle throat over main air mass flow for non-reacting (\*, blue: linear regression) and reacting (+, orange: linear regression) conditions.

$\phi = 0.43$  (orange line, +). Knowledge of the Mach number in the experiment is important for comparing, e. g., cases with reacting and non-reacting flows.

Subsequently, the steady blockage of the nozzle via steady-state air injection at two incidence angles (cf. FIG. 7.11) was investigated. As mentioned, when introducing the discharge coefficient in EQ. 7.3,  $C_d$  is a measure for the blockage of a nozzle. In order to compare the results of both  $90^\circ$  and  $45^\circ$  injection,  $C_d$  is plotted over the momentum flux ratio  $J$  in FIG. 7.23. The latter was varied by increasing the secondary air injection  $\bar{m}_s$ , and it is defined as

$$J = \frac{\bar{\rho}_s \bar{u}_s^2}{\bar{\rho}_m \bar{u}_m^2} = \frac{\bar{m}_s^2}{\bar{m}_m^2} \frac{A_{\text{nozzle}}^2 \bar{\rho}_m}{A_{\text{inj}}^2 \bar{\rho}_s}. \quad (7.8)$$

$A_{\text{nozz}}$  and  $A_{\text{inj}}$  are the cross-sectional areas of the main nozzle and the injector, respectively. The nozzle Mach number is calculated without secondary air injection and was varied from  $M = 0.3$  to  $M = 0.75$ , which corresponds to main air mass flows of  $\bar{m}_m = 33.3$  g/s to 83.3 g/s. Generally,  $C_d$  declines with increasing momentum flux ratio, i. e., growing injector mass flows.

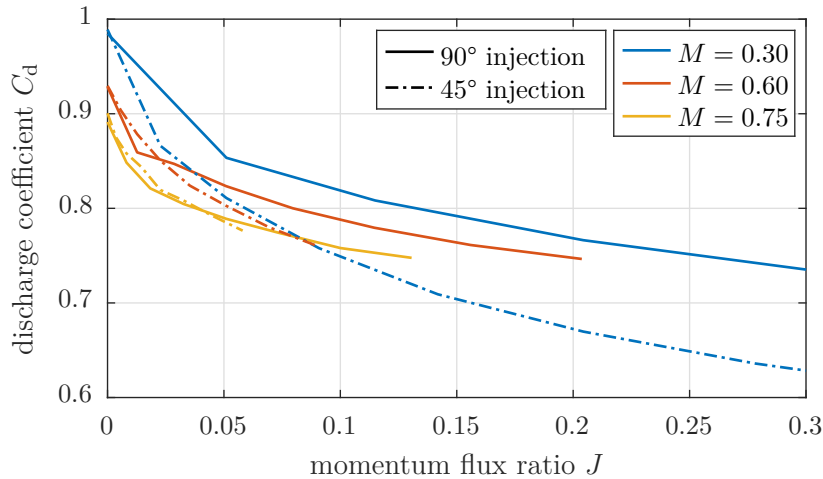


**Figure 7.23.:** Discharge coefficient of the main nozzle over momentum flux ratio of the injection at three different main air Mach numbers (calculated without injection). Results for injection angles of  $90^\circ$  (solid lines) and  $45^\circ$  (dashed lines).

This corresponds to an increase in blockage, as the actual mass flow through the nozzle is reduced, compared to the theoretical value. The slopes for varying Mach numbers are comparable for each injection angle. However, a steeper drop is observed for the case of  $45^\circ$  injection, especially for  $M = 0.30$  and  $M = 0.60$ . This indicates a higher blockage at the same injector mass flow for the injection angled towards the incoming main air flow. This coincides with observations by Miller et al. [111], who found a significant blockage increase versus normal injection. Tilted blowing has since become the standard for fluidic throat skewing and thrust control [9, 43, 48, 56]. The influence of an angled injection on dynamic measurements is investigated in the following section. However, for comparability and in respect to implementability at the high pressure test rig,  $90^\circ$  injection remains the standard configuration throughout this work.

### 7.5.3. Modulated Air Injection into a Subsonic Nozzle at Isothermal Conditions

For the experiments with harmonic excitation via the D633-7320 proportional valve, the test rig was set up as depicted in FIG. 7.10, unless stated otherwise. Main goal of the experiments was to gain insight into the dynamic characteristics of the actuator concept. Thus, measurements and data evaluation were realized, such that external influences could be excluded as far as possible. The first step was to ensure a constant piston displacement amplitude over the regarded frequency range, which was discussed in SUBSEC. 7.5.1. Throughout all tests, the maximum deflection amplitude was utilized. The measurements were then conducted in two steps, analog to the procedure detailed in SEC. 2.4. In a first step, the open loop reflection coefficient  $R_{ol}$  of the test rig termination was measured using the Multi-Microphone Method. Mono-frequency upstream loudspeaker forcing in a range from  $f_{exc} = 50$  Hz to 400 Hz was used. At a control signal of 0 V, the proportional valve was set to inject a steady mass flow corresponding to the mean mass flow of the dynamic measurement. This was necessary, because the reflection is dependent on the mean nozzle Mach number, which needs to be equal in both measurement steps. The valve mass flow was independently controlled using a pressure reducing valve, while simultaneously reading the mass flux from an in-line connected mass flow meter. In the second measurement step, the proportional valve was used for acoustic excitation. Application of the Multi-Microphone Method yielded the actuator transfer function from EQ. 2.45. However, the normalization with the control signal is neglected in this section, as the total amplitude is more descriptive in showing the actuator characteristics. Thus, a non-normalized or *total* actuator transfer function is introduced:

$$G_{tot} = \hat{g} - R_{ol}\hat{f}. \quad (7.9)$$

As the naturally reflected part  $R_{ol}\hat{f}$  is subtracted from the upstream propagating wave  $\hat{g}$ ,  $G_{tot}$  provides a measure for the acoustic wave solely generated by the acoustic actuator. In order to show the independence of external factors, an error bar plot is given in FIG. 7.24. It contains six different measurements conducted at a main air mass flow of  $m_m = 66.7$  g/s, corresponding to an unactuated nozzle Mach number of  $M = 0.60$ . Injection was realized with the D633-7320 valve at a mass flux ratio of  $m_s/m_m = 0.10$ , which corresponds to a momentum flux ratio of  $J = 0.20$ . The test rig was disassembled and reassembled in between the measurements, and further, two setups with different internal volumes (FIG. 7.10 and FIG. 7.13) were used. Yet, the maximum standard deviation is  $\approx 6\%$  throughout the entire frequency range.

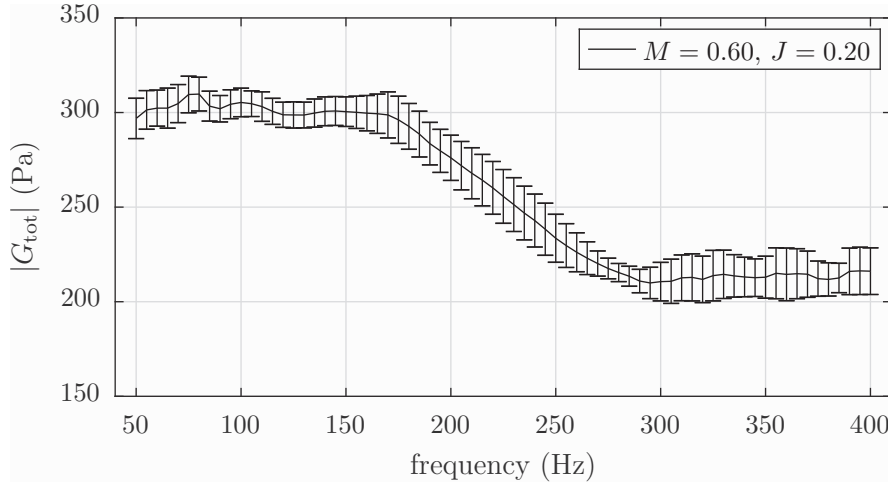


**Figure 7.24.:** Error bar plot of the total actuator transfer function  $G_{\text{tot}}$  for the same operating conditions at six different measurements across several weeks.

Thus, the measurement technique is only marginally dependent on the confinement, enabling comparisons between various test rig setups or experiments and numerical simulations.

The general run of the amplitude response features a plateau from 50 Hz to 180 Hz, followed by an approximately linear decline by  $\approx 30\%$  in magnitude and another plateau from 300 Hz to 400 Hz. It will be seen throughout the conducted measurements, that this characteristic run is more or less similar for any of the regarded cases, despite occasional deviations in the lower frequency range.

Note that a phenomenological explanation for this behavior was not found within the literature. The references mentioned in SEC. 7.2 focused on different operating conditions, which are not applicable in this work. The nozzle Mach number, for instance, is above unity in any of the previously regarded sources. In this investigation, however, subsonic conditions are of interest. Typical momentum flux ratios from the literature (e. g., references [9, 42, 186]) are significantly above unity, and thus, exceed reasonable values for application at the high pressure test rig. Furthermore, in investigations with dynamic excitation, generally the Strouhal number of the injector is regarded to retain comparability. For example, Vermeulen et al. [183] and Miller et al. [111] operated their injectors at  $Sr_s = \mathcal{O}(1)$ . However, typical Strouhal numbers in this work are significantly lower. For instance,  $Sr_s$  ranges from  $3.6 \times 10^{-3}$  to  $2.91 \times 10^{-2}$  in FIG. 7.24, which is two to three orders of magnitude lower. Consequently, due to the multitude of differently aimed investigations discussed throughout this work, no normalization of the injector frequency is used.

In order to gain information about the effectiveness of the actuation concept in comparison to simply mounting the valve at the measurement duct's (or combustor) wall, a corresponding experiment was conducted. The setup shown in FIG. 7.10 was used and nozzle actuation was realized as detailed above. For actuation on the combustor wall, the valve was flanged to a connector piece for exhaust gas analysis, using the same adapter length and diameter as for nozzle injection. In this case, the nozzle was replaced by an orifice, as the strong reflections impaired accuracy of the measurements. The same operating point as in the preceding results was used, complemented by two measurements at lower main air mass flows. The mass flux

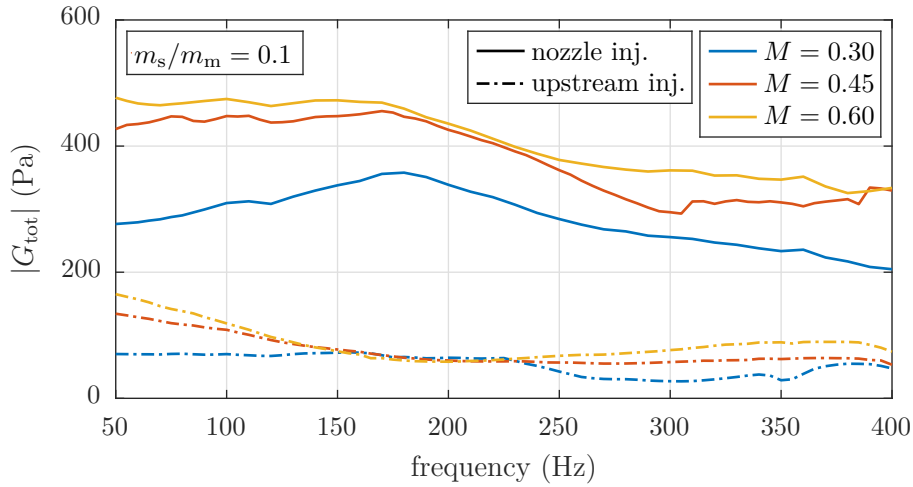


**Figure 7.25.:** Total actuator transfer function  $G_{\text{tot}}$  for three Mach numbers and two different injection locations. All measurements conducted at a constant ratio of secondary and main air mass flow:  $m_s/m_m = 0.1$ . Solid lines denote air injection into the nozzle throat and dash-dotted lines denote injection upstream of the nozzle.

ratio for all six configurations was kept constant. Note that the momentum flux ratio for nozzle injection and upstream injection on the combustor wall is not kept constant in this case, as the cross-sectional area of the main air flow is significantly larger. Hence, the mass flux ratio was considered the more reasonable comparison parameter in this case.

FIG. 7.25 depicts the result of this investigation. Solid lines denote excitation in the nozzle, while dash-dotted lines denote actuation upstream, on the wall of the measurement duct. A significant difference in the achievable amplitude is observed, with nozzle excitation being three to ten times more effective at the same main air mass flows. The general trend of higher amplitudes for increasing nozzle Mach numbers, denoted by colors, is the same for both injection locations. An exception is upstream injection in the range from 150 Hz to 250 Hz, where the three curves collapse. Furthermore, nozzle injection at  $M = 0.45$  delivers a slightly different trend of the actuation amplitude at higher frequencies. Deviations are within the error margin and supposedly result from the measurements being conducted on different days.

Note that direct mounting of the valve to the wall of the measurement duct is not ideal, as was pointed out by Bothien [18]. He showed that depending on the frequency range, an additional resonance tube delivers improved results. However, the amplitude gains using this method are not as pronounced and most importantly not as constant over a wide frequency range, as the gains possible with injection into the nozzle.

Subsequently, a comparison between injection into the nozzle at  $90^\circ$  and  $45^\circ$ , tilted towards the incoming main air, was conducted. For this investigation, the mass flux ratio was again set to  $m_s/m_m = 0.10$ , yielding a momentum flux ratio of  $J = 0.20$ . Another operating point with  $M = 0.15$  was added to those previously used. The result is depicted in FIG. 7.26, where solid lines denote  $90^\circ$  and dash-dotted lines  $45^\circ$  injection. Comparing each main air mass flow, denoted by graph colors, the angled injection constantly delivers higher actuation amplitudes. Deviations range up to 15%, with angled injection generally achieving about a ten percent increase versus normal injection. The deviation is relatively constant and apparently not dependent on the nozzle Mach number. Thus, a simple dependence on the

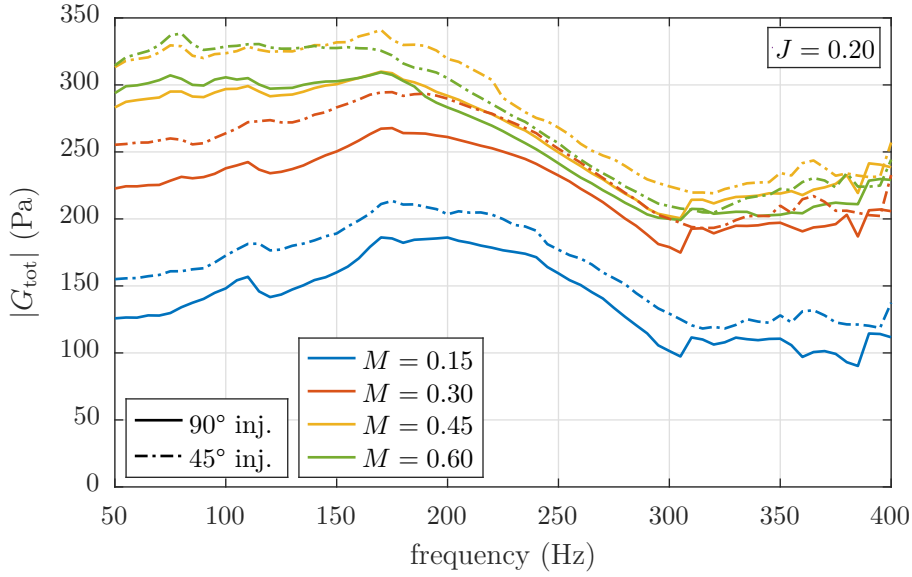


**Figure 7.26.:** Total actuator transfer function  $G_{\text{tot}}$  for a momentum flux ratio of  $J = 0.20$  at injection angles of  $90^\circ$  (solid) and  $45^\circ$  (dash-dotted). The unactuated nozzle Mach number was varied from  $M = 0.15$  to  $0.60$  (colors).

blockage, which varies with the main air mass flow (cf. FIG. 7.23), is not found. As mentioned in references [13, 110, 111], penetration depth of the jet, formation of vortex rings, and the injector Strouhal number are also highly important factors in characterizing fluid injection into a nozzle. However, as previously stated, a comparison to the literature is hardly possible, especially in terms of the occurring Strouhal numbers.

The preceding results show that the achievable amplitude with injection into the nozzle increases with main air mass flow or nozzle Mach number at a constant mass flux ratio between injection and main air. A saturation effect is found, which manifests in a relatively constant amplitude of  $G_{\text{tot}}$  above nozzle Mach numbers around  $M = 0.50$  (cf. FIG. 7.25, FIG. 7.26, and FIG. 7.31). This was observed for various measurements and is always apparent, when the momentum flux ratio is kept constant. As the typical operating point for the high pressure test rig incorporates a nozzle Mach number of  $M = 0.60$ , this finding is valuable in terms of investigating the achievable amplitude provided by the proposed actuator concept.

The importance of the momentum flux ratio, which was already stressed by various authors [76, 111, 183], is evinced by another investigation. The setup is similar to the preceding tests, incorporating normal and angled injection into the nozzle throat. However, instead of the momentum flux ratio, the valve mass flow was fixed to a value of  $m_s = 6.67 \text{ g/s}$ . Main air mass flows were varied in a range from  $m_m = 0.0 \text{ g/s}$  to  $66.7 \text{ g/s}$ , corresponding to the unactuated nozzle Mach numbers as presented in FIG. 7.27.

Several conclusions can be drawn from this plot. As in the preceding results, the angled injection delivers significantly higher actuation amplitudes as compared to normal injection. With decreasing momentum flux ratios, corresponding to increasing nozzle Mach numbers, this deviation decreases. To some extent, this might be connected to the blockage. As depicted in FIG. 7.23, the momentum flux ratio's influence on blockage also decreases with an increasing Mach number, when comparing normal to angled injection. Furthermore, the

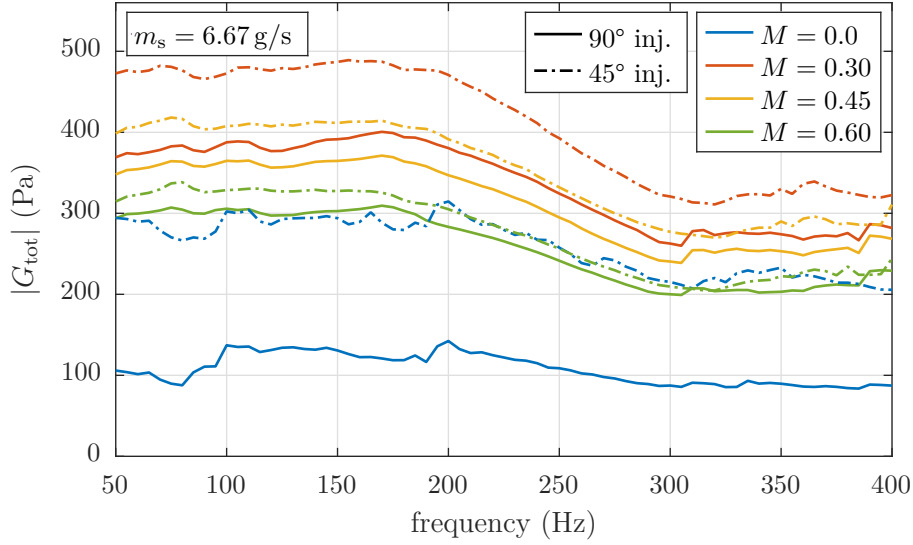


**Figure 7.27.:** Total actuator transfer function  $G_{\text{tot}}$  for a constant injection mass flow of  $m_s = 6.67$  g/s at injection angles of  $90^\circ$  (solid) and  $45^\circ$  (dash-dotted). The unactuated nozzle Mach number was varied from  $M = 0.0$  to  $0.60$  (colors).

actuation amplitude over main air Mach number apparently reaches a maximum between  $M = 0.0$  and  $M = 0.45$  for both injection strategies. This is remarkable, as the  $45^\circ$  injection is angled into the measurement duct and its maximum amplitude is still higher with a moderate main air mass flow. Hence, sound generation with the actuator concept requires a minimum main air mass flux in order to couple the actuation to the upstream cavity, which confirms the initial CFD simulation on the actuator's working principle. Above a threshold main air flow, the amplitude declines, supposedly due to a lowering momentum flux ratio.

The general run of all curves that were presented so far, is very similar, as was mentioned at the beginning of this subsection. In most cases, a constant amplitude is reached at lower and higher frequencies, respectively. The range in between is usually formed by a more or less pronounced magnitude decline. However, it has to be stated that the overall frequency response is considered to be comparably uniform. This uniformity depends on the operating conditions. However, no parameters were found, where the modulated injection into the nozzle generated intolerably large amplitude variabilities. Yet, it was observed that the presented dynamic pressure amplitudes are orders of magnitude lower than the pressure differentials obtained from steady-state nozzle injection at the same operating conditions. This behavior was found by Baruzzini et al. [9], as well. Thus, the frequency range below 50 Hz was investigated using an absolute pressure sensor, as mentioned in SUBSEC. 7.4.2 and a microphone, both located at the same axial position inside the measurement duct. A standard operating point was chosen:  $M = 0.60$ ,  $J = 0.20$  at  $90^\circ$  nozzle injection.

FIG. 7.28 depicts the dynamic pressure amplitudes measured with the absolute pressure sensor ( $\times$ ) and the microphone ( $\circ$ ), as well as the static pressure difference between no injection and steady injection ( $\square$ ) at the same main air mass flow. This value corresponds to an extrapolated "pressure amplitude at 0 Hz". At frequencies below 4 Hz the microphone yields lower amplitudes than the absolute pressure sensor, which is accounted to the venting

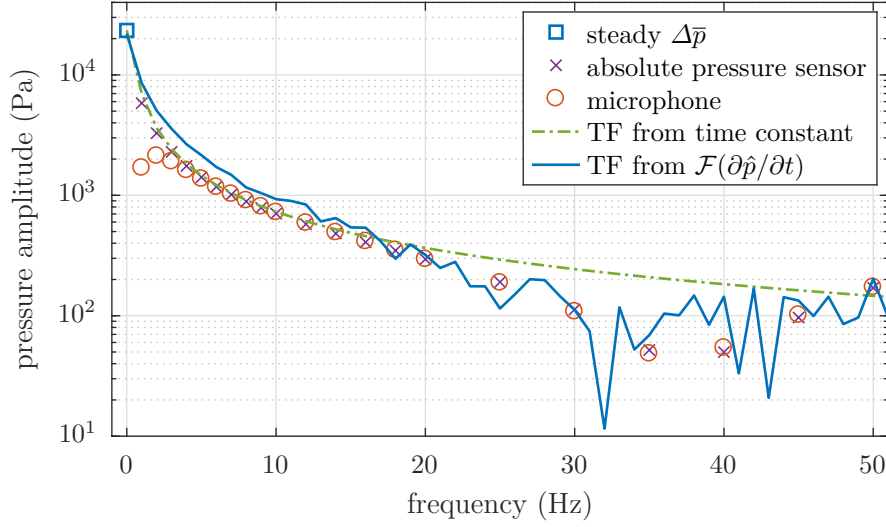


**Figure 7.28.:** Steady pressure difference ( $\square$ ), low frequency pressure amplitudes obtained with an absolute pressure sensor ( $\times$ ) and a condenser microphone ( $\circ$ ). Transfer functions calculated with the time constant (dash-dotted) and from the Fourier transform of the impulse response (solid).

of the microphone. At larger frequencies they agree quite well, showing the presumed low pass behavior of the actuator.

In addition to discrete data points, FIG. 7.28 incorporates continuous transfer functions. These were obtained from a step response experiment with an identical hardware configuration. Alterations were only made in data acquisition and in the method of air injection via the proportional valve. At the same main air mass flow, valve supply air was first stopped by a ball tap and then rapidly opened. The absolute pressure sensor was monitored, yielding the pressure difference between injection and no injection. Assuming a first order low-pass, the time constant  $\tau$  of the step response was calculated from the slope of the pressure increase. The transfer function  $G_{\text{sr}}$  (dash-dotted line) was then obtained with

$$G_{\text{sr}} = \frac{\Delta\bar{p}}{1 + i\omega\tau}. \quad (7.10)$$

An alternative transfer function was found by calculating the Fourier transform of the pressure signal's gradient, the result of which being denoted by a blue line in FIG. 7.28. Due to the low number of samples at low frequencies, the method produces inherently noisy results, which could be minimized by averaging multiple measurements. Still, the three methods produce similar results in the very low frequency range. Thus, in summary, the strong deviation between steady and dynamic measurements could be attributed to the low-pass characteristic of the injector concept.

In order to evaluate the proposed actuation concept to a comparable scheme that has already been applied in the literature, a mechanical actuation concept was implemented. As mentioned in the beginning of this chapter, the works of Hochgreb et al. [75] and Macquisten et al. [102] propose a siren-type actuator located in a nozzle throat downstream of a combustion chamber. The corresponding hardware was introduced in SEC. 7.4 and was designed to ensure

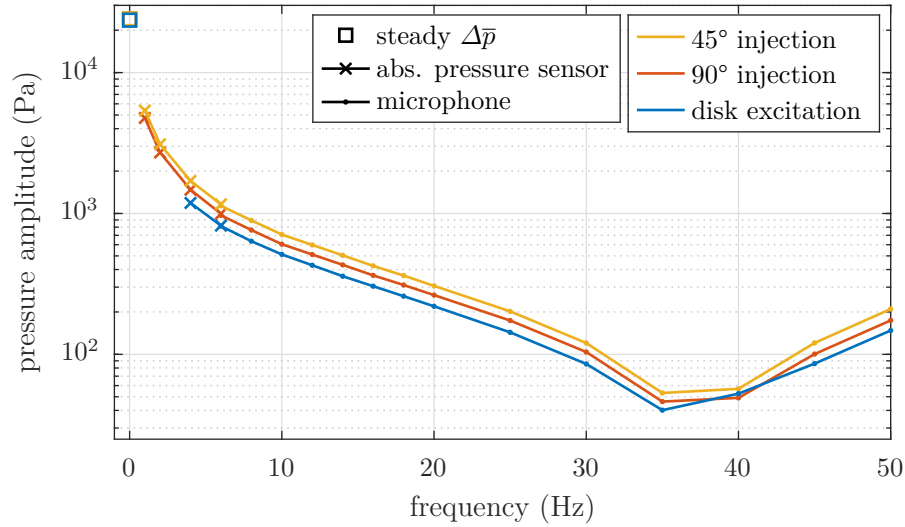


**Figure 7.29.:** Steady pressure difference ( $\square$ ), very low frequency pressure amplitudes obtained with an absolute pressure sensor ( $\times$ ), and low frequency pressure fluctuations from a condenser microphone (denoted with dots) for three different actuation types: 90° air injection (orange), 45° air injection (yellow), and excitation via a scalloped disk (blue).

a high degree of comparability to the injector concept. In order to find comparable operating conditions, the static nozzle blockage was matched. Accordingly, the discharge coefficient, or similarly the averaged pressure difference between cases of inactive and active actuation, was equalized for both mechanical and fluid excitation. The first step was determining the averaged pressure difference between the unactuated nozzle setup and actuation with the contour disk at a fixed main air mass flow. The same static pressure difference was then adjusted with both the 90° and the 45° air injection from the proportional valve. This was done for various main air mass flows and contour disks with three different amplitudes, respectively. As the trend for any of the investigated configurations is identical, only one case is shown here. It incorporates an unactuated nozzle Mach number of  $M = 0.6$ , a disk blockage amplitude of 5% and the corresponding momentum flux ratios of  $J = 0.32$  and  $J = 0.31$  for 90° and 45° air injection, respectively.

FIG. 7.29 shows the coinciding steady pressure differences ( $\square$ ) as discussed above, as well as dynamic pressure amplitudes measured with the absolute pressure sensor ( $\times$ ) and a microphone (dots). Data for the contour disk is represented in blue and air injection at 90° and 45° are colored in orange and yellow, respectively. The fluctuating amplitudes of all three configurations follow a similar path. Except from an outlier at 40 Hz the excitation with the contour disk has the lowest amplitude, albeit only by a small margin. Angled injection towards the incoming main air flow results in the highest excitation amplitudes. Note that the frequency range was reduced for clarity. However, the overall trend is identical for the entire frequency range and furthermore for any of the tested parameter combinations, including cases with higher-amplitude mechanical blockage.

In conclusion, for the investigated case with a subsonic nozzle and moderate blockage amplitudes, excitation with a contour disk performs inferior to air injection with proportional

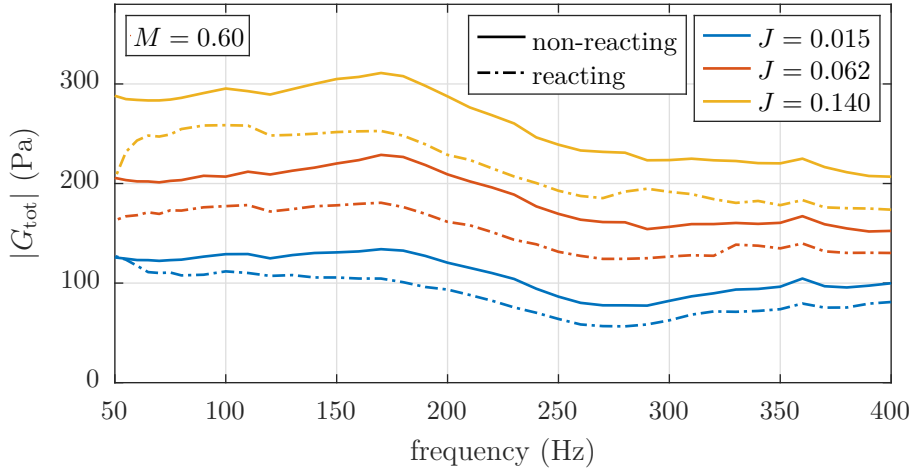


**Figure 7.30.:** Total actuator transfer function  $G_{\text{tot}}$  for an unactuated main air Mach number of  $M = 0.6$  at reacting ( $\phi = 0.43$ , dash-dotted) and non-reacting (solid) conditions. Momentum flux ratios were varied from  $J = 0.015$  to  $0.140$  (colors).

valves. In addition, injection at a  $45^\circ$  angle always yielded higher fluctuation amplitudes at lower momentum flux ratios than injection normal to the surface.

#### 7.5.4. Modulated Air Injection into a Subsonic Nozzle at Reacting Conditions

Further characterization of the injection concept was realized by incorporating reacting experiments with the test rig setup depicted in FIG. 7.13. At an equivalence ratio of  $\phi = 0.43$ , the temperature ratio between injected air and main air was  $T_s/T_m \approx 0.25$ , which approximately matches the value expected in the high pressure test rig. The first experiment was conducted at an unactuated nozzle Mach number of  $M = 0.60$  and varying momentum flux ratios, which was realized by three levels of secondary mass flows. FIG. 7.30 additionally shows results for non-reacting conditions at the same  $J$  as reference.

For both reacting and non-reacting conditions, actuation amplitudes increase with momentum flux ratio. Furthermore, excitation in a cold main flow delivers consistently higher fluctuation magnitudes. The deviation between amplitudes at reacting and non-reacting conditions are generally in the range of 10% to 20% at each momentum flux ratio. It has to be stated that the unactuated nozzle Mach number at two different temperature ratios might not be perfectly suited for a fair comparison. With cold air injection, the resulting nozzle Mach number will differ between cases with hot and cold main flow, due to mixing. Furthermore, the momentum flux ratio calculation becomes prone to errors, as the density in the nozzle throat cannot be accurately determined in cases with a temperature gradient. Yet, a general conclusion can be drawn in stating that a strong increase in main air temperature and thus temperature ratio  $T_s/T_m$  has only minor influence on the generation of upstream pressure fluctuations. This result confirms findings by Holdeman & Walker [76] and those in the preliminary CFD investigations (cf. FIG. 7.4).

Within the same experiment, additional operating parameters were varied, yielding a comparison between unactuated nozzle Mach numbers for a constant momentum flux ratio under reacting and non-reacting main flow conditions, respectively. FIG. 7.31 shows the

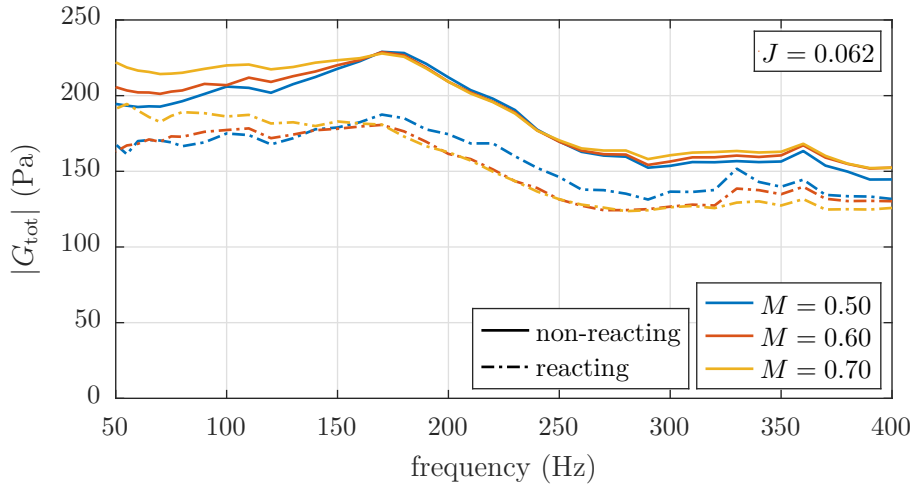


**Figure 7.31.:** Total actuator transfer function  $G_{\text{tot}}$  for a momentum flux ratio of  $J = 0.062$  at reacting ( $\phi = 0.43$ , dash-dotted) and non-reacting (solid) conditions. The unactuated nozzle Mach number was varied from  $M = 0.50$  to  $0.70$  (colors).

results, once again displaying the relevance of the momentum flux ratio in comparing various operational parameters. The amplitudes at varying main air mass flows collapse for reacting and non-reacting conditions, respectively. A saturation effect of the achievable amplitudes of  $G_{\text{tot}}$  for nozzle Mach numbers  $M > 0.5$  and constant momentum flux ratios was mentioned earlier and is observed here. Further, hot main flows result in 15 % to 20 % lower fluctuation magnitudes, which matches the observation made in FIG. 7.30. Note that the accuracy of  $M$  and  $J$  are equally error-prone and thus, the absolute difference has to be taken with care. However, the key message remains that the temperature influence on the actuator concept is not expected to be an issue for the implementation at the high pressure test rig.

Finally, it has to be mentioned that an additional investigation is required for determining an optimal layout of the injectors at the vane simulation section. As pointed out by Holdeman & Walker [76], an increasing number of holes at the same total injector area increases blockage, yet reduces penetration depth. Due to the assumed working mechanism of the actuator concept being blockage of the main air stream, an increased number of holes is presumed to perform best in terms of acoustic excitation. Yet, an increase of injector holes is highly dependent on the actual possibilities with the specialized liquid-cooled designs of the vanes in the test rig. Furthermore, inclination of the injection jets towards the incoming main air flow is recommended, the implementation of which also depends on hardware restrictions. Due to the expenses related to manufacturing an appropriate experimental setup for this investigation and the comparably large parameter space with different injector angles, total injector areas and number of injector holes, a numerical investigation is presumed to be more feasible.

## 7.6. Time-Domain Network Model: Impedance Tuning on the High Pressure Test Rig

In the preceding sections, the actuator concept was investigated in terms of several aspects. CFD simulations showed that the achievable amplitude is high enough for the prospected

application in the industrial test rig. Various experimental results showed that the concept performs superior to comparable methods, features a relatively constant amplitude response, and is robust in terms of operating conditions, such as mean temperature or Mach number variations.

However, as detailed in SEC. 2.4, implementation of the impedance tuning concept, additionally requires a proper phase relation between identification of the downstream propagating acoustic wave and incidence of the actuator's response. If this phase relation is improper, the output signal of the controller could not be generated in time, to successfully superimpose the required acoustic fluctuation on the upstream propagating wave. An investigation, covering this aspect was conducted using a time-domain network model and is presented in this section.

The required input, i. e., the simulated open-loop reflection coefficient (natural reflection, cf. SEC. 2.4) and the actuator transfer function were determined from combined RANS and LEE simulations, the results of which are presented in SUBSEC. 7.3.3.

A schematic of the time-domain network model is depicted in FIG. 7.32. It consists of basic elements such as transfer delays that represent constant area ducts, segments for extraction of the pressure readings, and the upstream and downstream reflection coefficients  $R_{us}$  and  $R_{ol}$ . Furthermore, the components necessary for impedance tuning, i. e., blocks for wave decomposition  $D$ , controller  $K$  and the actuator transfer function  $G$  are incorporated. Within this work it is set up to represent both the cold acoustic test rig from SEC. 7.4 and the industrial test rig's representation from FIG. 7.8.

### 7.6.1. Verification of the Time-Domain Network Model

First of all, the 1D network model's elements were verified, sequentially. Key steps in the verification are presented here. Firstly, the acoustic system depicted in FIG. 7.32 was simulated without the wave decomposition and controller elements, and compared to experimental results. In the second step, the online wave identification  $D$  was validated with the standard frequency-domain Multi-Microphone Method. Finally, the performance of the controller  $K$  was investigated and compared to experimental results.

For the initial simulation of the cold acoustic test rig, the geometric features and the operational parameters from the high-pressure experiment were applied in the model. I. e., typical mean temperatures, pressures, and flow velocities leading to an approximate nozzle Mach number of  $M = 0.6$  were applied. Upstream and downstream reflection coefficients and the actuator transfer function were obtained from experimental data. To that end, the Multi-Microphone Method was evaluated at the highlighted reference planes in FIG. 7.14. The identified discrete frequency-dependent functions from the experiment were translated into

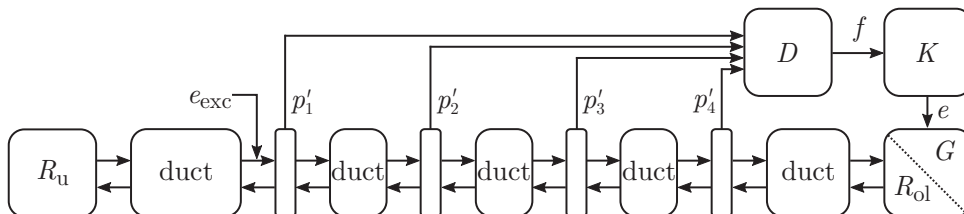


**Figure 7.32.:** Schematic of the 1D time-domain network model for verification of the active modification of the acoustic boundary condition

state-space realizations using system identification tools, as described in SEC. 2.4. Together with the microphone calibration factors, they were subsequently incorporated into the model using standard MATLAB routines. Broadband excitation with added noise was realized in a range from  $f = 50$  Hz to 500 Hz.

For comparison, the cross power spectral density of the upstream sensor (red frame in FIG. 7.14) and the excitation signal was calculated from the experimental data and from the network model. It is depicted in FIG. 7.33. The magnitudes of both match to a certain extent. Deviations result from the actuator transfer behavior, which was not included in the network model. Instead, a constant-amplitude excitation of the loudspeaker throughout the entire frequency range was assumed. Furthermore, the discrete experimental data for the upstream and downstream boundary conditions had to be translated into state-space realizations for inclusion in the model. In the process, they were smoothed and fitted using a sufficiently small number of poles in the *Vector Fitting* routine, in order to keep the system stable. In consequence, the corresponding gains differ slightly throughout the frequency range and thus, the magnitudes deviate, especially at the resonance peaks. However, the important conclusion from this result is that the frequencies of the extreme values are accurately reproduced by the 1D network model. Further, the slopes of both experimental and simulated spectra are in good agreement. Thus, the results indicate correctly implemented time delays.

Subsequently, a generic network model with flow and realistic boundary conditions was set up in order to verify the online wave decomposition's implementation. The resulting  $f$ -wave from the time-domain Multi-Microphone Method was compared to the established frequency-domain variant. FIG. 7.34 depicts magnitude and phase of the separately calculated  $f$ -waves, which are in very good agreement. The image at the top right shows an enlarged portion of the magnitude plot, which reveals accuracy of the implemented scheme. The Multi-Microphone Method in time domain is evaluated at the reference plane at the location of the upstream microphone. Accordingly, the frequency-domain evaluation is performed at the same location with a cross-correlation of the pressure and the excitation signal. The

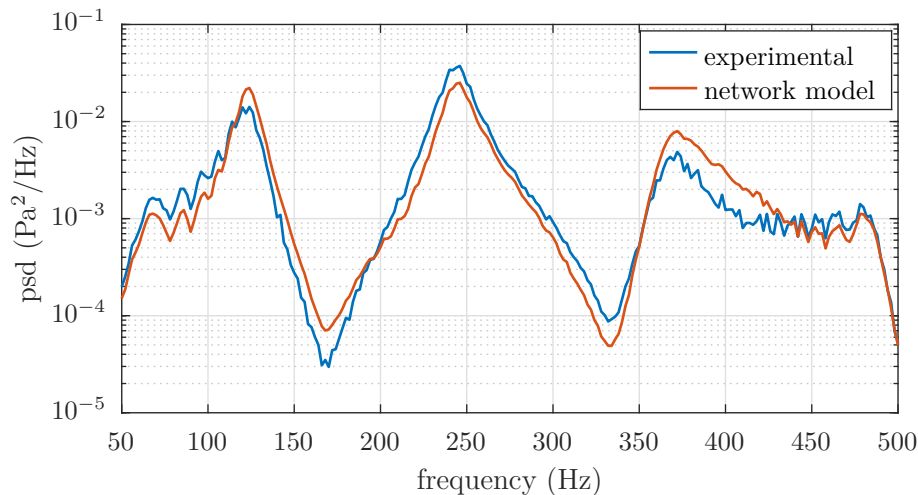


**Figure 7.33.:** Magnitude of the cross power spectral density between excitation and pressure reading at the reference plane in the cold acoustic test rig. Measured in the experiment (blue) and calculated with the 1D network model (orange).

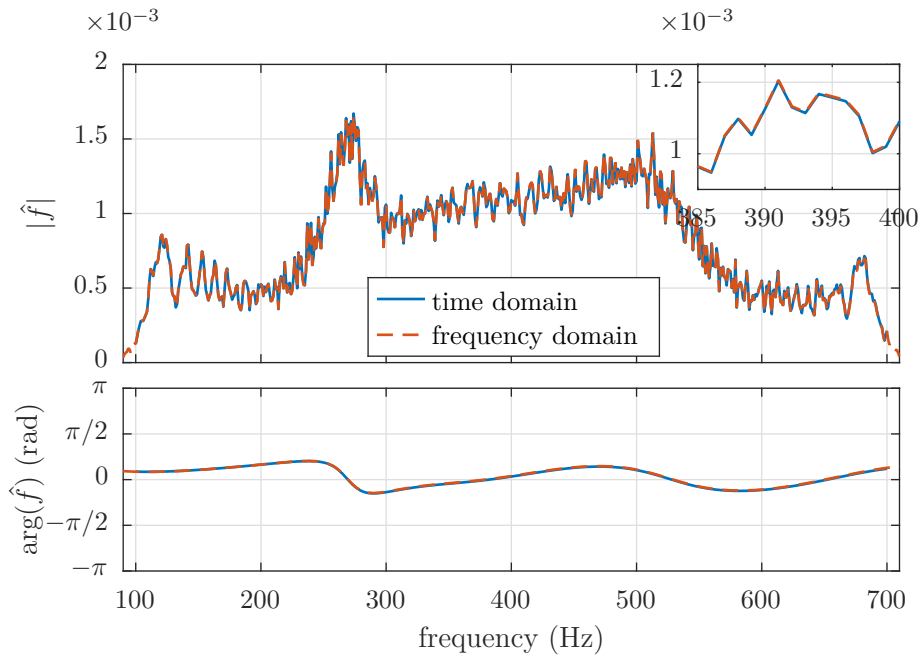


**Figure 7.34.:** Downstream traveling wave  $f$  for non-zero mean flow conditions in the 1D network model obtained from time-domain (blue) and frequency-domain (orange) Multi-Microphone Method. Top: magnitude with enlarged depiction of a small frequency range, bottom: phase at the reference plane.

determined phase plots shows no deviations, hence, the online wave identification is considered as verified.

Validity of the controller was tested using the results from an impedance tuning experiment conducted on the cold acoustic test rig from FIG. 7.14. In the experiment it was shown that the outlet boundary condition of the measurement duct could be successfully altered to various closed-loop reflection coefficients in a range from  $R = 0.2$  to  $1.0$  FIG. 7.35 shows exemplary results from this experiment. The open-loop reflection coefficient is denoted by a solid blue line. With a controller transfer function defined in a frequency range from 150 Hz to 350 Hz, the closed-loop reflection coefficient was adjusted (dashed blue line). The target was an absolute value of  $|R_{cl}| = 0.7$  and the original phase of  $R_{ol}$ . The jagged run of the magnitude of the experimental data (upper image) is presumably due to incorporated large open loudspeaker in close proximity to the outlet boundary.

In the model of the cold acoustic test rig, the open-loop reflection coefficient was smoothed and again fitted with as few poles as possible, in order to keep the simulation stable. As a result, the magnitude of  $R_{ol}$  (solid orange line) in the network model is much smoother than in the experiment. The same holds for the closed-loop reflection coefficient (dashed orange line). The controller was set exactly as in the experiment, leading to the absolute value of the acoustic boundary condition of  $|R_{cl}| \approx 0.7$  in a large frequency range. Deviations of the results presumably originate from the jagged experimental data. The phases of both the experimental and the simulated  $R_{cl}$  are depicted in the lower image. They are in very good agreement with the phase of the open-loop reflection coefficient, which was the target.

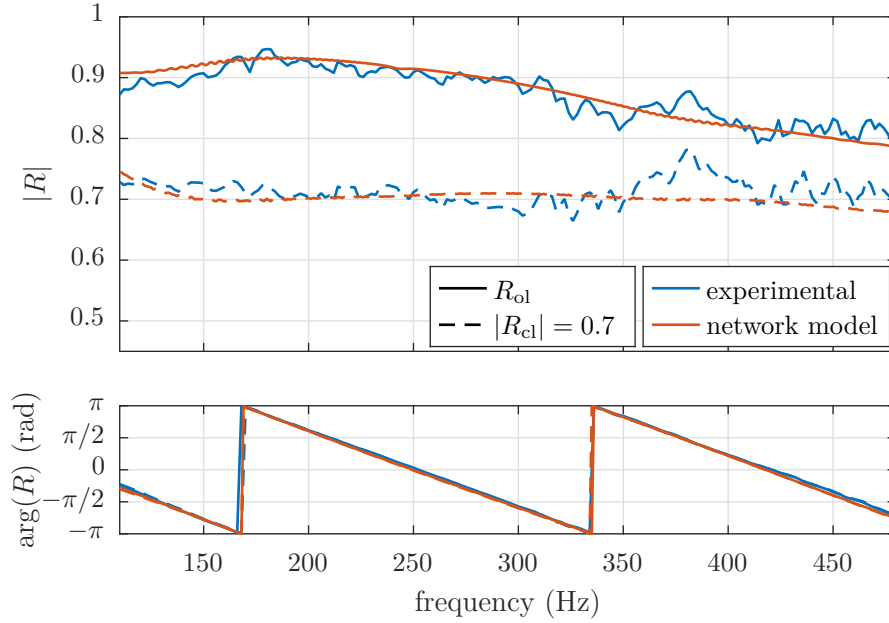


**Figure 7.35.:** Open-loop (solid) and closed-loop (dashed) reflection coefficients experimentally determined (blue) and calculated with the 1D network model. The closed-loop reflection coefficient was tuned to  $|R_{cl}| = 0.7$  in a frequency band from  $f = 150$  Hz to 350 Hz. Top: magnitude, bottom: phase between  $g$  and  $f$  at the reference plane.

Thus, proper functionality of the 1D network model including the online wave decomposition scheme and the controller has been shown.

### 7.6.2. Results of the Simulations with the Time-Domain Network Model

After its verification, the network model was used to simulate the industrial test rig and implementation of the active modification of the acoustic boundary condition. FIG. 7.36 shows the geometry, used for the simulation. All x-coordinates are normalized by the combustion chamber length  $L_{cc}$ , which is defined from the burner base plate to the throat of the VSS. The microphone array is denoted by black and blue dashed lines, the latter representing the axial location of microphone 1. Furthermore, it stands for reference plane 1, relevant for the online wave identification. The orange dashed line (ref. 2) represents the reference plane that

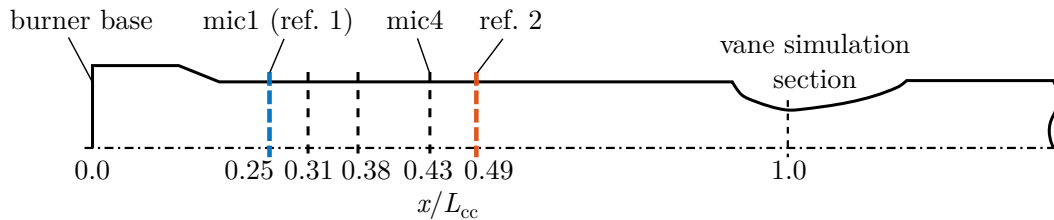


**Figure 7.36.:** Geometry as implemented in the 1D time-domain network model. Locations of the microphone array and reference planes (blue and orange) are normalized by the combustor length  $L_{cc}$ .

was used in the preliminary RANS/LEE simulation in SUBSEC. 7.3.3. The duct downstream of the VSS is cut off in this depiction. Its exact geometry is not required for the model, as it is already incorporated in the  $R_{o1}$ - and  $G$ -data from the input simulations.

The upstream boundary condition at the burner base plate was set to an arbitrary fixed value with zero phase taken from a comparable setup. This slight simplification does not impede validity of the results, as  $R_{us}$  has no influence on the downstream time delays, this investigation focuses on. The operational parameters implemented in the network model are summarized in TAB. 7.2 and TAB. 7.3.

Furthermore, the location of the sensor array in the combustion chamber is of high relevance. The layout given in FIG. 7.36 depicts a sensible option in terms of the constraining factors, which are summarized here. One key parameter is the length of the array, i. e., the axial extent from the upstream to the downstream microphone. Instructions for the appropriate length and layout of sensor arrays for the Multi-Microphone Method is given, for instance, by Schuermans [156]. In summary, the optimal spacing depends on several factors, such as the observed frequency range, damping, or uniformity of the temperature profile. Length and spacing were chosen according to the mentioned publication. The second parameter for the array positioning is the flame location. The microphones need to be located downstream of the flame, due to its acoustic-source character and strong influence on the temperature field. Finally, the distance from the microphone array to the downstream boundary is of significant importance in terms of the applicability of impedance tuning. As mentioned in SEC. 2.4, the time lag between detection of the downstream propagating wave  $f$  and incidence of the naturally reflected acoustic wave at the same reference location has to be larger than the time lag between emission of the actuator output signal and incidence at the sensor array. Note that time lag is not equivalent to the distance in this case, due to the presence of a non-zero bulk-velocity. Hence, the phase of the controller transfer function  $K$ , relating the aforementioned time delays, was investigated for several sensor array locations. According to EQ. 2.48,  $K$  was calculated using input data taken from the RANS/LEE simulations detailed in SUBSEC. 7.3.3.

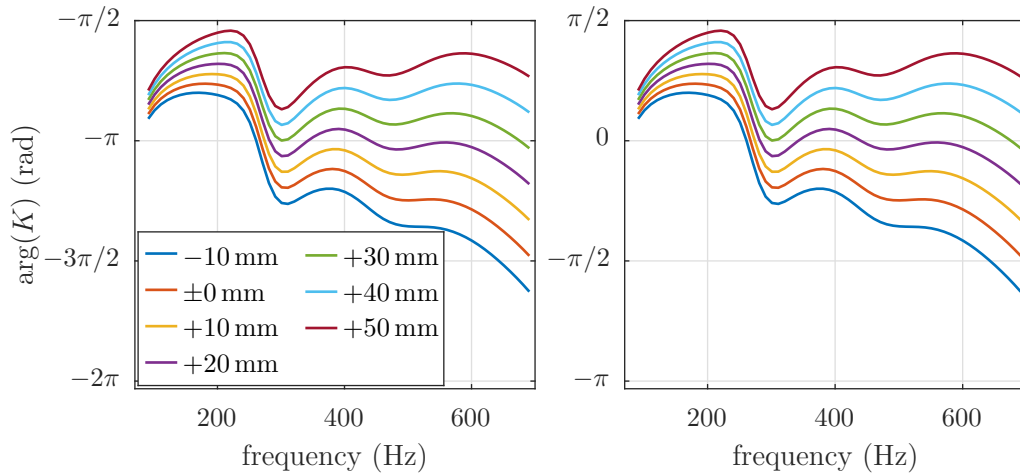


**Figure 7.37.:** Phase of the controller transfer function  $K$  for various offsets of the sensor array along the  $x$ -coordinate of the combustion chamber. Left:  $\arg(K)$  for  $|R_{cl}| = 0.2$ , right:  $\arg(K)$  for  $|R_{cl}| = 1.0$

FIG. 7.37 depicts the phase of the controller transfer function for several axially varied sensor array locations (denoted by colors) and two different closed-loop reflection coefficients (left and right). Since the reference plane for the online wave identification is set to the location of the first microphone, an artificial time lag corresponding to the distance from the first reference plane to the second (cf. FIG. 7.36) was incorporated into any calculation of  $K$ .

To account for various sensor array locations, the phase difference was varied in steps of the equivalent of 10 mm. A negative value, indicated in the legend of FIG. 7.37, corresponds to an upstream shift of the sensor array location, while a positive value denotes a downstream shift. At both  $R_{cl}$ -values, the phase runs are qualitatively similar, yet, their phases are shifted by  $\pi$ . The reason lies in the open-loop reflection coefficient, which assumes absolute values between both closed-loop values. Thus, the controller destructively interferes with the incident sound wave when controlling to a lower reflection coefficient ( $|R_{cl}| = 0.2$ ) and constructively interferes to attain an increased reflection ( $|R_{cl}| = 1.0$ ). For the applicability of the active control of the boundary condition, the slope of the controller transfer function's phase is highly relevant. A decreasing phase over the frequency renders the controller causal, i. e., the input signal arrives at the controller before the output signal needs to be send [18]. As depicted in FIG. 7.37, shifting the sensor array upstream increases the frequency ranges, in which this condition is met and therefore the probability of a successful application of the scheme. On the other hand, a downstream shift reduces the frequency ranges with decreasing phases, which diminishes the scheme's applicability range.

However, the array's distance to the burner base plate has a certain minimum, which is dictated by the flame location. Note that the flame's extent is not fixed and depends on the operating point. Furthermore, near-field effects are to be expected. Thus, the required distance to burner base plate is higher than the typical axial extent of the flame. Considering the constraints on the sensor array's location, the suggested layout in FIG. 7.36 is the optimum and will be used throughout the remainder of this section.

Subsequently, the 1D time-domain network model was set up according to FIG. 7.32. As in the preliminary investigation of  $K$ , the open-loop reflection coefficient and the actuator transfer function from the RANS/LEE simulation in SUBSEC. 7.3.3 were implemented in state-space form. All parameters were set up in order to realistically represent the high pressure test rig. External forcing was realized using a custom sweep function operating in a frequency range from 50 Hz to 800 Hz. Artificial noise was generated and superimposed on the excitation. The first simulation aims to demonstrate the control concept's ability of modifying the open loop-reflection coefficient to the following targeted absolute values:  $|R_{cl}| = [0.0, 0.2, 0.4, 1.0]$ . Results are depicted in FIG. 7.38. The required controller transfer functions were generated in frequency ranges, in which control was possible (denoted with colored dashed lines).

The open-loop reflection coefficient is colored in blue and the simulated closed-loop reflection factors for the desired magnitudes are presented in the remaining colors. The controlled frequency ranges are different for each configuration, as the setup of the control law depends on several factors and might not be possible in the same frequency bands for any desired  $R_{cl}$ . Main constraints were the stability of the network model, which could not be ensured for higher numbers of poles, i. e., control laws with higher accuracy.

For a virtually anechoic end (solid orange line), a maximum deviation of  $\Delta|R| = 0.08$  from the desired value (dashed orange line) is observed. Due to the low amplitudes, the phase values are not relevant in this case. For desired magnitudes of  $|R_{cl}| = 0.2$  and 0.4, deviations

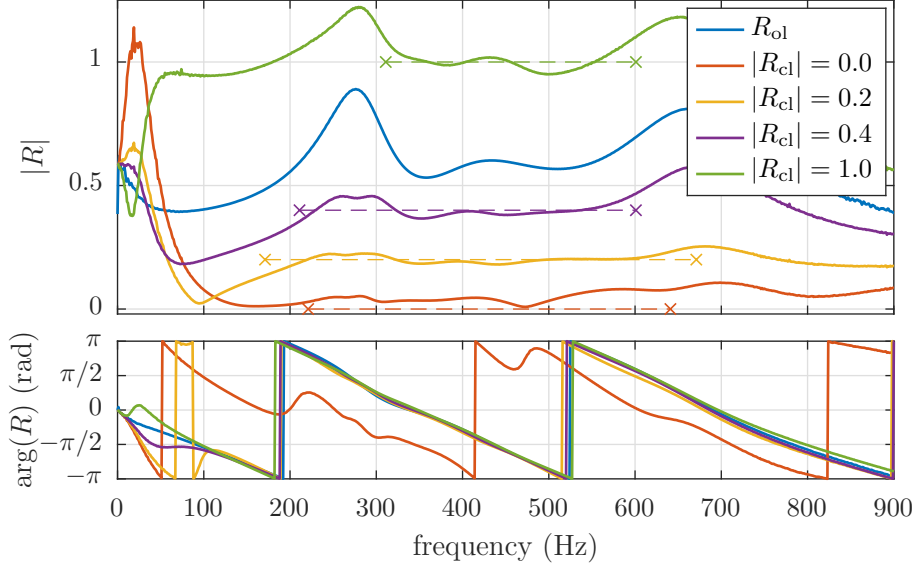


**Figure 7.38.:** Open-loop and closed-loop reflection coefficients. Top: magnitude of  $R_{ol}$  (blue),  $|R_{cl}| = 0.0$  (orange),  $|R_{cl}| = 0.2$  (yellow),  $|R_{cl}| = 0.4$  (purple), and  $|R_{cl}| = 1.0$  (green). Frequency ranges for control are indicated by dashed lines and the corresponding colors. Bottom: phase between  $g$  and  $f$  at the reference plane.

are  $\Delta|R| < 0.06$ . Modification to a fully reflective boundary condition was successful in a frequency range from 310 Hz to 600 Hz, with maximum deviations below 7% of the desired magnitude. At lower frequencies, control was not possible, which is presumed to originate from a badly conditioned controller transfer function, leading to strong reflections from  $f = 240$  Hz to 300 Hz.

The closed-loop phase for all configurations, except anechoic conditions, is accurately tuned in the corresponding frequency ranges. Setting up a controller transfer function in frequency bands, where the magnitude of  $R_{cl}$  coincides with the open-loop reflection coefficient, is intricate. The reason lies in the phase of  $K$ , which accordingly needs to incorporate jumps of  $180^\circ$ . Using smaller frequency bands, control would be possible.

Another key application of impedance tuning is phase modification of  $R_{cl}$ . In that way, virtual additional lengths of the combustor can be realized, effectively changing its resonance frequencies without physical alterations. In the according simulation, magnitudes of the closed-loop reflection coefficients were adjusted to the open-loop case, while the phase was varied. The results for four different virtual additional lengths from  $\Delta L = 0.1$  m to 1.2 m are shown in FIG. 7.39. The top and center image depict magnitude and phase of the open-loop and closed-loop reflection coefficients, respectively. Slopes of the phases are steeper for larger virtual extents of the combustion chamber. The simulated values of the virtual additional lengths are calculated from the closed-loop phases with

$$\Delta L = \frac{\Delta\varphi\bar{c}}{2\omega}, \quad (7.11)$$

where  $\Delta\varphi$  is the phase difference between  $R_{ol}$  and  $R_{cl}$ . Frequency-dependent values for  $\Delta L$  are depicted in the bottom image of FIG. 7.39. The frequency range, in which control was realized,

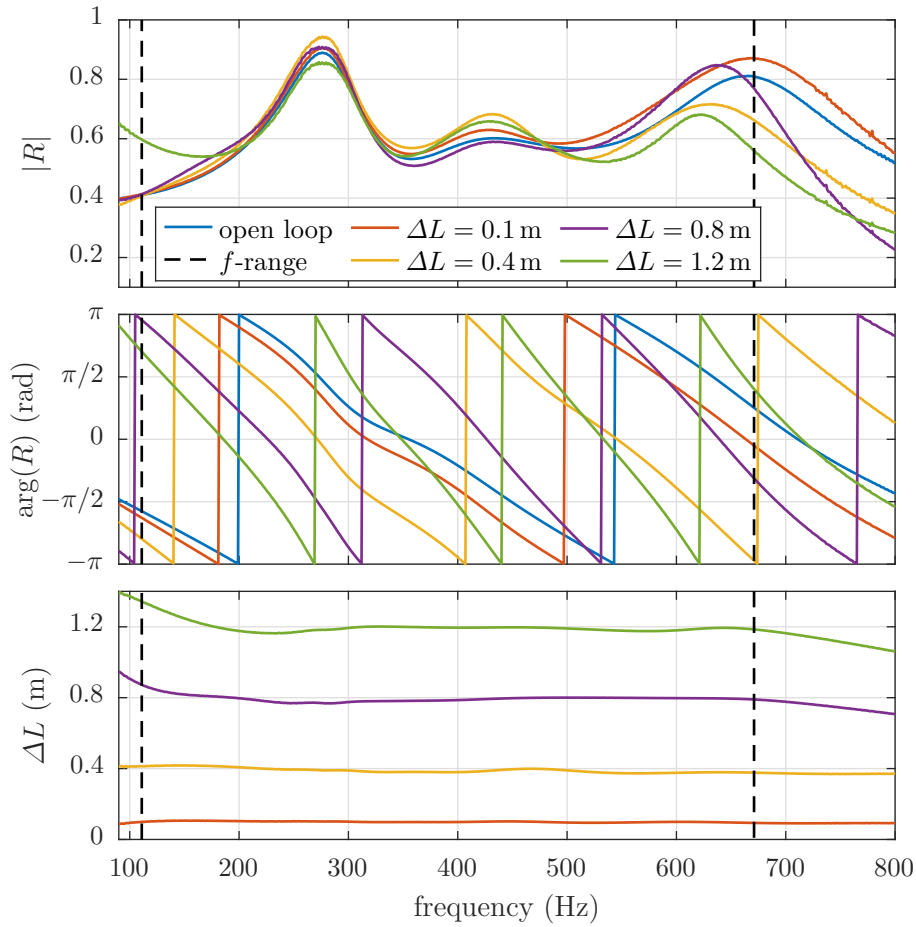


**Figure 7.39.:** Top: magnitude of the open-loop (blue) and four closed-loop reflection coefficients (remaining colors). Controlled frequency range:  $f = 111$  Hz to  $671$  Hz (black dashed line). Center: phase between  $g$  and  $f$  at the reference plane. Bottom: Virtual additional lengths for four different target values calculated from phase difference and controlled frequency range.

is delimited by dashed black lines. For virtual additional lengths of  $0.1$  m and  $0.4$  m, a high accuracy was achieved throughout the entire frequency range. Except for lower frequencies, the same holds for virtual additional lengths of  $0.8$  m and  $1.2$  m. Here, deviations from the targeted values increase to  $8\%$  and  $11\%$ , respectively. In the latter case, the magnitude of  $R_{cl}$  significantly deviates from the open-loop values, as well. Likewise, at frequencies above  $500$  Hz, the controlled magnitudes differ noticeably from the target value. Total deviations grow with virtual additional length. However, regarding the intermediate frequency range considered in this work, these errors are acceptable.

In the context of application at the industrial test rig, the controller's reaction to transient input signals is of great relevance. Due to combustion noise, not only consisting of time-harmonic signals, other signal types were simulated with the time-domain network model, as well. FIG. 7.40 depicts the actuator's response  $Ge$  (orange) to transient perturbation signals  $R_{cl}f$ , which are reflected at the system boundary, and the resulting upstream propagating

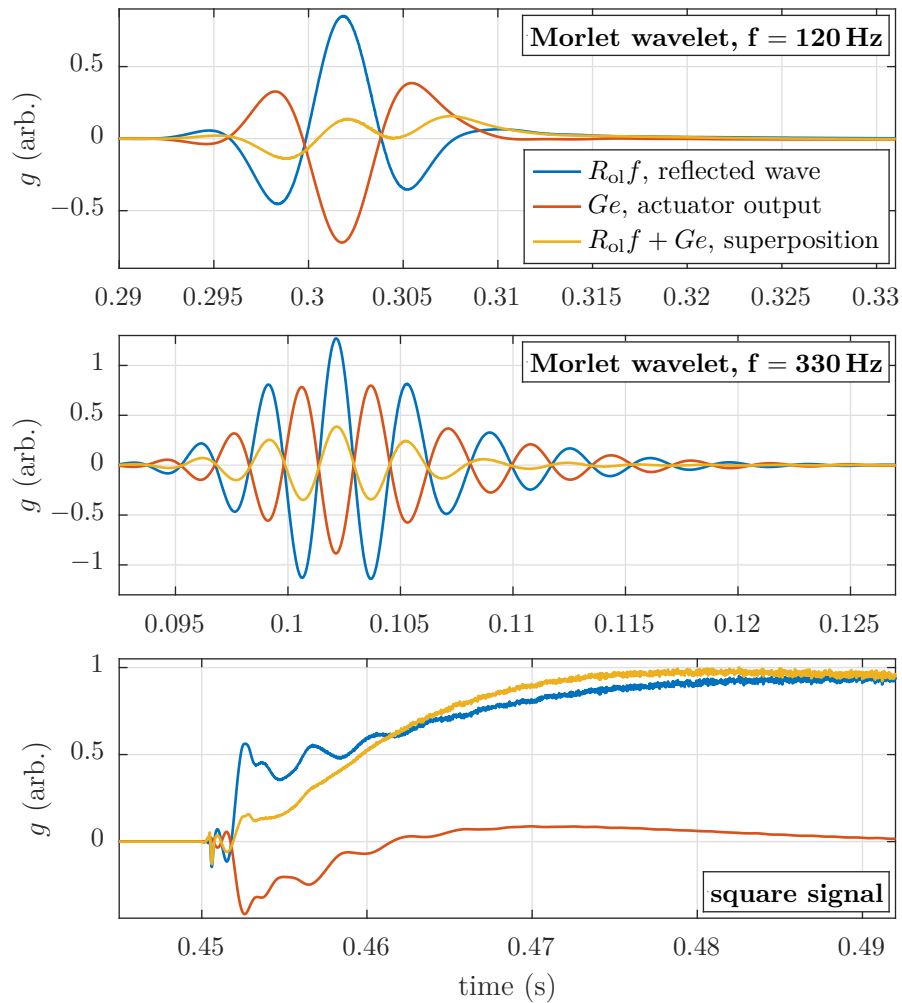


**Figure 7.40.:** Three transient perturbation signals, represented by the reflected wave  $R_{ol}f$  (blue), the corresponding actuator response signal  $Ge$  (orange) and the resulting superposition (yellow) at a set closed-loop reflection coefficient of  $|R_{cl}| = 0.2$  plotted over time.

wave  $g$ , which is a superposition of both (conf. EQ. 2.43). Results are plotted over time for three different transient input signals.

The first two are Morlet wavelets, which consist of a harmonic wave localized by a Gaussian window. They are centered at frequencies of  $f = 120$  Hz and  $330$  Hz, which are typical for such signals in the industrial test rig. The closed-loop reflection coefficient is set to  $|R_{cl}| = 0.2$  in every case shown. It is apparent that the controller functions as intended. Its reaction to the perturbation is instant, which shows in the incident wave being immediately superimposed with a corresponding actuator output. The resulting reflection coefficient, which may be deduced from the time series, matches the target value exactly and there are no overshoots or reverberations. The bottom image shows data for a square perturbation signal. As with the wavelets, the response is instant and no overshoot is apparent, despite the sharp input signal. Any fluctuations in the perturbation signal are immediately counteracted, thus, smoothing the acoustic wave returned into the system.

The above investigations, conducted in a realistically set up network model, show that the active modification of magnitude and phase of the acoustic boundary condition is possible as intended at the high pressure test rig. Although the distance between sensor array and injection location is limited and the injection channel for the modulated secondary air needs to have a minimum length, the time lags suffice for enabling the impedance tuning scheme. Furthermore, the time-resolved response to transient input signals is investigated and proper functionality of the controller is predicted.

### 7.7. Discussion of the Downstream Actuator Concept

In the beginning of this chapter, various actuator concepts are discussed in terms of their ability to fulfill the requirements posed in SEC. 3.4. The most promising concept is found to be a modulated air injection into the restriction downstream of the combustion chamber. Due to utilization of the blockage introduced by air injection into the smallest cross-section, a significant increase in efficiency of the secondary air injection is expected. Furthermore, the location far downstream is beneficial for the implementation of impedance tuning. Similar air injection schemes from the literature are reviewed, although they were conducted within the field of aviation research, and thus, focus on different operational parameters. However, some general physical relations are comparable and dimensionless parameters are adopted for use in this work.

Subsequently, CFD simulations under realistic test rig conditions were conducted. They show that the actuator concept is capable of achieving the required amplitudes, and thereby, deliver a mass flow target for the modulated secondary air. Furthermore, the mechanism of sound generation is indicated to be connected to an oscillating vortex shedding, rather than the injection acting as a volume source. As expected, a linear increase of the sound pressure amplitude with mean density in the test rig is shown. Technically relevant mean temperature variations do not exhibit a significant influence on the excitation amplitude, which is later substantiated by experimental results.

The required number of proportional valves is calculated using data from preliminary experiments. First of all, the regarded frequency range determines the type of valve that may be used. A larger frequency range comes at the cost of a lower throughput, which could be compensated for by an increased supply pressure. All things considered, it is expected that a reasonable amount of valves is sufficient for the actuation concept to achieve adequately large excitation amplitudes on the high pressure test rig with both investigated valves.

Further experiments were conducted on a modular atmospheric test rig, equipped with a generic nozzle. Under comparable circumstances, a 45° inclination of the injected mass flow towards the incoming main air flow proved to be more efficient than standard 90° injection. Furthermore, a siren-type mechanical actuation delivered lower amplitudes throughout all test cases. It was also shown that injection into the nozzle throat yields far higher amplitudes than a similar injection at the combustor wall, which confirms results of the CFD. The concept was further characterized by altering several operational parameters, while keeping characteristic variables constant. It was found that an increase in the unactuated nozzle Mach number at a constant momentum flux ratio yields a saturation effect in the achievable amplitude for values of  $M > 0.5$ . However, a minimum Mach number is required in order to couple the excitation to the combustion chamber acoustics.

In the last section, a one-dimensional time-domain network model of the high pressure test rig is detailed. The aim of this study was to verify that the relevant time lags for application of impedance tuning are in an appropriate ratio. The necessary boundary conditions and the actuator transfer function were computed with a combined RANS and LEE simulation. Initially, the sensor array location was examined in terms of the phase of the actuator transfer function. Results show that the scheme is applicable in large portions of the regarded frequency range. The broadband active modification of the acoustic boundary condition was demonstrated by successfully imposing various absolute values of closed-loop reflection coefficient and several virtual additional lengths of the combustion chamber. Furthermore, the system's response to a transient input signal was presented and the controller was found to function in a robust and reliable way.

Aside from the purpose described in this thesis, the presented actuator concept may be used for other applications, as well. For example, it could be utilized for active instability control in a closed-loop configuration designed for impedance control, as pointed out by Bothien et al. [21]. Alternatively an open-loop scheme could be utilized, such as the one described by Čosić et al. [40]. An advantage over the active instability control approaches described in references [71, 163] is the working medium. In the mentioned publications, the valves were used for a modulated fuel injection. However, due to the composition of natural gas, corrosion of the valves poses an issue. The problem can be eliminated by instead using the proposed injection of air into the first vane stage.

Note that active control of combustion instabilities is not limited to stationary gas turbines. It may also be of relevance in aviation, where the use of compressor or fan bleed air for thrust control or thrust vectoring is already considered feasible [43, 110]. The additional instruments for incorporation of active instability control merely include suitable sensors and a controller. Further, the utilized valves need to be capable of air flow modulation at the required frequencies. However, as pointed out in references [63, 77, 142], even solenoid valves are viable options, when incorporated in suitable closed-loop control schemes.



# CHAPTER 8

---

## Conclusion

---

Among the crucial steps in the development of new gas turbine combustion systems are experimental investigations to determine the susceptibility to thermoacoustic instabilities. In early development stages, the transfer behavior of combustors is measured at atmospheric pressure conditions. The results are used as input for low-order network models, which aim to predict the stability characteristics of the combustion system. A subsequent step consists of high pressure tests. As the operational parameters may be adapted to those of the engine, reliability and comparability of the results are increased. However, the acoustic boundary conditions may differ, as for instance, interaction with neighboring combustors cannot be reproduced in single-burner test rigs [84]. Thus, the risk of encountering combustion instabilities in full scale engine tests remains. In the worst case, alterations of the advanced design become necessary, which is highly expensive for the manufacturer. Incorporation of an active modification of the acoustic boundary conditions, especially that downstream of the combustion chamber, would remedy this issue.

Bothien et al. [18, 20–22, 24, 26] and Moeck et al. [112] successfully developed such a method for broadband and discrete active impedance control with different actuators and applied it to combustion test rigs. *Impedance tuning* allows for imposing of quasi-arbitrary boundary conditions on an acoustically actuated test rig termination. Thus, fully reflecting conditions may be simulated without the need for a choked exit, anechoic conditions are possible, and virtually variable combustor lengths can be imposed without hardware modifications. Employment of the scheme on a test rig with high correlation to the engine, thus, enables a highly realistic direct assessment of several characteristics. The entire operating envelope of a new combustor system can be thoroughly tested in terms of exhaust gas emissions, efficiency, acoustic behavior, and their interrelations. Thereby, especially the risk of susceptibility to thermoacoustic oscillations can be strongly minimized before moving to full scale engine tests.

The necessary equipment for impedance tuning, complemented by an additional sensor array, may further be used to determine the flame transfer behavior. As the operating conditions are very similar to those in the engine, the results are highly reliable compared to those obtained from atmospheric experiments.

In essence, the aim of this thesis is a concept for a high pressure test rig allowing for a thermoacoustic characterization and impedance tuning at the combustor outlet. The required hardware modifications need to account for the existing test rig geometry, which closely resembles the engine. The proposed concept comprises actuators and sensors both upstream

and downstream of the flame. Once the equipment is implemented, the industrial test rig will grant efficient opportunities for the development of new combustor systems and advances in the research on thermoacoustic phenomena. Within the following passages, the corresponding investigations and key results of this thesis are summarized.

The fixed design of the industrial test rig impedes a straightforward measurement of acoustic pressure and particle velocity directly upstream of the burner, which are required for a thermoacoustic characterization. Hence, suitable methods for determination of these variables needed to be developed. The first option, described in the thesis, is a sensor array located in a passage of constant cross-section upstream of the combustor plenum. This method requires additional determination of the plenum's transfer behavior. The corresponding calculations incorporate an analytical approach to obtain the transfer behavior, which is complemented by numerical simulations. Thereby, the acoustic variables may be obtained in a flexible and accurate way. The second option utilizes the unsteady pressure drop over the burner. It allows for calculation of the velocity fluctuations at the burner inlet (cf. reference [160]). Both proposed options are expected to be viable solutions. Their individual advantages and disadvantages are discussed and practical considerations will determine a final implementation.

Determination of the acoustic variables inside the combustor is imperative for the realization of impedance tuning. However, as the combustion chamber comprises a curved geometry with a variable cross-sectional area, the standard method for a plane wave decomposition needed to be adapted. The solution to Webster's horn equation [189] and its extension to mean flows by Rienstra [144] were used for development of a frequency-domain and a time-domain variant of the Multi-Microphone Method for ducts with non-uniform cross-sections. On account of the combustion chamber's shape, the necessary solutions to the wave equation can only be obtained using numerical simulations. The results show the method to yield accurate reconstructions of the apparent sound pressure field for both frequency-domain and time-domain implementations of the technique. Note that the final employment in the high pressure test rig requires additional simulations with mean flow in order to determine the scattering matrices between the probes. In this step, the proposed relocation of the sensor array to the combustion chamber bottom should be investigated. As these simulations are required in any case, the benefit of the adjustment is easily assessed, with a potentially strong increase in the method's accuracy.

The developed method is of high relevance for the determination of acoustic properties in any applications that incorporate segments of slowly varying cross-sectional areas. Especially in the case of combustion chambers for stationary applications or aviation, acoustic measurements generally require the rigs to be redesigned. Straight ducts need to be employed to utilize standard techniques for wave identification. This simplification becomes unnecessary by incorporating the proposed method. Thereby, a higher correlation between test rig and engine can be achieved and costs for redesigning can be reduced.

For the acoustic excitation upstream of the burner, a siren actuator is proposed. It fulfills the stated requirements and has proven its reliability in similar applications (e. g., references [36, 49, 83, 152, 160]). A siren may be tailored to the needs of the regarded high pressure test rig and experienced manufacturers are available. In this work, the location and several options of mounting are investigated in terms of FEM simulations. The results indicate that the best performance is achieved by forcing at the burner base plate via symmetrically arranged inlet holes. However, in combination with a sensor array in the flow sleeve, a positioning further

upstream at the flow box is required. A horn-shaped connection performed best among the investigated mounting options at that location. Yet, its theoretical advantage has to be carefully weighed up against the required expenditures.

The core of this thesis is the actuator design for the region downstream of the flame. Acoustic excitation at this location is the key element for impedance tuning and it is required for measurements of the flame transfer matrix. It has to fulfill demanding requirements, the sum of which, no current actuator type is capable of. Initially, several possible actuators are discussed. From this discussion, a concept is derived. It employs proportional valves injecting modulated air into the restriction downstream of the combustion chamber. A literature survey on related injection concepts (e.g., references [9, 42, 43, 110, 111]) yielded initial indications for the implementation of the method. Subsequently, CFD simulations were conducted to determine the achievable amplitude and the corresponding mass flow to be injected. Furthermore, the simulations indicated that the concept's underlying mechanism is based on oscillatory vortex shedding rather than acting as an acoustic volume source.

In subsequent experimental investigations, the necessary amount of valves was sought. Given a sufficient supply pressure, the number of required valves is considered to be feasible for application at the high pressure test rig. Furthermore, several of the actuation concept's properties were characterized using an atmospheric test rig. A generic nozzle allowed for a modulated secondary air injection with a proportional valve. Dependence on the nozzle Mach number, the momentum flux ratio, injection angle, and exhaust gas temperatures are discussed. Furthermore, it is shown that nozzle injection performs superior to an upstream injection at the combustor wall. It also delivers higher fluctuation amplitudes than comparable mechanical actuation at the nozzle throat, which was for example employed by Hochgreb et al. [75]. In the final step, a time-domain network model is described, which verifies the actuation concept's functionality with regard to the occurring time lags in the high pressure test rig.

In summary, the numerical and experimental investigations show that the actuator concept is capable of fulfilling the demanding requirements for achieving sufficient acoustic forcing amplitudes and how this amplitude scales with different operating parameters. Further, simulations indicate that the time lags are favorable for the implementation of impedance tuning at the regarded industrial test rig.

Note that additional application purposes for the developed actuation concept are possible. Due to its ability to generate high amplitude pressure fluctuations, it may be viable for active instability control in both stationary and aviation gas turbines. With the move towards lean combustion processes in airborne gas turbines, an active instability control gains importance. Especially, aviation applications with fluidic thrust control [43] could profit, as only few additional instruments are required, simplifying the implementation.

### 8.1. Additional Efforts for the Final Implementation

In this work, a concept for both an implementation of a thermoacoustic characterization, i.e., measurement of the flame transfer matrix, and the active modification of the downstream acoustic boundary condition in an existing industrial combustion test rig from SIEMENS PG are detailed. With the help of a small number of finalizing investigations, this specific test rig and also similar facilities can be outfitted with the proposed sensors and actuators. Thereby, significant advancements in the field of thermoacoustic investigations for new combustor systems are possible.

For the final hardware implementation of the upstream sensors detailed in CHAP. 4, one of the two proposed approaches needs to be chosen according to practical and monetary considerations. If the concept from SEC. 4.2 is to be implemented, validating numerical or experimental investigations are to be conducted. These are required, as the proposed concept was based on simplified geometries and focused on derivation of a procedure, applicable in high pressure tests. Thus, in the next step, the exact plenum geometry has to be incorporated and the obtained transfer matrix needs to be conditioned to be valid in the entire operational parameter space. If the alternative approach from SEC. 4.3 is followed, additional input parameters, describing the burner, need to be fitted. Likewise, experimental investigations are necessary, which presumably need to be conducted on the high pressure test rig.

In CHAP. 5, an extension of the Multi-Microphone Method for ducts of non-uniform cross-section was developed, in order to allow for a wave decomposition in the combustion chamber. Final implementation of the concept requires an additional numerical investigation for determination of the scattering matrices between each of the sensors and the reference planes. Within this study, eligible locations of the pressure sensors with respect to hardware restrictions need to be investigated. Inclusion of practically applicable positions at the bottom of the combustor wall is highly recommended, as significant increases in the method's accuracy are expected. With the resulting data, performance of the sensor locations can be evaluated and sensor positions can be finalized. Ultimately, calibration of the sensors and their installation on the test rig enable application of the concept. Note that a potential for errors remains due to ceramic liners, which may cause significant damping. The effect needs to be compensated for by incorporation of an appropriate wave propagation constant (cf. reference [175]). Furthermore, a significant axial temperature gradient could impede application of the Multi-Microphone Method and would require additional modifications to the wave decomposition scheme. Possible solutions to various families of mean temperature profiles in quiescent conditions are presented in references [103, 171–173]. In the regarded high pressure test rig, mean Mach numbers at the sensor array approach – and in some operational points exceed – values of  $M = 0.1$ , necessitating a scheme that works under mean flow conditions.

The options for positioning of a siren for upstream acoustic forcing of the test rig are discussed in CHAP. 6. Depending on the sensor concept in the upstream region, excitation at the burner base plate may not be viable. If both alternatives are possible, the performance differences need to be weighed up against practical and monetary considerations regarding the hardware implementation. The final step is the compilation of specifications for the production of the siren according to the elaborations in SUBSEC. 6.1.1.

Application of the proposed concept for downstream acoustic excitation requires acquisition of suitable proportional valves, the availability of which has been affirmed. As explained in CHAP. 7, an additional investigation for determination of the final layout of the injector holes in the vane simulation section is necessary. The amount of holes needs to be investigated in terms of internal structure and material properties of the liquid-cooled vanes. Furthermore, inclination of the injection channels towards the incoming main air is to be studied. Issues related to cooling deficiencies with inactive secondary air supply need to be considered, as well. Depending on the eventual amount of available valves, achieving of the required air mass flow at the respective supply pressure is presumed to pose the demand of an extra compressor. In summary, the modifications for downstream acoustic excitation necessitate design and

manufacturing of special vanes and an infrastructure for secondary air supply. Additionally, the proportional valves themselves and their control units need to be acquired.

Once the entire setup is implemented and tested, regular measurements by technical personnel require development of graphical user interfaces. Key features should enable sensor calibration, flame transfer matrix measurements, and application of the active modification of the acoustic boundary condition. These steps generally require simultaneous acoustic excitation and pressure measurements. Further, online monitoring for sensor failures should be included. Implementation of impedance tuning initially requires attendance of a specifically trained engineer.



---

## Bibliography

---

- [1] M. Åbom. ‘A Note on the Experimental Determination of Acoustical Two-Port Matrices’. In: *Journal of Sound and Vibration* 155.1 (1992), pp. 185–188. DOI: [10.1016/0022-460X\(92\)90655-H](https://doi.org/10.1016/0022-460X(92)90655-H).
- [2] M. Åbom and H. Bodén. ‘Error analysis of two-microphone measurements in ducts with flow’. In: *The Journal of the Acoustical Society of America* 83.6 (1988), pp. 2429–2438. DOI: [10.1121/1.396322](https://doi.org/10.1121/1.396322).
- [3] P. Akbari, R. Nalim, and N. Mueller. ‘A Review of Wave Rotor Technology and its Applications’. In: *Journal of Engineering for Gas Turbines and Power* 128.4 (Jan. 2006), pp. 717–735. DOI: [10.1115/1.2204628](https://doi.org/10.1115/1.2204628).
- [4] A. Ali, C. Rodriguez, A. Neely, and J. Young. ‘Combination of Fluidic Thrust Modulation and Vectoring in a 2D Nozzle’. In: *48th AIAA/ASME/SAE/ASEE Joint Propulsion Conference and Exhibit*. Paper no. AIAA 2012-3780. 2012, pp. 1–13. DOI: [10.2514/6.2012-3780](https://doi.org/10.2514/6.2012-3780).
- [5] A. Andreini, B. Facchini, A. Innocenti, and D. Pampaloni. ‘Investigation of Mean-flow Effects on Tubular Combustion Chamber Thermoacoustics Using a Burner Transfer Matrix Approach’. In: *Proceedings of the 2014 COMSOL Conference*. 2014, pp. 1–7.
- [6] Ansaldo Energia. *Gas Turbines - GT26*. English. accessed on 03-23-2018. 2018. URL: <https://www.ansaldoenergia.com/Pages/GT26.aspx>.
- [7] M. Baptista, A. Rasheed, B. Badding, and O. Velagandula. ‘Response in a Multi-tube Pulsed Detonation Combustor-Turbine Hybrid System’. In: *Proc. AIAA Aerospace Sciences Meeting and Exhibit, January 9-12, Reno, Nevada, USA*. Paper no. AIAA 2006-1234. 2006, pp. 1–12. DOI: [10.2514/6.2006-1234](https://doi.org/10.2514/6.2006-1234).
- [8] V. Bartels. ‘Headset with Active Noise-Reduction System for Mobile Applications’. In: *Journal of the Audio Engineering Society* 40.4 (1992), pp. 277–281.
- [9] D. Baruzzini, N. Domel, and D. N. Miller. ‘Pulsed Injection Flow Control for Throttling in Supersonic Nozzles-A Computational Fluid Dynamics Design Study’. In: *Proc. 37th AIAA Fluid Dynamics Conference and Exhibit, 25-28 June, Miami, FL, USA*. Paper no. AIAA 2007-4215. 2007, pp. 1–15. DOI: [10.2514/6.2007-4215](https://doi.org/10.2514/6.2007-4215).
- [10] V. Bellucci. ‘Modeling and Control of Gas Turbine Thermoacoustic Pulsations’. PhD thesis. Technische Universität Berlin, 2009.

- [11] V. Bellucci, B. Schuermans, D. Nowak, P. Flohr, and C. O. Paschereit. ‘Thermoacoustic Modeling of a Gas Turbine Combustor Equipped With Acoustic Dampers’. In: *ASME Journal of Turbomachinery* 127.2 (2005), pp. 372–379. DOI: [10.1115/1.1791284](https://doi.org/10.1115/1.1791284).
- [12] C. A. Belsterling. *Fluidic Systems Design*. John Wiley & Sons, Inc., 1971.
- [13] E. E. Bender, D. N. Miller, B. R. Smith, P. J. Yagle, P. J. Vermeulen, and S. H. Walker. ‘Simulation of Pulsed Injection in a Cross Flow Using 3-D Unsteady CFD’. In: *Fluids 2000 Conference and Exhibit*. Paper no. AIAA 2000-2318. 2000, pp. 1–9. DOI: [10.2514/6.2000-2318](https://doi.org/10.2514/6.2000-2318).
- [14] B. C. Bobusch, J. P. Moeck, C. O. Paschereit, and S. Sadig. ‘Thermoacoustic Stability Analysis of a Kerosene-Fueled Lean Direct Injection Combustor Employing Acoustically and Optically Measured Transfer Matrices’. In: *Proc. of ASME Turbo Expo 2012*. Paper no. GT2012-69034. 2012, pp. 781–794. DOI: [0.1115/GT2012-69034](https://doi.org/0.1115/GT2012-69034).
- [15] B. C. Bobusch. ‘Fluidic Devices for Realizing the Shockless Explosion Combustion Process’. PhD thesis. Technische Universität Berlin, 2015, pp. 1–188. DOI: [10.14279](https://doi.org/10.14279).
- [16] H. Bodén and M. Åbom. ‘Influence of errors on the two-microphone method for measuring acoustic properties in ducts’. In: *The Journal of the Acoustical Society of America* 79.2 (1986), pp. 541–549. DOI: [10.1121/1.393542](https://doi.org/10.1121/1.393542). eprint: <http://dx.doi.org/10.1121/1.393542>.
- [17] M. R. Bothien, J. P. Moeck, and C. O. Paschereit. ‘Experimental Validation of Linear Stability Analysis in Premixed Combustors Supported by Active Control’. In: *Proc. of the 14th International Congress on Sound and Vibration*. 2007.
- [18] M. R. Bothien. ‘Impedance Tuning: A Method for Active Control of the Acoustic Boundary Conditions of Combustion Test Rigs’. PhD thesis. Technische Universität Berlin, 2008.
- [19] M. R. Bothien, J. P. Moeck, A. Lacarelle, and C. O. Paschereit. ‘Time Domain Modelling and Stability Analysis of Complex Thermoacoustic Systems’. In: *Proceedings of the Institution of Mechanical Engineers, Part A: Journal of Power and Energy* 221.5 (Jan. 2007), pp. 657–668. DOI: [10.1243/09576509JPE384](https://doi.org/10.1243/09576509JPE384).
- [20] M. R. Bothien, J. P. Moeck, and C. O. Paschereit. ‘Impedance Tuning of a Premixed Combustor Using Active Control’. In: *Proc. of ASME Turbo Expo, May 14-17, Montreal, Canada*. Paper no. GT2007-27796. 2007, pp. 607–617. DOI: [10.1115/GT2007-27796](https://doi.org/10.1115/GT2007-27796).
- [21] M. R. Bothien, J. P. Moeck, and C. O. Paschereit. ‘Active control of the acoustic boundary conditions of combustion test rigs’. In: *Journal of Sound and Vibration* 318.4-5 (2008), pp. 678–701. DOI: [10.1016/j.jsv.2008.04.046](https://doi.org/10.1016/j.jsv.2008.04.046).
- [22] M. R. Bothien, J. P. Moeck, and C. O. Paschereit. ‘Assessment of Different Actuator Concepts for Acoustic Boundary Control of a Premixed Combustor’. In: *Journal of Engineering for Gas Turbines and Power* 131.2 (2009), p. 021502. DOI: [10.1115/1.2969088](https://doi.org/10.1115/1.2969088).
- [23] M. R. Bothien, J. P. Moeck, and C. O. Paschereit. ‘Experimental Validation of Linear Stability Analysis in a Premixed Combustor by Actively Tuning its Acoustic

- Boundary Conditions’. In: *Proc. ASME Turbo Expo, June 8-12, Orlando, USA*. Paper no. GT2009-60019. 2009, pp. 787–798. DOI: [10.1115/GT2009-60019](https://doi.org/10.1115/GT2009-60019).
- [24] M. R. Bothien, J. P. Moeck, and C. O. Paschereit. ‘Comparison of Linear Stability Analysis With Experiments by Actively Tuning the Acoustic Boundary Conditions of a Premixed Combustor’. In: *Journal of Engineering for Gas Turbines and Power* 132.12 (2010), p. 121502. DOI: [10.1115/1.4000806](https://doi.org/10.1115/1.4000806).
- [25] M. R. Bothien, N. Noiray, and B. Schuermans. ‘A Novel Damping Device for Broadband Attenuation of Low-Frequency Combustion Pulsations in Gas Turbines’. In: *Journal of Engineering for Gas Turbines and Power* 136.4 (2013), p. 041504. DOI: [10.1115/1.4025761](https://doi.org/10.1115/1.4025761).
- [26] M. R. Bothien and C. O. Paschereit. ‘Tuning of the Acoustic Boundary Conditions of Combustion Test Rigs With Active Control: Extension to Actuators With Nonlinear Response’. In: *Journal of Engineering for Gas Turbines and Power* 132.9 (2010), p. 091503. DOI: [10.1115/1.4000599](https://doi.org/10.1115/1.4000599).
- [27] M. R. Bothien, D. A. Penelli, M. Zajadatz, and K. Döbbling. ‘On Key Features of the AEV Burner Engine Implementation for Operational Flexibility’. In: *Proc. ASME Turbo Expo, June 3-7, San Antonio, Texas, USA*. 2013, pp. 1–9. DOI: [10.1115/GT2013-95693](https://doi.org/10.1115/GT2013-95693).
- [28] Bundesverband der Deutschen Heizungsindustrie. *NO<sub>x</sub>-Emission bei Feuerungsanlagen - Entstehung, Reduktionsmöglichkeiten, Messtechnik und aktuelle Grenzwerte*. 2016.
- [29] A. Buttler, J. Hentschel, S. Kahlert, and M. Angerer. *Statusbericht Flexibilitätsbedarf im Stromsektor - Eine Analyse der aktuellen marktwirtschaftlichen und technischen Herausforderungen an Speicher und Kraftwerke im Zuge der Energiewende*. German. accessed on 23-03-2018. Technische Universität München - Lehrstuhl für Energiesysteme. Mar. 2015. URL: [https://www.es.mw.tum.de/fileadmin/w00bhq/www/pdf/Statusbericht\\_Flexibilitaetsbedarf\\_2014\\_Final.pdf](https://www.es.mw.tum.de/fileadmin/w00bhq/www/pdf/Statusbericht_Flexibilitaetsbedarf_2014_Final.pdf).
- [30] B. Caldecott and J. McDaniels. *Stranded generation assets: Implications for European capacity mechanisms, energy markets and climate policy*. English. accessed on 03-26-2018. Jan. 2014. URL: <http://www.smithschool.ox.ac.uk/research/sustainable-finance/publications/Stranded-Generation-Assets.pdf>.
- [31] N. Caldwell, A. Glaser, and E. Gutmark. ‘Acoustic Interactions of a Pulse Detonation Engine’. In: *Proc. AIAA Aerospace Sciences Meeting and Exhibit, January 9-12, Reno, Nevada, USA*. Paper no. AIAA 2006-1233. 2006, pp. 1–10. DOI: [10.2514/6.2006-1233](https://doi.org/10.2514/6.2006-1233).
- [32] G. Campa and S. M. Camporeale. ‘Application of Transfer Matrix Method in Acoustics’. In: *Proceedings of the COMSOL Conference, Paris, France*. 2010, pp. 1–7.
- [33] G. Campa and S. M. Camporeale. ‘Eigenmode Analysis of the Thermoacoustic Combustion Instabilities Using a Hybrid Technique Based on the Finite Element Method and the Transfer Matrix Method’. In: *Advances in Applied Acoustics* 1.1 (2012), pp. 1–14.
- [34] A. M. Cargill. ‘Low frequency acoustic radiation from a jet pipe-a second order theory’. In: *Journal of Sound and Vibration* 83.3 (1982), pp. 339–354. DOI: [10.1016/S0022-460X\(82\)80097-7](https://doi.org/10.1016/S0022-460X(82)80097-7).

- [35] M. Cazalens, S. Roux, C. Sensiau, and T. Poinso. ‘Combustion Instability Problems Analysis for High-Pressure Jet Engine Cores’. In: *Journal of Propulsion and Power* 24.4 (2008), pp. 770–778. DOI: [10.2514/1.30938](https://doi.org/10.2514/1.30938).
- [36] W. S. Cheung, G. J. M. Sims, R. W. Copplestone, J. R. Tilston, C. W. Wilson, S. R. Stow, and A. P. Dowling. ‘Measurement and Analysis of Flame Transfer Function in a Sector Combustor Under High Pressure Conditions’. In: *Proc. ASME Turbo Expo, June 16-19, Atlanta, Georgia, USA*. Paper no. GT2003-38219. 2003, pp. 187–194. DOI: [10.1115/GT2003-38219](https://doi.org/10.1115/GT2003-38219).
- [37] J. Y. Chung and D. A. Blaser. ‘Transfer function method of measuring in-duct acoustic properties’. In: *Journal of the Acoustical Society of America* 68.3 (1980), pp. 907–913. DOI: [10.1121/1.384778](https://doi.org/10.1121/1.384778).
- [38] COMSOL 5.2a Acoustics Module. *COMSOL Multiphysics - Acoustics Module*. User’s Guide. 2017.
- [39] COMSOL 5.2a Reference Manual. *COMSOL Multiphysics - Reference Manual*. User’s Guide. 2016.
- [40] B. Ćosić, B. C. Bobusch, J. P. Moeck, and C. O. Paschereit. ‘Open-Loop Control of Combustion Instabilities and the Role of the Flame Response to Two-Frequency Forcing’. In: *Journal of Engineering for Gas Turbines and Power* 134.6 (2012), p. 061502. DOI: [10.1115/1.4005986](https://doi.org/10.1115/1.4005986).
- [41] B. Ćosić, T. G. Reichel, and C. O. Paschereit. ‘Acoustic Response of a Helmholtz Resonator Exposed to Hot-Gas Penetration and High Amplitude Oscillations’. In: *Journal of Engineering for Gas Turbines and Power* 134.10 (2012), p. 101503. DOI: [10.1115/1.4007024](https://doi.org/10.1115/1.4007024).
- [42] K. A. Deere. ‘Summary of fluidic thrust vectoring research conducted at NASA langley research center’. In: *21st AIAA Applied Aerodynamics Conference, 23-26 June, Orlando, FL, USA*. Paper no. AIAA-2003-3800. 2003, pp. 1–18. DOI: [10.2514/6.2003-3800](https://doi.org/10.2514/6.2003-3800).
- [43] K. A. Deere, B. L. Berrier, J. D. Flamm, and S. K. Johnson. ‘A Computational Study of a New Dual Throat Fluidic Thrust Vectoring Nozzle Concept’. In: *41st AIAA/ASME/SAE/ASEE Joint Propulsion Conference and Exhibit, 10 - 13 July, Tucson, AZ, USA* (2005), pp. 1–16. DOI: [10.2514/6.2005-3502](https://doi.org/10.2514/6.2005-3502).
- [44] I. D. J. Dupère and A. P. Dowling. ‘The Use of Helmholtz Resonators in a Practical Combustor’. In: *Journal of Engineering for Gas Turbines and Power* 127.2 (2005), pp. 268–275. DOI: [10.1115/1.1806838](https://doi.org/10.1115/1.1806838).
- [45] K. Ehrenfried. *Strömungsakustik*. 1st ed. Mensch & Buch, July 2004.
- [46] F. Farisco. ‘Thermo-acoustic characterization of the burner-turbine interface in a can-annular combustor using CFD’. PhD thesis. Enschede, The Netherlands: University of Twente, 2016, pp. 1–140.
- [47] F. Farisco, L. Panek, B. Janus, and J. B. W. Kok. ‘Numerical Investigation of the Thermo-Acoustic Influence of the Turbine on the Combustor’. In: *Proc. ASME Turbo*

- Expo, June 15-19, Montreal, Canada*. Paper no. GT2015-42071. 2015, pp. 1–10. DOI: [10.1115/GT2015-42071](https://doi.org/10.1115/GT2015-42071).
- [48] M. Ferlauto and R. Marsilio. ‘Numerical Investigation of the Dynamic Characteristics of a Dual-Throat-Nozzle for Fluidic Thrust-Vectoring’. In: *AIAA Journal* 55.1 (2017), pp. 86–98. DOI: [10.2514/1.J055044](https://doi.org/10.2514/1.J055044).
- [49] E. Freitag, H. Konle, M. Lauer, C. Hirsch, and T. Sattelmayer. ‘Pressure Influence on the Flame Transfer Function of a Premixed Swirling Flame’. In: *Proc. ASME Turbo Expo, May 8-11, Barcelona Spain*. Paper no. GT2006-90540. 2006, pp. 477–486. DOI: [10.1115/GT2006-90540](https://doi.org/10.1115/GT2006-90540).
- [50] E. Freitag. ‘On the Measurement and Modelling of Flame Transfer Functions at Elevated Pressure’. PhD thesis. Technische Universitaet Muenchen, 2009, pp. 1–213.
- [51] General Electric. *TAPS II Combustor - Final Report*. English. accessed on 04-30-2018. Mar. 2014. URL: [https://www.faa.gov/about/office\\_org/headquarters\\_offices/apl/research/aircraft\\_technology/cleen/reports/media/TAPS\\_II\\_Public\\_Final\\_Report.pdf](https://www.faa.gov/about/office_org/headquarters_offices/apl/research/aircraft_technology/cleen/reports/media/TAPS_II_Public_Final_Report.pdf).
- [52] A. Gentemann, A. Fischer, S. Evesque, and W. Polifke. ‘Acoustic Transfer Matrix Reconstruction and Analysis for Ducts with Sudden Change of Area’. In: *9th AIAA/CEAS Aeroacoustics Conference and Exhibit, May 12-14, 2003, Hilton Head, South Carolina*. Paper no. AIAA 2003-3142. 2003, pp. 1–11. DOI: [10.2514/6.2003-3142](https://doi.org/10.2514/6.2003-3142).
- [53] A. Giauque, F. Nicoud, and M. Brear. ‘Numerical assessment of stability criteria from disturbance energies in gaseous combustion’. In: *13th AIAA/CEAS Aeroacoustics Conference (28th AIAA Aeroacoustics Conference)*. 2007, pp. 1–12. DOI: [10.2514/6.2007-3425](https://doi.org/10.2514/6.2007-3425).
- [54] C. J. Greenshields. *OpenFOAM User Guide*. v5.0. OpenFOAM Foundation Ltd. July 2017.
- [55] E. M. Greitzer, C. S. Tan, and M. B. Graf. *Internal Flow - Concepts and Applications*. Cambridge University Press, 2006.
- [56] R. Gu and J. Xu. ‘Effects of Cavity on the Performance of Dual Throat Nozzle During the Thrust-Vectoring Starting Transient Process’. In: *Journal of Engineering for Gas Turbines and Power* 136.1 (2014), p. 0145021. DOI: [10.1115/1.4025243](https://doi.org/10.1115/1.4025243).
- [57] D. Guicking. ‘On the invention of active noise control by Paul Lueg’. In: *Journal of the Acoustical Society of America* 87.5 (1990), pp. 2251–2254. DOI: [10.1121/1.399195](https://doi.org/10.1121/1.399195).
- [58] D. Guicking and K. Karcher. ‘Active Impedance Control for One-Dimensional Sound’. In: *Journal of Vibration, Acoustics, Stress, and Reliability in Design* 106.July 1984 (1984), pp. 393–396. DOI: [10.1115/1.3269207](https://doi.org/10.1115/1.3269207).
- [59] F. Gunter and F. Fahrenholz. ‘Final report on a study of rocket thrust control by gas injection’. In: *Massachusetts Institute of Technology Naval Supersonic Laboratory* (1961). Technical Report 448.

- [60] B. Gustavsen. *User's Guide for vectfit3.m (Fast, Relaxed Vector Fitting) for Matlab*. SINTEF Energy Research. N-7465 Norway, 2008.
- [61] B. Gustavsen and A. Semlyen. 'Rational approximation of frequency domain responses by vector fitting'. In: *IEEE Transactions on Power Delivery*. Vol. 14. 3. 1999, pp. 1052–1061. DOI: [10.1109/61.772353](https://doi.org/10.1109/61.772353).
- [62] D. Guyot, B. Bobusch, and C. Paschereit. 'Active Combustion Control Using a Fluidic Oscillator for Asymmetric Fuel Flow Modulation'. In: *AIAA/ASME/SAE/ASEE 44th Joint Propulsion Conference and Exhibit, July 21-23, Hartford, CT*. Paper no. AIAA 2008-4956. 2008, pp. 1–19. DOI: [10.2514/6.2008-4956](https://doi.org/10.2514/6.2008-4956).
- [63] D. Guyot, M. R. Bothien, J. P. Moeck, and C. O. Paschereit. 'Active control of combustion instability using fuel flow modulation'. In: *Proceedings in Applied Mathematics and Mechanics* 7.1 (Dec. 2007), pp. 4090015–4090016. DOI: [10.1002/pamm.200700715](https://doi.org/10.1002/pamm.200700715).
- [64] D. Guyot and C. O. Paschereit. 'Optical Transfer Function Measurements for a Swirl Burner at Atmospheric Pressure'. In: *Proc. AIAA Joint Propulsion Conference & Exhibit, August 2-5, Denver, Colorado, USA*. 2009. DOI: [10.2514/6.2009-5413](https://doi.org/10.2514/6.2009-5413).
- [65] C. R. Hanna and J. Slepian. 'The Function and Design of Horns for Loudspeakers (Reprint)'. In: *Journal of the Audio Engineering Society* 25.9 (1977), pp. 573–585.
- [66] N. Hanraths. 'Numerical Simulation of the Acoustic Response Resulting from the Periodic Injection of Fluid into a Subsonic Nozzle'. Master thesis. TU Berlin, 2016, pp. 1–70.
- [67] Y. Hardalupas and M. Orain. 'Local measurements of the time-dependent heat release rate and equivalence ratio using chemiluminescent emission from a flame'. In: *Combustion and Flame* 139.3 (Nov. 2004), pp. 188–207. DOI: [10.1016/j.combustflame.2004.08.003](https://doi.org/10.1016/j.combustflame.2004.08.003).
- [68] C. Hassa, J. Heinze, and K. Stursberg. 'Investigation of the Response of an Air Blast Atomizer Combustion Chamber Configuration on Forced Modulation of Air Feed at Realistic Operating Conditions'. In: *Journal of Engineering for Gas Turbines and Power* 125.4 (2003), pp. 872–878. DOI: [10.1115/1.1584478](https://doi.org/10.1115/1.1584478).
- [69] M. A. Heckl. 'Non-linear Acoustic Effects in the Rijke Tube'. In: *Acta Acustica united with Acustica* 72.1 (1990), pp. 63–71.
- [70] E.-G. Hencke and D. Manske. *Statusreport 2013 - Fossil befeuerte Großkraftwerke in Deutschland*. German. accessed on 03-26-2018. Dec. 2013. URL: [https://m.vdi.de/uploads/media/3544\\_BR0\\_TW\\_GEU\\_Statusreport\\_Fossil\\_befeuerte\\_Grosskraftwerke.pdf](https://m.vdi.de/uploads/media/3544_BR0_TW_GEU_Statusreport_Fossil_befeuerte_Grosskraftwerke.pdf).
- [71] J. Hermann and A. Orthmann. 'Combustion Dynamics: Application of Active Instability Control to Heavy Duty Gas Turbines'. In: *RTO-EN-20* (2001), pp. 1–16.
- [72] I. Hernández, G. Staffelbach, T. Poinso, J. C. Román, and J. B. W. Kok. 'LES and acoustic analysis of thermo-acoustic instabilities in a partially premixed model combustor'. In: *Combustion, Flow and Spray Dynamics for Aerospace Propulsion* 341.1-2 (2013), pp. 121–130. DOI: [10.1016/j.crme.2012.11.003](https://doi.org/10.1016/j.crme.2012.11.003).

- [73] B. Higgins, M. Q. McQuay, F. Lacas, J. C. Rolon, N. Darabiha, and S. Candel. ‘Systematic measurements of OH chemiluminescence for fuel-lean, high-pressure, premixed, laminar flames’. In: *Fuel* 80 (2001), pp. 67–74. DOI: [10.1016/S0016-2361\(00\)00069-7](https://doi.org/10.1016/S0016-2361(00)00069-7).
- [74] B. Higgins. ‘On the sound produced by a current of hydrogen gas passing through a tube’. In: *Journal of Natural Philosophy, Chemistry and the Arts* 1 (1802), pp. 129–131.
- [75] S. Hochgreb, I. Ayranci, D. Dennis, W. Bainbridge, and S. Cant. ‘Forced and Self-Excited Instabilities from Lean Premixed, Liquid-Fuelled Aeroengine Injectors at High Pressures and Temperatures’. In: *Proc. ASME Turbo Expo, June 3-7, San Antonio, Texas, USA*. Paper no. GT2013-95311. 2013, V01BT04A023. DOI: [10.1115/GT2013-95311](https://doi.org/10.1115/GT2013-95311).
- [76] J. D. Holdeman and R. E. Walker. ‘Mixing of a Row of Jets with a Confined Crossflow’. In: *AIAA Journal* 15.2 (1977), pp. 243–249. DOI: [10.2514/3.60622](https://doi.org/10.2514/3.60622).
- [77] Z. Hong, J. M. Haynes, J. T. Herbon, and K. R. Mcmanus. ‘Dynamic Suppression in Liquid-Fueled Combustors Using Fuel-Modulation’. In: *Proc. ASME Turbo Expo, June 11-15, Copenhagen, Denmark*. 2012, pp. 1277–1286. DOI: [10.1115/GT2012-69703](https://doi.org/10.1115/GT2012-69703).
- [78] Y. Huang and V. Yang. ‘Dynamics and stability of lean-premixed swirl-stabilized combustion’. In: *Progress in Energy and Combustion Science* 35.4 (2009), pp. 293–364. DOI: [10.1016/j.pecs.2009.01.002](https://doi.org/10.1016/j.pecs.2009.01.002).
- [79] S. Hubbard and A. P. Dowling. ‘Acoustic Resonances of an Industrial Gas Turbine Combustion System’. In: *Journal of Engineering for Gas Turbines and Power* 123.4 (2001), pp. 766–773. DOI: [10.1115/1.1370975](https://doi.org/10.1115/1.1370975).
- [80] A. Innocenti, A. Andreini, and B. Facchini. ‘Numerical Identification of a Premixed Flame Transfer Function and Stability Analysis of a Lean Burn Combustor’. In: *Energy Procedia* 82 (2015), pp. 358–365. DOI: [10.1016/j.egypro.2015.11.803](https://doi.org/10.1016/j.egypro.2015.11.803).
- [81] International Energy Agency. *World Energy Outlook 2017 - Executive Summary*. English. accessed on 03-23-2018. 2017. URL: <https://www.iea.org/publications/freepublications/publication/world-energy-outlook-2017---executive-summary---english-version.html>.
- [82] J. F. van Kampen, J. B. W. Kok, and T. H. van der Meer. ‘Efficient retrieval of the thermo-acoustic flame transfer function from a linearized CFD simulation of a turbulent flame’. In: *International Journal for Numerical Methods in Fluids* 54 (2007), pp. 1131–1149. DOI: [10.1002/flid](https://doi.org/10.1002/flid). arXiv: [fld.1](https://arxiv.org/abs/fld.1) [DOI: [10.1002](https://doi.org/10.1002)].
- [83] M. Kapucu, J. B. W. Kok, and P. R. Alemela. ‘Comparison of Two Methods for Flame Transfer Function Measurements: Moog Valve of Siren and the Impact of Results on the Instability Analysis in a High Pressure Combustor’. In: *Proc. ASME Turbo Expo, June 11-15, Copenhagen, Denmark*. Paper no. GT2012-69250. 2012, pp. 897–907. DOI: [10.1115/GT2012-69250](https://doi.org/10.1115/GT2012-69250).
- [84] P. Kaufmann, W. Krebs, R. Valdes, and U. Wever. ‘3D Thermoacoustic Properties of Single Can and Multi Can Combustor Configurations’. In: *Proc. ASME Turbo*

- Expo, June 9-13, Berlin, Germany.* Paper no. GT2008-50755. 2008, pp. 527–538. DOI: [10.1115/GT2008-50755](https://doi.org/10.1115/GT2008-50755).
- [85] J. Kopitz and W. Polifke. ‘CFD-based application of the Nyquist criterion to thermoacoustic instabilities’. In: *Journal of Computational Physics* 227.14 (2008), pp. 6754–6778. DOI: [10.1016/j.jcp.2008.03.022](https://doi.org/10.1016/j.jcp.2008.03.022).
- [86] K. Kostrzewa, B. Noll, M. Aigner, J. Lepers, W. Krebs, B. Prade, and M. Huth. ‘Validation of advanced computational methods for determining flame transfer functions in gas turbine combustion systems’. In: *Proc. ASME Turbo Expo, May 14-17, Montreal, Canada.* Paper no. GT2007-27267. 2007, pp. 145–155. DOI: [10.1115/GT2007-27267](https://doi.org/10.1115/GT2007-27267).
- [87] W. Krebs, S. Bethke, J. Lepers, P. Flohr, C. Johnson, and S. Sattinger. ‘Thermoacoustic Design Tools And Passive Control: Siemens Power Generation Approaches’. In: *Combustion Instabilities In Gas Turbine Engines: Operational Experience, Fundamental Mechanisms, and Modeling.* American Institute of Aeronautics and Astronautics, 2005, pp. 89–111. DOI: [10.2514/5.9781600866807.0089.0112](https://doi.org/10.2514/5.9781600866807.0089.0112).
- [88] S. M. Kuo and D. R. Morgan. ‘Active Noise Control: A Tutorial Review’. In: *Proc. IEEE* 87.6 (1999), pp. 943–973. DOI: [10.1109/5.763310](https://doi.org/10.1109/5.763310).
- [89] D. Laera, G. Campa, S. M. Camporeale, E. Bertolotto, S. Rizzo, F. Bonzani, A. Ferrante, and A. Saponaro. ‘Modelling of thermoacoustic combustion instabilities phenomena: Application to an experimental test rig’. In: *Energy Procedia* 45 (2014), pp. 1392–1401. DOI: [10.1016/j.egypro.2014.01.146](https://doi.org/10.1016/j.egypro.2014.01.146).
- [90] N. Lamarque and T. Poinso. ‘Boundary Conditions for Acoustic Eigenmodes Computation in Gas turbine Combustion Chambers’. In: *AIAA Journal* 46.9 (2008), pp. 2282–2292. DOI: [10.2514/1.35388](https://doi.org/10.2514/1.35388).
- [91] M. Lauer and T. Sattelmayer. ‘On the Adequacy of Chemiluminescence as a Measure for Heat Release in Turbulent Flames With Mixture Gradients’. In: *Journal of Engineering for Gas Turbines and Power* 132.6 (2010), p. 061502. DOI: [10.1115/1.4000126](https://doi.org/10.1115/1.4000126).
- [92] A. H. Lefebvre. ‘Lean Premixed/Prevaporized Combustion’. In: *Workshop, 20-21 Jan., Cleveland, OH, United States.* Report no. NASA-CP-2016, E-9255. NASA. 1977, pp. 1–50.
- [93] H. Levine and J. Schwinger. ‘On the Radiation of Sound from an Unflanged Circular Pipe’. In: *Physical Review* 73.4 (1948), pp. 383–406. DOI: [10.1103/PhysRev.73.383](https://doi.org/10.1103/PhysRev.73.383).
- [94] T. Lieuwen. ‘Modeling Premixed Combustion-Acoustic Wave Interactions: A Review’. In: *Journal of Propulsion and Power* 19.5 (2003), pp. 765–781. DOI: [10.2514/2.6193](https://doi.org/10.2514/2.6193).
- [95] T. Lieuwen, H. Torres, C. Johnson, and B. T. Zinn. ‘A Mechanism of Combustion Instability in Lean Premixed Gas Turbine Combustors’. In: *Journal of Engineering for Gas Turbines and Power* 123.1 (2001), pp. 182–189. DOI: [10.1115/1.1339002](https://doi.org/10.1115/1.1339002).
- [96] T. C. Lieuwen and V. Yang. *Combustion Instabilities in Gas Turbine Engines: Operational Experience, Fundamental Mechanisms, and Modeling.* Ed. by F. K. Lu, V. Yang, and T. C. Lieuwen. Vol. 210. Progress in Astronautics and Aeronautics. UT Arlington: American Institute of Aeronautics and Astronautics, Inc., 2005, pp. 1–634.

- [97] M. J. Lighthill. ‘On sound generated aerodynamically I. General theory’. In: *Proceedings of the Royal Society of London* 211.1107 (1952), pp. 564–587. DOI: [10.1098/rspa.1954.0049](https://doi.org/10.1098/rspa.1954.0049).
- [98] L. Ljung. *System Identification: Theory for the User*. 2nd. Prentice Hall, Upper Saddle River, New Jersey, 1999, pp. 475–476. DOI: [10.1016/0005-1098\(89\)90019-8](https://doi.org/10.1016/0005-1098(89)90019-8).
- [99] F. K. Lu and E. M. Braun. ‘Rotating Detonation Wave Propulsion: Experimental Challenges, Modeling, and Engine Concepts’. In: *Journal of Propulsion and Power* 30.5 (2014), pp. 1125–1142. DOI: [10.2514/1.B34802](https://doi.org/10.2514/1.B34802).
- [100] P. Lueg. *Process of Silencing Sound Oscillations*. US Patent no. 2,043,416. 1936.
- [101] J. Luetche. ‘Testing and Validation of Large Gas Turbines’. In: *Proc. POWER-GEN Europe, Milano, Italy, June 21- 23*. 2016, pp. 1–13.
- [102] M. A. Macquisten, M. Whiteman, S. R. Stow, and A. J. Moran. ‘Exploitation of Measured Flame Transfer Functions for a Two- Phase Lean Fuel Injector to Predict Thermoacoustic Modes in Full Annular Combustors’. In: *Proc. ASME Turbo Expo, June 16-20, Düsseldorf, Germany*. Paper no. GT2014-25036. 2014, V04AT04A003. DOI: [10.1115/GT2014-25036](https://doi.org/10.1115/GT2014-25036).
- [103] B. Manoj Kumar and R. I. Sujith. ‘Exact Solution for One-Dimensional Acoustic Fields in Ducts With Polynomial Mean Temperature Profiles’. In: *Journal of Vibration and Acoustics* 120 (1998), pp. 965–969. DOI: [10.1115/1.2893927](https://doi.org/10.1115/1.2893927).
- [104] F. Marble and S. Candel. ‘Acoustic disturbance from gas non-uniformities convected through a nozzle’. In: *Journal of Sound and Vibration* 55.2 (Nov. 1977), pp. 225–243. DOI: [10.1016/0022-460X\(77\)90596-X](https://doi.org/10.1016/0022-460X(77)90596-X).
- [105] C. E. Martin, L. J.-L. Benoit, Y. Sommerer, F. Nicoud, and T. Poinsot. ‘Large-Eddy Simulation and Acoustic Analysis of a Swirled Staged Turbulent Combustor’. In: *AIAA Journal* 44.4 (2006), pp. 741–750. DOI: [10.2514/1.14689](https://doi.org/10.2514/1.14689).
- [106] M. S. Mason and W. J. Crowther. ‘Fluidic Thrust Vectoring for Low Observable Air Vehicles’. In: *2nd AIAA Flow Control Conference, 28 June - 1 July, Portland OR, USA*. Paper no. AIAA 2004-2210. 2004, pp. 1–11. DOI: [10.2514/6.2004-2210](https://doi.org/10.2514/6.2004-2210).
- [107] G. A. Mensah and J. P. Moeck. ‘Acoustic Damper Placement and Tuning for Annular Combustors: An Adjoint-Based Optimization Study’. In: *Journal of Engineering for Gas Turbines and Power* 139.6 (2017), p. 061501. DOI: [10.1115/1.4035201](https://doi.org/10.1115/1.4035201).
- [108] G. A. Mensah and J. P. Moeck. ‘Limit Cycles of Spinning Thermoacoustic Modes in Annular Combustors: A Bloch-Wave and Adjoint Perturbation Approach’. In: *Proc. ASME Turbo Expo, June 26-30, Charlotte, NC, USA*. Paper no. GT2017-64817. 2017, V04BT04A046. DOI: [10.1115/GT2017-64817](https://doi.org/10.1115/GT2017-64817).
- [109] J. H. Miles. ‘Acoustic transmission matrix of a variable area duct or nozzle carrying a compressible subsonic flow’. In: *Journal of the Acoustical Society of America* 69.6 (1981), pp. 1577–1586. DOI: [10.1121/1.385961](https://doi.org/10.1121/1.385961).

- [110] D. N. Miller, P. J. Yaglef, and J. W. Hamstra. ‘Fluidic Throat Skewing for Thrust Vectoring in Fixed-Geometry Nozzles’. In: *37th Aerospace Sciences Meeting and Exhibit*. Paper no. AIAA 99-0365. 1999, pp. 1–9. DOI: [10.2514/6.1999-365](https://doi.org/10.2514/6.1999-365).
- [111] D. N. Miller, P. J. Yagle, E. E. Bender, B. R. Smith, and P. J. Vermeulen. ‘A Computational Investigation of Pulsed Injection into a Confined, Expanding Crossflow’. In: *15th AIAA Computational Fluid Dynamics Conference* June (2001). Paper no. AIAA 2001-3026, pp. 1–11. DOI: [10.2514/6.2001-3026](https://doi.org/10.2514/6.2001-3026).
- [112] J. P. Moeck, M. R. Bothien, and C. O. Paschereit. ‘An Active Control Scheme for Tuning Acoustic Impedances’. In: *Proc. 13th AIAA/CEAS Aeronautics Conference*. Paper no. AIAA 2007-3540. 2007, pp. 1–14. DOI: [doi:10.2514/6.2007-3540](https://doi.org/10.2514/6.2007-3540).
- [113] J. P. Moeck, M. Oevermann, R. Klein, C. O. Paschereit, and H. Schmidt. ‘A two-way coupling for modeling thermoacoustic instabilities in a flat flame Rijke tube’. In: *Proceedings of the Combustion Institute* 32.1 (2009), pp. 1199–1207. DOI: [10.1016/j.proci.2008.05.062](https://doi.org/10.1016/j.proci.2008.05.062).
- [114] J. P. Moeck, D. A. Lacoste, D. Durox, T. F. Guiberti, T. Schuller, and C. O. Laux. ‘Stabilization of a methane-air swirl flame by rotating nanosecond spark discharges’. In: *IEEE Transactions on Plasma Science* 42.10 (2014), pp. 2562–2563. DOI: [10.1109/TPS.2014.2322955](https://doi.org/10.1109/TPS.2014.2322955).
- [115] J. P. Moeck, D. A. Lacoste, C. O. Laux, and C. O. Paschereit. ‘Control of combustion dynamics in a swirl-stabilized combustor with nanosecond repetitively pulsed discharges’. In: *51st AIAA Aerospace Sciences Meeting including the New Horizons Forum and Aerospace Exposition*. January. 2013, pp. 1–11. DOI: [10.2514/6.2013-565](https://doi.org/10.2514/6.2013-565).
- [116] J. P. Moeck and C. O. Paschereit. ‘Nonlinear Interactions of Multiple Linearly Unstable Thermoacoustic Modes’. In: *International Journal of Spray and Combustion Dynamics* 4.1 (2012), pp. 1–28. DOI: [10.1260/1756-8277.4.1.1](https://doi.org/10.1260/1756-8277.4.1.1).
- [117] J. P. Moeck. ‘Analysis, Modeling, and Control of Thermoacoustic Instabilities’. PhD thesis. Technische Universität Berlin, 2010, pp. 1–242.
- [118] M. L. Munjal and A. G. Doige. ‘Theory of a two source-location method for direct experimental evaluation of the four-pole parameters of an aeroacoustic element’. In: *Journal of Sound and Vibration* 141.2 (1990), pp. 323–333. DOI: [10.1016/0022-460X\(90\)90843-0](https://doi.org/10.1016/0022-460X(90)90843-0).
- [119] M. L. Munjal, F. P. Mechel, M. Vorländer, P. Költzsch, M. Ochmann, A. Cummings, W. Maysenhölder, W. Arnold, and O. V. Rudenko. ‘Muffler Acoustics’. In: *Formulas of Acoustics*. Ed. by Fridolin Mechel. 2nd Ed. Springer Berlin Heidelberg New York, 2008, pp. 793–841. DOI: [10.1115/1.4037833](https://doi.org/10.1115/1.4037833).
- [120] M. L. Munjal, M. Vorländer, P. Költzsch, M. Ochmann, A. Cummings, W. Maysenhölder, W. Arnold, and O. V. Rudenko. *Formulas of Acoustics*. Ed. by Fridolin Mechel. 2nd. Berlin, Heidelberg, New York: Springer Verlag, 2008, pp. 1–1275. DOI: [10.1115/1.4037833](https://doi.org/10.1115/1.4037833).

- [121] M. Munjal. *Acoustics of Ducts and Mufflers With Application to Exhaust and Ventilation System Design*. A Wiley-Interscience publication. Wiley, 1987.
- [122] R. M. Munt. ‘The interaction of sound with a subsonic jet issuing from a semi-infinite cylindrical pipe’. In: *Journal of Fluid Mechanics* 83.4 (1977), pp. 609–640. DOI: [10.1017/S0022112077001384](https://doi.org/10.1017/S0022112077001384).
- [123] F. Nicoud and T. Poinsot. ‘Thermoacoustic instabilities: Should the Rayleigh criterion be extended to include entropy changes?’ In: *Combustion and Flame* 142.1-2 (2005), pp. 153–159. DOI: [10.1016/j.combustflame.2005.02.013](https://doi.org/10.1016/j.combustflame.2005.02.013).
- [124] S. Niether, N. Hanraths, C. O. Paschereit, L. Panek, and J. P. Moeck. ‘Acoustic Combustor Forcing by Unsteady Air Injection into a Nozzle with High Subsonic Mean Flow’. In: *Proc. ASME Turbo Expo, June 26-30, Charlotte, NC, USA*. Paper no. GT2017-64608. 2017, V04BT04A032. DOI: [10.1115/GT2017-64608](https://doi.org/10.1115/GT2017-64608).
- [125] N. Noiray and B. Schuermans. ‘Theoretical and experimental investigations on damper performance for suppression of thermoacoustic oscillations’. In: *Journal of Sound and Vibration* 331.12 (2012), pp. 2753–2763. DOI: [10.1016/j.jsv.2012.02.005](https://doi.org/10.1016/j.jsv.2012.02.005).
- [126] V. Nori and J. Seitzman. ‘Evaluation of Chemiluminescence as a Combustion Diagnostic under Varying Operating Conditions’. In: *Proc. AIAA Aerospace Sciences Meeting and Exhibit, January 7 - 10, Reno, Nevada, USA*. 2008, pp. 1–14. DOI: [10.2514/6.2008-953](https://doi.org/10.2514/6.2008-953).
- [127] H. F. Olson and E. G. May. ‘Electronic Sound Absorber’. In: *Journal of the Acoustical Society of America* 25.6 (1953), pp. 1130–1136. DOI: [10.1121/1.1907249](https://doi.org/10.1121/1.1907249).
- [128] C. O. Paschereit, B. Schuermans, W. Polifke, and O. Mattson. ‘Measurement of Transfer Matrices and Source Terms of Premixed Flames’. In: *Journal of Engineering for Gas Turbines and Power* 124.2 (2002), pp. 239–247. DOI: [10.1115/1.1383255](https://doi.org/10.1115/1.1383255).
- [129] C. O. Paschereit, P. Flohr, and E. J. Gutmark. ‘Combustion Control by Vortex Breakdown Stabilization’. In: *Journal of Turbomachinery* 128.4 (2006), pp. 679–688. DOI: [10.1115/1.2218521](https://doi.org/10.1115/1.2218521).
- [130] C. O. Paschereit and E. Gutmark. ‘The Effectiveness of Passive Combustion Control Methods’. In: *Proc. ASME Turbo Expo, June 14-17, Vienna, Austria*. Paper no. GT2004-53587. 2004, pp. 361–374. DOI: [10.1115/GT2004-53587](https://doi.org/10.1115/GT2004-53587).
- [131] C. O. Paschereit, E. Gutmark, and W. Weisenstein. ‘Coherent structures in swirling flows and their role in acoustic combustion control’. In: *Physics of Fluids* 11.9 (1999), pp. 2667–2678. DOI: [10.1063/1.870128](https://doi.org/10.1063/1.870128).
- [132] K. S. Peat. ‘Evaluation of Four-Pole Parameters for Ducts with Flow by the Finite Element Method’. In: *Journal of Sound and Vibration* 84.3 (1982), pp. 389–395. DOI: [10.1016/0022-460X\(82\)90485-0](https://doi.org/10.1016/0022-460X(82)90485-0).
- [133] A. D. Pierce. *Acoustics: An Introduction to its Physical Principles and Applications*. Acoustical Society of America, 1991.

- [134] G. Pilla, D. Galley, D. A. Lacoste, F. Lacas, D. Veynante, and C. O. Laux. ‘Stabilization of a Turbulent Premixed Flame Using a Nanosecond Repetitively Pulsed Plasma’. In: *Plasma Science, IEEE Transactions on* 34.6 (2006), pp. 2471–2477. DOI: [10.1109/TPS.2006.886081](https://doi.org/10.1109/TPS.2006.886081).
- [135] T. Poinsot, C. L. Chatelier, S. M. Candel, and E. Esposito. ‘Experimental Determination of the Reflection Coefficient of a Premixed Flame in a Duct’. In: *Journal of Sound and Vibration* 107.2 (1986), pp. 265–278. DOI: [10.1016/0022-460X\(86\)90237-3](https://doi.org/10.1016/0022-460X(86)90237-3).
- [136] W. Polifke, C. O. Paschereit, and K. Döbbling. ‘Constructive and Destructive Interference of Acoustic and Entropy Waves in a Premixed Combustor with a Choked Exit’. In: *Journal of Acoustics and Vibration* 6.3 (2001), pp. 135–146. DOI: [10.20855/ijav.2001.6.382](https://doi.org/10.20855/ijav.2001.6.382).
- [137] W. Polifke, C. O. Paschereit, and T. Sattelmayer. ‘A Universally Applicable Stability Criterion for Complex Thermo-Acoustic Systems’. In: *18. Deutsch-Niederländischer Flammentag*. VDI-Bericht Nr.1313. VDI Verlag GmbH. 1997, pp. 455–460.
- [138] A. Rasheed, A. Furman, and A. J. Dean. ‘Experimental Investigations of an Axial Turbine Driven by a Multi-tube Pulsed Detonation Combustor System’. In: *Proc. AIAA/ASME/SAE/ASEE Joint Propulsion Conference and Exhibit, July 10-13, Tucson, Arizona, USA*. July. Paper no. AIAA 2005-4209. 2005, pp. 1–13. DOI: [10.2514/6.2005-4209](https://doi.org/10.2514/6.2005-4209).
- [139] A. Rasheed, A. Furman, and A. J. Dean. ‘Wave Attenuation and Interactions in a Pulsed Detonation Combustor-Turbine Hybrid System’. In: *Proc. AIAA Aerospace Sciences Meeting and Exhibit, January 9-12, Reno, Nevada, USA*. Paper no. AIAA 2006-1235. 2006, pp. 1–12. DOI: [10.2514/6.2006-1235](https://doi.org/10.2514/6.2006-1235).
- [140] S. Rea, S. James, C. Goy, and M. J. F. Colechin. ‘On-line combustion monitoring on dry low NO<sub>x</sub> industrial gas turbines’. In: *Measurement Science and Technology* 14.7 (2003), pp. 1123–1130. DOI: [10.1088/0957-0233/14/7/330](https://doi.org/10.1088/0957-0233/14/7/330).
- [141] G. A. Richards, D. L. Straub, and E. H. Robey. ‘Passive Control of Combustion Dynamics in Stationary Gas Turbines’. In: *Journal of Propulsion and Power* 19.5 (2003), pp. 795–810. DOI: [10.2514/2.6195](https://doi.org/10.2514/2.6195).
- [142] G. A. Richards, J. D. Thornton, E. H. Robey, and L. Arellano. ‘Open-Loop Active Control of Combustion Dynamics on a Gas Turbine Engine’. In: *Journal of Engineering for Gas Turbines and Power* 129.1 (2007), pp. 38–48. DOI: [10.1115/1.2204978](https://doi.org/10.1115/1.2204978).
- [143] S. W. Rienstra and A. Hirschberg. *An Introduction to Acoustics*. Eindhoven University of Technology, Mar. 2014, pp. 1–296.
- [144] S. W. Rienstra. ‘Webster’s Horn Equation Revisited’. In: *SIAM Journal on Applied Mathematics* 65.6 (2005), pp. 1981–2004. DOI: [10.1137/S0036139902413040](https://doi.org/10.1137/S0036139902413040).
- [145] Rolls-Royce. *SAGE 6 - ALECSYS (Advance Lean Combustion System)*. English. accessed on 04-30-2018. Mar. 2017. URL: <http://www.cleansky.eu/sites/default/files/inline-files/6.%20SAGE%20%20-%20ALECSYS.pdf>.

- [146] G. D. Roy, S. M. Frolov, A. A. Borisov, and D. W. Netzer. ‘Pulse detonation propulsion: Challenges, current status, and future perspective’. In: *Progress in Energy and Combustion Science* 30.6 (2004), pp. 545–672. DOI: [10.1016/j.pecs.2004.05.001](https://doi.org/10.1016/j.pecs.2004.05.001).
- [147] T. Sattelmayer. ‘Influence of the Combustor Aerodynamics on Combustion Instabilities From Equivalence Ratio Fluctuations’. In: *Journal of Engineering for Gas Turbines and Power* 125.1 (2003), pp. 11–19. DOI: [10.1115/1.1365159](https://doi.org/10.1115/1.1365159).
- [148] T. Sattelmayer and W. Polifke. ‘Assessment of methods for the computation of the linear stability of combustors’. In: *Combustion Science and Technology* 175.3 (2003), pp. 453–476. DOI: [10.1080/00102200302382](https://doi.org/10.1080/00102200302382).
- [149] A. Saurabh, R. Steinert, J. P. Moeck, and C. O. Paschereit. ‘Swirl Flame Response to Traveling Acoustic Waves’. In: *Proc. ASME Turbo Expo, June 16-20, Düsseldorf, Germany*. Paper no. GT2014-26829 SWIRL. 2014, V04BT04A043. DOI: [10.1115/GT2014-26829](https://doi.org/10.1115/GT2014-26829).
- [150] K. C. Schadow and E. Gutmark. ‘Combustion instability related to vortex shedding in dump combustors and their passive control’. In: *Progress in Energy and Combustion Science* 18 (1992), pp. 117–132.
- [151] D. Schäuble, D. Volkert, D. Jacobs, and K. Töpfer. *CO<sub>2</sub>-Emissionsgrenzwerte für Kraftwerke - Ausgestaltungsansätze und Bewertung einer möglichen Einführung auf nationaler Ebene*. German. accessed on 23-03-2018. Institute for Advanced Sustainability Studies. Apr. 2014. URL: [http://www.iass-potsdam.de/sites/default/files/files/working\\_paper\\_emissionsgrenzwerte\\_0.pdf](http://www.iass-potsdam.de/sites/default/files/files/working_paper_emissionsgrenzwerte_0.pdf).
- [152] M. Schmid, N. Trott, R. Kathan, D. Fanaca, and T. Sattelmayer. ‘Experimental Investigation of the Influence of Water Injection on Acoustic Properties of the Exhaust System of a Gas Turbine Combustion Test Rig’. In: *Proc. of ASME Turbo Expo, June 6-10, Vancouver, British Columbia, Canada*. Paper no. GT2011-46366. 2011, pp. 1129–1139. DOI: [10.1115/GT2011-46366](https://doi.org/10.1115/GT2011-46366).
- [153] G. Schmidt. ‘Erweiterung der akustischen Wellenzerlegung für reale Brennkammergeometrien: Theorie und experimentelle Validierung’. Master thesis. TU Berlin, 2015.
- [154] P. Schmitt, T. Poinsot, B. B. H. Schuermans, and K. P. Geigle. ‘Large-eddy simulation and experimental study of heat transfer, nitric oxide emissions and combustion instability in a swirled turbulent high-pressure burner’. In: *Journal of Fluid Mechanics* 570.2007 (2007), pp. 17–46. DOI: [10.1017/S0022112006003156](https://doi.org/10.1017/S0022112006003156).
- [155] E. W. Schneehagen. ‘Akustische Simulation der Fremddregung eines Brennkammerversuchsstandes’. Master thesis. TU Berlin, 2016.
- [156] B. Schuermans. ‘Modeling and Control of Thermoacoustic Instabilities’. PhD thesis. École Polytechnique Fédérale de Lausanne, 2003.
- [157] B. Schuermans, V. Bellucci, F. Guethe, F. Meili, P. Flohr, and C. O. Paschereit. ‘A Detailed Analysis of Thermoacoustic Interaction Mechanisms in a Turbulent Premixed Flame’. In: *Proc. ASME Turbo Expo, June 14-17, Vienna, Austria*. Paper no. GT2004-53831. 2004, pp. 539–551. DOI: [10.1115/GT2004-53831](https://doi.org/10.1115/GT2004-53831).

- [158] B. Schuermans, V. Bellucci, and C. O. Paschereit. ‘Thermoacoustic Modeling and Control of Multi Burner Combustion Systems’. In: *Proc. ASME Turbo Expo, June 16-19, Atlanta, Georgia, USA*. Paper no. GT2003-38688. 2003, pp. 509–519. DOI: [10.1115/GT2003-38688](https://doi.org/10.1115/GT2003-38688).
- [159] B. Schuermans, F. Guethe, and W. Mohr. ‘Optical Transfer Function Measurements for Technically Premixed Flames’. In: *Journal of Engineering for Gas Turbines and Power* 132.8 (2010), p. 081501. DOI: [10.1115/1.3124663](https://doi.org/10.1115/1.3124663).
- [160] B. Schuermans, F. Guethe, D. Pennell, D. Guyot, and C. O. Paschereit. ‘Thermoacoustic Modeling of a Gas Turbine Using Transfer Functions Measured Under Full Engine Pressure’. In: *Journal of Engineering for Gas Turbines and Power* 132.11 (2010), p. 111503. DOI: [10.1115/1.4000854](https://doi.org/10.1115/1.4000854).
- [161] B. Schuermans, W. Polifke, and C. O. Paschereit. ‘Modeling Transfer Matrices of Premixed Flames and Comparison with Experimental Results’. In: *Proc. ASME Turbo Expo, June 7-10, Indianapolis, Indiana, USA*. Paper no. 99-GT-132. 1999, V002T02A024. DOI: [10.1115/99-GT-132](https://doi.org/10.1115/99-GT-132).
- [162] B. Schuermans, W. Polifke, C. O. Paschereit, and J. H. van der Linden. ‘Prediction of Acoustic Pressure Spectra in Combustion Systems Using Swirl Stabilized Gas Turbine Burners’. In: *Proc. of IGTI TE2000, May 13-16, Munich, Bavaria, Germany*. Paper no. 2000-GT-0105. 2000, V002T02A025. DOI: [10.1115/2000-GT-0105](https://doi.org/10.1115/2000-GT-0105).
- [163] J. R. Seume, N. Vortmeyer, W. Krause, J. Hermann, C.-C. Hantschk, P. Zangl, S. Gleis, D. Vortmeyer, and A. Orthmann. ‘Application of Active Combustion Instability Control to a Heavy Duty Gas Turbine’. In: *Journal of Engineering for Gas Turbines and Power* 120.10 (1998), pp. 721–726. DOI: [10.1115/1.2818459](https://doi.org/10.1115/1.2818459).
- [164] A. F. Seybert. ‘Experimental determination of acoustic properties using a two-microphone random-excitation technique’. In: *Journal of the Acoustical Society of America* 61 (1977), pp. 1362–1370. DOI: [10.1121/1.381403](https://doi.org/10.1121/1.381403).
- [165] C. S. Shin, H. D. Kim, T. Setoguchi, and S. Matsuo. ‘A Computational Sstudy of Thrust Vectoring Control Using Dual Throat Nozzle’. In: *Journal of Thermal Science* 19.6 (2010), pp. 486–490. DOI: [10.1007/s11630-010-0413-x](https://doi.org/10.1007/s11630-010-0413-x).
- [166] SIEMENS AG. English. accessed on 03-19-2018. Feb. 2018. URL: [https://www.siemens.com/content/dam/internet/siemens-com/global/products-services/energy/pg/gas-turbines/application-pages/2018-02-28-sgt5-9000hl-en/2018-02-28-sgt5-9000hl-en/resources/img/01\\_stage\\_360/HL-Class\\_01.jpg](https://www.siemens.com/content/dam/internet/siemens-com/global/products-services/energy/pg/gas-turbines/application-pages/2018-02-28-sgt5-9000hl-en/2018-02-28-sgt5-9000hl-en/resources/img/01_stage_360/HL-Class_01.jpg).
- [167] SIEMENS Energy. *SGT5-8000H heavy duty gas turbine (50Hz)*. English. accessed on 03-23-2018. 2018. URL: <https://www.siemens.com/global/en/home/products/energy/power-generation/gas-turbines/sgt5-8000h.html#!/>.
- [168] H. Sigloch. *Technische Fluidmechanik*. Berlin, Heidelberg: Springer Berlin Heidelberg, 2012. DOI: [10.1007/978-3-642-22845-2](https://doi.org/10.1007/978-3-642-22845-2).
- [169] C. E. Spyropoulos. ‘A Sonic Oscillator’. In: *Proceedings of the Fluid Amplification Symposium*. Vol. 3. Harry Diamond Laboratories. Washington, D.C., 1964.

- [170] J. W. Strutt (3rd Baron Rayleigh). ‘The Explanation of Certain Acoustical Phenomena’. In: *Nature* 18 (July 1878), pp. 319–321. DOI: [10.1038/018319a0](https://doi.org/10.1038/018319a0).
- [171] P. B. Subrahmanyam, R. I. Sujith, and T. C. Lieuwen. ‘A family of exact transient solutions for acoustic wave propagation in inhomogeneous, non-uniform area ducts’. In: *Journal of Sound and Vibration* 240.4 (2001), pp. 705–715. DOI: [10.1006/jsvi.2000.3261](https://doi.org/10.1006/jsvi.2000.3261).
- [172] P. B. Subrahmanyam, R. I. Sujith, and T. C. Lieuwen. ‘Propagation of Sound in Inhomogeneous Media: Exact, Transient Solutions in Curvilinear Geometries’. In: *Journal of Vibration and Acoustics* 125.2 (2003), pp. 133–136. DOI: [10.1115/1.1553471](https://doi.org/10.1115/1.1553471).
- [173] R. I. Sujith, G. A. Waldherr, and B. T. Zinn. ‘An exact solution for one-dimensional acoustic fields in ducts with an axial temperature gradient’. In: *Journal of Sound and Vibration* 184.3 (1995), pp. 389–402. DOI: [10.1006/jsvi.1995.0323](https://doi.org/10.1006/jsvi.1995.0323).
- [174] S. K. Thumuluru and T. Lieuwen. ‘Characterization of acoustically forced swirl flame dynamics’. In: *Proceedings of the Combustion Institute* 32.2 (2009), pp. 2893–2900. DOI: [10.1016/j.proci.2008.05.037](https://doi.org/10.1016/j.proci.2008.05.037).
- [175] H. Tijdeman. ‘On the Propagation of Sound Waves in Cylindrical Tubes’. In: *Journal of Sound and Vibration* 39.1 (1975), pp. 1–33. DOI: [10.1121/1.1911130](https://doi.org/10.1121/1.1911130).
- [176] N. Tran, S. Ducruix, and T. Schuller. ‘Analysis and Control of Combustion Instabilities by Adaptive Reflection Coefficients’. In: *13th AIAA/CEAS Aeroacoustics Conference (28th AIAA Aeroacoustics Conference)* (2007). DOI: [10.2514/6.2007-3716](https://doi.org/10.2514/6.2007-3716).
- [177] E. H. Truckenbrodt. *Fluidmechanik: Band 2: Elementare Strömungsvorgänge dichtveränderlicher Fluide sowie Potential- und Grenzschichtströmungen*. 4th ed. Springer-Verlag Berlin Heidelberg, 2008. DOI: [10.1007/978-3-540-79024-2](https://doi.org/10.1007/978-3-540-79024-2).
- [178] United Nations Framework Convention on Climate Change. *The Paris Agreement*. English. accessed on 03-23-2018. 2018. URL: [http://unfccc.int/paris\\_agreement/items/9485.php](http://unfccc.int/paris_agreement/items/9485.php).
- [179] U.S. Energy Information Administration. *International Energy Outlook*. English. accessed on 03-22-2018. 2017. URL: [https://www.eia.gov/outlooks/ieo/pdf/0484\(2017\).pdf](https://www.eia.gov/outlooks/ieo/pdf/0484(2017).pdf).
- [180] U.S. Energy Information Administration. *Table A.3. Carbon Dioxide Uncontrolled Emission Factors*. English. accessed on 03-26-2018. 2018. URL: [https://www.eia.gov/electricity/annual/html/epa\\_a\\_03.html](https://www.eia.gov/electricity/annual/html/epa_a_03.html).
- [181] Vattenfall. *Braunkohlenkraftwerk Boxberg*. German. accessed on 03-26-2018. 2012. URL: [https://corporate.vattenfall.de/globalassets/deutschland/energie\\_im\\_fokus/energieproduktion/kohle/boxberg/aus-braunkohle-wird-energie\\_boxberg.pdf](https://corporate.vattenfall.de/globalassets/deutschland/energie_im_fokus/energieproduktion/kohle/boxberg/aus-braunkohle-wird-energie_boxberg.pdf).
- [182] P. J. Vermeulen, C.-F. Chin, and W. K. Yu. ‘Mixing of an Acoustically Pulsed Air Jet with a Confined Crossflow’. In: *Journal of Propulsion and Power* 6.6 (1990), pp. 777–783. DOI: [10.2514/3.23284](https://doi.org/10.2514/3.23284).

- [183] P. J. Vermeulen, P. Grabinski, and V. Ramesh. ‘Mixing of an Acoustically Excited Air Jet With a Confined Hot Crossflow’. In: *Journal of Engineering for Gas Turbines and Power* 114.1 (1992), pp. 46–54. DOI: [10.1115/1.2906306](https://doi.org/10.1115/1.2906306).
- [184] Vibro-Meter. *Piezoelectric Pressure Transducer Type CP 235*. accessed on 03-20-2018. Meggit SA. Rte de Moncor 4, P.O. Box, CH-1701 Fribourg, Switzerland, 2017.
- [185] H. Viets. ‘Flip-Flop Jet Nozzle’. In: *AIAA Journal* 13.10 (1975), pp. 1375–1379. DOI: [10.2514/3.60550](https://doi.org/10.2514/3.60550).
- [186] Z. X. Wang, J. W. Shi, L. Zhou, B. Zhang, X. L. Sun, and H. Yan. ‘Investigation on Fluidic Throat Control of Fixed Geometric Nozzle and Coupling Performance with Aero-Engine’. In: *Proc. ASME Turbo Expo, June 15-19, Montreal, Canada*. Paper no. GT2015-43162. 2015, V001T01A019. DOI: [10.1115/GT2015-43162](https://doi.org/10.1115/GT2015-43162).
- [187] J. Warnatz, U. Maas, and R. W. Dibble. *Combustion*. 4th ed. Berlin, Heidelberg: Springer-Verlag, 2006, pp. 1–388.
- [188] D. Wassmer, B. Schuermans, C. O. Paschereit, and J. P. Moeck. ‘An Acoustic Time-of-Flight Approach for Unsteady Temperature Measurements: Characterization of Entropy Waves in a Model Gas Turbine Combustor’. In: *Journal of Engineering for Gas Turbines and Power* 139.4 (2016). Paper no: GTP-16-1289, p. 041501. DOI: [10.1115/1.4034542](https://doi.org/10.1115/1.4034542).
- [189] A. G. Webster. ‘Acoustical Impedance, and the Theory of Horns and of the Phonograph’. In: *Proceedings of the National Academy of Sciences of the United States of America* 5.7 (1919), pp. 275–282. DOI: [10.1073/pnas.5.7.275](https://doi.org/10.1073/pnas.5.7.275).
- [190] A. Widenhorn, B. Noll, and M. Aigner. ‘Impedance Boundary Conditions for the Numerical Simulation of Gas Turbine Combustion Systems’. In: *Proc. ASME Turbo Expo, June 9-13, Berlin, Germany*. Paper no. GT2008-50445 IMPEDANCE. 2008, pp. 341–351. DOI: [10.1115/GT2008-50445](https://doi.org/10.1115/GT2008-50445).
- [191] P. Wolf, G. Staffelbach, A. Roux, L. Gicquel, T. Poinso, and V. Moureau. ‘Massively parallel LES of azimuthal thermo-acoustic instabilities in annular gas turbines’. In: *Combustion for Aerospace Propulsion* 337.6-7 (2009), pp. 385–394. DOI: [10.1016/j.crme.2009.06.003](https://doi.org/10.1016/j.crme.2009.06.003).
- [192] R. F. H. Woodberry and R. J. Zeamer. *Solid Rocket Thrust Vector Control*. Tech. rep. NASA SP-8114. Dec. 1974, pp. 1–199.
- [193] M. Zajadatz, R. Lachner, S. Bernero, Christian Motz, and P. Flohr. ‘Development and Design of Alstom’s Staged Fuel Gas Injection EV Burner for NOx Reduction’. In: *Proc. ASME Turbo Expo, May 14-17, Montreal, Canada*. Paper no. GT2007-27730. 2007, pp. 559–567. DOI: [10.1115/GT2007-27730](https://doi.org/10.1115/GT2007-27730).
- [194] R. J. Zeamer. ‘Liquid-Injection Thrust Vector Control’. In: *Journal of Spacecraft and Rockets* 14.6 (1977), pp. 321–322. DOI: [10.2514/3.57203](https://doi.org/10.2514/3.57203).
- [195] D. Zhao, Z. Lu, H. Zhao, X. Y. Li, B. Wang, and P. Liu. ‘A review of active control approaches in stabilizing combustion systems in aerospace industry’. In: *Progress in*

- Aerospace Sciences* 97.January (2018), pp. 35–60. DOI: [10.1016/j.paerosci.2018.01.002](https://doi.org/10.1016/j.paerosci.2018.01.002).
- [196] K. Zhou and J. C. Doyle. *Essentials of Robust Control*. Louisiana: Prentice Hall, 1999, pp. 1–425.
- [197] V. L. Zimont, V. Moreu, V. Battaglia, and R. Modi. ‘RANS and LES Modeling of the GE10 Burner’. In: *Energy and Power Engineering 3* (2011), pp. 607–615. DOI: [10.4236/epe.2011.35076](https://doi.org/10.4236/epe.2011.35076).
- [198] B. T. Zinn and T. C. Lieuwen. ‘Combustion Instabilities: Basic Concepts’. In: *Combustion Instabilities In Gas Turbine Engines: Operational Experience, Fundamental Mechanisms, and Modeling*. American Institute of Aeronautics and Astronautics, 2005, pp. 3–26. DOI: [10.2514/5.9781600866807.0003.0026](https://doi.org/10.2514/5.9781600866807.0003.0026).



# APPENDIX A

## Validation Case For The Analytical Transfer Matrix Method with Mean Flow

The analytic transfer matrices for mean flow conditions, discussed in SUBSEC. 4.2.3, were validated with various test cases. One of these, adapted from the book of Ehrenfried [45], is presented here. It incorporates an increasing cross-sectional jump and a low-Mach number mean flow. A schematic of the setup is depicted in FIG. A.1. Assumptions for the analytical

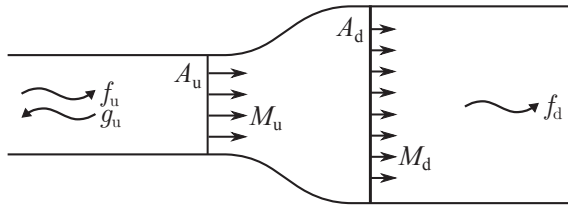


**Figure A.1.:** Test case for comparison of the results from the two transfer matrix approaches to an analytical result. Two ducts of different diameters are connected via a cross-sectional jump. Mean flow is denoted by the corresponding Mach numbers.

solution of the problem are plane wave propagation, no thermal conductivity, inviscid media, and negligence of boundary layers. Further assuming non-reflecting terminations at both outlets, the acoustic pressures inside the upstream and downstream ducts read:

$$\begin{aligned} p'_u(x,t) &= \hat{f}_u e^{i(\omega t - k^+ x)} + \hat{g}_u e^{i(\omega t + k^- x)} \\ p'_d(x,t) &= \hat{f}_d e^{i(\omega t - k^+ x)}. \end{aligned} \quad (\text{A.1})$$

The downstream propagating wave in the upstream duct  $\hat{f}_u$  acoustically excites the system. Ehrenfried [45] further assumes an incompressible flow, which allows for the conservation of mass (EQ. 2.2) and energy (EQ. 2.4) to be rearranged to calculate the amplitudes of the downstream and upstream propagating waves  $\hat{f}_d$  and  $\hat{g}_u$ :

$$\hat{f}_u(M_u + 1) + \hat{g}_u(M_u - 1) = \frac{A_d}{A_u} \hat{f}_d(M_d + 1) \quad (\text{A.2a})$$

$$\hat{f}_u(1 + M_u) + \hat{g}_u(1 - M_u) = \hat{f}_d(1 + M_d). \quad (\text{A.2b})$$

In the calculation, the maximum Mach number does not exceed  $M = 0.2$ , thus ensuring incompressible flow. Furthermore, the acoustic excitation amplitude is chosen sufficiently small, only allowing for linear acoustics. The ratio of cross-sectional areas is  $A_d/A_u = 2$ . The reference case could be modified in order to deliver a transfer matrix as output, which is omitted here. Instead, the equivalent ratios of sound pressure and particle velocity upstream and downstream are compared to those obtained from the two transfer matrix approaches.

The acoustic pressure is scaled with the characteristic acoustic impedance  $\bar{\rho}\bar{c}$ , in order to arrive at non-dimensional quantities. The phase angles, calculated with the two transfer matrix approaches, match those obtained with the analytical reference in all four plots. Further, the absolute values of the depicted ratios agree quite well for the first three plots, when focusing on the frequency range from 50 Hz to 400 Hz. In all investigated cases, the TMM from Greitzer et al. [55] delivers higher absolute values, while the transfer matrix derived by Munjal [121] yields lower absolute values. Within all four plots, the same tendency is observed. For the transfer behavior from upstream to downstream particle velocity, maximal deviations amount to approximately 10% above and below the reference results.

Several other test cases further substantiate this outcome. In any case, the tendency of slight overestimations obtained from the TMM derived by Greitzer et al. [55] and underestimations of the TMM results of Munjal [121] are observed. Thus, both methods should be incorporated in the development of a prediction of the plenum's transfer behavior, initially.

In summary, the applied methods have shown to produce results that can be used as a basis for the fit to numerical data. Note that this fit is required anyways, before arriving at a reliable transfer matrix representation with mean flow.

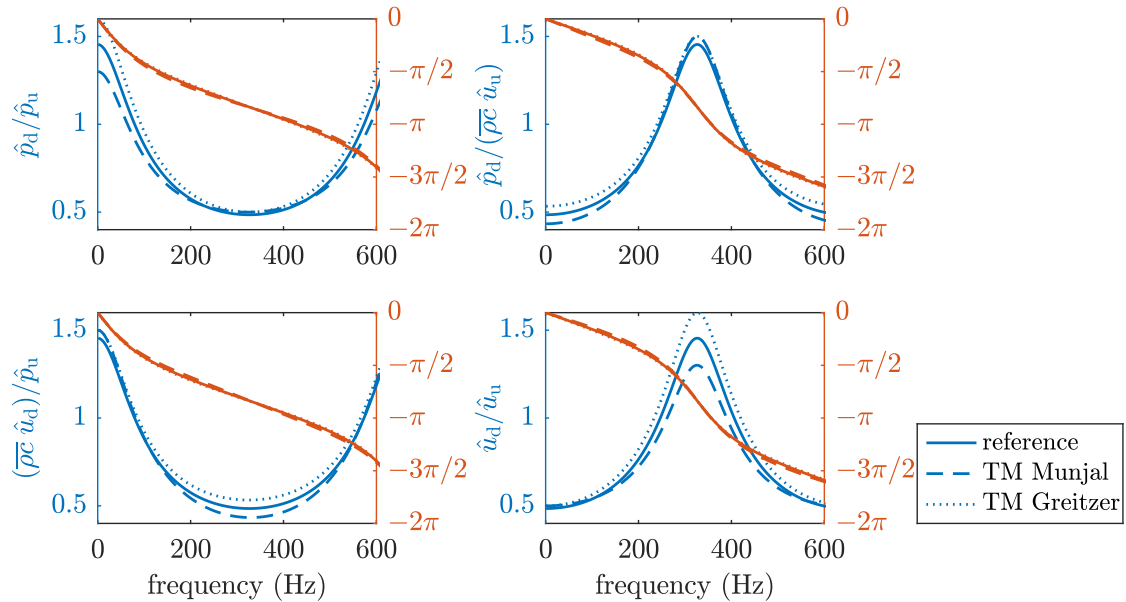


**Figure A.2.:** Downstream to upstream ratios of acoustic pressure and particle velocity for a cross-sectional jump with low-Mach number mean flow. Calculated from an analytical reference case (solid) and using the transfer matrix method of Munjal [121] (dashed) and of Greitzer et al. [55] (dotted)